Incorporating strength constraints in a simultaneous material anisotropy and topology optimization of composite laminate structures

Lander Vertonghen

To cite this version:

Lander Vertonghen. Incorporating strength constraints in a simultaneous material anisotropy and topology optimization of composite laminate structures. Mechanics [physics]. Sorbonne Université, 2023. English. NNT : 2023SORUS194 . tel-04562726

HAL Id: tel-04562726
https://theses.hal.science/tel-04562726

Submitted on 29 Apr 2024

Thèse de doctorat de Sorbonne Université

Spécialité : Mécanique

Incorporating strength constraints in a simultaneous material anisotropy and topology optimization of composite laminate structures

Incorporation de contraintes de résistance dans une optimisation simultanée de la topologie et de l'anisotropie de structures composites stratifiés

Présentée par

Lander Vertonghen

Préparée à l'ONERA – The French Aerospace Lab – 92320 Châtillon
Institut Jean le Rond d'Alembert – Sorbonne Université / CNRS UMR 7190
Ecole doctorale : ED391 SMAER

Thèse soutenue le 28 avril 2023 devant le jury composé de

M. Erik LUND	Professor, Aalborg University	Président du Jury
M. Rafael ESTEVEZ	Professeur, Université de Grenoble Alpes	Rapporteur
M. Frédéric MESSINE	Professeur, Université de Toulouse	Rapporteur
M. Daniël PEETERS	Assistant professor, Delft University of Technology	Examinateur
Mme. Angela VINCENTI	Professeure, Sorbonne Université	Examinatrice
M. Boris DESMORAT	Maître de Conférence HDR, Sorbonne Université	Directeur de thèse
M. François-Xavier IRISARRI	Ingénieur de recherche, ONERA	Encadrant
M. Dimitri BETTEBGHOR	Ingénieur de recherche, ONERA	Encadrant
M. Attilio CHIAPPINI	Ingénieur, Airbus Atlantic	Invité

Acknowledgments

As a start, I would like to thank my promoter Boris Desmorat, and both my supervisors François-Xavier Irisarri and Dimitri Bettebghor for their advise and motivation throughout these 3 years, not all being equally easy moments. You helped me persevere, and guided me in each your respective field, to broaden my knowledge and better the outcome of this research. Tank you for all the insightful technical and never-lasting discussions we had during this time, it has been a pleasure working with each of you.

Thank you also to the members of my defense jury, starting with Pr. Lund for having accepted to be chairman of the committee. I am grateful for the discussions we had during conferences on this research topic. A special thank you to Dr. Peeters to have been part of the jury, but foremost also to have brought me in contact with ONERA and this research opportunity. Also a thank you to Pr. Vincenti, to have shown interest and followed this research. Thank you to Pr. Messine for having accepted to review this work as an external jury, from a topology optimization background applied in a different field. Lastly, I would like to thank Pr. Estevez, for his time as a reviewer of this thesis, but also to have been part of the yearly progress meetings and having followed this research throughout the 3 years.

I am grateful to Airbus Atlantic which made this thesis possible, by providing the opportunity for this research and being able to collaborate on the topic. I am more specifically tankful to Attilio Chiappini for the discussions we have had on the progress and outcome of this research and its future integration into industry.

I would then like to thank the whole MC^2 team at ONERA, both permanent staff and fellow PhD students, colleagues who became friends underway, for the cheerful moments which helped take my mind off the research. Thank you in particular for all the good times playing card games during breaks. I would like to specifically thank the optimization crew, Enrico, Florent, Cédric and Ludovic for the discussions and help on the topic.

Thank you to all my friends which have been present for me during these 3 years, whether in France, Belgium or the Netherlands. There has not been much time to see each other but thank you for your support each time we met up, by managing to keep some sanity and get my mind of the research.

To end, I would like to thank my parents and family for always believing in me, and being supportive all along this journey to make my dreams come true. And finally, thank you Eva also for your support, believe and pushing me to pursue this research opportunity.

Table of Contents

Acknowledgments iii

Table of Contents v

List of Figures ix

List of Tables xv

Nomenclature xvii

Résumé xx

1 Introduction 1

2 State of the Art 5
- 2.1 An Introduction to Structural Optimization 5
- 2.2 Compliance Minimization with Isotropic Material 6
  - 2.2.1 Topology Parametrization 7
  - 2.2.2 Optimization Algorithms 9
- 2.3 Strength-Based Topology Optimization 11
  - 2.3.1 Stress Singularity 11
  - 2.3.2 Computational Cost 12
  - 2.3.3 Strength Criteria 14
  - 2.3.4 Optimization Algorithms 14
- 2.4 Anisotropy Considerations in Optimization 15
  - 2.4.1 Material Anisotropy in Topology Optimization 15
  - 2.4.2 Macroscopic Parametrization for Composite Laminates 17
  - 2.4.3 Integration of Strength Constraints for Laminate Optimization 20
  - 2.4.4 Specific Numerical Issues with Anisotropy 22
- 2.5 Polar Formalism 22
  - 2.5.1 Polar Parameters Definition 22
  - 2.5.2 Admissible Design Space 23
  - 2.5.3 Physical Interpretation of the Polar Invariants 24
  - 2.5.4 Composite Laminate Case 25
  - 2.5.5 Use in Topology Optimization 26
- 2.6 Conclusion and Thesis Objective 27

3 Definition of a Gradient-Based Strategy for Concurrent Topology and Anisotropy Optimization 29
- 3.1 Introduction 29
- 3.2 Optimization Problem Parametrization 29

3.2.1 Topology Parametrization . . . 30
3.2.2 Anisotropy Parametrization . . . 30
3.2.3 Orthotropic Material Domain of Existence . . . 31
3.2.4 Domain of Existence Remapping . . . 32
3.3 Optimization Strategy . . . 33
3.4 Compliance and Volume Gradients Definition . . . 35
3.5 Results and Discussion . . . 36
3.5.1 About the Proper Use of η_1 to Escape Local Optima . . . 38
3.5.2 Optimization with Thermodynamic Bounds . . . 40
3.5.3 Optimization with Laminates within the Geometric Domain . . . 46
3.6 Conclusion . . . 48

4 Optimization Constraint and Gradient Derivation Based on an Elliptic Stress Criterion for the Simultaneous Density and Orthotropic Material Orientation Optimization 51
4.1 Introduction . . . 51
4.2 Isotropic Stress Criterion . . . 52
4.2.1 Optimization Constraint Definition . . . 52
4.2.2 Optimization Constraint Gradient . . . 54
4.3 Elliptic Failure Criterion for a Combined Density and Orthotropic Material Orientation Optimization . . . 57
4.3.1 Elliptic Failure Criteria . . . 57
4.3.2 Optimization Constraint Definition . . . 59
4.3.3 Optimization Constraint Gradient . . . 61
4.4 Towards Complex Application Cases . . . 64
4.4.1 Advanced Failure Criterion . . . 64
4.4.2 Adapting to 3D Optimization . . . 64
4.4.3 Commercial FEM Integration . . . 64
4.4.4 Multi-Loading Optimizations . . . 65
4.5 Conclusion . . . 65

5 Stress-Based Density and Material Orientation Topology Optimization: Applications 67
5.1 Introduction . . . 67
5.2 Different Problem Formulations . . . 67
5.3 Stress-Based Topology Optimization with Isotropic Stiffness and Strength . . . 69
5.3.1 Influence of the Aggregation Parameter μ . . . 69
5.3.2 Influence of the Optimization Problem Formulation . . . 71
5.4 Stress-Based Topology Optimization with Isotropic Stiffness and Strength Anisotropy Induced by 3D Printing . . . 74
5.5 Stress-Based Topology Optimization with Fixed Anisotropic Stiffness and Strength . . . 76
5.5.1 Tsai-Wu Failure Criterion . . . 77
5.5.2 Influence of the Choice of the Failure Criterion . . . 79
5.5.3 Influence of the Optimization Objective Normalization . . . 79
5.6 Concurrent Density and Material Orientation Optimization for Steered UD Composite Fibers 82
5.6.1 Filter on Material Orientations . . . 82
5.6.2 Initial Material Orientation Influence . . . 82
5.6.3 Influence of the Choice of the Anisotropic Failure Criterion . . . 84
5.6.4 Influence of an Increased Loading . . . 85
5.6.5 Comparison with Literature . . . 88
5.7 Conclusion . . . 89

6 Topology Optimization of Laminates taking a Conservative Strain Envelope into account 91
6.1 Introduction . . . 91
6.2 Conservative Strain Envelope Definition . . . 92
6.3 Equivalent Strain Value for the Optimization Constraint . . . 94
6.4 Conservative Strain Envelope Gradient Definition . . . 94
6.5 Validation of the Strain-Based Topology Optimization . . . 96
6.6 Topology and Anisotropy Optimization with a Conservative Tsai-Wu Strain Envelope . . . 99
6.6.1 Considering Material Orientations for a Uni-Directional Ply . . . 99
6.6.2 Considering Laminates . . . 101
6.7 Influence of Different Optimization Problem Formulations with a User-Defined Envelope . . . 103
6.7.1 Volume Minimization with a Strain-Based Strength Constraint . . . 104
6.7.2 Compliance Minimization with a Volume Constraint . . . 104
6.7.3 Volume Minimization with Strain-Based Strength and Compliance Constraints . . . 106
6.7.4 Compliance Minimization with Strain-Based Strength and Volume Constraints . . . 107
6.8 Indirect Buckling Delay Control . . . 109
6.8.1 Influence of the Compressive Allowable Value X_c with a Uni-Directional Ply . . . 109
6.8.2 Influence of the Compressive Stress Allowable Values with a Laminate . . . 111
6.9 Conclusion . . . 112

7 Conclusion and Perspectives 115
7.1 Conclusion . . . 115
7.2 Perspectives . . . 118

Communications 119

Bibliography 121

A Tsai-Wu Criterion Strain Invariants 133

B Finite Element Model 135

List of Figures

1 Topologies et distributions d’anisotropie obtenues par des optimisations simultanées en densité et anisotropie en élargissant progressivement le domaine de conception en anisotropie : de gauche à droite, solutions obtenues pour un matériau isotrope, pour un matériau UD optimisé en orientation, solution stratifiée à partir de pli constitués de ce même matériau UD (bornes géométriques) et solution orthotrope générale (borne thermodynamiques). xxiii
2 Solutions pour la minimisation du volume avec une contrainte de résistance de Tsai-Wu pour différentes directions d’impression Z. Les éléments représentés ont une densité optimisée supérieure à 0,3. xxiv
3 Topologie et distribution des critères de résistance locale pour la minimisation du volume avec différents critères de rupture elliptiques (Tsai-Wu, Tsai-Hill et Hoffman) pour des orientations UD de 0°, 45° et 90° (illustrées par la flèche jaune). Les éléments représentés ont une densité optimisée supérieure à 0,3. xxv
4 Solution pour une minimisation du volume avec une contrainte de compliance et un critère de rupture Tsai-Wu pour l’optimisation de la topologie et de l’orientation d’un pli UD. Les éléments représentés ont une densité optimisée supérieure à 0,3. xxvi
5 Solution pour une minimisation de volume avec un critère de déformation conservateur considérant la topologie et un stratifié. Les éléments représentés ont une densité optimisée supérieure à 0,3. xxvii
6 Facteur critique de flambage λ_{crit} et mode propre des solutions de minimisation du volume considérant des stratifiés avec une enveloppe de déformation définie par l’utilisateur avec des admissibles de compression élevées ou faibles. Les éléments représentés ont une densité optimisée supérieure à 0,3. xxvii

1.1 Additive manufacturing products. 1
1.2 Solution compliance minimization with a sequential approach of optimizing the anisotropy on a fixed isotropic topology on the left, and of a concurrent topology and anisotropy optimization on the right, for the same volume. 2
1.3 Influence of different mechanical considerations (compliance, strength and buckling) in topology optimization the final results with an isotropic material. 3

2.1 Difference in (a) size, (b) shape and (c) topology optimization. 5
2.2 Density interpolation functions. 7
2.3 MMC optimization results. 9
2.4 Level-Set topology definition. 9
2.5 Volume minimization problem with two stress constraints exhibiting a stress singularity. . . . 11
2.6 Original (a) and relaxed (b) design space of the problem in Figure 2.5. 12
2.7 Stress-based benchmark optimization problem and results obtained by (a) Verbart *et al.*, (b) Le *et al.*, (c) Holmberg *et al.* and (d) Senhora *et al.*. 14
2.8 Test strain used to evaluate the homogenized stiffness properties of a microstructure. 15
2.9 Variable microstructure distribution. 15

2.10 Laminate layup consisting of different UD plies, rotated from the laminate reference frame xyz to the ply's reference frame 123 by δ. 18
2.11 Cartesian and polar representation of: (a) a vector and (b) a second order tensor in a reference frame rotated by δ. 23
2.12 Engineering material properties distribution within the thermodynamic bounds, for fixed isotropic modules $T_0 = 26.9$ GPa and $T_1 = 24.7$ GPa, with the geometric bounds traced in black. 25
2.13 Laminate properties within the geometric bounds of the polar formalism. 26

3.1 Geometric bounds within the thermodynamic domain. 32
3.2 Compliance design space with respect to thickness and ply orientation. 34
3.3 Monotonous MMA approximation versus non-monotonous and convex GCMMA approximation. 34
3.4 Overview of the optimization strategy SplitMMA. 35
3.5 Test case representation, with the filter size indicate in orange. 37
3.6 Domain of existence mirroring by including the consideration of negative η_1. 39
3.7 Optimized anisotropy with only η_1 being positive on a fixed topology. 39
3.8 Design space of the compliance function with respect to η_1 and ϕ_1 in $[0,1[\times[-90°,90°]$ when varied in the red-outlined area of Figure 3.7. 39
3.9 Design space of the compliance function with respect to η_1 and ϕ_1 in $]-1,1[\times[-90°,90°]$ when varied in the red-outlined area of Figure 3.7. 40
3.10 Results of the cantilever beam test case (#1) with thermodynamic bounds, for the sequential and simultaneous optimizations of the topology and anisotropy with the AD algorithm and SplitMMA strategy. Anisotropy variables are shown where $\rho \geq 0.9$. 41
3.11 Results of the bridge test case (#2) with thermodynamic bounds, for the sequential optimizations of the topology and anisotropy with the AD algorithm and SplitMMA strategy. Anisotropy variables are shown where $\rho \geq 0.9$. 42
3.12 Results of the bridge test case (#2) with thermodynamic bounds, for the simultaneous optimizations of the topology and anisotropy with the AD algorithm and SplitMMA strategy. Anisotropy variables are shown where $\rho \geq 0.9$. 43
3.13 Difference between the anisotropic values obtained with SplitMMA and the optimized values obtained by applying the optimality criteria to SplitMMA solution for the sequential approach of test case (#1). 43
3.14 Difference between the anisotropic values obtained with SplitMMA and the optimized values obtained by applying the optimality criteria to SplitMMA solution for the concurrent approach of test case (#1). 44
3.15 Results of the concurrent topology and anisotropy optimization with SplitMMA for test case (#1), with η_1 in $[-\eta_1^L, \eta_1^L]$: the anisotropic modules distribution within the thermodynamic bounds, the associated optimization variables α and β and the anisotropic modules on the topology. Values shown for elements with $\rho \geq 0.9$. 44
3.16 Results of Peeters *et al.* for test case (#3) with lamination parameters: (a) the topology, (b) V_1 and (c) V_3. 46
3.17 Optimization results of test case (#3) with geometric bounds: (a) the topology, (b) V_1 and (c) V_3. 47
3.18 Comparison between a sequential and concurrent topology and laminate optimization. 48
3.19 Topology and anisotropy distributions for simultaneous optimizations with different degrees of anisotropy: isotropic material design, steered-fiber design, laminated solution (geometric bounds) and general orthotropic materials (thermodynamic bounds). 49
3.20 Anisotropic modules distribution within the geometric bounds for the concurrent topology and anisotropy optimization with SplitMMA for test case (#1). Modules included where $\rho \geq 0.9$. 50
3.21 Optimized anisotropy orientation and ϕ_1 for the geometric bounds optimization of Figure 3.19. Modules shown for elements with $\rho \geq 0.9$. 50

4.1 Effect of different μ values on the lower KS aggregation of the maximum of the three functions. 54
4.2 Numerical steps used to compute the value of the global failure optimization constraint for a Von Mises criterion with an isotropic material. 55
4.3 Tsai-Wu, Tsai-Hill and Hoffman elliptic failure criteria envelope in the $\sigma_1 - \sigma_2$ and $\sigma_2 - \tau_{12}$ material reference plane for the properties of Table 4.1. 58
4.4 Numerical steps used to obtain the global failure optimization constraint for an elliptic failure criterion with an anisotropic material. 60

5.1 L-bracket test case representation. 68
5.2 Influence of the aggregation parameter μ on stress-based topology optimization with an isotropic material and a Von Mises criterion. Information shown for optimized elements with a final density ≥ 0.3. 70
5.3 Influence of the optimization problem (Problem 2, Problem 3 and Problem 4) with an isotropic material and a Von Mises criterion. Information shown for optimized elements with a final density ≥ 0.3. 72
5.4 Topology convergence rate of the solutions of Figure 5.3 with isotropic material, for a volume minimization with a strength constraint (Problem 2), a volume minimization with a strength and compliance constraint (Problem 3) and a volume minimization with a compliance constraint (Problem 4). 73
5.5 Solutions for volume minimization with a Tsai-Wu strength constraint representing additive manufacturing for different printing (extrusion) directions corresponding to the Z axis. Information shown for optimized elements with a final density ≥ 0.3. 75
5.6 Local strength constraint for the 90° printing direction solution with a reverse loading condition. Information shown for optimized elements with a final density ≥ 0.3. 76
5.7 Local strength constraint of the optimized solution for additive manufacturing at 90° with a reverse applied load. Information shown for optimized elements with a final density ≥ 0.3. . . 76
5.8 Tsai-Wu failure criterion envelope for the properties of Table 5.4 in the $\sigma_1 - \sigma_2$ material reference plane. 77
5.9 Local strength constraint of the results for volume minimization with a Tsai-Wu criterion for a range of fixed UD orientations. Information shown for optimized elements with a final density ≥ 0.3. 78
5.10 Topology for a volume minimization with a Tsai-Wu failure criterion and fibers at 90° (Problem 2), as shown in Figure 5.9. 79
5.11 Results of a compliance minimization with fixed UD fibers at 90°, a Tsai-Wu criterion and a 25% increase of volume compared to the topology of Figure 5.10 (Problem 5). Information shown for optimized elements with a final density ≥ 0.3. 79
5.12 Tsai-Wu, Tsai-Hill and Hoffman elliptic failure criteria envelope in the $\sigma_1 - \sigma_2$ and $\sigma_2 - \tau_{12}$ material reference plane for the properties of Table 5.4. 80
5.13 Local strength constraint of the results for volume minimization with different elliptic failure criteria for 0°, 45° and 90° UD orientations. Information shown for optimized elements with a final density ≥ 0.3. 80
5.14 Comparison of the final topology for volume minimization with a Tsai-Hill criterion and UD fibers at 90°: on the left, the solution of Figure 5.13 with $N_0 = 50$, and on the right unsuccessful $N_0 = 25$. 81
5.15 Comparison of the final topology for volume minimization with a Tsai-Wu criterion and UD fibers at 90°: on the left, the solution of Figure 5.13 with $N_0 = 50$, and on the right with $N_0 = 25$. 81
5.16 Local strength constraint of the results for volume minimization with a Tsai-Wu criterion for both topology and orientation optimization of a UD ply with different initialization of the orientations: uniform $\phi_1 = 0°$ on the left, uniform $\phi_1 = 90°$ in the middle and distributed ϕ_1 on the right. Information shown for optimized elements with a final density ≥ 0.3. 83
5.17 Initial local strength constraint distribution for the optimization of Figure 5.16. 84

5.18 Tsai-Wu, Tsai-Hill and Hoffman elliptic failure criteria envelopes in the $\sigma_1 - \sigma_2$ material reference plane for the properties of Table 5.5. 85

5.19 Local strength constraint of the results for volume minimization with Tsai-Wu, Tsai-Hill and Hoffman failure criteria for both density and material orientation optimization of a UD ply. Information shown for optimized elements with a final density ≥ 0.3. 85

5.20 Solution for a volume minimization with a Tsai-Wu failure criterion for both topology and orientation optimization of a UD ply with an increased load F = 800 N. Information shown for optimized elements with a final density ≥ 0.3. 86

5.21 Solution for a volume minimization with compliance and a Tsai-Wu failure criterion for both topology and orientation optimization of a UD ply with an increased load. Information shown for optimized elements with a final density ≥ 0.3. 87

5.22 Results obtained by Ma *et al.* for topology and orientation optimization for compliance minimization with volume and a Tsai-Wu failure criterion with a UD fiber: (a) density and fiber distribution, (b) Tsai–Wu value distribution. 88

5.23 Solution for a compliance minimization with volume and a Tsai-Wu failure criterion for both density and material orientation optimization of a UD ply (Problem 5). Information shown for optimized elements with a final density ≥ 0.3. 88

6.1 Second-order and fourth-order strain envelopes for any ply orientation for a Tsai-Wu failure criterion. 93

6.2 Steps used to obtain the global failure optimization constraint for a strain-based criterion. . . 95

6.3 Von Mises stress criterion expressed in terms of global strains and its approximated strain envelope. 97

6.4 Comparison of a volume minimization strength-based topology optimization with a stress-based and strain-based formulation of the Von Mises criterion, and for different t values for $\boldsymbol{\varepsilon}_{eq}$ of Equation 6.6. 98

6.5 Unsuccessful strain-based topology optimization with different t values for $\boldsymbol{\varepsilon}_{eq}$ of Equation 6.6. 98

6.6 Conservative Tsai-Wu strain envelope for the material properties in Table 6.3. 100

6.7 Solution for a volume minimization with respect to both material density and orientation, with a conservative Tsai-Wu strain criterion for both topology and orientation optimization of a UD ply. Information shown for optimized elements with a final density ≥ 0.3. 100

6.8 Solution for a volume minimization with respect to both material density and orientation, with a Tsai-Wu stress criterion for both topology and orientation optimization of a UD ply. Information shown for optimized elements with a final density ≥ 0.3. 101

6.9 Solution for a volume minimization with a conservative Tsai-Wu strain criterion considering the topology and a laminate. Information shown for optimized elements with a final density ≥ 0.3. 102

6.10 Anisotropy initialization for a UD orientation or laminate topology optimization. 102

6.11 Solution for a volume minimization with a conservative Tsai-Wu strain criterion considering the topology and a laminate. Information shown for optimized elements with a final density ≥ 0.3. 103

6.12 User-defined and conservative Tsai-Wu strain envelope. 104

6.13 Results of a volume minimization considering laminates with a user-defined strain-envelope constraint. Information shown for optimized elements with a final density ≥ 0.3. 105

6.14 Results of a topology optimization considering laminates for a compliance minimization with volume constraint. Information shown for optimized elements with a final density ≥ 0.3. . . . 105

6.15 Anisotropic modules' distribution within the geometric and thermodynamic domain. 106

6.16 Results of a volume minimization considering laminates with user-defined strain-envelope and compliance constraints. Information shown for optimized elements with a final density ≥ 0.3. 107

6.17 Results of a compliance minimization considering laminates with user-defined strain-envelope and volume constraints. Information shown for optimized elements with a final density ≥ 0.3. 108

6.18 Anisotropic module distribution within the geometric and thermodynamic domain for the compliance minimization with a user-defined strain-envelope and volume constraints of Figure 6.17. 108
6.19 Results of a volume minimization with respect to material orientation and density with a Tsai-Wu strength constraint for a range of longitudinal compressive allowable X_c. Information shown for optimized elements with a final density ≥ 0.3. 110
6.20 Buckling load multiplier λ_{crit} and eingenmode for the optimized designs with decreasing X_c values. Respective solutions are the right solution in Figure 5.16 and the ones in Figure 6.19. Information shown for optimized elements with a final density ≥ 0.3. 111
6.21 Buckling load multiplier λ_{crit} and eingenmode for the optimized designs. Information shown for optimized elements with a final density ≥ 0.3. 112

A.1 Second-order and fourth-order strain envelopes for any ply orientation for a Tsai-Wu failure criterion. 133

List of Tables

2.1 Optimality criteria for the compliance minimization within the thermodynamic bounds. . . . 27

3.1 Orthotropic base ply material properties. 32
3.2 Material properties for the optimizations of the test cases of Figure 3.5. 37
3.3 Continuation strategy of the optimization parameters in number of iterations for the different optimization approaches. 38
3.4 MMA and GCMMA algorithm settings for the SplitMMA strategy for compliance minimization. 38

4.1 Material strength properties for different failure criteria. 58

5.1 MMA and GCMMA algorithm settings for the SplitMMA strategy with strength constraints. 69
5.2 Isotropic material properties and optimization parameters for a strength-based topology optimization. 70
5.3 3D Printing induced material properties and optimization parameters for a strength-based topology optimization. 74
5.4 Fixed orthotropic UD material properties and optimization parameters for a strength-based topology optimization. 76
5.5 Optimization and UD fiber properties for simultaneous topology and orientation optimization with strength constraint. 82

6.1 Stress and strain-based topology optimization properties with an isotropic material and Von Mises criterion. 96
6.2 Strain coefficient for the user-defined envelope to express a Von Mises stress criterion in terms of global strains. 97
6.3 Optimization parameters and UD ply properties for optimizations with a conservative Tsai-Wu strain-based constraint. 99
6.4 Optimization parameters and user-defined strain envelope properties for optimizations with a strain-based constraint. 104
6.5 Volume and buckling load multiplier differences for the results with different longitudinal compressive allowable X_c. 111
6.6 User-defined strain envelope reduced allowable values. 111

Nomenclature

Acronyms

AD	Alternate Directions
FEM	Finite Element Method
GCMMA	Global Convergent Method of Moving Asymptotes
KS	Kreisselmeier-Steinhauser aggregation function
LKS	Lower Kreisselmeier-Steinhauser aggregation function
M_{nd}	Measure of non-discreteness
MMA	Method of Moving Asymptotes
MPVC	mathematical Programming with vanishing Constraints
OC	Optimality Criterion
UD	Uni-Directional

Greek

α, β	Optimization variables representing the anisotropic modules defined by the implicit remapping of the domain of existence	[-]
γ	Anisotropy variable	[°,-]
$\gamma_{xy_{\max}}$	Shear strain allowable	[-]
$\boldsymbol{\varepsilon}$	Strain vector	[-]
$\varepsilon_x, \varepsilon_x, \gamma_{xy}$	Strain components	[-]
$\boldsymbol{\varepsilon}^{eq}$	Equivalent strain vector	[-]
ε_{x_t}	Magnitude of the tensile strain allowable in x-direction	[-]
ε_{x_c}	Magnitude of the compressive strain allowable in x-direction	[-]
ε_{y_t}	Magnitude of the tensile strain allowable in y-direction	[-]
ε_{y_c}	Magnitude of the compressive strain allowable in y-direction	[-]
η_0, η_1	Normalized anisotropic modules	[-]
η_0^L, η_1^L	Normalized anisotropic modules of the base ply	[-]
ρ	Optimization density variable	[-]
$\rho_{\min}$	Minimal density value	[-]
$\tilde{\rho}$	FEM analysis density variable	[-]
λ_{crit}	Critical buckling load multiplier	[-]
$\boldsymbol{\lambda}_k$	Adjoint vector for the strength gradient of cluster k	[-]
μ	Aggregation parameter	[-]
ν	Poisson's ratio	[-]
ν_{12}	In-plane Poisson's ratio	[-]
ϕ_1	Direction of orthotropy	[°]
ψ	Optimization variable	[°,-]
$\boldsymbol{\sigma}$	Stress vector	[MPa]
σ_1,σ_2,τ_{12}	Stress components in the global reference frame	[MPa]

Greek

σ_x,σ_y,τ_{xy}	Stress components in the local ply's reference system	[MPa]
$\boldsymbol{\sigma}^{FEM}$	Stress vector from a FEM analysis	[MPa]
$\boldsymbol{\sigma}^{micro}$	Micro stress vector	[MPa]
σ^{VM}	Von Mises stress	[MPa]
σ^{Y}	Yield stress	[MPa]

Latin

$[A]$	In-plane stiffness tensor	[MPa]
A, B	Quadratic components of an elliptic failure criterion	[-]
a_{12}, a_{11}, a_{10}	Coefficients of second-order conservative Tsai-Wu strain envelope	[-]
$a_{24}, a_{23}, a_{22}, a_{21}, a_{20}$	Coefficients of fourth-order conservative Tsai-Wu strain envelope	[-]
$[B]$	Strain-displacement matrix	[1/mm]
C_0	Compliance constraint value	[mJ]
E	Young's Modulus isotropic material	[GPa]
E_{11}	Young's Modulus along the fibers in a Uni-Directional ply	[GPa]
E_{22}	Young's Modulus transverse to the fibers in a Uni-Directional ply	[GPa]
$\mathbf{F}$	Force vector	[N]
F	Applied force	[N]
$[F]$	Matrix defining the stress-based failure criterion	[1/MPa^2]
$fail_m$	Failure definition	[-]
F^*_{12}	Bi-axial stress coefficient	
$\mathbf{G}$	Vector defining the stress-based failure criterion	[1/MPa]
G	Shear modulus isotropic material	[GPa]
G_{12}	In-plane shear modulus	[GPa]
g_i	Local strength constraint	[-]
$\bar{g}$	Local strength constraint with Mathematical Programming with Vanishing Constraints	[-]
$\bar{g}_{\max}$	Maximum local strength constraint with Mathematical Programming with Vanishing Constraints	[-]
g_k^{LKS}	Strength optimization constraint for cluster k	[-]
I_1, I_2	Strain invariants	[-]
k	Cluster number	[-]
K	Shape of orthotropy	[-]
K^L	Shape of orthotropy of the base ply	[-]
$[K]$	FEM stiffness matrix	[N/mm]
$[k]$	Local FEM stiffness matrix	[N/mm]
N	Number of elements in aggregation	[-]
N_0	Normalization factor	[-]
$[M]$	Matrix defining the strain-based failure criterion	[-]
M^*_{12}	Bi-axial strain coefficient	[-]
$\mathbf{N}$	Vector defining the strain-based failure criterion	[-]
p	SIMP exponent	[-]
$[Q]$	Stiffness tensor	[GPa]
r	Stress relaxation exponent	[-]
R_0, R_1	Anisotropic modules	[GPa]
R_0^L, R_1^L	Anisotropic modules of the base ply	[GPa]
R_ρ	Density filter radius	[mm]
R_{ϕ_1}	Orientation filter radius	[mm]

S	Shear strength allowable	[MPa]
s_1	Strength load multiplier	[-]
t	Equivalent strain exponent	[-]
T_0, T_1	Isotropic modules	[GPa]
T_0^L, T_1^l	Isotropic modules of the base ply	[GPa]
$u_1, u_2, u_3, u_4, u_5, u_6$	Material property to compute the conservative Tsai-Wu strain envelope	[-]
$\boldsymbol{U}$	Displacement vector	[mm]
V_0	Volume of the design mesh	[mm^3]
v_f	Volume fraction	[%]
$[V]$	Von Mises transformation matrix	[-]
V_i	Lamination parameters	[-]
X	Magnitude of the stress allowable along the fibers	[MPa]
X_t	Magnitude of the tensile stress allowable along the fibers	[MPa]
X_c	Magnitude of the compressive stress allowable along the fibers	[MPa]
Y	Magnitude of the stress allowable transverse to the fibers	[MPa]
Y_t	Magnitude of the tensile stress allowable transverse the fibers	[MPa]
Y_c	Magnitude of the compressive stress allowable transverse the fibers	[MPa]

Résumé

Les matériaux composites stratifiés, de par leur anisotropie, offrent à l'ingénieur des degrés de liberté supplémentaires pour la conception mécanique de pièces structurelles. Cependant, exploiter ce potentiel nécessite le développement et la mise en œuvre de méthodes spécifiques durant la phase de conception. Les structures primaires composites actuelles sont le plus souvent dimensionnées à l'aide d'une optimisation paramétrique faite sur une forme figée. A l'inverse, exploiter pleinement l'anisotropie du matériau lors de l'optimisation topologique de la forme des pièces reste un défi scientifique. Ce travail de thèse vise à réconcilier ces deux démarches afin de mieux dimensionner des pièces composites dès la phase conceptuelle. L'optimisation topologique consiste à distribuer aux mieux la matière pour minimiser un critère mécanique en utilisant une variable de densité continue décrivant la présence (densité de 1) ou l'absence (densité qui tend vers 0) de matière en chaque point de la structure. Ranaivomiarana *et al.* [1] a démontré que la forme idéale d'une pièce dépend de l'anisotropie du matériau pour la minimisation de la compliance (ce qui équivaut à maximiser la raideur). La solution obtenue pour une optimisation simultanée par rapport à la densité et l'anisotropie s'avère plus rigide et moins encombrante que la solution obtenue pour une optimisation séquentielle de la topologie avec un matériau isotrope, suivie de l'optimisation de l'anisotropie sur cette forme figée. Toutefois, l'algorithme des directions alternées utilisé par Ranaivomiarana [2] est spécifique à la minimisation de la compliance et n'est pas applicable à l'optimisation topologique avec d'autres objectifs ou contraintes. Or, le dimensionnement d'une pièce dans une perspective d'application industrielle implique de nombreux critères mécaniques supplémentaires, par exemple de résistance ou de flambement. De plus, il a été démontré dans le cadre de l'optimisation topologique avec un matériau isotrope que l'ajout de ces critères change drastiquement les formes optimales [3]. L'objectif de cette thèse est donc de définir une méthode d'optimisation topologique en densité et anisotropie, adaptée aux matériaux composites, tout en considérant des critères mécaniques de tenue du matériau comme contraintes d'optimisation supplémentaires.

La littérature scientifique consacrée à la prise en compte de critères de rupture dans l'optimisation topologique est assez riche dans le cas des matériaux isotropes [4, 5]. Les difficultés théoriques et numériques associées au problème sont bien identifiées et des travaux récents [3] proposent des techniques de plus en plus matures pour les surmonter. Ces techniques ont également été démontrées être pertinentes dans le cas de le prise en compte de la rupture et d'anisotropie, que ce soit en considérant des matériaux orthotropes à orientations fixes [6], en sélectionnant parmi des plis prédéterminés pour obtenir un stratifié [7] ou avec des fibres courbes [8, 9]. Cependant, un consensus se dégage autour de l'utilisation d'algorithmes à gradient lorsque d'autres critères mécaniques (tel la rupture ou le flambement) doivent être pris en compte en optimisation topologique. L'algorithme MMA (Method of Moving Asymptotes) [10], le plus largement employé dans la littérature, a ainsi été retenu pour la suite de cette thèse.

La première phase des travaux a permis de développer une stratégie d'optimisation basée sur MMA pour l'optimisation topologique en densité et anisotropie, et de comparer les résultats avec les solutions obtenues avec le critère d'optimalité utilisé par Ranaivomiarana [2]. Le problème considéré de minimisation de compliance C $= \mathbf{U}^T[K]\mathbf{U}$ à efforts imposés sous contrainte de volume maximal V_0 est résumé par Equation 1. Les déplacements $\mathbf{U}$ sont obtenus par une analyse éléments finis en résolvant l'équilibre classique $[K]\mathbf{U} = \mathbf{F}$. $[K]$ est la matrice de rigidité du système, et $\mathbf{F}$ le vecteur de force. Les variables d'optimisation considérées en chaque élément correspondent à la densité de matière ρ, à l'orientation d'anisotropie ϕ_1 et aux modules anisotropes du matériau. L'anisotropie est représentée au moyen du formalisme polaire, et restreinte au cas des matériaux orthotropes 2D. Le formalisme polaire exprime un tenseur d'élasticité du quatrième ordre à l'aide d'invariants scalaires. Les modules anisotropes η_0 et η_1 sont exprimés à partir de ces invariants tensoriels, et contraints par les bornes thermodynamiques, pour assurer que le tenseur d'élasticité reste défini positif. Cette contrainte a été incorporée de manière implicite dans l'optimisation au moyen d'une opération de mapping.

$$\begin{aligned} \min_{\rho,\phi_1,\eta_0,\eta_1} \quad & \mathbf{U}^T[K]\mathbf{U} \\ \text{s.t.} \quad & V(\rho) \leq V_0 \\ & \rho_{min} \leq \rho \leq 1 \\ & -\pi \leq \phi_1 \leq \pi \\ & 2\eta_1^2 - 1 < \eta_0 < 1 \end{aligned} \tag{1}$$

L'algorithme d'optimisation MMA consiste à résoudre de façon séquentielle une série de problèmes d'optimisation approchés convexes (Sequential Approximate Optimization). Les approximations de la fonction objectif et des contraintes du problème d'optimisation sont construites à partir de l'évaluation exacte de leurs valeurs et de leurs dérivées au point courant à chaque itération. Cela a impliqué un travail important sur la prise en compte de l'anisotropie et l'obtention des gradients par rapport à ces variables. Pour cela, le problème d'optimisation a été traité en plusieurs étapes, en étudiant d'abord chaque variable séparément. La stratégie d'optimisation finale retenue consiste à différencier le type d'approximation en fonction de la nature des variables. La surface de réponse par rapport aux densités et aux modules anisotropes se comporte de manière plutôt régulière, ce qui permet l'utilisation de l'approximation monotone de l'algorithme MMA. A contrario, la surface de réponse est fortement non linéaire par rapport à l'orientation, pour laquelle une approximation convexe est mieux adaptée. Par ailleurs, il a été observé que les optimisations à gradient sont très sensibles à l'initialisation des variables, phénomène bien connu dans la littérature traitant d'optimisation topologique en densité seule et accentué par l'introduction de variables d'anisotropie du matériau. Une démarche d'initialisation est proposée dont l'efficacité a été démontrée sur plusieurs cas tests numériques, qui consiste, en partant d'une initialisation uniforme, à optimiser d'abord l'anisotropie du matériau pour adapter celle-ci aux chemins d'efforts, avant d'optimiser simultanément densité et anisotropie. Les résultats obtenus ont été comparés aux solutions obtenues par Ranaivomiarana [2], les deux procédures d'optimisation ayant été implémentées en Python au cours de ces travaux. La stratégie proposée permet, avec une optimisation à base de gradients, de retrouver efficacement les solutions obtenues avec le critère d'optimalité des directions alternées.

L'usage d'un algorithme à gradient permet de remplacer les bornes thermodynamiques sur les modules d'anisotropie par les bornes géométriques, spécifiques aux composites stratifiés [11], permettant ainsi de générer des résultats nouveaux par rapport à la littérature. La Figure 1 présente l'évolution de la compliance optimisée en densité et anisotropie distribuées pour différents domaines de conception en anisotropie, à fraction volumique égale : la solution isotrope, la solution avec un matériau unidirectionnel dont l'orientation est optimisée, la solution stratifiée et la solution obtenue dans le domaine thermodynamique pour laquelle le matériau est défini mathématiquement mais inconnu en pratique. La topologie finale diffère entre ces quatre exemples et la raideur augmente avec le domaine de conception en anisotropie.

La deuxième partie de ces travaux s'est focalisée sur la prise en compte de critères de rupture, dans les cas d'anisotropie pour lesquelles il est possible de postuler des valeurs admissibles pertinentes en contrainte ou en déformation. La résistance a d'abord été évaluée pour des fibres courbes par un critère anisotrope elliptique. Le formalisme polaire a également été utilisé pour exprimer les admissibles dans le repère global. Ce type d'optimisation pose trois difficultés principales : i) l'espace de conception peut dégénérer lorsque des contraintes d'optimisation sont formulées à partir des contraintes mécaniques évaluées sur le modèle éléments finis de la pièce, ii) la contrainte mécanique est une dimension locale, il y a donc une contrainte d'optimisation par élément du maillage, et iii) le coût numérique du calcul du gradient peut devenir prohibitif,

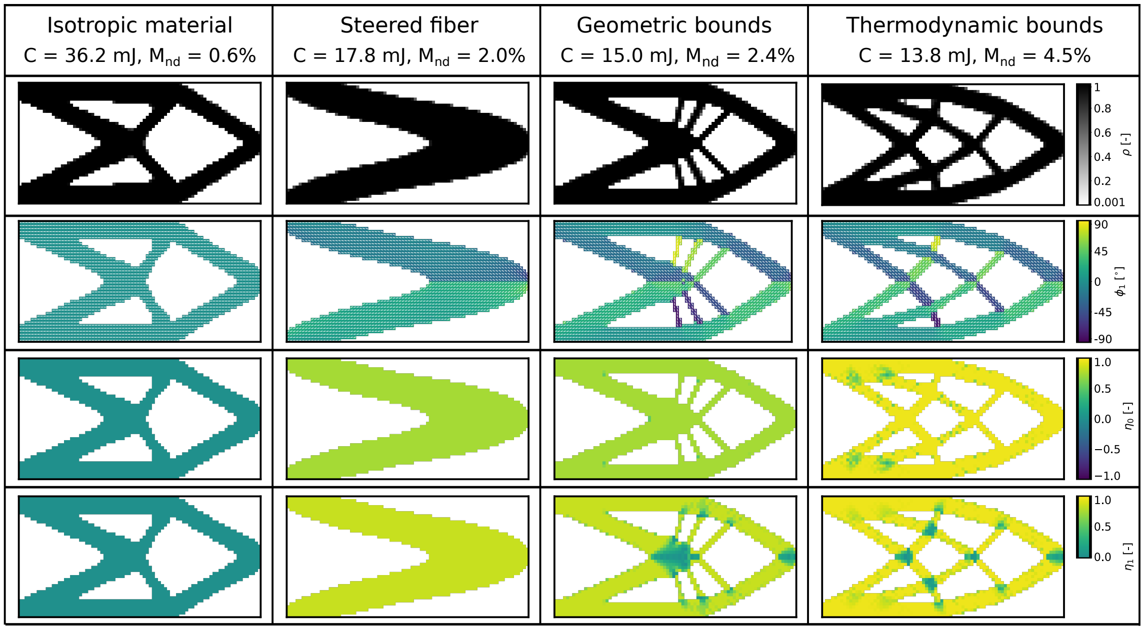

Figure 1: Topologies et distributions d'anisotropie obtenues par des optimisations simultanées en densité et anisotropie en élargissant progressivement le domaine de conception en anisotropie : de gauche à droite, solutions obtenues pour un matériau isotrope, pour un matériau UD optimisé en orientation, solution stratifiée à partir de pli constitués de ce même matériau UD (bornes géométriques) et solution orthotrope générale (borne thermodynamiques).

puisque la contrainte mécanique en un élément dépend du champ complet des variables d'optimisation. Dans ces travaux, le problème de singularité de la contrainte mécanique et celui de sa nature locale ont été palliés par l'utilisation d'une technique de relaxation et d'agrégation simultanée, au moyen de la fonction "lower Kreisselmeier–Steinhauser" (LKS) [5]. Cette technique permet d'obtenir une unique contrainte d'optimisation g^{LKS} qui approche par valeur inférieure la valeur maximale du critère de rupture g parmi les éléments de la structure. Les gradients de ce critère de rupture sont calculés par le biais de la méthode adjointe pour accélérer les optimisations. Le calcul du gradient a été incorporé dans un code d'optimisation et d'éléments finis 2D implémenté sous Python.

Le premier exemple d'application considéré représente une pièce imprimée en 3D par dépôt de fil selon un motif de remplissage isotrope dans chaque couche. La rupture de cette configuration peut être caractérisé par un critère de Tsai-Wu isotrope transverse [12], avec des admissibles plus faibles dans la direction d'impression Z. L'optimisation est réalisée en 2D dans un plan de coupe transverse à la pièce contenant la direction d'impression. Le matériau est uniforme dans la pièce et son orientation figée. L'optimisation est répétée pour trois orientations différentes du matériau. La Figure 2 montre les résultats obtenus pour une poutre en L, avec le critère de rupture anisotrope orienté avec la direction d'impression représentée par la flèche jaune. La solution optimisée est sensible à la direction d'impression, et des barres plus massives se forment dans les zones sollicitées dans les directions les plus faibles du matériau. Ainsi l'anisotropie du critère de rupture utilisé en contrainte de optimisation influe significativement sur la topologie optimisée et la raideur de la pièce.L'analyse détaillée des solutions montre que la contrainte d'optimisation agrégée est satisfaite lors de l'optimisation. Néanmoins, certaines valeurs de la critère de la rupture local g sont supérieures à 0, ce qui découle de l'usage d'une approximation par valeur inférieure (LKS).

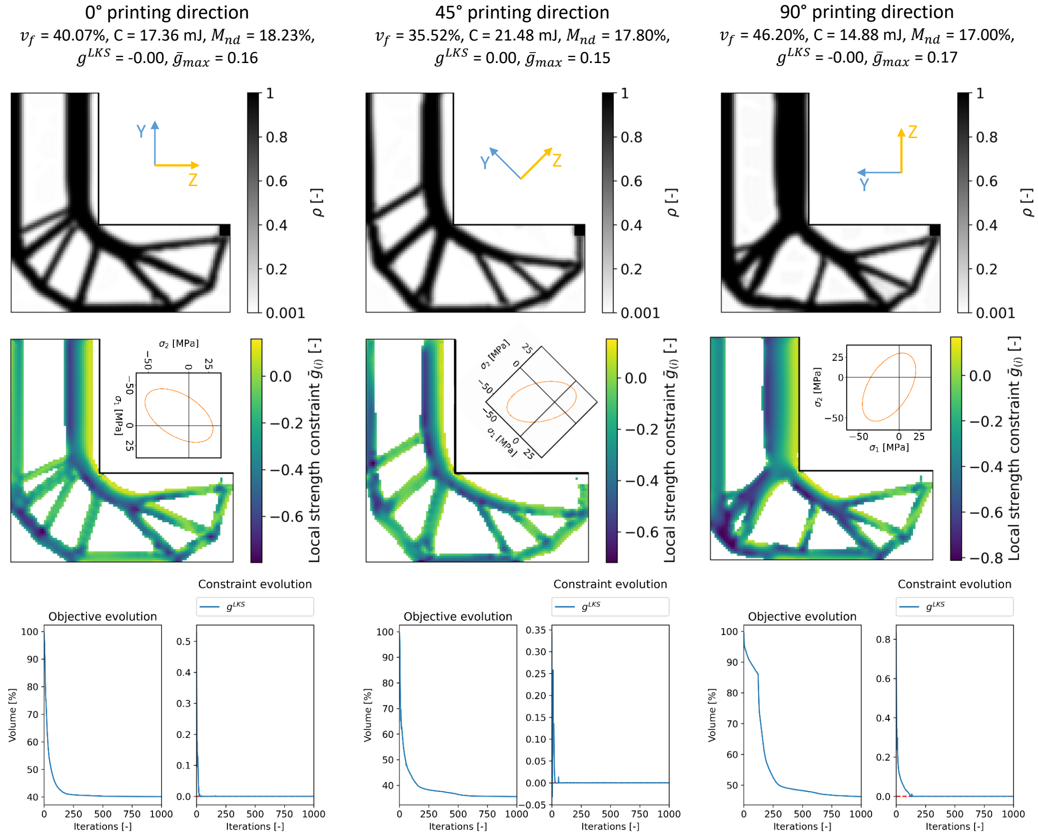

Figure 2: Solutions pour la minimisation du volume avec une contrainte de résistance de Tsai-Wu pour différentes directions d'impression Z. Les éléments représentés ont une densité optimisée supérieure à 0,3.

Un deuxième cas d'étude a eu pour objectif d'évaluer l'influence du choix du critère de rupture sur la solution optimisée, dans le cas d'un matériau unidirectionnel (UD) uniforme sur la pièce et dont l'orientation est figée. Une comparaison de résultats obtenus pour avec différentes orientions et critères de rupture est présentée en Figure 3. De façon générale, les barres constitutives des solutions optimisées tendent à s'aligner avec le direction de la fibre, c'est-à-dire le direction de plus grande raideur et résistance. Les barres sollicitées par des efforts transverses aux fibres sont plus massives, ayant des admissibles de magnitude inférieure. Les critères considérés sont des critères elliptiques proches dans leur formulation mathématique mais dans lesquelles les influences respectives des composantes du tenseur des contraintes s'expriment différemment. Ainsi, les solutions obtenues sont globalement proches, mais témoignent bien d'une certaine influence du chois du critère.

La méthode proposée est ensuite appliquée pour la prise en compte simultanée de la distribution de la matière et de l'orientation distribuée du matériau UD. La solution pour une minimisation de volume avec une contrainte de compliance et de rupture pour les fibres courbes est montré en Figure 4. L'ajout de la contrainte de rupture modifie la topologie de la solution, avec une forme incurvée pour minimiser la concentration de contraintes à la place de l'angle droit observé dans le cas d'une optimisation sans critère de rupture. Des amas de matière se forment au niveau des jonctions entre les barres, au niveau desquelles l'état de contraintes est multiaxial. Comme les admissibles d'un pli UD sont très différents dans les directions longitudinales, transverses et en cisaillement, c'est la rupture transverse, la plus faible, qui est critique aux jonctions. L'optimisation ajoute donc de la matière dans ces zones pour satisfaire aux contraintes d'optimisation. Placer des fibres

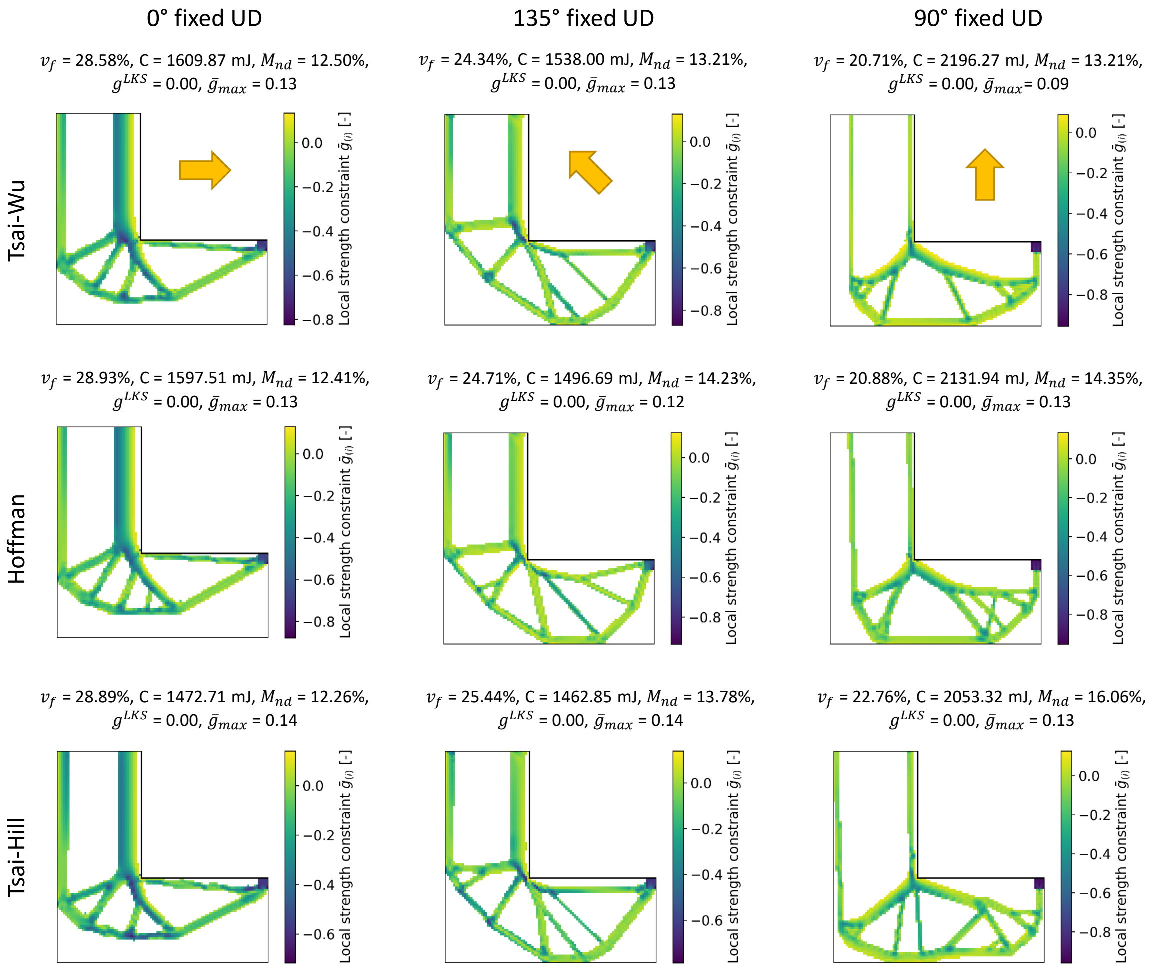

Figure 3: Topologie et distribution des critères de résistance locale pour la minimisation du volume avec différents critères de rupture elliptiques (Tsai-Wu, Tsai-Hill et Hoffman) pour des orientations UD de 0°, 45° et 90° (illustrées par la flèche jaune). Les éléments représentés ont une densité optimisée supérieure à 0,3.

dans plusieurs directions permettrait d'améliorer le design. C'est l'objet de la dernière partie de cette thèse avec l'étude de la prise en compte de la rupture dans le cas des stratifiés.

Cependant, pour un stratifié représenté par son tenseur d'élasticité homogénéisé, un critère elliptique de type Tsai-Wu ne peut être appliqué directement à l'échelle du pli composite. En effet, de par l'homogénéisation, la séquence d'empilements et donc l'orientation des plis sont inconnues. Pour contrer cette limitation, il a été choisi d'exprimer une enveloppe de rupture minimale en déformation, correspondant à l'intersection des enveloppes obtenues pour toutes les orientations de plis possibles, dans la mesure où sous un chargement de membrane, tous les plis partagent les même déformations globales. Une stratégie d'optimisation, toujours basée sur la méthode d'agrégation et de relaxation de la LKS, a été développée, puis validée dans le cas d'un matériau isotrope en vérifiant la bonne correspondance entre les résultats d'une optimisation réalisée avec un critère de Von Mises exprimé en contrainte et d'une optimisation réalisée avec un critère de Von Mises exprimé en déformation. Par après, des optimisations en prenant compte des stratifiés, par le biais des paramètres polaires et les bornes géométriques, ont été effectuées avec une enveloppe de déformation maximale admis-

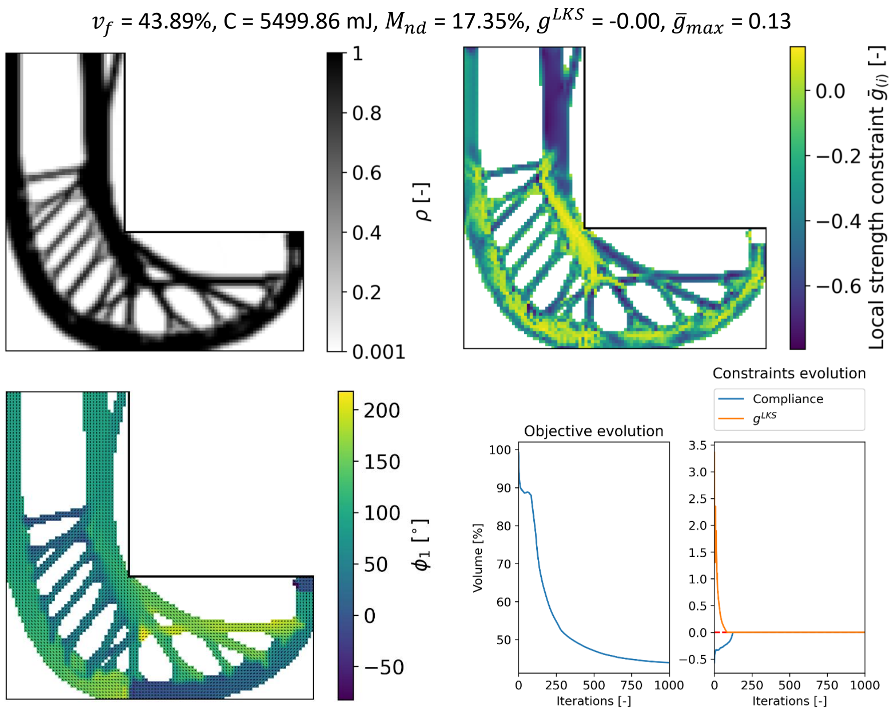

Figure 4: Solution pour une minimisation du volume avec une contrainte de compliance et un critère de rupture Tsai-Wu pour l'optimisation de la topologie et de l'orientation d'un pli UD. Les éléments représentés ont une densité optimisée supérieure à 0,3.

sible. Les résultats d'une optimisation sont présentés en Figure 5. La topologie et l'anisotropie diffèrent du cas précédent, dans lequel seules la densité et l'orientation d'un matériau UD étaient optimisés. La solution obtenue dans le cas de stratifiés se compose de barres UD et d'empilements croisés (0°/90°) aux jonctions.

Dernièrement, la prise en compte indirecte du flambement dans l'optimisation a été évaluée. Le critère de rupture elliptique et l'enveloppe de rupture minimale en déformation sont définis avec des admissibles distincts pour la traction et la compression, on cherche à étudier la pertinence de réduire les admissibles en compression pour favoriser la traction dans la structure et ainsi retarder le flambement. Les résultats montrent, pour une faible pénalité en volume, des gains significatifs pour le facteur critique de flambement en fonction de la réduction des admissibles appliqué. Les résultats d'analyses aux valeurs propres, réalisées en post-processing, d'optimisation pour un même cas de charge avec deux enveloppes de rupture en déformation différentes sont présentés en Figure 6. Jouer sur la valeur des admissible en compression pour privilégier la traction dans la structure permet bien d'augmenter le facteur critique de flambement.

Ces travaux de thèse ont ainsi permis d'inclure des critères de tenue mécaniques dans l'optimisation topologique en tenant compte de l'anisotropie. A cet effet, une stratégie d'optimisation à gradient a été proposée avec des critères de rupture elliptique, tout en obtenant les dérivées par rapport aux différentes variables. La pertinence de la méthode a été démontrée par différents exemples numériques. Cette stratégie d'optimisation ouvre des perspectives telles que l'application à un problème en 3D ou la prise en compte implicite du flambage dans l'optimisation topologique.

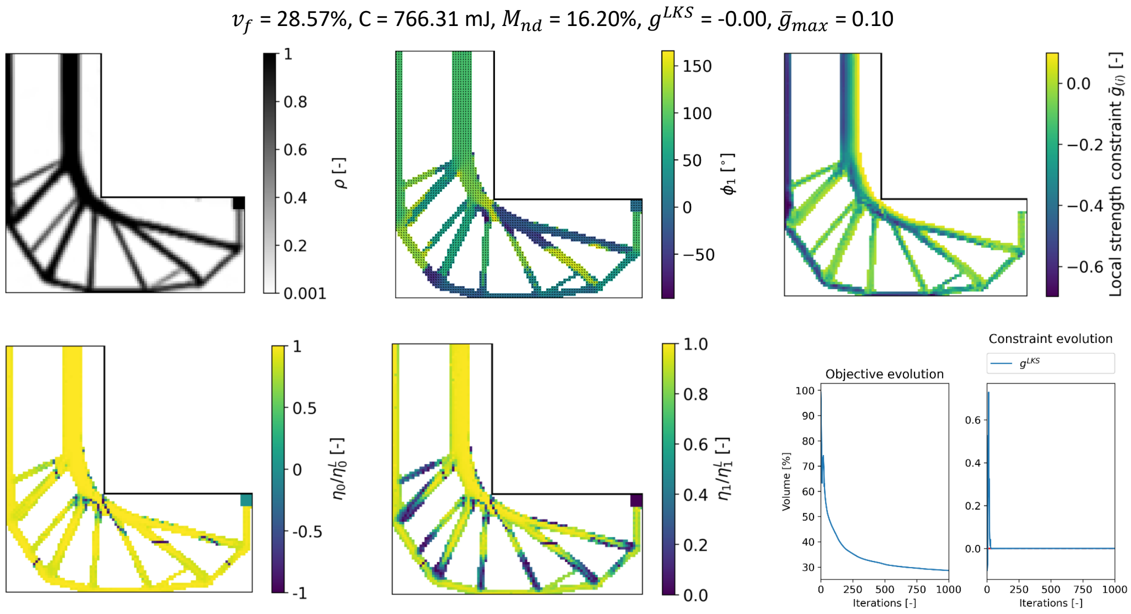

Figure 5: Solution pour une minimisation de volume avec un critère de déformation conservateur considérant la topologie et un stratifié. Les éléments représentés ont une densité optimisée supérieure à 0,3.

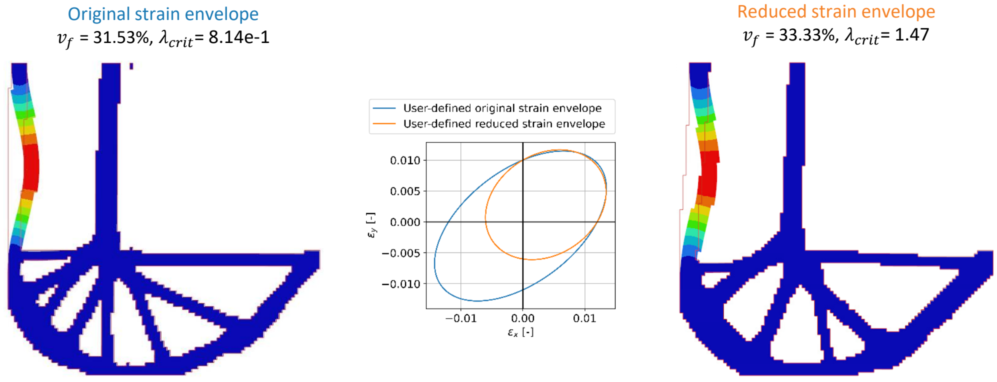

Figure 6: Facteur critique de flambage λ_{crit} et mode propre des solutions de minimisation du volume considérant des stratifiés avec une enveloppe de déformation définie par l'utilisateur avec des admissibles de compression élevées ou faibles. Les éléments représentés ont une densité optimisée supérieure à 0,3.

Chapter 1

Introduction

In the field of transportation, the reduction of greenhouse gas emissions and costs implies the need to always reduce the amount of material used and thus the total mass of the vehicles, while fulfilling mechanical requirements, such as strength. During the design phases, structural engineers in design offices try to reach the best compromises through the use of structural optimization algorithms to find efficient shapes. Material engineers meanwhile seek the best mix of materials to take into account mechanical stresses and environment issues. These two design steps have traditionally been separated in design offices. This research aims to consider both these steps simultaneously.

Additive manufacturing processes, such as 3D printing or fiber placement, have seen an increase in interest due to the opportunity for more versatile structural configurations available to designers. Examples of products obtained by such method are illustrated in Figure 1.1. These novel processes allow to place material more freely, and are less restricted by manufacturing constraints present in traditional production methods such as requiring a constant cross-section in extrusion or tool heads not having access in restricted spaces in machining. Furthermore, these novel additive manufacturing processes provide the possibility to change material during the process to better match local requirements, or dictate the orientation in which the material is being added, and therefore control anisotropic properties.

(a) By 3D printing[1].

(b) By fiber placement[2].

Figure 1.1: Additive manufacturing products.

New conceptual tools and strategies have been developed to fully take advantage offered by those new production methods to unrestricted material placement, such as topology optimization. Topology optimization seeks to define the optimal material distribution of a structure for defined load cases applied to a

---

[1] https://www.businesswire.com/news/home/20140204005189/en/EOS-and-Airbus-Group-Innovations-Team-on-Aerospace-Sustainability-Study-for-Industrial-3D-Printing, accessed on the 27/01/2023.

[2] https://www.labelbreed.nl/collaborations/marleen-kaptein-nlr/fibre-placement-chair/, accessed on the 27/01/2023.

design space. Initial research of topology optimization methods have generally been focused on incorporating isotropic material. Nonetheless, besides material distribution, additive manufacturing also offers control over the material orientation and its associated anisotropic properties. Additional research must be conducted to evaluate and incorporate those added design possibilities effectively in a topology optimization framework. The wish to incorporate anisotropy in topology optimization have also been identified in a survey among topology optimization users by Subedi *et al.* [13], including industrial users, such as Airbus Atlantic.

Current design strategies consist of a sequential approach. Gains on mechanical properties are obtained by optimizing the anisotropy on already existing isotropic structures. However, the optimized topology has not been designed with anisotropy in mind. The downside of this disregard has already been demonstrated for compliance (C) minimization problems, compliance being the inverse of the global stiffness of a structure. When comparing the sequential approach of first optimizing the topology followed by the anisotropy to the simultaneous optimization of both topology and anisotropy at the same time, different topologies are obtained [1]. Such different solutions are shown in Figure 1.2 for the optimization of a suspended bridge for a given volume. The concurrent approach yields a structure which is less bulky, with an improvement of around 6% in stiffness. This shows the importance of considering anisotropy and topology simultaneously, as it provides novel shapes and improved designs. Nonetheless, to efficiently consider anisotropy in the optimizations, convenient parametrizations should be used. Such parametrizations are well defined for 2D membrane and 3D shell structures, but remain a research topic for the more general 3D cases [2].

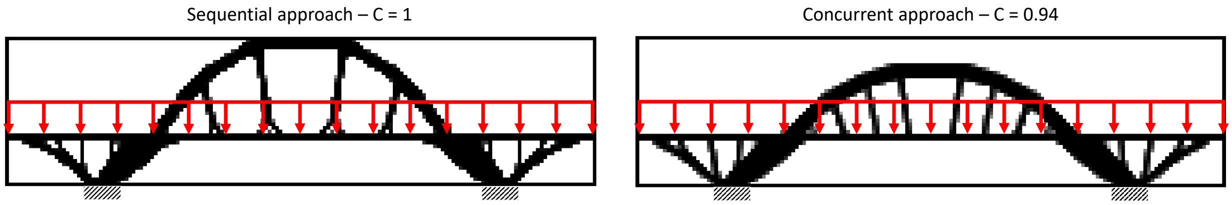

Figure 1.2: Solution compliance minimization with a sequential approach of optimizing the anisotropy on a fixed isotropic topology on the left, and of a concurrent topology and anisotropy optimization on the right, for the same volume.

Only considering compliance is not always sufficient for industrial applications, other mechanical requirements such as strength and buckling could be critical depending on the load cases. These additional mechanical properties should therefore also be incorporated during the optimization. Gao *et al.* [3] highlighted this influence by optimizing a T-shaped structure with an isotropic material, considering a combination of different mechanical properties (compliance, strength and buckling). Different final topologies were obtained, as displayed in Figure 1.3. It shows two important aspects, the first one being that if only compliance is minimized, the critical buckling factor λ_{crit} is low and the maximum Von Mises stress $\sigma^{VM}_{\max}$ high, as they are not considered. This is not ideal, as this solution could experience an early loss of structural integrity. Secondly, the remaining optimizations in Figure 1.3 show that considering additional optimization constraints influences the final topology. In case of the last optimization, the design is driven by compliance, strength and buckling requirements. Because of their effect on the optimized topology, these constraints should also be incorporated in optimizations with anisotropy, where the current research is focused on including anisotropic strength criteria.

Indeed, if for compliance alone, simultaneously optimizing the topology and anisotropy already yields better solutions with different topologies, it is reasonable to expect that anisotropic strength constraints will also alter the optimized topology. Furthermore, if a sequential approach were still to be used with first an isotropic material and therefore an isotropic strength criterion, the optimized solutions would not account for the failure mechanisms typical of anisotropic material, involving tensile-compressive dissymmetry and distinction of directional dependent allowables. Both the influence on the optimized topology and the correct strength criterion consideration motivates the research conducted in this thesis to evaluate anisotropic

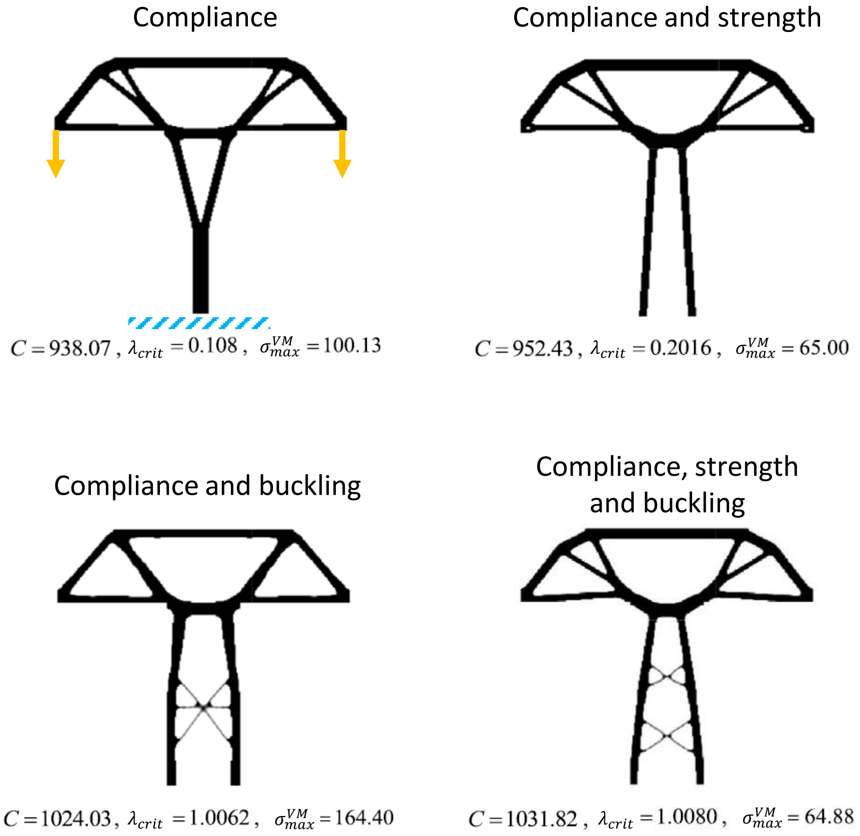

Compliance

$C = 938.07$, $\lambda_{crit} = 0.108$, $\sigma^{VM}_{max} = 100.13$

Compliance and strength

$C = 952.43$, $\lambda_{crit} = 0.2016$, $\sigma^{VM}_{max} = 65.00$

Compliance and buckling

$C = 1024.03$, $\lambda_{crit} = 1.0062$, $\sigma^{VM}_{max} = 164.40$

Compliance, strength and buckling

$C = 1031.82$, $\lambda_{crit} = 1.0080$, $\sigma^{VM}_{max} = 64.88$

Figure 1.3: Influence of different mechanical considerations (compliance, strength and buckling) in topology optimization the final results with an isotropic material [3].

strength in topology optimization. Additionally, to obtain realistic allowable values for anisotropic strength and for its broadly use in the aerospace industry due to its high specific mechanical properties, the type of considered anisotropy is restricted to Uni-Directional (UD) fibers and composite laminates.

The research objective of this thesis is therefore to incorporate strength criteria in a simultaneous topology and material anisotropy optimization framework, in order to obtain structures made of composite laminates. This research has been carried out at ONERA, in collaboration with Sorbonne Université and funded by Airbus Atlantic. The current thesis is a continuation of a previous thesis by Narindra Ranaivomiarana [2], performed in the same research setting. The overall project aim is to take material anisotropy into account as additional design variables to further increase the performances of the optimized parts, by capitalizing on novel manufacturing methods such as additive manufacturing. The previous work focused on elaborating a theoretical basis to take the anisotropic stiffness behavior of materials into account in topology optimization, in both two and three dimensions. An optimization framework was developed using these anisotropy parametrizations, limited to stiffness maximization with respect to the topology and anisotropy simultaneously, by means of an Alternate Directions algorithm. This algorithm can however not consider other mechanical requirements in the optimization. Therefore, a gradient-based optimization strategy with respect to both topology and anisotropy simultaneously must first be devised in this research. Gradient-based algorithms can incorporate generic constraints in topology optimization for a wide application, and are more specifically explored herein to consider strength constraints. Identifying the correct formulation of the optimization constraints based on anisotropic strength criteria for either UD fibers and laminates will be required, as well as computing their gradient. This research will consider 2D topology optimizations, in order to concentrate on the scientific challenges of integrating material anisotropy in a gradient-based optimization with strength constraints.

The content of this thesis is constructed as follows. A review of topology optimization and state of the art for strength incorporation and anisotropy optimization is performed in Chapter 2. The chapter also discusses in more detail the theory of the polar formalism used to represent the anisotropy in this work. Chapter 3 is dedicated to setting up a gradient-based optimization strategy by means of the Methods of Moving Asymptotes (MMA) for the simultaneous topology and anisotropy optimization. Both thermodynamic and geometric bounds on the polar parameters are incorporated implicitly in the optimization. The former encompasses any admissible stiffness tensor of a generic material in two dimensions, whereas the latter one represents the membrane stiffness homogenization of any laminate made from a given base ply. The strategy is tested numerically to escape local minima and validated against an optimality criteria method, the Alternate Directions (AD) algorithm used in [2]. Chapter 4 details the methodology to incorporate stress-based anisotropic strength criteria in a topology optimization framework. The two main issues, the stress singularity problem and computational cost of the gradient, are addressed by means of a lower Kreisselmeier-Steinhauser (KS) aggregation function to relax the problem and use an adjoint formulation to obtain the gradient. These solutions provided in literature for isotropic material are then used to incorporate elliptic strength criteria for anisotropic materials in topology optimization. Chapter 5 presents results of such stress-based topology optimizations with anisotropic strength criteria for different types of optimizations, with either an isotropic material or Uni-Directional (UD) fibers. To extend the consideration to laminates, Chapter 6 considers a conservative strain envelope to represent strength. As the selected laminate homogenization by means of the polar formalism does not provide a stacking sequence during the optimization process, individual ply orientations are unknown. A typical stress-based strength criterion can therefore not be applied. Such a conservative strain envelope is considered at the complete laminate scale to describe the conditions which do not result in failure for any ply orientation. A strain-based framework for topology optimization is therefore developed. The framework is first validated for an isotropic material by comparing solutions with a Von Mises criterion expressed in stress and strain. Afterwards, novel results considering strength and composite laminates are provided for different optimization problem formulations. A specific investigation is also performed on indirect buckling delay by reducing the compressive strength allowables and favor tension in the optimized solution. Lastly, this thesis is concluded in Chapter 7 by summarizing the outcomes. Additionally, follow-up scientific perspectives are discussed.

Chapter 2

State of the Art

This section presents the topology optimization concept, and its specific case of strength optimizations. Furthermore, a literature review is presented in the case of optimizations with anisotropic material. The notation convention used next is [ ] for matrices representation and **bold** for vectors representation.

2.1 An Introduction to Structural Optimization

Structural optimization is a mathematical strategy to improve mechanical properties of a structure, such as stiffness, buckling or vibrations, for a constant volume, or inversely by reducing the volume while satisfying the required mechanical properties. Analytical solutions for stiffness maximization have been provided for trusses, so called Mitchell structure [14]. Thereafter, numerical techniques have been proposed. Those early methods involved size and shape optimization (Eschenauer and Olhoff [15], Rozvany [16]), which is akin to a parametric study on predefined structure characteristics. Size optimization only varies the cross sectional properties of truss elements, on a fixed ground structure, whereas shape optimization consists in deforming the geometry of the structure.

Later approaches for structural optimization lead to the appearance of topology optimization [17]: it has a more versatile application, by defining a structure without prior knowledge or assumption of underlying characteristics nor shape [18, 19]. For every point in the domain, the aim of topology optimization is to define where material should be distributed. It is the only approach capable of making holes appear during the optimization which were not present in initially. The difference between the three concepts of structural optimization are highlighted in Figure 2.1.

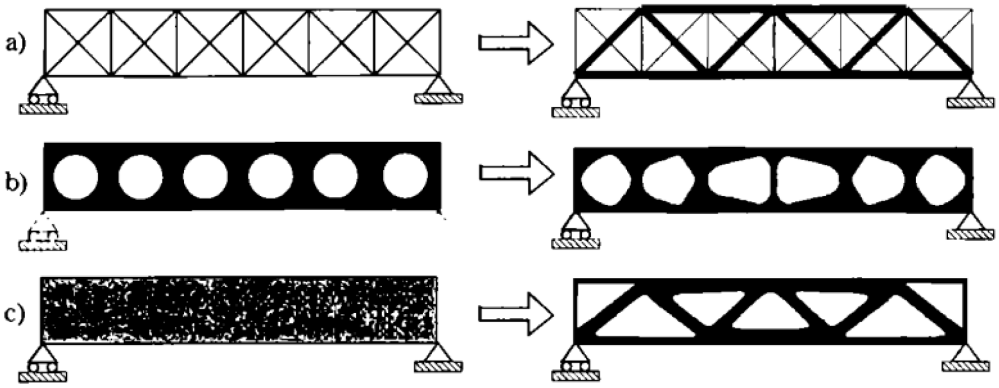

Figure 2.1: Difference in (a) size, (b) shape and (c) topology optimization [18].

Topology optimization is a mathematical minimization problem, written in its most general form as given in Equation 2.1.

$$\begin{aligned} \min_{\boldsymbol{x}} \quad & f(\boldsymbol{x}) \\ \text{s.t.} \quad & h(\boldsymbol{x}) = 0 \\ & g(\boldsymbol{x}) < 0 \\ & \boldsymbol{x} \in [\boldsymbol{x}_{\min}, \boldsymbol{x}_{\max}] \end{aligned} \tag{2.1}$$

To obtain the values of the considered mechanical responses, a Finite Element Method (FEM) analysis is solved. This consists in finding the displacement $\boldsymbol{U}$ through $[K]\boldsymbol{U} = \boldsymbol{F}$, where $[K]$ is the stiffness matrix of the structure, and $\boldsymbol{F}$ the force vector. $[K]\boldsymbol{U} = \boldsymbol{F}$ is known as the state equation. The mechanical responses are then derived from the displacements. Moreover, the different parts of the optimization problem formulation are as follows:

- $f(\boldsymbol{x})$ is the objective function. This is the value of function of the system which is to be improved, usual in term of a minimization.
- $\boldsymbol{x}$ are the optimization variables with respect to which the improvement is performed. They are collected as a vector. These are the parameters defining the system and are to be modified in order to improve the objective. The variables are in the range of the bounds imposed on each of them.
- $h(\boldsymbol{x})$ and $g(\boldsymbol{x})$ are respectively equality and inequality constraints imposed to the optimization to be satisfied. These can be of global (*e.g.*, buckling, vibrations) or local (*e.g.*, stress, displacement) mechanical type, manufacturing, volume.

All variables are used in the problem, but not all have an influence on the objective or the constraints. Different objectives, variables and constraints have been introduced in topology optimization problems. Each aspect will be discussed more in detail in the following sections. Furthermore, depending on the type of problem, different mathematical approaches are possible to resolving the topology optimization problem, and will be discussed shortly.

2.2 Compliance Minimization with Isotropic Material

The standard topology optimization problem is the one of the compliance (C) minimization with an isotropic material and a volume constraint V_0, as presented in Problem A. $\boldsymbol{\rho}$ are the variables representing the topology. Compliance is the inverse of the stiffness. By minimizing the compliance, the stiffest structure is obtained.

$$\begin{aligned} \min_{\boldsymbol{\rho}} \quad & C(\boldsymbol{\rho}) \\ \text{s.t.} \quad & V(\boldsymbol{\rho}) \leq V_0 \\ & \boldsymbol{\rho} \in [\rho_{\min}, 1] \end{aligned} \tag{Problem A}$$

Compliance is defined as the work of the external forces, obtained from Equation 2.2 [18].

$$C = \mathbf{U}^T [K] \mathbf{U} \tag{2.2}$$

The following section will first review the different possibilities to describe the topology, followed by the optimization algorithm used to solve Problem A.

2.2.1 Topology Parametrization

Topology optimizations started to consider structures made of isotropic material [17, 20]. The topology is the design variable, and can be characterized with density [19] or boundary methods [21]. The former assigns a density representing the presence or absence of material, whereas the latter describes the boundary of the domain by means of mathematical functions.

Density Methods

The density method approach consists in an element-wise discretization of the distribution of the material density ρ. An early strategy is the Solid Isotropic Material Penalization (SIMP) interpolation [17, 22], as expressed in Equation 2.3. A constant Young's modulus E_0 representing the pristine material property is multiplied by density variable ρ, penalized by the SIMP exponent p, to obtain the mechanical Young's modulus E. This corresponds to multiplying the complete stiffness tensor, as shown by Equation 2.4 [23]. The value of the density represents the presence ($\rho = 1$) and absence of material ($\rho = \rho_{\min}$). The lower bound on the density $\rho_{\min}$ is used to avoid numerical instabilities in the analysis. Indeed, if the density were to be zero, the stiffness of an element would also be zero in the FEM analysis. The stiffness matrix then becomes singular and the FEM problem can not be solved.

$$E = \rho^p E_0 \tag{2.3}$$

$$[Q] = \frac{\rho^p E_0}{1-\nu^2} \begin{bmatrix} 1 & \nu & 0 \\ \nu & 1 & 0 \\ 0 & 0 & \frac{1+\nu}{2} \end{bmatrix} \tag{2.4}$$

The SIMP exponent p is ≥ 1. In a two dimensional context, a SIMP exponent $p = 1$ is equivalent to the optimization of the thickness of a membrane. By using $p > 1$, an equivalent homogenized stiffness tensor is obtained for intermediate densities, depending on the ratio of material to void. This represent the properties of microstructures bound by the Hashin-Shtrikman conditions. The Hashin–Shtrikman conditions estimate the theoretical lower and upper bound for the elastic moduli of a homogeneous, isotropic mixture of different materials, based on the elastic moduli and volume fractions of the constituents. However, as the SIMP exponent p is increased even further, the homogenization properties lay outside the feasible Hashin-Shtrikman bounds, except for densities tending to $\rho = 1$ or $\rho_{\min}$ limit, as represented in Figure 2.2. Not adhering to the Hashin-Shtrikman bounds for intermediate densities is nonetheless allowed in topology optimization, as the aim is to obtain distinct results with densities at both ends of the interpolation. Indeed, with a SIMP exponent $p > 1$, the stiffness of intermediate density are penalized. This becomes the incentive of the optimization to drive the densities towards the bounds of presence or not of material to obtain distinct topologies with minimal intermediate densities.

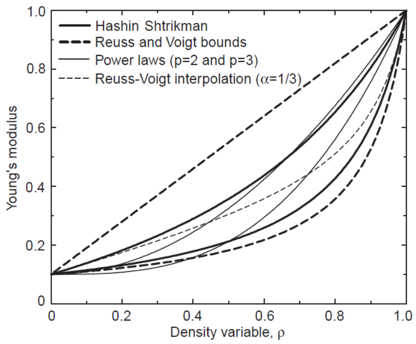

Figure 2.2: Density interpolation functions [22].

Alternatively, a modified SIMP interpolation can also be used, to remove the need for a lower density ρ_{min}. A minimal value for the Young's modulus E_{min} is introduced to assign stiffness to FEM elements, as given by Equation 2.5 [24].

$$E = E_{\text{min}} + \rho_e^p (E_0 - E_{\text{min}}) \tag{2.5}$$

This modified SIMP interpolation was also exploited in case of anisotropy. Instead of using a pristine and minimal Young's modulus, they are replaced by a pristine and a minimal stiffness tensor, analogously to Equation 2.5 [25, 26, 27, 28].

Besides the SIMP approach, other density interpolation strategies have been proposed. Another well used one is the Rational Approximation for Material Properties (RAMP) interpolation [29], as given in Equation 2.6. Here, the interpolation is controlled by the RAMP exponent q.

$$E = \frac{E_0}{1 + q(1-\rho)} \tag{2.6}$$

When using other penalizations than a linear one (when $p > 1$ or $q > 0$), numerical issues such as checkerboards appear in the optimized solution. This consists in a pattern of discrete densities that numerically approximates a continuous stiffness distribution [30, 31]. This is however not acceptable from a mechanical point-of-view. To alleviate the checkerboard problem, and simultaneously impose a length scale control, numerical strategies have been used. A perimeter control strategy [32] limits the length of the topology boundary, which limits the amount of internal holes. Alternatively, filtering techniques have been proposed. They can be applied to the density variables directly [24, 33, 34], or their derivatives [20].

Other numerical issues in topology optimization concerns the aim to converge to a global optimum. This problematic is closely related to the choice of the SIMP interpolation exponent. Svanberg [35] showed that when the stiffness matrix is linear with respect to the optimization variables, stiffness optimization problems are convex. With a density variable, this condition represent thickness optimization, and does do not yield discrete solutions with densities of either ρ_{min} or 1. Usual techniques to obtain distinct topologies involve raising the SIMP exponent p slowly throughout the iterations, or in discrete steps. A review of different numerical strategies has been performed by Rozvany [16]. Automatic strategies have also been proposed, see Rojas-Labanda and Stolpe [36] for example.

Finally, the element-wise density distribution over a domain can also be controlled by spatial interpolation functions, such as NURBS or splines [6]. The interpolation functions are of degree N+1 compared to the optimization problem: the coordinates of the element are the first components, whereas the last component represents the element's density. Such interpolation functions are defined by a number of control points which multiply pre-defined shape functions. The values of these control points are then the optimization variables. An iso-line of the interpolation function defines the boundary of the topology.

Feature-Mapping Methods

The method of morphable component (MMC) [37], similar to the geometric projection method [38], relies on the density principle by assigning a density ρ to each element. However, the distribution is controlled by external parameters that define geometric primitives. These primitives correspond to predefined geometries, such as bars [39] or plates [27], which are projected as a density distribution onto the FEM mesh. The optimization variables are the size and location parameters, dictating the properties of the component, such as the length or width. Where no component is present, a minimal density is assigned to the mesh to avoid numerical problems in the resolution of the FEM analysis. For further information, Wein *et al.* [40] reviewed the use of feature-mapping methods in topology optimization. An example of such a component strategy is displayed in Figure 2.3.

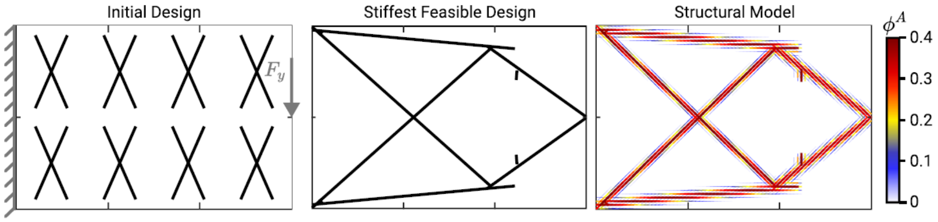

Figure 2.3: MMC optimization results [39].

Level-Set Methods

The Level-Set method [41, 42] is another strategy to parametrize the topology. It is a boundary definition method, based on a mathematical function defining an element-wise value over the domain. Afterwards, a threshold value on that mathematical function dictates the boundary of the topology. Level-Set methods are similar in their topology description as NURBS/splines methods. Nonetheless, the focus of NURBS/splines methods is to manipulate the value of the control points to conduct the optimization, whereas Level-Set methods use perturbation techniques on the topology and its boundary to evaluate the alteration direction of the boundary during the optimization. The mathematical conditions of the presence of density for Level-Set methods are given in Equation 2.7, and represented in Figure 2.4. Nevertheless, Level-Set methods also require regularization of the problem. An extensive review of Level-Set methods, from the different mathematical formulations and possible gradient computation to regularization techniques, is given by van Dijk *et al.* [43].

$$\begin{aligned} \phi(X) > c \leftrightarrow X \in \Omega(material) \\ \phi(X) = c \leftrightarrow X \in \Gamma(interface) \\ \phi(X) < c \leftrightarrow X \in (D\backslash\Omega)(void) \end{aligned} \tag{2.7}$$

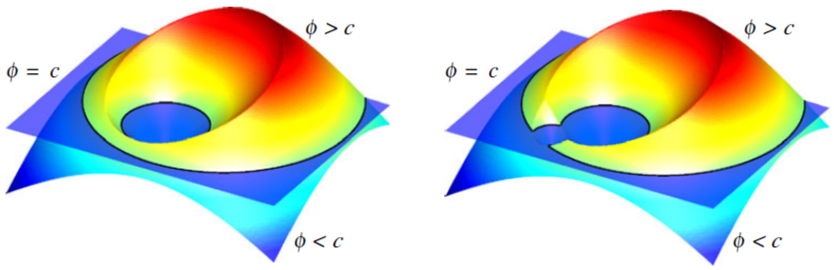

Figure 2.4: Level-Set topology definition [43].

2.2.2 Optimization Algorithms

Compliance minimization problems have been solved with a variety of algorithm types. There exists three main algorithm families to perform the optimizations: optimality criteria, metaheuristic algorithms and gradient-based strategies. All three of them are shortly discussed next. An overview with benchmarking of gradient-based algorithm and optimality criteria was performed by Rojas-Labanda and Stolpe [44].

Optimality Criteria

Optimality criteria have only been used in compliance minimization problems. Compliance problems have the advantage of having a separate contribution of each element to the overall compliance, which allows using an optimality criterion to update all variables separately. Sigmund [19] used a heuristic optimality criterion update scheme for isotropic materials, whereas the optimality criterion used in the Alternate Directions (AD) of Allaire *et al.* [45] has a proof of convergence, for both isotropic and anisotropic material [2]. In both cases, the strategy consists in performing a mechanical analysis to obtain the required information to solve a closed-form conditions to update the variables until convergence is obtained in an iteratively manner.

Metaheuristic Algorithms

Metaheuristic algorithms are zeroth order algorithms, which do not require gradient information of the objective or constraints. Therefore, they can be applied to any type of problems, which does not even require to be continuous. A popular class is the evolutionary algorithm. The principle of evolutionary algorithms is based on natural selection. An initial population representing the design variables is created. Then for each new generation of the population, the fittest solutions are retained, while a mutation or cross-over of the lesser ones is performed in order to seek statistical improvement of the solution. Balamurugan *et al.* [46] used such evolutionary algorithm for compliance minimization.

Other metaheuristic strategies involve particle swarm or ant colony, also nature inspired. The objective will improve following the trend of the majority of the population, where randomness and new search directions are provided by outlier solutions. Application to compliance minimization have been performed by Luh and Lin [47] with ant colony, whereas Luh *et al.* [48] used particle swarm. Nonetheless, due to the exponential combinatorial possibilities when the number of design variables, *i.e.* the number of elements in the FEM of the problem, increases, non-gradient approaches are not well suited for topology optimization problems [49]. Their computational cost to treat all the combinatorial possibilities becomes prohibitive. Furthermore, topology optimizations with metaheuristic strategies require regularization schemes to connect elements.

Finally, the initial Evolutionary Structural Optimization (ESO) [50] framework started as a metaheuristic method. The ESO method consists in removing a percentage of elements who are least solicited from a structure at each iteration. Afterwards, to handle different type of optimization problems, such as buckling [51], the element removal decision became based on a sensitivity number, equivalent to a gradient computation. The ESO strategy is improved upon with the the Bi-directional ESO (BESO) [52] framework, which allows to both remove and add elements. This gives the optimization more freedom, and allows to better converge to local minima.

Gradient-Based Algorithms

A gradient-based strategy uses the gradient information to update the design variables. Algorithms may use the first derivative information only, but may also incorporate the second derivative. These methods incorporating the second derivative are more accurate in representing the response surface, but require a higher computational cost to obtain the information. For more complex problems than compliance, obtaining the first derivative is not straightforward, obtaining the second is even less practical. Basic unconstrained optimization problems can use the steepest descent direction, but more complicated problems require so-called mathematical programming for non-linear optimizations. The non-linear part is represented by the addition of non-linear equality and inequality constraints. The idea is then to create local approximations of the problem at the current design point with the gradient information. These approximations are constructed in such a way that dedicated algorithms can solve them efficiently. Gradient-based strategy can be applied to a large range of problems, but requires the gradient information to be accurately and efficiently provided. Such sequential approximation approaches are applied for the largest topology optimization problems, see [53] for a review.

The different type of approximations of the problem include among others Sequential Linear Programming (SLP), Sequential Least Square Quadratic Programming, Augmented Lagrangian, CONvex LINearization (CONLIN) [54] or Methods of Moving Asymptotes (MMA) [10]. Dedicated algorithms to solve the approximated problems include among others the primal-dual method or interior point method. SLP consists in solving successive linearized problems at the current iteration, whereas SLSQP uses a quadratic approximation. The Augmented Lagrangian is an improved quadratic penalty method. CONLIN linearizes or uses an inverse approximation, depending on the sign of the gradient. MMA consists in a monotonous approximation, which can be controlled by the values of the asymptotes. Svanberg [55] also proposed a modification on MMA, the Global Convergent MMA (GCMMA). The GCMMA approximation is convex and non-monotonous, which is better suited to approach a minima without oscillations due to its non-monotonous property. Zuo *et al.* [56] combined the monotonous Method of Moving Asymptotes (MMA) to initially converge faster towards a minima for compliance minimization, and then switched to the Global Convergent MMA (GCMMA).

2.3 Strength-Based Topology Optimization

Strength constraints have been incorporated in topology optimization to account for material failure with density-based methods [4, 57, 58, 5], NURBS [59], Level-Set [60] or BESO [61]. The focus of this section will be on introducing strength constraints in a SIMP density-based framework. Two main problems are recognized. The first one involves the nature and value of the local stress, while the second one concerns the computational cost for optimizations.

2.3.1 Stress Singularity

Strength optimizations are subjected to singularity problems. This means that for a continuous variation of the design variables, it is only possible to attain the optimal solution of a problem by going through a violated state of the optimization constraints [62]. In topology optimization, this is represented by the fact that the optimum is usually present in a a degenerated subspace, which can thus be difficult for gradient optimizations to reach [63, 64]. This condition can be visualized by the example presented in Figure 2.5. The original design space for this problem is shown in Figure 2.6 (a). The pinkish zone represents the feasible domain of the constraint, whereas the gray lines are iso-lines for constant objective value of the design space. The arrow shows the direction for the objective's improvement. It is visible that the optimal design satisfying the constraint is point D. Nonetheless, reaching this point with classical gradient-based algorithms is almost impossible. Point D is only connected by a line to the rest of the feasible domain, meaning the gradients with respect to A_2 should be 0 to attain it.

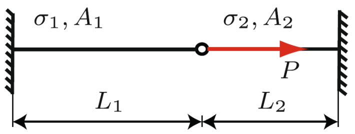

Parameters:
$P = 1$
$\sigma_{\text{lim}} = 1$
$E = 1$
$L_1 = 6/10, L_2 = 4/10$
$\rho_1 = 1, \rho_2 = 2$
$m = 0.6A_1 + 0.8A_2$

Figure 2.5: Volume minimization problem with two stress constraints exhibiting a stress singularity [5].

To be able to attain this optimal point D numerically, the stress constrains are relaxed in a gradient-based framework, as shown in Figure 2.6 (b). In this state, gradient-based optimization algorithms are able to reach the optimum of point D. Such a stress relaxation technique, called ϵ-relaxation, was first proposed in truss optimization [63] and later successfully adapted for continuum topology optimization [65, 66]. This involved the relaxation of the stress constraints for low density elements, alleviating the singularity issue. The method was improved to an easier implementation, the so called *qp-approach* [67]. This method uses a different stiffness interpolation exponent when computing the stress than the one used to evaluate the local stiffness matrix. The *qp-approach* was shown to be a special case of the ϵ-relaxation, where the relaxation parameter depends on the element's density [67].

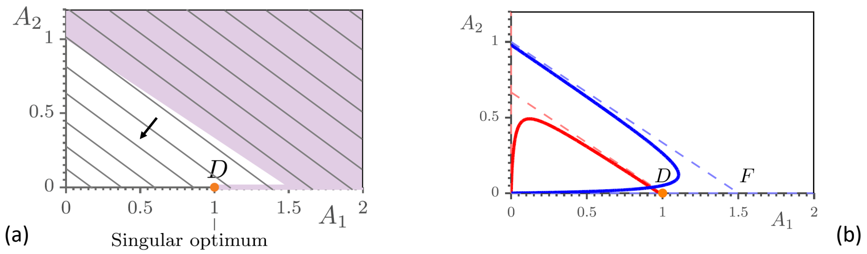

Figure 2.6: Original (a) and relaxed (b) design space of the problem in Figure 2.5 [5].

The *qp-approach* can also be linked to another local density related problem: the stress measure. As a density interpolation approach characterizes a fraction of void and material, the macro stress (applied at the element level) does not represent the actual stress within the microstructure made of void and material. In case of a SIMP interpolation, the relation between the void/material ratio and microstructure is unknown, as the aim is to achieve distinct (0/1) designs. Not using the micro-stress falsifies the progress of the optimization for intermediate densities, potentially leading to a trivial all void design in case of volume minimization with a stress-based strength constraint [4]. Therefore, an equivalent micro-stress measure is derived in combination with the *qp-approach* [4, 57, 67]. When characteristics of a microstructure are taken into account, a relation between the macro and micro-stress is obtained, as demonstrated by Duysinx and Bendsoe [68] for rank-2 microstructures. Nonetheless, a relaxation technique still needs to be applied.

The approximation of the stress is another issue in topology optimization with failure constraints. Firstly, the structured ground mesh cannot follow oblique features, leading to serrated edges with intermediate densities [69]. Svard [70] suggested an interior value extrapolation to approximate the boundary stress by an extrapolation of the stress in the distinct material. Secondly, depending on the number of elements, the mesh resolution may not be sufficient to accurately represent stress concentrations. Lastly, a FEM analysis is based on a displacement formulation for the elements, for which stress' evaluations may be rather inexact [71]. These conditions can be circumvented by using a finer ground mesh, resulting in higher numerical cost. Instead, better suited element types based on a different formulation can be used [3].

2.3.2 Computational Cost

Introducing strength constraints in topology optimization entails several other difficulties. Stress by nature is a local entity, which is usually represented with an individual constraint per element. This results in a number of constraints equal to the number of elements. However, a large number of constraints can become limiting for gradient optimizers. Moreover, the computational cost for the gradient of each constraint is prohibitive, as it requires one FEM analysis per gradient. To avoid handling too many constraints, one could imagine constraining the maximum stress only. However, this is difficult since trying to minimize the maximum stress constraint value is difficult, as the location of the maximum can change throughout iterations, resulting in ill-defined sensibilities [72]. Additionally, the maximum operation is non-differentiable.

Several tactics have been proposed which address these issues simultaneously. The most widely used strategy consists in aggregating all the element-wise strength constraint values into a single one [73]. The aggregation is usually done with either the p-norm [74] or the upper Kreisselmeier–Steinhauser (KS) [3] function. These functions regroup the whole set of stress values and approximate the maximum value from an upper value. A p-norm function can only aggregate positive values, whereas the KS function can handle both positive and negative values. These aggregation techniques also avoid differentiability issues when the location of highest stress changes between iterations. Verbart *et al.* [5] showed the combined relaxation and aggregation property with the same function: a lower KS aggregation. The lower KS approximates the maximum from a lower value. Furthermore, Verbart *et al.* [5] used an equivalent problem formulation, based on the concept of Mathematical Programming with Vanishing Constraints (MPVC) [75]. This approach has proven to work well [76, 77], although underestimating the local strength constraint. When using an aggregation function, one FEM analysis is still required per optimization constraint, but by aggregating the constraints, the number of constraints and therefore additional FEM analysis decreases drastically. Instead of the local constraint aggregation, Senhora et al. [58] used the Augmented Lagrangian (AL) algorithm which allows to include all the stress constrains in the objective function by penalizing them, instead of aggregating them into a constraint. This techniques also employs one additional FEM analysis to compute all the stress gradients. The drawback of an aggregation into a single constraint, is loosing control over the local behavior of the stress. It means that with an aggregation, only the most critical locations will be considered, with the other ones becoming less influent for the optimization.

In order to preserve a more direct control over the stress distribution while decreasing the number of constraints, Bruggi and Duysinx [78] proposed using a set of *active stress constraints*, including elements close to or violating the failure constraint. This feature works well for coarser meshes, but as the mesh is refined, an increasing number of elements reaches this target and again increases the amount of constraints and subsequent gradient computation cost. An intermediate strategy to control the number of optimization constraints, is to use several aggregation zones. This was proposed by París *et al.* [79, 80] with "block aggregation". The method segments the design in different geometric blocks who internally use aggregation, nonetheless it is difficult to define the number and size of these regions for an effective analysis [4].

Other strategies have been proposed to create clusters of elements, based on mathematical rules. For example, Holmberg *et al.* [57] used a "stress level technique" (as given by Equation 2.8) and "distributed stress technique" (as given by Equation 2.9) to assign the elements to a predefined amount of clusters. The first one involves regrouping the element with stress of similar magnitude, whereas the second one distributes equally similar magnitude to have similar aggregated cluster value. Re-clustering during the optimization was also considered, based on heuristic schemes. Re-clustering however introduces discontinuities in the optimization problem, which did not hinder the convergence [57]. These (re-)clustering strategies aim to provide an automatic control over the stress distribution and therefore achieve lighter solutions. Performing re-clustering during the optimization, with a "stress level technique" generates simple solutions which avoid stress concentrations.

$$\underbrace{\sigma_1 \geq \sigma_2 \geq \sigma_3 \geq \ldots.. \geq \sigma_{\frac{n_e}{n_c}}}_{\text{cluster 1}} \geq \underbrace{\ldots.. \geq \sigma_{\frac{2n_e}{n_c}}}_{\text{cluster 2}} \geq \ldots.. \geq \sigma_{\frac{(n_e-1)n_c}{n_c}} \geq \underbrace{\ldots.. \geq \sigma_{n_e}}_{\text{cluster } n_c} \tag{2.8}$$

$$\underbrace{\sigma_1}_{\text{cluster 1}} \geq \underbrace{\sigma_2}_{\text{cluster 2}} \geq \ldots.. \geq \underbrace{\sigma_{\frac{n_e}{n_c}-1}}_{\text{cluster } (n_c-1)} \geq \underbrace{\sigma_{\frac{n_e}{n_c}}}_{\text{cluster } n_c} \geq \underbrace{\sigma_{\frac{n_e}{n_c}+1}}_{\text{cluster 1}} \geq \ldots.. \geq \underbrace{\sigma_{n_e}}_{\text{cluster } n_c} \tag{2.9}$$

Figure 2.7 shows obtained results for volume minimization with Von Mises stress constraints on the L-bracket benchmark problem with different strategies presented earlier. Despite the use of different strategies, the final topologies exhibit similar characteristics, namely a rounded topology is created to alleviate the stress concentration at the re-entrant corner. A more comprehensive review of optimization strategies for stress constraint topology optimization is given by da Silva *et al.* [64].

Rectifier

As aggregations approximate the maximal value of the strength constraint over a set of elements, either from below with a lower KS or from above with an upper KS or p-norm, it does however not coincide with the exact maximum. In order to take the actual maximum value into account with an aggregation approach, rectifier approaches have been suggested to obtain the correct constraint value [81]. This consists in multiplying the

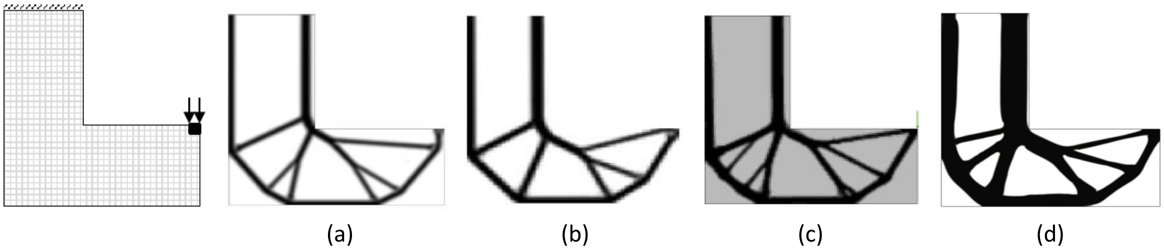

Figure 2.7: Stress-based benchmark optimization problem and results obtained by (a) Verbart *et al.* [5], (b) Le *et al.* [4], (c) Holmberg *et al.* [57] and (d) Senhora *et al.* [58].

aggregation value by a term which is dependent on the ratio of the actual maximum and aggregated value. Moreover, heuristic schemes have been added to introduce a damping factor to alleviate oscillations with the rectifier, as it is not considered in the gradient computations. An example of such rectifier c_s^k is given in Equation 2.10 [3], where s_0 represents the damping factors. σ_{KS} is the value of the aggregated stresses, whereas $\sigma_{\max}^{VM}$ is the maximum stress used in the aggregation. Such a rectifier approach has successfully been used with a p-norm [4] and the upper KS [3] aggregation function. Yang *et al.* [82] used the rectifier approach on elements which are only close or above the constraint limit, similar to the *active set elements*.

$$c_s^{(k)} = \begin{cases} \frac{\sigma_{\max}^{VM^{(k)}}}{\sigma_{KS}^{(k)}}, & \text{if } k = 1 \\ (1 - s_0)\frac{\sigma_{\max}^{VM^{(k)}}}{\sigma_{KS}^{(k)}} + s_0 c_s^{(k-1)}, & \text{otherwise} \end{cases} \tag{2.10}$$

2.3.3 Strength Criteria

Stress-based topology optimizations with isotropic material are often carried out with the Von Mises criterion [3, 4, 57], even considering design dependent loads [83]. Nonetheless, other criteria have also been incorporated. Bruggi and Duysinx [78] and Luo and Kang [84] used the Drucker–Prager criterion still with isotropic material, which generalizes the Von Mises criterion and can differentiate between tensile and compressive allowables. Instead, Pereira *et al.* [66] used the Raghava criterion considering isotropic material. This criterion also differentiates tensile and compressive allowables. An elliptic Tsai-Wu criterion was used for additive manufacturing by Mirzendehdel *et al.* [12] in a Level-Set framework with isotropic stiffness and transversely isotropic strength. This strength criterion, beyond the differentiation of traction and compression, also incorporates a directional component. In case of additive manufacturing in successive ±45 raster layers, the strength properties can be assumed uniform within the layers, with anisotropic strength properties being aligned with the printing direction.

2.3.4 Optimization Algorithms

Strength-based topology optimization problems for isotropic materials are solved by means of gradient-based optimizers. A variety of algorithms has been used, including among others the Augmented Lagrangian [58, 64, 66], MMA [3, 4, 57, 5, 74], CONLIN [68] or SLP [80]. In general, gradient-based algorithms are the most extensively used in topology optimization because of their versatility, even for other constraints such as buckling [3, 85], vibration [86] or manufacturing constraints [87, 88]. Gradient-based optimizers are also widely used in the case of anisotropy as discussed next.

2.4 Anisotropy Considerations in Optimization

The focus of the following literature analysis is twofold: Section 2.4.1 details with the overall parametrizations of anisotropic material stiffness in topology optimization and Section 2.4.2 deals with composite laminates optimization, since one of the main objectives of the present work is to bridge the gap between these two distinct fields in structural optimization. Composite laminate optimization is extensively reviewed by Xu *et al.* [89]. Once again, the main focus is placed on the parametrization of the material elastic properties. Thereafter, handling anisotropic strength properties in composite optimizations is detailed in Section 2.4.3. Finally, a small discussion is provided on numerical implementation issues with anisotropy in Section 2.4.4.

2.4.1 Material Anisotropy in Topology Optimization

Three main classes of methods can be extracted from the literature to handle material anisotropy in topology optimization, namely, multi-scale parametrizations, direct parametrization of the elastic tensor and multi-material methods.

Multi-Scale Approaches

A multi-scale approach is based on a microstructure in a representative elementary volume (REV). The macroscopic stiffness tensor of the REV $[Q^H]$ is obtained by homogenization of the stiffness properties of its constituents. Several homogenization methods can be used such as strain energy methods [90] or asymptotic methods [91]. An example of asymptotic homogenization is given by Equation 2.11. $\boldsymbol{\chi}_e^{0(ij)}$ are the test strains as presented in Figure 2.8 and $\boldsymbol{\chi}_e^{(ij)}$ the corresponding response strains. The macroscopic stiffness properties are then used in the later process to set up the FEM analysis in topology optimization. Even when using a mixture of only isotropic material and void at the microscale, depending on the layout of the microstructure, an anisotropic macroscopic stiffness can be obtained.

Once the macroscopic anisotropic properties are obtained, these microstructures can be rotated to attain preferred directional properties in the optimization. However, this creates the issue of connectivity between cells at the microscopic scale, whether a single microstructure is used, but also for a variable microstructure [92] as shown in Figure 2.9. With variable microstructures, it is possible to work with a pre-compiled database of microstructures and their homogenized properties, which have even been interpolated between missing points [93]. The multi-scale approach involves optimization variables at different scales: the anisotropic stiffness is defined by the variables representing the REV microstructure, whereas the variables at a macroscopic level dictate the orientation of the anisotropy. For further information on multi-scale methods and their application to topology optimization, a review has been performed by Wu *et al.* [94].

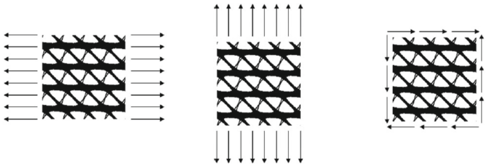

Figure 2.8: Test strain used to evaluate the homogenized stiffness properties of a microstructure [92].

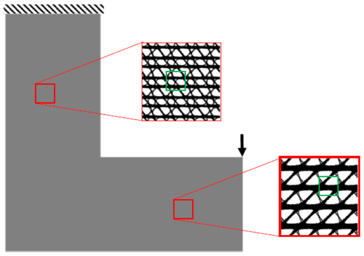

Figure 2.9: Variable microstructure distribution [92].

$$Q_{ijkl}^H = \frac{1}{|V|}\sum_{e=1}^{n}\int_{V_e}(\boldsymbol{\chi}_e^{0(ij)} - \boldsymbol{\chi}_e^{(ij)})^T[Q](\boldsymbol{\chi}_e^{0(ij)} - \boldsymbol{\chi}_e^{(ij)})dV_e \tag{2.11}$$

Direct Definition of the Stiffness Tensor

An alternative approach to incorporate anisotropic stiffness properties is not to change the microstructure, but instead directly define the stiffness properties of a given anisotropic material. The first discussed strategy is where a given anisotropic material is rotated. Usually, this strategy is employed with composite Uni-Directional (UD) plies, made of fibers running in one direction held together by a matrix, either in laminates [95] or in 3D printing [96]. In a fixed reference frame, changing the orientation of an anisotropic material results in a different stiffness tensor and therefore mechanical properties. The same material orientation can be applied over the complete structure, which is usually referred to as constant stiffness. When instead the orientations vary spatially, variable stiffness is obtained. For either, the orientation becomes an additional design variable in the optimization, whether it varies globally or point-wise for each element. The point-wise orientations can be defined independently of one another, or obtained by interpolation functions similar to the Level-Set method [97, 98].

Optimizations with variable stiffness can be classified as Continuous Fiber Angle Optimization (CFAO) [99]. CFAO and topology optimization have been used with transversely isotropic material in 2D [28] and 3D [100]. More specifically, the challenges of accounting for variable anisotropy in topology optimization for additive manufacturing have been reviewed by Zhang *et al.* [101]. They highlight the need to incorporate process modeling in the optimization. Dapogny *et al.* [102] considered the effect of anisotropic infill patterns on compliance minimization, whereas the anisotropic stiffness along the printing path was taken into account by Liu *et al.* [103] in a topology optimization framework.

When considering material density and orientation for compliance minimization, most research employed the MMA algorithm [26, 27, 96, 104, 105, 106, 107], or its global convergent GCMMA approximation [108]. Bruyneel [23] compared several gradient-based algorithms for the optimization, finding that a combination of MMA and GCMMA [109] achieves a stable and fastest convergence with equivalent objective values to the other algorithms. For multiple load cases, Setoodeh *et al.* [110] considered a linear combination of the compliance values as objective. The optimization uses an optimality criteria to obtain the optimal angle for separate each load case. The separate optimal orientations are then combined with the linear objective combination to obtain the overall optimized orientation.

The definition and inclusion of the material rotation for mechanical calculations have been performed by several strategies. The most common approach is to apply a change of reference frame by means of a second order tensor rotation in 2D [111]. Nomura *et al.* [104] used the components of the orientation vector in an isoparametric projection as optimization variables. In the same framework, Lee *et al.* [108] simultaneously used the vector's magnitude to represent the density variable. Different orientation descriptions for an anisotropic tensor have also been utilized in 3D topology optimization. Zhou *et al.* [26, 96, 105] used an orientation tensor, described by a normalized orientation vector. Alternatively, Schmidt *et al.* [106] used two successive rotations around different axis. Finally, Smith and Norato [27, 107] used quaternions to represent the general orientation of a plate in a geometric projection topology optimization.

On the other hand, instead of using a rotation, the components of the stiffness tensor in 2D or 3D can directly be the optimization variables as performed in the Free Material Optimization (FMO) framework [112]. Nonetheless, FMO requires compatibility constraints on these components to ensure the stiffness tensor remains mechanically admissible, enforced by means of semi-definite programming with an interior point solver [113]. Thereafter, to identify microstructures obtained by FMO, inverse homogenization techniques are used [114]. In such a context, Hu *et al.* [115] considered the connectivity of adjacent microstructures, whereas Tyburec *et al.* [116] applied clustering to FMO results to seek modular designs for the microstructures. Instead, Weldeyesus and Stolpe [117] proposed a restriction of the FMO approach to represent laminates. FMO for membrane stiffness is considered for separate layers, and assembled taking into account shell kinematics. Nomura *et al.* [25] used an approach similar to FMO for topology optimization with UD fibers, by defining the components of an orientation tensor as variables.

Finally, the stiffness tensor can also be parametrized by means of invariants quantities, such as with the polar formalism for general anisotropy in 2D [118] or by harmonic decomposition for a transversely isotropic material in 3D [2]. Simple mathematical conditions on the invariants then ensure the stiffness tensor remains thermodynamically admissible. These mathematical conditions are akin to the constraints imposed by the semi-definite programming in case of FMO. The invariant quantities define the anisotropic modules of the material, and the direction of anisotropy is then dictated by an orientation definition.

Multi-material

Also named as multi-phase materials [119], topology optimization considering multiple material aims to find beside the presence or absence of material, also the best local elastic properties from a pre-selected range of materials [120]. The stiffness tensor related to an element is obtained as a linear combination of the stiffness of pre-selected materials, given by Equation 2.12. The aim is to obtain one weight w_i as 1, with all other ones as 0, meaning only one material property remains. The aim is to obtained element-wise one well defined material at the end of the optimization. The pre-selected materials can either be isotropic or anisotropic [121], or both type can be considered in the same optimization [106]. Multi-material strategies have been used in a stress based topology optimization in [122] or buckling in [123].

$$[Q] = \sum_{i=1}^{e} w_i [Q]_i = w_1[Q]_1 + w_2[Q]_2 + ... + w_e[Q]_e, \quad 0 \leq w_i \leq 1 \tag{2.12}$$

A special framework adapted to composites, the Discrete Material Optimization (DMO) strategy, was developed by Stegmann and Lund [124]. It uses the multi-material optimization principle to find the best ply orientation in a variable stiffness, constant thickness laminate layup [125, 126]. Smith and Norato [27, 107] used the DMO method for a 3D compliance minimization problem, to obtain a constant stiffness laminate on a plate represented by a geometric projection in topology optimization. DMO is extended to the Discrete Material and Thickness Optimization (DMTO) framework [127], which also incorporates ply drops by assigning a density to each ply as in topology optimization. Instead of predefined candidates, Peeters and Abdalla [128] considered continuous orientations in a similar framework to define ply drops in the optimization for a variable stiffness variable thickness laminate.

2.4.2 Macroscopic Parametrization for Composite Laminates

A composite laminate consists in a stacking sequence of UD plies, each with a given orientation δ, as shown in Figure 2.10. Two different reference frames can be distinguished. The first one is the global laminate coordinate system frame xyz, in which the macroscopic stiffness tensor is expressed. The second material coordinate system 123 is defined for each UD ply, and is rotated by δ with respect to the global reference frame. The macroscopic stiffness of the laminate is computed from the stacking sequence by means of Classical Laminate Plate Theory (CLPT) or higher order theories [129].

Altering both a ply's orientation and through the thickness location in the stacking sequence influences the stiffness properties at the laminate level. Instead of representing each separate ply and its orientation, specific homogenization techniques have been developed for laminates made of a base ply to represent their overall stiffness. These techniques loose the implicit stacking sequence information, but represent a laminate' stiffness for all possible permutation of ply orientations and through the thickness location with a reduced number of variables. This feature is not only helpful to reduce the computational cost of optimizations over a direct fiber orientation approach [131], but homogenization techniques also provide a more regular design space [132]. Indeed, "one of the major challenges in design optimization of laminated composite structures is the non-convexity of the design space, i.e. the risk of ending up with a local optimum solution is

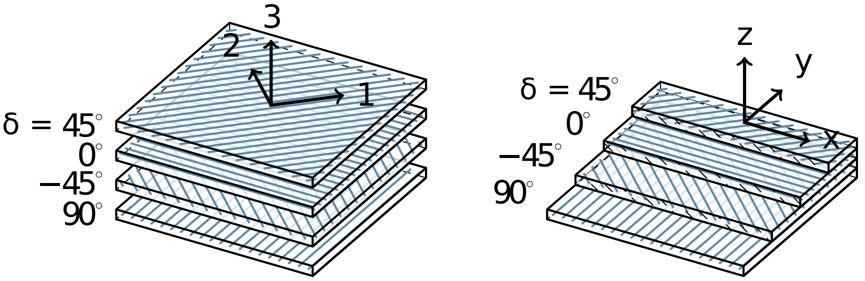

Figure 2.10: Laminate layup consisting of different UD plies, rotated from the laminate reference frame xyz to the ply's reference frame 123 by δ [130].

high" [125] when discrete orientations and layups are used directly. Instead, at the end of a laminate optimization with homogenized stiffness, a second design step to retrieve the actual stacking sequence is required.

Lamination Parameters

The most used homogenization technique are the lamination parameters [133]. This strategy is based on four lamination parameters V_i to represent a 2D stiffness tensor, as computed by means of Equation 2.13 for membrane stiffness. They represent the layup information, both the amount of plies N, with the same thickness proportion, and their orientation δ. To obtain the in-plane stiffness tensor $[A]$, the lamination parameters V_i are combined with material properties of the base ply, as expressed in Equation 2.14. Γ are matrices with material properties expressed by means of the Tsai-Paganao parameters defined in a fixed reference frame [134], with respect to the components of the base ply stiffness tensor. Similar definitions are available for the coupling $[B]$ and out-of-plane $[D]$ stiffness tensor. When optimizing with respect to lamination parameters, the V_i become the variables. However, their values are bound by trigonometric relations. A more comprehensive review of lamination parameters can be found in [135].

$$\begin{aligned} V_1, V_3 &= \frac{1}{N}\sum_{k=1}^{N}\cos(2\delta_k, 4\delta_k) \\ V_2, V_4 &= \frac{1}{N}\sum_{k=1}^{N}\sin(2\delta_k, 4\delta_k) \end{aligned} \tag{2.13}$$

$$[A] = h(\Gamma_0 + \Gamma_1 V_1 + \Gamma_2 V_2 + \Gamma_3 V_3 + \Gamma_4 V_4) \tag{2.14}$$

Lamination parameters are mainly used in optimizations with variable stiffness laminates. It can be used when only the anisotropy needs to be optimized [136, 137] or in combination with the optimization of the thickness or topology [138]. Peeters *et al.* [139] combined topology and lamination parameters for compliance minimization, in an integrated but not simultaneous optimization of both topology and anisotropy. Only the variable driving the best improvement is updated at each iteration, with a maximum number of consecutive times. The optimization is performed with a predictor-corrector interior point gradient-based algorithm on a convex approximation of the problem. Similarly, Tong *et al.* [140] used a sequential approach for compliance minimization, alternating between topology and lamination parameters optimization for each FEM analysis. Later, they applied the optimization to a leading edge for a compliant design [141], while using GCMMA to optimize both density and lamination parameters simultaneously. Instead, Bohrer and Kim [142] used MMA to optimize both density and lamination parameters simultaneously. Moreover, they proposed a restriction on the lamination parameters feasible region, in order to facilitate the layup retrieval in subsequent steps. Finally, Hu *et al.* [143] also included steering constraints on the layup retrieval, after having used MMA in a sequential manner to resolving the topology and lamination parameters optimization.

Polar Parameters

Whereas lamination parameters represent the elastic modules of composite laminates in a fixed reference frame, the polar parameters provide a general representation of both the elastic modules and the local frame [118]. The polar parameters are an invariant-based representation of a 2D stiffness tensor, which facilitates the consideration of rotations and change of reference frame. The polar formalism can be applied not only to composite laminates, but encompasses any 2D material's stiffness tensor. The domain of existence of the polar parameters for any material is delimited by the thermodynamic bounds. These thermodynamic bounds are a simple condition on the polar parameters, and are the equivalent to the constraints on the components of the stiffness tensor in FMO. Laminated structures constituted from a known base ply are defined conveniently as a subset of the thermodynamic domain on the polar parameters, the geometric domain [11]. The corresponding geometric bounds have only been used thus far in thickness optimization problems with a gradient-based algorithm [144, 9, 145]. Nonetheless, the polar parameters have been used as design variables in a topology optimization considering the thermodynamic bounds in [1], based on an optimality criteria algorithm, the Alternate Directions. The polar formalism and the conditions for the different domains of existence are discussed in more detail in Section 2.5.

Jibawy *et al.* [146] used the polar formalism to optimize only the in-plane $[A]$ stiffness tensor of a laminate. They considered special stacking sequences, namely angle and cross plied ones, thereby restricting the domain of the polar parameters. This was used to perform stiffness maximization by means of optimality criteria, and afterwards be able to determine a matching feasible stacking sequence over the domain. Later, the polar parameters have also been used to perform optimization with the complete ABD laminate properties. Montemurro *et al.* [147] used the polar parameters to maximize the stiffness of laminates with specific elastic properties, such as in-plane isotropy, for a minimal number of plies by means of a genetic algorithm. This was extended to other objectives, such as vibration or strength by Vincenti *et al.* [148]. A genetic algorithm was used by Montemurro *et al.* [149] to optimize the anisotropy of both the skin and stiffeners for minimum mass with buckling constraints, in combination with the amount and location of the stiffeners.

Montemurro and Catapano [150] proposed a two-level strategy for buckling optimization with respect to thickness and layup in a variable stiffness laminate framework, the optimizations still being solved with a genetic algorithm. The polar parameters distribution is described by a B-spline, while the kinematics include an extension of the polar parameters to the first order shear deformation theory [151]. Still in a similar framework, manufacturing constraints have been considered with the polar parameters for mass minimization with buckling constraints [144]. When the polar invariants are constant, a steering constraint can be expressed on the variation of direction of anisotropy [152]. Izzi *et al.* [9] adapted the framework to use the SLSQP gradient-based optimization algorithm, while also describing the thickness variation with a B-spline.

Lastly, Savine [145] used the polar formalism to optimize laminates in a framework combining variable stiffness and thickness optimization of a 3D shell structure and layout optimization of stiffeners using a projection based method. The optimization problem consisted in mass minimization with buckling and edge loads constraints in a gradient-based framework using MMA.

Laminate Retrieval

Whether the lamination parameters or polar parameters are used to represent the homogenize stiffness of laminates, a second step must involve retrieving an actual layup matching the stiffness distribution. This step is often performed with metaheuristic algorithms [153], in the case of generic laminates. The purpose of the optimization is to match the optimized stiffness distribution obtained at the end of the first continuous optimization step based on an homogenized description of the laminates. The main computational cost lies in the first step that combines gradient-based optimization and structure model evaluations. The second step is analytical which enables the use of metaheuristic algorithms. Note that a good matching can be difficult or impossible to obtain, depending on the choice of the manufacturing constraints introduced in the layup retrieval phase. Resulting designs can be sub-optimal. This point is dealt in further detail in [154].

A possible way to avoid this retrieval step, is to constrain the homogenized stiffness of a laminate in the first optimization step. Several special layup configurations can be defined, with a direct relationship to the homogenized laminate stiffness tensor. For instance, Jibawy *et al.* [146] considered the homogenized stiffness of a layup consisting in $\pm\alpha$ orientation in their optimizations. On the other hand, Montemurro and Catapano [152] simplified the second level by only using quasi-trivial layups. This facilitates the retrieval of the layups, as quasi-trivial layups present advantageous properties [155], notably a zero [B] coupling matrix regardless of the layer's orientation. Lastly, Savine [145] used "double-double" layups, consisting of two ply orientations regrouped in predefined geometric set, as to obtain a quasi-homogeneous laminate.

2.4.3 Integration of Strength Constraints for Laminate Optimization

Whereas a Von Mises stress criterion is applied directly to any isotropic structure, defining failure for a laminated structure is not as straightforward. The constituent UD plies of a laminate show besides anisotropic stiffness, also anisotropic strength, both properties defined in the ply's reference frame. The allowables differ longitudinally, along the fibers, from to the transverse direction, mainly dominated by the matrix. For preliminary and detail design stages, laminate failure is often represented by first ply failure, where each individual ply in the laminate is checked with an appropriate anisotropic strength criterion. Failure for the complete laminate is then assumed to occur as soon as any ply fails. For even more detailed analysis, progressive models are used to design and verify the integrity of laminates. These progressive models take load redistribution into account when certain defects occur or individual plies fail within the laminate [156]. For first ply failure as discussed and used for the remaining of this research, perfect ply bonding is assumed and inter-laminar stresses between different plies are neglected. These stresses are a consequence of the stiffness mismatch in the stacking sequence, for which guidelines are provided to reduce the effect of inter-laminar stresses [129].

Checking a first ply failure with an anisotropic strength criterion is done with all quantities expressed in the same reference frame, usually that of the ply. This entails that the global stresses applied to the laminate are rotated to the ply's reference system, to obtain the local stresses to be used in the strength criterion. An elliptic strength criterion is then applied, the most used one being the Tsai-Wu criterion [129]. This strength criterion consists in a single condition considering all the applied stresses at the same time. For such elliptic strength criterion, failure is defined by the safety factor s_1 obtained from the quadratic relation of Equation 2.15. $[F]$ and $\boldsymbol{G}$ are based on the type of failure criterion and material properties. The solution s_1 represents the load multiplier that can be applied to the stress state to reach the failure envelop defined by the considered failure criterion. However, using s_1 directly in gradient-based optimizations would lead to load-dependent solutions [157]. This is alleviated by using the failure index to define the failure measure, which corresponds to the inverse of the safety factor s_1. The failure index indicates how much the current stress state is in proportion to the critical one to achieve failure according to the criterion. Using the polar formalism, Catapano *et al.* [158] proposed an invariant parametrization of the Tsai-Wu, Tsai-Hill and Hoffman anisotropic failure criteria.

$$s_1^2 \boldsymbol{\sigma}^T [F] \boldsymbol{\sigma} + s_1 \boldsymbol{\sigma}^T \boldsymbol{G} - 1 = 0 \tag{2.15}$$

The Tsai-Wu criterion has initially been used with genetic algorithms to define the stacking sequence in constant stiffness, constant thickness laminates optimizations [159, 160]. Afterwards, the Tsai-Wu criterion has been used with gradient-based optimization, such as in variable stiffness constant thickness laminate, considering strength, stiffness and manufacturing constrains by Ding *et al.* [161]. Each ply is modeled, where the spatial distribution of the orientations is obtained with a radial basis function. The optimizations are solved with MMA, where the local strength is taken into account as optimization constraint with a p-norm aggregation on the failure indexes. For additive manufacturing, Liu *et al.* [162] compared stress-based Von Mises topology optimizations to experiments and found that the deposition path influences the structural strength. Mirzendehdel *et al.* [12] included an anisotropic failure criterion to capture this behavior, with the anisotropy orientation of the failure criterion coinciding with the extrusion of the layer direction. Nonetheless, the material stiffness remains isotropic. Different designs were obtained based on the solicitation of the tensile or compressive strength. Roiné [6] used a UD ply in their topology optimizations with different anisotropic failure criteria, still for fixed ply orientations, solved with GCMMA. Instead, Dogru [163] included a Tsai-Wu failure criterion in a ESO like framework, for topology optimization with yet again fixed orientations of the anisotropy. Recently on the other hand, Ma *et al.* [8] considered strength in topology and fiber orientation optimizations by means of MMA. Compliance minimizations are performed with a volume constraint and Tsai-Wu criterion, where the optimization constraint is obtained by means of a p-norm and rectifier approach to consider the anisotropic strength.

These strength criteria (Tsai-Wu, Tsai-Hill and Hoffman) use all stresses applied to the ply in a single condition, and do not differentiate between failure mechanisms. There exist other more complex first ply failure criteria, such as Puck or Hashin, that are based on separate conditions for the fiber and matrix failure. These type of criteria have been used with genetic algorithms. Deveci *et al.* [164] incorporated the Puck failure criterion in buckling optimization for constant stiffness constant thickness laminates. Lopez *et al.* [165] compared the Puck failure criteria with Tsai-Wu, obtaining highly different solutions depending on the failure criteria for a same load case. Instead, Irisarri *et al.* [166] used the Hashin strength criteria for the layup design of stiffened panels.

Using a stress-based strength criterion for first ply failure requires the knowledge of the laminate stacking sequence to be able to use all required quantities in the same reference frame. For a homogenized stiffness representation of a laminate without layup knowledge, IJsselmuiden *et al.* [167] suggested a conservative strain failure envelope, based on the Tsai-Wu elliptic criterion. The envelope computes the common admissible strain space for all possible ply orientations, as to not have failure. Khani *et al.* [168] later used this envelope to design and optimize variable stiffness composites plates, with a laminate stiffness homogenization by means of the lamination parameters. The optimization uses a bound formulation on the failure index, with a convex approximation based on the gradient of the strength response and solved by the dual-method with Lagrangian multipliers [169]. With the specific construction of the convex approximation, the adjoint gradient formulation can be used. Hong *et al.* [170] instead used a p-norm aggregation of the strain envelope failure index to incorporate the conservative strain envelope in a variable stiffness composite plate optimization. On the other hand, Catapano and Montemurro [171] used the polar decomposition of a Tsai-Wu criterion to relate anisotropic strength and stiffness properties, by averaging the failure indexes of each ply over the layup. However, selecting the threshold for the averaged failure indexes now becomes important, as the averaging operation is not conservative. Catapano and Montemurro [172] used this stiffness to strength relation in strength optimizations with manufacturing constraints for a variable stiffness design with constant thickness. Izzi *et al.* [9] further integrated variable thickness in the framework, the optimization problem being solved with a gradient-based algorithm.

Finally, in the DMTO framework, Lund [7] proposed a strategy to consider anisotropic strength criteria for the different ply candidates. Both stress and strain based criteria are included. However, by using a penalization to make layers disappear, the stress singularity issue is encountered. Therefore, the $qp-appraoch$ [67] is applied directly on the failure indexes, the latter being computed with the penalized stiffness. The element layer-wise failure indexes are then computed in the same way as the stiffness tensor, but by applying above-linear penalization when forming the sum of the candidate's failure indexes (see Equation 2.12). All the combined failure indexes are then aggregated with a p-norm, and the thickness minimization is solved with a SLP gradient-based algorithm. In the same framework, Xu *et al.* [173] integrated the Hashin strength criterion and solved the optimizations with MMA. Finally, strength constraints have also been considered in the FMO framework for topology optimizations in 2D [71, 174] and 3D [175]. Weldeyesus [176] considered strength criteria in the dedicated FMO framework for laminated plates and shells.

2.4.4 Specific Numerical Issues with Anisotropy

Whereas filtering techniques are enforced on the densities to counter numerical artifacts and have a length scale control, a similar approach has been applied to the orientations to enforce the continuity on the anisotropy distribution [121]. Another concern with orientation optimizations, is the possibility to staying trapped in local optima when the orientations are a continuous variable in $[0, 2\pi]$ [105]. Indeed, when at the bound of the interval, *e.g.* 2π, if an orientation of $2\pi + 0.01$ is optimal, this would only be feasible by a huge variable variation to return to an orientation value of 0.01. The bound restricts attaining a better minima. Using the orientation deconstruction into a ratio of two scalars, Nomura *et al.* [104] and Duriez [177] circumvented both these restrictions. The two scalars were then filtered with a regular linear filter by Duriez [177]. Instead, Nomura *et al.* [104] filtered both scalars based on a Helmholtz-type differential equation, whereas this filtering techniques has been used directly on the orientations by Silva *et al.* [178].

Schmidt *et al.* [106] also based their orientation filter strategy on the decomposition of the orientation into two scalars, but added the consideration of nearly opposite orientations (whose difference is $\approx 180°$). First, the dot product between two orientations to be filtered is checked before filtering the scalars. If the difference is less than 90°, the opposite of the scalar values would be used. This ensures that near similar physical orientations would not be wrongfully averaged out. Finally, despite not being a direct orientation filter, Jantos *et al.* [111] applied a filter technique on the components of the stiffness tensor by means of a convolution.

2.5 Polar Formalism

This section gives a more comprehensive overview of the polar formalism, which is used in this work, and its incorporation in the topology optimization framework with the Alternate Directions (AD) algorithm. The polar formalism was introduced by Verchery [179]. A review of the polar formalism specifically applied to anisotropic elasticity was performed by Vannucci [118].

2.5.1 Polar Parameters Definition

The polar parameters defining the components of a symmetric fourth order elastic tensor consists in five frame invariants quantities. The scalar parameters T_0 and T_1 represent the isotropic modules, whereas R_0 and R_1 are the scalar parameters representing the anisotropic modules. The fifth invariant quantity is the angular difference $\phi_0 - \phi_1$. Finally, by selecting either the value of the orientation ϕ_1 or ϕ_0, the Cartesian components can be defined. The relationships between the polar parameters and the Cartesian components of the elastic tensor [Q] are given by Equation 2.16, in case of a general anisotropic material.

$$\begin{array}{rcrcrcrcr} Q_{1111} & = & T_0 & + & 2T_1 & + & R_0\cos 4\phi_0 & + & 4R_1\cos 2\phi_1 \\ Q_{1122} & = & -T_0 & + & 2T_1 & - & R_0\cos 4\phi_0 & & \\ Q_{1112} & = & & & & & R_0\sin 4\phi_0 & + & 2R_1\sin 2\phi_1 \\ Q_{2222} & = & T_0 & + & 2T_1 & + & R_0\cos 4\phi_0 & - & 4R_1\cos 2\phi_1 \\ Q_{2212} & = & & & & - & R_0\cos 4\phi_0 & + & 4R_1\sin 2\phi_1 \\ Q_{1212} & = & T_0 & & & - & R_0\cos 4\phi_0 & & \end{array} \tag{2.16}$$

Alternatively, the polar parameters can be obtained from the components of a stiffness tensor by the relation of Equation 2.17.

$$\begin{array}{rcrcrcrcrcrcr} 8T_0 & = & Q_{1111} & & & - & 2Q_{1122} & + & 4Q_{1212} & & & + & Q_{2222} \\ 8T_1 & = & Q_{1111} & & & + & 2Q_{1122} & & & & & + & Q_{2222} \\ 8R_0e^{4i\phi_0} & = & Q_{1111} & + & 4iQ_{1112} & - & 2Q_{1122} & - & 4Q_{1212} & - & 4iQ_{1222} & + & Q_{2222} \\ 8R_0e^{2i\phi_1} & = & Q_{1111} & + & 2iQ_{1112} & & & & & + & 2iQ_{1222} & + & Q_{2222} \end{array} \tag{2.17}$$

An advantage of the polar formalism is the ease for a change of reference frame by a rotation δ as defined in Figure 2.11. In order to express the components of the tensor from the frame $1-2$ to $x-y$, the new angles become $\phi_0-\delta$ and $\phi_1-\delta$, and resulting in the operation in Equation 2.18.

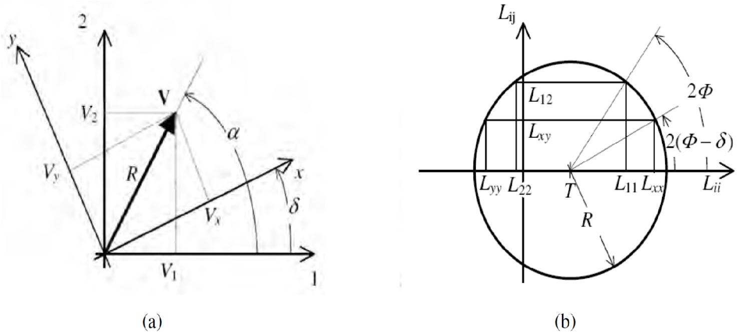

Figure 2.11: Cartesian and polar representation of: (a) a vector and (b) a second order tensor in a reference frame rotated by δ [180].

$$
\begin{array}{lcrcrcrcr}
Q_{xxxx} & = & T_0 & + & 2T_1 & + & R_0\cos 4(\phi_0-\delta) & + & 4R_1\cos 2(\phi_1-\delta) \\
Q_{xxyy} & = & -T_0 & + & 2T_1 & - & R_0\cos 4(\phi_0-\delta) & & \\
Q_{xxxy} & = & & & & & R_0\sin 4(\phi_0-\delta) & + & 2R_1\sin 2(\phi_1-\delta) \\
Q_{yyyy} & = & T_0 & + & 2T_1 & + & R_0\cos 4(\phi_0-\delta) & - & 4R_1\cos 2(\phi_1-\delta) \\
Q_{yyxy} & = & & & & - & R_0\cos 4(\phi_0-\delta) & + & 4R_1\sin 2(\phi_1-\delta) \\
Q_{xyxy} & = & T_0 & & & - & R_0\cos 4(\phi_0-\delta) & &
\end{array}
\tag{2.18}
$$

The polar parameters of the compliance tensor $[S]=[Q]^{-1}$ of an anisotropic material can also be defined by the same procedure, and are related to the stiffness polar parameters as given by Equation 2.19. $t_0, t_1, r_0, r_1, \varphi_0$ and φ_1 are the compliance parameters counterparts of $T_0, T_1, R_0, R_1, \phi_0$ and ϕ_1.

$$
\begin{aligned}
t_0 &= 4\frac{(T_0T_1-R_1^2)}{\Delta} \\
t_1 &= \frac{T_0^2-R_0^2}{\Delta} \\
r_0e^{4i\varphi_0} &= 4\frac{R_1^2e^{4i\phi_1}-T_1R_0e^{4i\phi_0}}{\Delta} \\
r_1e^{2i\varphi_1} &= -2R_1^2e^{4i\phi_1}\frac{T_0-R_0e^{4i(\phi_0-\phi_1)}}{\Delta} \\
\Delta = 16T_1(T_0^2-R_0^2) &- 32R_1^2(T_0-R_0\cos 4(\phi_0-\phi_1))
\end{aligned}
\tag{2.19}
$$

2.5.2 Admissible Design Space

The five invariants of the polar formalism can not assume any value in case they represent an elastic stiffness tensor. Such a tensor should satisfy the thermodynamic bounds of a material, meaning it should be positive definite. This is satisfied for the conditions given in Equation 2.20.

$$
\begin{cases}
T_0 > 0 \\
T_1 > 0 \\
T_0 - R_0 > 0 \\
T_1(T_0^2-R_0^2) > 2R_1^2(T_0-R_0\cos 4(\phi_0-\phi_1))
\end{cases}
\tag{2.20}
$$

Furthermore, as the anisotropic modules are modules of a complex number, by definition Equation 2.21 applies to them.

$$\begin{cases} R_0 \geq 0 \\ R_1 \geq 0 \end{cases} \tag{2.21}$$

All conditions listed above are the mathematical conditions of a thermodynamic admissible stiffness tensor. Such tensor does however not guarantee that a physical or known material can be associated to it. Finding a material or microstructure corresponding to a given admissible set of polar parameters values is an open problem in the general case, for which there might not always exist a manufacturable solution. A proof of the thermodynamic conditions on the polar parameters is given by Vannucci and Desmorat [181].

2.5.3 Physical Interpretation of the Polar Invariants

The polar decomposition of Equation 2.16 allows for an easy *algebraic* characterization of the elastic symmetries of a material and its stiffness tensor. In total, five different types of symmetry can be defined [118], shortly explained next.

Ordinary orthotropy

The first symmetry is that for ordinary orthotropy, which is obtained for the condition of Equation 2.22.

$$\phi_0 - \phi_1 = K\frac{\pi}{4}, K \in \{0, 1\} \tag{2.22}$$

For a set of polar modules T_0, T_1, R_0 and R_1, two discrete values are possible for K (0 or 1), defining the shape of orthotropy. Each of the K value represents different elastic properties of a material. Historically, K = 1 materials have been called *low shear* modulus, whereas K = 0 materials have been called *high shear* modulus by Cheng and Pedersen [182]. Nonetheless, this appellation has its shortcomings, as the overall elastic properties changes for either K values, and not only the shear properties [158, 183].

The components of an orthotropic elastic tensor can then be obtained by means of Equation 2.23, where ϕ_1 represents the direction of orthotropy.

$$\begin{array}{rcrcrcrcr} Q_{1111} & = & T_0 & + & 2T_1 & + & (-1)^K R_0 \cos 4\phi_1 & + & 4R_1 \cos 2\phi_1 \\ Q_{1122} & = & -T_0 & + & 2T_1 & - & (-1)^K R_0 \cos 4\phi_1 & & \\ Q_{1112} & = & & & & & (-1)^K R_0 \sin 4\phi_1 & + & 2R_1 \sin 2\phi_1 \\ Q_{2222} & = & T_0 & + & 2T_1 & + & (-1)^K R_0 \cos 4\phi_1 & - & 4R_1 \cos 2\phi_1 \\ Q_{2212} & = & & & & - & (-1)^K R_0 \cos 4\phi_1 & + & 4R_1 \sin 2\phi_1 \\ Q_{1212} & = & T_0 & & & - & (-1)^K R_0 \cos 4\phi_1 & & \end{array} \tag{2.23}$$

The thermodynamic condition on the stiffness tensor of Equation 2.20 can be reduced to Equation 2.24 in case of an orthotropic material.

$$T_1[T_0 + (-1)^K R_0] > 2R_1^2 \tag{2.24}$$

An overview of the distribution of the mechanical engineering properties obtained within the thermodynamic domain is given in Figure 2.12, for a defined set of T_0 and T_1 values.

R_0 orthotropy

R_0 orthotropy is obtained when $R_0 = 0$. The stiffness tensor then only depends on R_1. The rotation of the stiffness tensor will then behave like a second order tensor, instead of a fourth-order one [184].

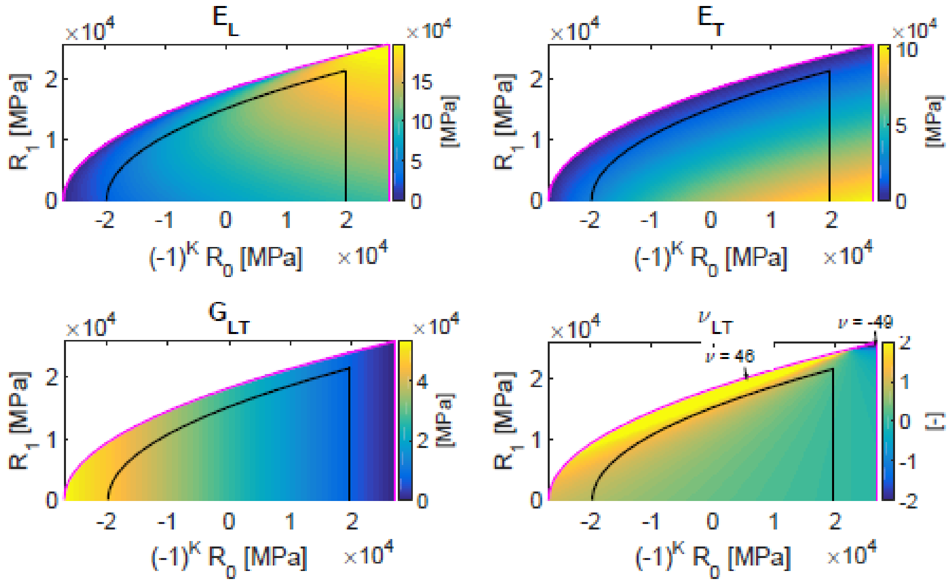

Figure 2.12: Engineering material properties distribution within the thermodynamic bounds, for fixed isotropic modules $T_0 = 26.9$ GPa and $T_1 = 24.7$ GPa, with the geometric bounds traced in black [2].

r_0 orthotropy

r_0 orthotropy is obtained when $r_0 = 0$. Due to the intricate relation between R_0 and r_0 (Equation 2.19), this condition is not similar to R_0 orthotropy. Therefore other material properties are obtained, an example is given by Vannucci [185].

Square orthotropy

Square symmetry is obtained when $R_1 = 0$. This is the 2D equivalent of the 3D tetragonal symmetry class.

Isotropy

Elastic properties of an isotropic material are obtained when $R_0 = R_1 = 0$. For this condition, the Cartesian components are not dependent of the orientations. This leaves only T_0 and T_1 as non-zero invariants. They are related to the shear G and bulk κ modulus in 2D by means of Equation 2.25.

$$T_0 = G \quad ; \quad T_1 = \frac{1}{2}\kappa \tag{2.25}$$

Nonetheless, for any type of anisotropic material, T_0 and T_1 preserve this mechanical meaning: they are a generalization of the bulk and shear moduli.

2.5.4 Composite Laminate Case

Vannucci [11] also expressed a subset of the polar parameters with orthotropic properties, representing the possible homogenized stiffness of a laminate made up of a unique base ply. This subset is labeled as geometrical bounds. With a fixed orientation ϕ_1 aligned with that of the base ply, the design space described by the geometric bounds is equivalent to that of the lamination parameters. The polar invariants of the base ply are denoted by the superscript L in the equations, and remain constant. The geometric feasible domain is constructed from these base invariants. From the dimensionless quantities defined in Equation 2.26, the geometric bounds conditions are given by Equation 2.27. ρ_0 and ρ_1 are the only variable quantities, as they involve R_0 and R_1 respectively.

$$\rho = \frac{R_0^L}{R_1^L}; \rho_0 = \frac{R_0}{R_0^L}; \rho_1 = \frac{R_1}{R_1^L}; \tau_0 = \frac{T_0^L}{R_0^L}; \tau_1 = \frac{T_1^L}{R_1^L} \tag{2.26}$$

$$\begin{gathered} 2\rho_1^2 - 1 \leq (-1)^{K-K^L} \rho_0 \\ \rho_0 \leq 1 \end{gathered} \tag{2.27}$$

Figure 2.13 presents the geometric domain within the thermodynamic domain, for a given base ply which has a $K^L = 0$ orthotropy. It highlights the special layup conditions.

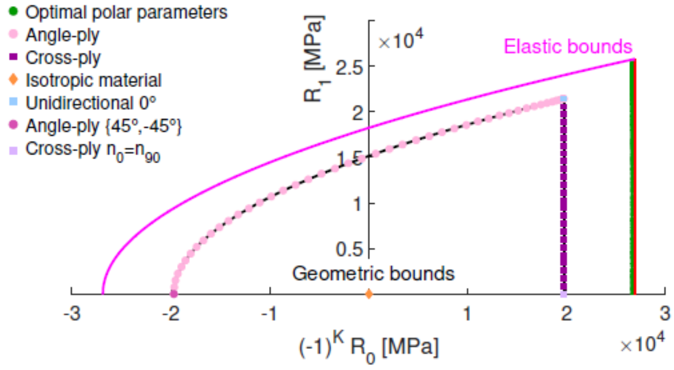

Figure 2.13: Laminate properties within the geometric bounds of the polar formalism [2].

2.5.5 Use in Topology Optimization

Topology optimization considering 2D orthotropy was performed by Ranaivomiarana [2] with the polar parameters and the Alternate Directions (AD) algorithm for compliance minimization. The AD algorithm is based on alternating the minimization of the complementary energy, followed by the minimization with respect to the design variables. The minimization of the complementary energy is performed with a FEM analysis. Thereafter, the stress state is used to minimize the compliance with respect to the design variables with optimality criteria in closed-form expressions. In this step, first the anisotropy properties are updated, followed by the optimization with respect to the densities with a filtering strategy to avoid checkerboard. The optimization strategy is valid for a generalized compliance problem. This entails both force and displacement based optimizations.

Anisotropy

This section details the anisotropic optimality conditions for compliance minimization, as derived by Pedersen [186] and Julien [180]. The update of all the anisotropy variables is performed with a fixed stress state for all conditions. The optimal orientation ϕ_1^{opt} is given by the direction of the maximum value of the absolute of the principal stresses σ_I and σ_{II}. The optimality conditions for the three anisotropic invariants are based on the stress ratio X, which dependents on T and R, the spheric and deviatoric parts of the stress tensor. The optimal value of R_0 is constant for an interval of stress ratio X. An overview of all the anisotropic optimality criteria is given in Table 2.1.

Density

The topology problem is modeled according to the classical SIMP interpolation, although the material is not isotropic, with an exponent p and a minimum density ρ_{min}. The density update strategy is performed in two

Table 2.1: Optimality criteria for the compliance minimization within the thermodynamic bounds.

$X = \frac{R}{\lvert T\rvert}$	$0 \quad\quad \sqrt{\frac{T_0}{2T_1}}$	$\sqrt{\frac{T_0}{2T_1}} \quad\quad \sqrt{\frac{T_0}{T_1}}$	$\sqrt{\frac{T_0}{T_1}} \quad\quad +\infty$
ϕ_1^{opt}	$\text{Dir}\{\max(\lvert\sigma_I\rvert,\lvert\sigma_{II}\rvert)\}$		
K^{opt}	0 or 1	0	
R_0^{opt}	$K=0$: $0 \leq R_0^{\text{opt}} < T_0$ $K=1$: $0 \leq R_0^{\text{opt}} < T_0 - 2T_1X^2$	$2T_1X^2 - T_0 < R_0^{\text{opt}} < T_0$	T_0^+
R_1^{opt}	T_1X		$\frac{T_0^-}{X}$

steps [1]. The first part consists in finding the optimal element-wise densities. This is achieved by introducing the volume constraint in the compliance minimization problem by means of a Lagrangian multiplier k, as given in Equation 2.28. The optimal densities are then obtained by differentiating Equation 2.28 with respect to the density, as given in Equation 2.29. Lastly, a bisection operation is performed to obtain the value of k that satisfies the volume constraint of Equation 2.30.

$$\min_{\boldsymbol{\rho}} \quad \frac{1}{\boldsymbol{\rho}^p}\sigma^T Q_{\text{opt}}^{-1}(R_0^{\text{opt}}, R_1^{\text{opt}}, K^{\text{opt}}, \phi_1^{\text{opt}})\sigma + k\boldsymbol{\rho} \tag{2.28}$$

$$\rho^{\text{opt}}(k) = \max\left(\rho_{\min}, \min\left(1, \left(\frac{p\sigma^T Q_{\text{opt}}^{-1}(R_0^{\text{opt}}, R_1^{\text{opt}}, K^{\text{opt}}, \phi_1^{\text{opt}})\sigma}{k}\right)^{\frac{1}{p+1}}\right)\right) \tag{2.29}$$

$$\int_\Omega \rho^{\text{opt}}(k)d\Omega = V_0 \tag{2.30}$$

After a conclusive bisection operation to find the correct k and the associated ρ^{opt} has been performed, a filter is applied. This consists in an energy filter [187], detailed in Equation 2.31, where the E_i are filtered strain energies. A linear decreasing weighting factor w_{ij} from an element's centroid $\mathbf{x_i}$ is used to calculate E_i, with the updated separate densities ρ of the previous step as constants. The filter weights w_{ij} are obtained according to Equation 2.32, for centroids $\mathbf{x_j}$ within the filter radius R.

$$\tilde{\rho}^{\text{opt}}(k) = \max\left(\rho_{\min}, \min\left(1, \left(\frac{pE_i}{k}\right)^{\frac{1}{p+1}}\right)\right) \quad \text{with} \quad E_i = \frac{1}{\frac{1}{\rho_i^p}\sum_{j=1}^N w_{ij}} \sum_{j=1}^N \left(\frac{1}{\rho_j^p} w_{ij}\sigma_j : C_j^{-1} : \sigma_j\right) \tag{2.31}$$

$$w_{ij} = R - \lvert\mathbf{x_i} - \mathbf{x_j}\rvert \tag{2.32}$$

Equation 2.31 is still solved in combination with a bisection on k by means of Equation 2.30 to obtain the filtered densities, satisfying the volume constraint. The results presented in Figure 1.2 were obtained with this alternate direction strategy. The concurrent strategy optimizing both topology and anisotropy resulted in stiffer solutions with different topologies than a sequential approach. The sequential approach consisted in defining the topology by first minimizing the compliance with an isotropic material, followed by the optimization with respect to the anisotropy on that fixed topology.

2.6 Conclusion and Thesis Objective

The polar formalism has shown to be an effective anisotropy parametrization to be used in 2D anisotropy optimization, and used successfully in topology optimization for compliance minimization with thermodynamically admissible stiffness tensors. However, the dedicated Alternate Directions (AD) algorithm used in [1] is limited to compliance minimization problems. Moreover, closed form solutions for compliance minimization have only been derived for thermodynamic material thus far, the geometric domain representing laminates having only been used in gradient-based optimizations with variable thickness. The ability to consider the geometric bounds is a first necessity to switch to gradient-based algorithms.

In addition, the state of the art review has shown that gradient-based algorithms are also required for incorporating strength criteria in topology optimization. The isotropic material case is well documented for density-based topology optimizations. The stress singularity and computational challenges are well understood, and many strategies have been proposed to address these challenges. On the other hand, anisotropic strength criteria are necessary to represent laminates failure. Strength optimizations with solely material anisotropy representing composite laminates are also well documented and compatible with gradient-based optimization techniques. This research will use and evaluate those latter methods to integrate strength constraints in a concurrent topology and anisotropy optimization.

Nonetheless, except for recent contributions considering UD fiber orientation [8] or composite layup [7], little research combines the two considerations of distributed material anisotropy and density in case of strength-based optimizations for composite laminates. For its invariant-based parametrization, and possibility to consider either thermodynamically admissible material or composite laminates, the polar formalism is selected to parametrize material anisotropy along a SIMP density-based topology optimization framework, solved with the versatility offered by gradient-based optimizers. The three main focus points addressed in this work are:

- Develop a concurrent topology and anisotropy optimization strategy with a gradient-based algorithm. Such optimization strategy is required to integrate strength constraints. Due to its wide use in either topology or anisotropy optimization, the MMA algorithm is selected to define the gradient-based optimization strategy. The strategy will be validated against results obtained by the AD algorithm for thermodynamically admissible materials first, to address the challenges of considering different type of variables in a gradient-based optimization. The aim is to reproduce similar solutions and equivalent compliance gains when anisotropy and topology are considered simultaneously in the gradient-based strategy. After the validation with thermodynamic bounds corresponding to general orthotropic materials, the use of a gradient-based framework enables to perform a 2D material anisotropy optimization considering the geometric domains representing laminated composite materials.
- Incorporate an anisotropic stress-based strength criterion with a UD material, whose material orientation is optimized along the topology. This part will allow to develop the understanding of using anisotropic strength criteria in topology optimization. It will also serve to define the strength optimization constraint, with an adaptation of the techniques for isotropic stress-based optimization. The combined relaxation and aggregation strategy of Verbart [5] will be used to setup this part, as it is useful for the third focus point. Finally, it will provide insight into the efficient computation of the strength constraint gradient by means of the adjoint method.
- Incorporate an anisotropic strain-based strength criteria for laminates. As a homogenized stiffness representation of a composite laminate is used by means of the polar formalism and therefore no layup information is available, a strength criterion for a complete laminate optimization will be expressed as a strain-based envelope. This entails first setting up a topology optimization with a strain constraint, for which little research is available [7]. Inspiration will be used from the stress-based optimizations, where the combined relaxation and aggregation technique of the lower KS aggregation is investigated to perform successful strain-based topology optimization. Furthermore, the correct strength envelop should be enforced, representing a conservative envelope for any orientation. Lastly, the correct strength constraint and gradient computation by means of the adjoint method still are to be obtained.

Chapter 3

Definition of a Gradient-Based Strategy for Concurrent Topology and Anisotropy Optimization

3.1 Introduction

This chapter introduces a novel gradient-based framework for distinct topology (i.e. black and white) optimizations, while incorporating material anisotropy modeled by means of the polar formalism. Current topology optimizations with the polar formalism are based on optimality criteria [1], and limited to performing compliance minimization for thermodynamically feasible materials. The suggested optimization approach uses sequential approximations, based on the Methods of Moving Asymptotes. The material density, orientation and anisotropic modules are updated separately at each iteration, in parallel sub-problems constructed with different types of approximations and settings. The proposed optimization approach is successfully validated for compliance minimization against the Alternate Directions method for general orthotropic materials, defined by the thermodynamic bounds. The importance of the anisotropy initialization in the gradient-based approach is highlighted to obtain stiffer solutions. The gradient-based strategy is also extended to incorporate geometric bounds on the polar parameters, defining the domain of existence of composite laminates. Obtained results for compliance minimization with laminates are compared to published results using lamination parameters. Finally, new solutions are presented showing the improvement of the compliance with increased consideration of the anisotropy design domains.

3.2 Optimization Problem Parametrization

This sections deals with a two-dimensional compliance minimization problem. The corresponding mathematical formulation reads as follows:

$$\begin{aligned} \min_{\boldsymbol{\rho},\boldsymbol{\gamma}} \quad & C(\boldsymbol{\rho},\boldsymbol{\gamma}) \\ \text{s.t.} \quad & V(\boldsymbol{\rho})/V_0 \leq v_f \\ & g(\boldsymbol{\gamma}) < 0 \\ & \boldsymbol{\rho} \in [\rho_{\min}, 1] \end{aligned} \tag{3.1}$$

where $C = \mathbf{U}^T\mathbf{K}\mathbf{U}$ is the compliance. $\boldsymbol{\rho}$ represents the topology distributed optimization variable, and the material anisotropy distributed variables are regrouped under the $\boldsymbol{\gamma}$ variables.

The volume ratio $V(\boldsymbol{\rho})/V_0$ is bound by a prescribed volume fraction v_f constraint ($v_f \in [0, 1]$), while the anisotropy variables are subjected to physical constraints $g(\boldsymbol{\gamma})$. The mechanical problem is solved by means of the Finite Element Method (FEM), where $\mathbf{U}$ is the solution to $[K]\mathbf{U} = \mathbf{F}$, $[K]$ being the global stiffness matrix and $\mathbf{F}$ the force vector.

3.2.1 Topology Parametrization

The topology is parametrized by means of a density approach, where each element i is assigned a scalar density value $\rho_{(i)}$. The densities take value in $[\rho_{\min}, 1]$, where $\rho_{\min}$ is set to 10^{-3} to avoid having a near singularity stiffness matrix and subsequent numerical problems with the FEM resolution. To obtain distinct black an white solutions, a penalization exponent p is used to penalize intermediate densities and converge to the presence ($\rho = 1$) or absence ($\rho = \rho_{\min}$) of material. This method is similar to the classical SIMP (Solid Isotropic Material with Penalization) approach, although it is applied here to the case of anisotropic materials. Thus, each element i is assigned a stiffness tensor $[Q_{(i)}]$ used for the mechanical analysis:

$$[Q_{(i)}] = \rho_{(i)}^{p} [Q_0] \,, \tag{3.2}$$

where $[Q_0]$ is the pristine elastic tensor of the element.

In order to have a length scale control and avoid numerical artifacts such as checkerboard, a density filter is used [31]. The filtered densities $\widetilde{\rho_e}$ are the physical variables used to setup the FEM analysis with Equation 3.2 and compute the volume constraint, while the densities ρ_i are the optimization variables:

$$\widetilde{\rho_e} = \frac{\sum_{i \in \Omega_e} w_{ei} \rho_i}{\sum_{i \in \Omega_e} \rho_i} \,. \tag{3.3}$$

Ω_e is the set of elements i whose centroid $\mathbf{x_i}$ is within the filter radius R of the centroid $\mathbf{x_e}$ of element e. The associated filter weights w_{ei} are obtained as

$$w_{ei} = R - |\mathbf{x_i} - \mathbf{x_e}| \,. \tag{3.4}$$

3.2.2 Anisotropy Parametrization

Material in-plane anisotropy is represented by means of the polar formalism [179]. The elastic behavior of the material is imposed to be orthotropic, in which case the polar formalism expresses its fourth order elasticity tensor by means of 5 invariants [118]: the four modules T_0, T_1, R_0 and R_1 and the orthotropy shape parameter K. The parameter K takes a discrete value 0 or 1. A more detailed presentation of the polar formalism is given in Section 2.5. Equation 3.5 shows the relation between the Cartesian components and the polar ones for an orthotropic stiffness tensor, where the angle ϕ_1 represents the direction of orthotropy:

$$\begin{array}{lcrcrcrcr}
Q_{1111} & = & T_0 & + & 2T_1 & + & (-1)^K R_0 \cos 4\phi_1 & + & 4R_1 \cos 2\phi_1 \\
Q_{1122} & = & -T_0 & + & 2T_1 & - & (-1)^K R_0 \cos 4\phi_1 & & \\
Q_{1112} & = & & & & & (-1)^K R_0 \sin 4\phi_1 & + & 2R_1 \sin 2\phi_1 \\
Q_{2222} & = & T_0 & + & 2T_1 & + & (-1)^K R_0 \cos 4\phi_1 & - & 4R_1 \cos 2\phi_1 \\
Q_{2212} & = & & & & - & (-1)^K R_0 \cos 4\phi_1 & + & 4R_1 \sin 2\phi_1 \\
Q_{1212} & = & T_0 & & & - & (-1)^K R_0 \cos 4\phi_1 & &
\end{array} \,. \tag{3.5}$$

T_0 and T_1 dictate the spherical behavior of the stiffness tensor and must both be strictly positive. They are kept constant in the optimization, as the trivial stiffest solution would be for T_0 and T_1 to have infinite values. Thus, the material optimization is performed with respect to the parameters that influence the anisotropic terms in Equation 3.5: the polar invariants R_0, R_1 and K and the orientation ϕ_1. The normalized anisotropic material parameters η_0 and η_1 are introduced, defined as:

$$\begin{aligned}\eta_0 &= \frac{(-1)^K R_0}{T_0}\,,\\ \eta_1 &= \frac{R_1}{\sqrt{T_0 T_1}}\,.\end{aligned} \tag{3.6}$$

The normalization not only allows to reduce the amount of variables, by regrouping R_0 and K into η_0, but foremost includes the discrete variable K into a continuous one. Continuous variables facilitate a gradient-based optimization process, as these processes are not suited to handle discrete variables. As the isotropic modules T_0 and T_1 remain constant during the optimization, they do not require normalization. The elasticity tensor of Equation 3.5 is now defined as follows:

$$\begin{array}{llrcrcrcl} Q_{1111} & = & T_0 & + & 2T_1 & + & \eta_0 T_0 \cos 4\phi_1 & + & 4\eta_1\sqrt{T_0T_1}\cos 2\phi_1 \\ Q_{1122} & = & -T_0 & + & 2T_1 & - & \eta_0 T_0 \cos 4\phi_1 & & \\ Q_{1112} & = & & & & & \eta_0 T_0 \sin 4\phi_1 & + & 2\eta_1\sqrt{T_0T_1}\sin 2\phi_1 \\ Q_{2222} & = & T_0 & + & 2T_1 & + & \eta_0 T_0 \cos 4\phi_1 & - & 4\eta_1\sqrt{T_0T_1}\cos 2\phi_1 \\ Q_{2212} & = & & & & - & \eta_0 T_0 \cos 4\phi_1 & + & 4\eta_1\sqrt{T_0T_1}\sin 2\phi_1 \\ Q_{1212} & = & T_0 & & & - & \eta_0 T_0 \cos 4\phi_1 & & \end{array}\,. \tag{3.7}$$

3.2.3 Orthotropic Material Domain of Existence

Thermodynamic Bounds

Whereas T_0 and T_1 dictate the spheric behavior of the stiffness tensor, and must both be strictly positive, η_0 and η_1 can not assume any value. The thermodynamic bounds constrain the anisotropic variables to ensure the elasticity tensor remains positive definite, represented by the condition of Equation 3.8 [118] when written with dimensionless variables. The thermodynamic domain represents any possible material, whether it is a real material or yet unknown one.

$$2\eta_1^2 - 1 < \eta_0 < 1 \tag{3.8}$$

Geometric Bounds

The thermodynamic domain represents the theoretical space of all admissible material properties. In order to obtain a final result which can be produced, a subset of the thermodynamic bounds will be considered for further work. This subset represents a stiffness set of homogenized orthotropic laminates and is labeled as geometrical bounds [11]. The assumption for this geometrical set is that a laminate is constructed from a unique orthotropic base layer, whose properties are denoted by the superscript L in the subsequent equations and have a constant value.

Starting from the geometric domain definition given in Equation 2.27 [11], the geometric bounds can be written as a function of the normalized variables η_0 and η_1, and the normalized anisotropic material properties of the orthotropic base layer η_0^L and η_1^L. It reads as:

$$2\left(\frac{\eta_1}{\eta_1^L}\right)^2 - 1 \le \frac{\eta_0}{\eta_0^L} \le 1\,. \tag{3.9}$$

Interestingly, Equation 3.8 and Equation 3.9 share the same form. Thus, by taking a base ply whose normalized anisotropic properties tends towards 1, *i.e.* $\eta_0^L = \eta_1^L = 1 - \varepsilon$, with ε an infinitely small positive number, the geometric domain tends to overlap with the thermodynamic domain and both domains can be described using Equation 3.9. The representation of the geometric bounds within the thermodynamic bounds is shown in Figure 3.1 for two orthotropic base plies with a different shape of orthotropy, whose material properties are listed in Table 3.1.

Table 3.1: Orthotropic base ply material properties [11].

UD carbon-epoxy T300/5204				Braided carbon-epoxy type BR-45a			
Modules	Values	Polar parameters	Values	Modules	Values	Polar parameters	Values
E_{11} [GPa]	181.0	T_0^L [GPa]	26.9	E_{11} [GPa]	40.4	T_0^L [GPa]	17.8
E_{22} [GPa]	10.3	T_1^L [GPa]	24.7	E_{22} [GPa]	19.6	T_1^L [GPa]	15.4
G_{12} [GPa]	7.2	η_0^L [-]	0.73	G_{12} [GPa]	25.0	η_0^L [-]	-0.41
ν_{12} [-]	0.28	η_1^L [-]	0.83	ν_{12} [-]	0.75	η_1^L [-]	0.22

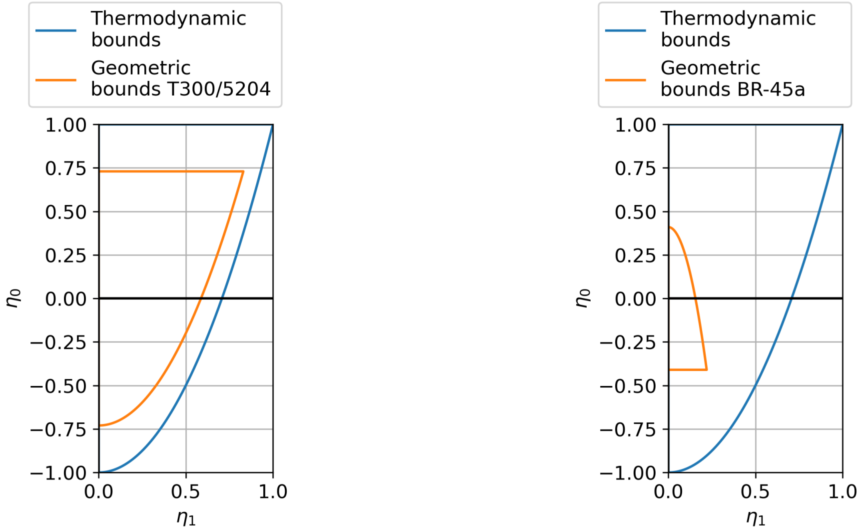

(a) For a UD carbon-epoxy T300/5204 base ply.

(b) For braided carbon-epoxy type BR-45a base ply.

Figure 3.1: Geometric bounds within the thermodynamic domain.

3.2.4 Domain of Existence Remapping

Either the geometric or thermodynamic bounds become an optimization constraint to be satisfied for each separate element of the ground structure mesh, as each element has a different set of normalized anisotropic variables (η_0, η_1). Therefore, an additional number of constraints equal to the number of elements used in the ground structure is included in the optimization problem. This however raises two possible issues: firstly, depending on the gradient optimization algorithm, the updated variables can temporarily violate the constraint depending on the regularity of the problem and variable step size. This is a valid characteristic for the MMA algorithm chosen in this research, which can come back from an infeasible design point. This overshoot of the constraint could however then prove to be fatal, as the stiffness tensor provided to the FEM analysis would then become ill-conditioned and terminate the optimization. Secondly, the optimization algorithm is efficient for few constraints (generally < 100), and hence using one constraint per element lengthens the optimization routine. For both these reasons, a remapping technique based on a change of variable is introduce to satisfy the domain of existence. It is feasible as all constraints only depend on each element's individual properties, with no cross influence with other variables.

Analogously to the method presented by Izzi *et al.* [9], the geometric or thermodynamic bounds on the anisotropy modules are expressed as a remapping of the bounds to a square $[0, 1]^2]$ by a change of variable presented in Equation 3.10. By using this remapping, the inequality constraint on the physical anisotropy variables η_0 and η_1 will become a bound on the optimization variable α and β. Such bounded optimization variables are implicitly satisfied in the optimization method, and therefore speed up the process.

The parametrization with the new design variables, α and β, defining the anisotropic modules, η_0 and η_1, is given by:

$$\begin{aligned}\frac{\eta_0}{\eta_0^L} &= 1 - 8\alpha(1-\alpha)\beta \\ \frac{\eta_1}{\eta_1^L} &= 2\alpha - 1\ ,\end{aligned} \tag{3.10}$$

With this parametrization, the following property holds:

$$\begin{cases}\alpha \in [0,1] \\ \beta \in [0,1]\end{cases} \rightarrow 2\left(\frac{\eta_1}{\eta_1^L}\right)^2 - 1 \leq \frac{\eta_0}{\eta_0^L} \leq 1 \tag{3.11}$$

Proof: the inequality $2\left(\frac{\eta_1}{\eta_1^L}\right)^2 - 1 \leq 1$ implies that $-1 \leq \frac{\eta_1}{\eta_1^L} \leq 1$, therefore Equation 3.10 implies $0 \leq \alpha \leq 1$. Furthermore, when considering $0 < \alpha < 1$, the inequality $1 - \frac{\eta_0}{\eta_0^L} \geq 0$ reads $8\alpha(1-\alpha)\beta$ so that $\beta \geq 0$. Also, the inequality $\frac{\eta_0}{\eta_0^L} - (2\left(\frac{\eta_1}{\eta_1^L}\right)^2 - 1) \geq 0$ reads $8\alpha(1-\alpha)(1-\beta) \geq 0$ so that $\beta \leq 1$. When considering $\alpha = 0$ or 1, meaning $\frac{\eta_0}{\eta_0^L} = 1$, β is undetermined and can be chosen in $[0,1]$.

Finally, the bounds on ϕ_1 are also normalized in the software implementation to be in the [0,1] range. This is only as a numerical step to follow the recommendations to use the optimization algorithm. Furthermore, by using the proposed remapping, the non-linear feasible domain boundary given in Equation 3.9 is replaced by $\boldsymbol{\alpha}, \boldsymbol{\beta} \in [0,1]^2$. Therefore, Problem 3.1 can be rewritten as:

$$\begin{aligned}\min_{\boldsymbol{\rho},\boldsymbol{\phi_1},\boldsymbol{\alpha},\boldsymbol{\beta}} \quad & C(\boldsymbol{\rho},\boldsymbol{\phi_1},\boldsymbol{\alpha},\boldsymbol{\beta}) \\ \text{s.t.} \quad & V(\boldsymbol{\rho})/V_0 \leq v_f \\ & \boldsymbol{\rho} \in [\rho_{\min}, 1] \\ & \boldsymbol{\phi_1} \in [-\frac{\pi}{2}, \frac{\pi}{2}] \\ & \boldsymbol{\alpha}, \boldsymbol{\beta} \in [0,1]^2\end{aligned} \quad . \tag{3.12}$$

3.3 Optimization Strategy

The MMA optimization algorithm [10, 188] is used to solve Problem 3.12. The MMA algorithm is based on an iterative optimization process that consists in solving a succession of approximated convex sub-problems. At each iteration, a sub-problem is constructed based on the values and gradients at the current iteration point of both the objective and constraint functions with respect to the optimization variables.

Several approximation types can be used to construct this sub-problem, and have been found to influence the convergence and the progress of the optimization. Since the regularity of the design space taken into account in the problem differs with respect to the nature of the variable, a strategy called SplitMMA is suggested to solve Problem 3.12. A compliance design space with respect to thickness and orientation is shown in Figure 3.2. It shows the difference in regularity with respect to both variables. The MMA algorithm provides different approximation type, of which two are considered, MMA and Global Convergent MMA (GCMMA). The difference between the two approximations can be seen in Figure 3.3, where the black line is a fictive function, with the monotonous MMA and convex GCMMA approximation in dash line. The MMA approximation will lead to the new updated value being close to the asymptote and have a large variation. This comes at the cost of possible imprecision on the approximation, depending on the regularity of the design space. This can lead to the oscillations on the variable between iterations. On the other hand, the GCMMA approximation resembles more a quadratic approximation, and is more conservative. In general, MMA is privileged to quickly attain an optimum, but lacks the properties for the final convergence to a local minima, whereas GCMMA is much better at this later part due to its conservative characteristics. GCMMA, however, would take much longer to reach a minimum from an initial point far away from the optimum [56]. The SplitMAA strategy uses approximations which are already better tailored to a variable's influence, to facilitate convergence as was hinted by Bruyneel *et al.* [189].

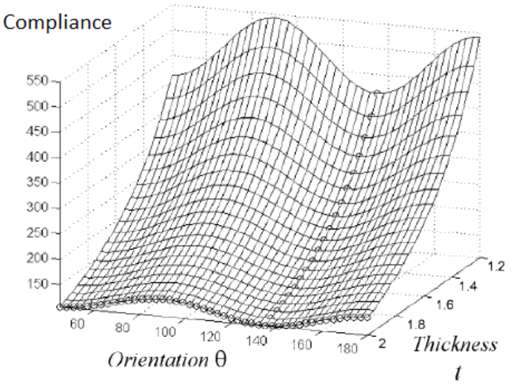

Figure 3.2: Compliance design space with respect to thickness and ply orientation [189].

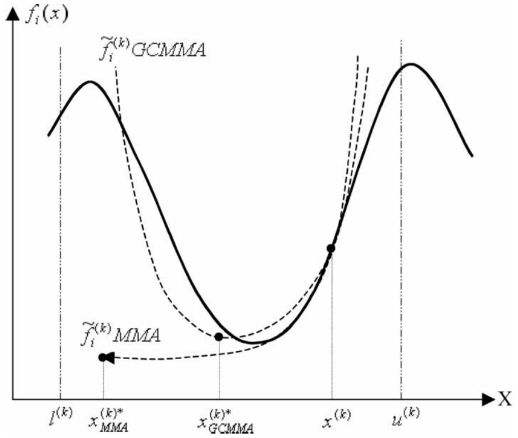

Figure 3.3: Monotonous MMA approximation versus non-monotonous and convex GCMMA approximation [56].

The general functioning of MMA is retained in the suggested strategy. But instead of constructing a unique sub-problem taking into account all the variables at each iteration, three separate sub-problems are devised depending on the type of variable (density, orientations and anisotropic modules) and their derivatives. These sub-problems are then solved in parallel at each iteration, meaning once per FEM analysis. All gradients can then be computed from this common mechanical analysis. The old variables and asymptote update history is however kept independently per sub-problem throughout the optimization. This process parallelization leads to neglecting the cross-influences of the sub-sets of variables, which has little influence on the resolution of Problem 3.12. Indeed, the volume and domain of existence constraints are separate and do not depend on the same variable. Optimizing with respect to each type of variable separately with SplitMMA allows to construct more simple sub-problems to be solved, with independent settings for the solver. Those settings can be individually tailored to the behavior of the optimization in junction with an adequate selection of the approximation type to improve convergence.

The density variables are optimized with the standard monotonous MMA approximation, shown to behave well in literature [18, 189], and its own set of algorithm settings dictating the asymptotes update. Equally, to update the anisotropic modules η_0 and η_1, the optimization with respect to α and β is performed with a separate call of MMA and its monotonous approximation, giving good convergence. Having this separate MMA call allows to use a different set of settings to guide the optimization of the anisotropic components. Finally, the orientations are optimized with the convex but non-monotonous Global Convergent MMA (GCMMA) without inner iterations. This helps to mitigate the highly non-linear behavior and design space of the compliance with respect to the orientation. This GCMMA call has again its individual set of parameters. Using GCMMA to optimize with respect to orientations is similar to the works performed by Kiyono *et al.* [121], whereas it was also used with lamination parameters [136, 141]. An overview of the optimization strategy is given in Figure 3.4.

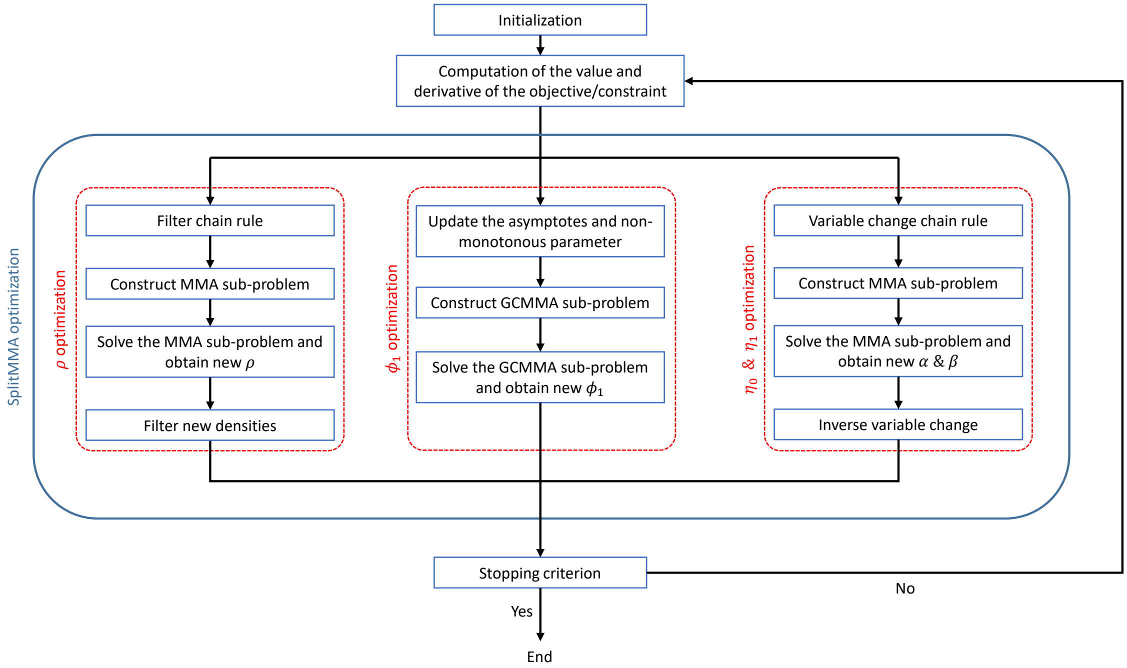

Figure 3.4: Overview of the optimization strategy SplitMMA.

3.4 Compliance and Volume Gradients Definition

The gradient of the volume with respect to the density variables can be obtained straightforwardly as follows, where $V_{(i)}$ is the volume of each element:

$$\frac{\partial V}{\partial \tilde{\rho}_{(i)}} = V_{(i)} \, . \tag{3.13}$$

In the case of the compliance sensitivity, the gradient formulation is self adjoint [18]. Therefore, the gradient with respect to density $\tilde{\rho}_{(i)}$ of element i is given by:

$$\frac{\partial C}{\partial \tilde{\rho}_{(i)}} = -\mathbf{U}_{(i)}^T \frac{\partial [k]_{(i)}}{\partial \tilde{\rho}_{(i)}} \mathbf{U}_{(i)} = -\mathbf{U}_{(i)}^T p \tilde{\rho}_{(i)}^{p-1} [k]_{(i)} \mathbf{U}_{(i)} \, , \tag{3.14}$$

where $\mathbf{U}_{(i)}$ is the displacement vector of the element's nodes at the current iteration, whilst $[k]_{(i)}$ is the element's local stiffness matrix. The implementation of these matrices in the FEM analysis is further developed in Appendix B.

The sensitivity with respect to the direction of anisotropy ϕ_1 can be obtain analogously to the sensitivities with respect to the density [121, 100], as:

$$\frac{\partial C}{\partial {\phi_1}_{(i)}} = -\mathbf{U}_{(i)}^T \frac{\partial [k]_{(i)}}{\partial {\phi_1}_{(i)}} \mathbf{U}_{(i)} \, . \tag{3.15}$$

where the local stiffness matrix is given by:

$$[k]_{(i)} = \iint_{S_{(i)}} [B]^T \tilde{\rho}_{(i)}^p [Q_{(i)}][B] dS_{(i)} \, , \tag{3.16}$$

with $[B]$ the strain-displacement matrix of the element, and S is the surface over which the element is integrated.

As the stiffness tensor does not depend on the coordinates of the element, the partial derivative of Equation 3.15 reads:

$$\frac{\partial [k]_{(i)}}{\partial {\phi_1}_{(i)}} = \iint_{S_{(i)}} [B]^T \tilde{\rho}^{p}_{(i)} \frac{\partial [{Q_0}_{(i)}]}{\partial {\phi_1}_{(i)}} [B] dS_{(i)} \,. \tag{3.17}$$

The gradient of the stiffness tensor $[{Q_0}_{(i)}]$ can be obtained straightforwardly from Equation 3.7, and the numerical integration is performed in the same way than in the original FEM analysis. The sensitivities with respect to η_0 and η_1 are obtained similarly.

To obtain the gradient with respect to the design variables α and β, the following chain rule must be applied:

$$\begin{aligned} \frac{\partial C}{\partial \alpha} &= \frac{\partial C}{\partial \eta_0}\frac{\partial \eta_0}{\partial \alpha} + \frac{\partial C}{\partial \eta_1}\frac{\partial \eta_1}{\partial \alpha} \\ \frac{\partial C}{\partial \beta} &= \frac{\partial C}{\partial \eta_0}\frac{\partial \eta_0}{\partial \beta} + \frac{\partial C}{\partial \eta_1}\frac{\partial \eta_1}{\partial \beta} \end{aligned} \,. \tag{3.18}$$

Finally, the influence of the density filter on the sensitivities is taken into account using a another chain rule, as follows:

$$\frac{\partial f}{\partial \rho_{(i)}} = \sum_{e \in \Omega_i} \frac{\partial f}{\partial \tilde{\rho}_{(e)}} \frac{\partial \tilde{\rho}_{(e)}}{\partial \rho_{(i)}} \,, \tag{3.19}$$

with:

$$\frac{\partial \tilde{\rho}_{(e)}}{\partial \rho_{(i)}} = \frac{w_{ei}}{\sum_{j \in \Omega_e} w_{ej}} \,, \tag{3.20}$$

where f can be either the objective or a constraint, such as the compliance or volume [3].

3.5 Results and Discussion

The methodology presented in this chapter was implemented in Python. Only the MMA and GCMMA routine was integrated from a standalone[1]. The following results were all obtained in Python framework. Furthermore, the Alternate Directions, with the methodology of Section 2.5.5, was equally implemented in Python to provide the results for the comparison.

The proposed strategy is applied to the three test cases shown in Figure 3.5. The first considered test case (#1) is the cantilever beam problem of aspect ratio of 2:1. The prescribed volume fraction v_f is 50%, with a mesh size of 0.5×0.5 mm^2 and a 1.1 mm filter radius on the densities R_ρ. A 200 N downwards load is distributed over the 5 middle nodes on the right hand size, while the left hand is clamped. The second test case (#2) is the suspended bridge problem with a prescribed volume fraction v_f of 20%, a mesh size of 1.875×1.85 mm^2 and a 5.75 mm filter radius on the densities R_ρ. A 900 N downwards load is distributed over the deck, while some elements at the bottom are clamped. The deck is 2 elements thick. The clamping areas are symmetric, as defined in Figure 3.5. The black elements only have their anisotropy optimized, their densities remaining 1. Both test cases (#1) and (#2) are used in [1]. The third test case (#3) is the cantilever beam problem of aspect ratio 1:1 used in [139]. The prescribed volume fraction v_f is 60%, with a mesh size of 5×5 mm^2. A 9.5 mm filter radius on the densities R_ρ is assumed here, while in the original work, an implicit filter is used. A downwards distributed load totaling 10 N is applied across the 2 right most

---

[1] https://github.com/arjendeetman/GCMMA-MMA-Python, accessed on the 17/11/2020

bottom nodes, while the left hand is clamped. A regular mesh is used in all cases, as is the most convenient for topology optimization. This however does not prohibit the proposed optimization strategy from being applied on an unstructured mesh. For test case (#1) and (#2), the density filter radius is taken according to the common practice as to have two to three elements within the radius. On the other hand, the radius in test case (#3) is taken as to match the topology of Peeters *et al.* [139], since their filter is implicitly implemented in their approach.

The material properties used for the test cases are presented in Table 3.2. The results presented in Section 3.5.2 are obtained using the thermodynamic bounds of Equation 3.8. These strict inequalities are enforced by using Equation 3.9 with $\eta_0^L = \eta_1^L = 1 - \varepsilon$, where an offset $\varepsilon = 0.05$ is imposed. The isotropic modules T_0 and T_1 are set equal to T_0^L and T_1^L respectively. In Section 3.5.3, results are obtained using the geometric bounds defined by Equation 3.9, in which case the materials given in Table 3.2 correspond to the base plies of the composite laminates. The isotropic modules T_0 and T_1 are still equal to T_0^L and T_1^L.

Table 3.2: Material properties for the optimizations of the test cases of Figure 3.5.

Test case (#1) and (#3) material properties				Test case (#2) material properties			
Modules	Values	Polar parameters	Values	Modules	Values	Polar parameters	Values
E_{11} [GPa]	181.0	T_0^L [GPa]	26.9	E_{11} [GPa]	177.0	T_0^L [GPa]	26.6
E_{22} [GPa]	10.3	T_1^L [GPa]	24.7	E_{22} [GPa]	10.8	T_1^L [GPa]	24.3
G_{12} [GPa]	7.2e3	η_0^L [-]	0.73	G_{12} [GPa]	7.6	η_0^L [-]	0.71
ν_{12} [-]	0.28	η_1^L [-]	0.83	ν_{12} [-]	0.27	η_1^L [-]	0.82

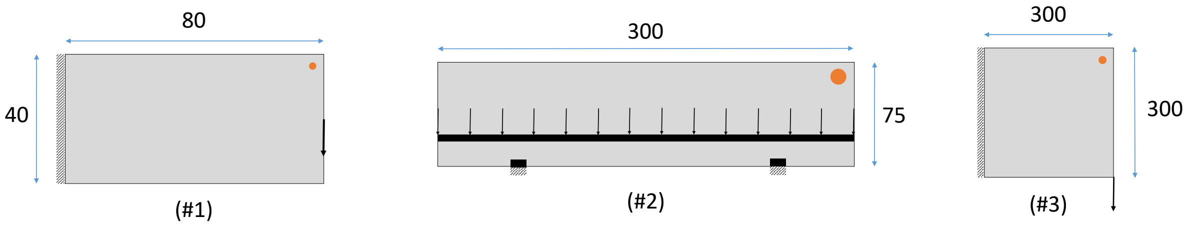

Figure 3.5: Test case representation, with the filter size indicate in orange.

The continuation strategy for the optimizations is given in Table 3.3. All optimizations are carried out for a fixed number of iterations. The filter reduction phase consists in gradually decreasing the density filter radius every 15 iterations until its value is smaller than the smallest element dimension. In this step, the SIMP exponent p is still equal to 5. The filter reduction is used to minimize the amount of intermediate density values, measured by the measure of non-discreteness (M_{nd}) [24]:

$$M_{nd} = \frac{\sum_{e=1}^{n} 4\widetilde{\rho}_e(1-\widetilde{\rho}_e)}{n} \times 100\% \,. \tag{3.21}$$

The algorithm settings for the SplitMMA strategy are given in Table 3.4. The initial density and anisotropy distributions are uniform. The density is set to the imposed volume fraction of the optimization, whereas the anisotropy is initialized with $\phi_1 = 0°$, $\eta_1 = 0.001$. η_0 is set to its maximum possible value. For the thermodynamic bounds, with a $\varepsilon = 0.05$ offset to satisfy the strict inequality, η_0 is thus initialized as 0.95. When the geometric bounds are used, the anisotropy is initialized with $\phi_1 = 0°$, $\eta_1 = 0.001$ and

Table 3.3: Continuation strategy of the optimization parameters in number of iterations for the different optimization approaches.

	Sequential SplitMMA	Sequential AD	Concurrent SplitMMA	Concurrent AD
SIMP p = 1	-	-	35	35
SIMP p = 3	90	90	90	90
SIMP p = 5	35	35	35	35
Filter reduction	90, where $R_{\rho_{new}} = 0.8 \times R_{\rho_{old}}$ every 15 iterations			
Anisotropy optimization	35	35	-	-
Total number of iterations	250	250	250	250

$\eta_0 = \eta_0^L$. Finally, the AD optimizations that are used as reference in Section 3.5.2, are initialized with all its anisotropic components equal to 0.

Table 3.4: MMA and GCMMA algorithm settings for the SplitMMA strategy for compliance minimization.

	MMA ρ	GCMMA ϕ_1	MMA α & β
epsimin	10^{-10}	10^{-10}	10^{-10}
raa0	10^{-5}	0.01	10^{-4}
raa0eps	-	10^{-6}	-
move	0.5	-	0.2
albefa	0.9	0.985	0.965
asyinit	0.8	0.7	0.7
asyincr	1.2	1.2	1.2
asydecr	0.8	0.6	0.6

3.5.1 About the Proper Use of η_1 to Escape Local Optima

This section details specific considerations for the optimization with respect to η_1 in the scope of topology optimization. From the definition of α given in Equation 3.10, η_1 is allowed to vary in $[-\eta_1^L, \eta_1^L]$. The effect of this choice is here discussed on a fixed topology, and serves to highlight an important strategy to escape local minima. A negative η_1 implies that the highest stiffness is aligned at 90° with respect to ϕ_1 [2]. As a matter of fact, the domain of existence is mirrored, as shown in Figure 3.6. In that case the domain describes all possible laminates and their rotation by 90° with respect to the reference frame defined by the ϕ_1. Thus all laminates are contained twice in the design space. Nonetheless, having η_1 negative does not change other properties of the polar formalism.

Starting from a uniform density distribution at the beginning of a topology optimization, distinct features will appear during the iterations as the topology becomes distinct. At a critical moment when those features appear, the direction of the maximum of the principal stresses changes abruptly. However, only using positive η_1 does not allow ϕ_1 to align with the direction of the maximum of the principal stresses. This condition is the optimality criterion for compliance minimization as detailed in Section 2.5.5. Indeed, before the abrupt stress direction switch, the trend of the anisotropy properties η_1 and ϕ_1 are in accordance with the stress state. However, when a feature appears, ϕ_1 can not follow this sudden switch in a gradient-based framework. This is highlighted with the following example, recreated on a fixed topology with η_0 fixed at 1-ε. Figure 3.7 shows the ϕ_1 and η_1 distribution when optimized on the fixed isotropic topology of test case (#1).

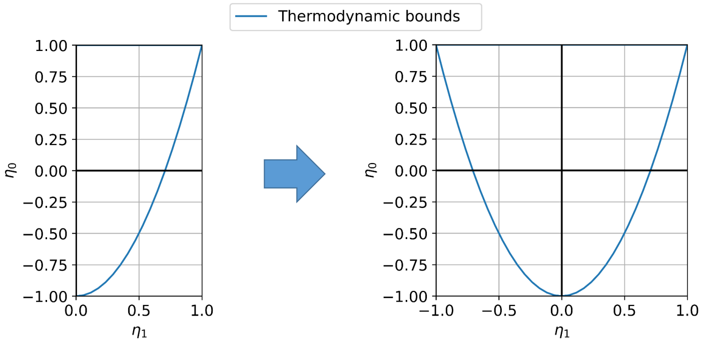

Figure 3.6: Domain of existence mirroring by including the consideration of negative η_1.

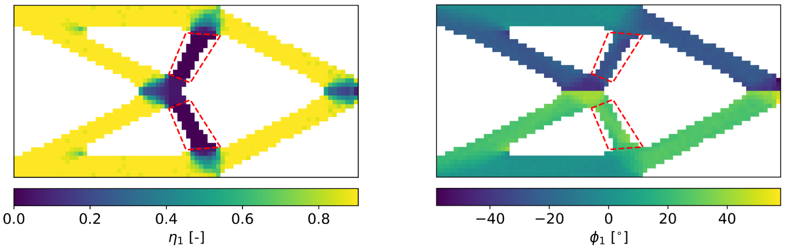

Figure 3.7: Optimized anisotropy with only η_1 being positive on a fixed topology.

The example shows that in the red-outlined area, the orientation ϕ_1 is perpendicular to the bars. Furthermore, the anisotropy represented by η_0 and η_1 means a square symmetry stiffness is obtained in these bars. Both these properties are sub-optimal for stiffness maximization. The value of the compliance is plotted in Figure 3.8, when varying η_1 in $[0, 1[$ and ϕ_1 in $[-90°, 90°]$ in the red-outlined area.

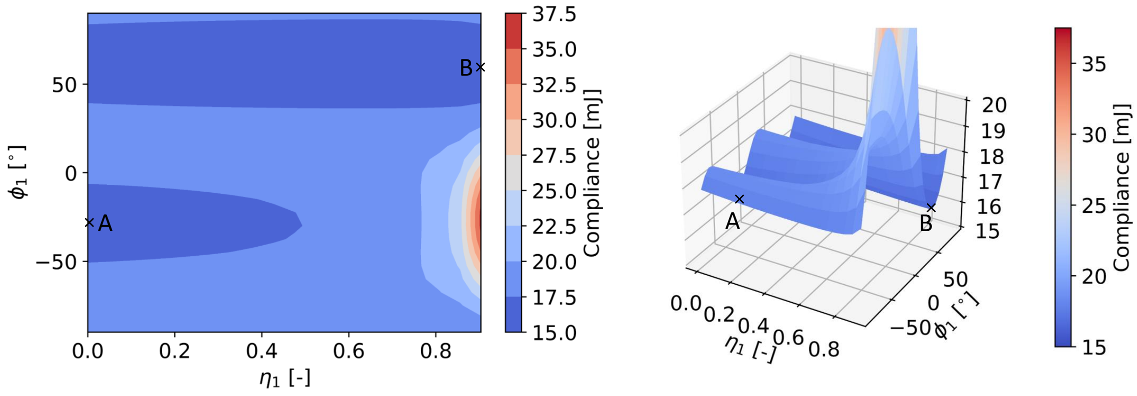

Figure 3.8: Design space of the compliance function with respect to η_1 and ϕ_1 in $[0, 1[\times [-90°, 90°]$ when varied in the red-outlined area of Figure 3.7.

The design space shows two different optima for this simple case. One at point A, which is associated to the results shown in Figure 3.7. The other minimum is at point B. It represents the solution with the Alternate Directions, where a UD material is obtained aligned with the bars. In Figure 3.7, the gradient-based optimization is trapped into the valley that corresponds to the local minimum A that lies on the boundary $\eta_1 = 0$. The Alternate Directions attains point B, as there is no step size limitation between consecutive iterations, which allows for a sudden switch in the direction of the maximum of the principal stresses.

Figure 3.9 shows the value of the compliance function over the design space with η_1 in the range $]-1, 1[$ and ϕ_1 still in $[-90°, 90°]$. The design space is extended with respect to η_1, which enables the gradient-based optimizer to reach from point A the true optima, in point C, which corresponds to point B from a mechanical viewpoint. In this extended design space point A is no more a local optimum.

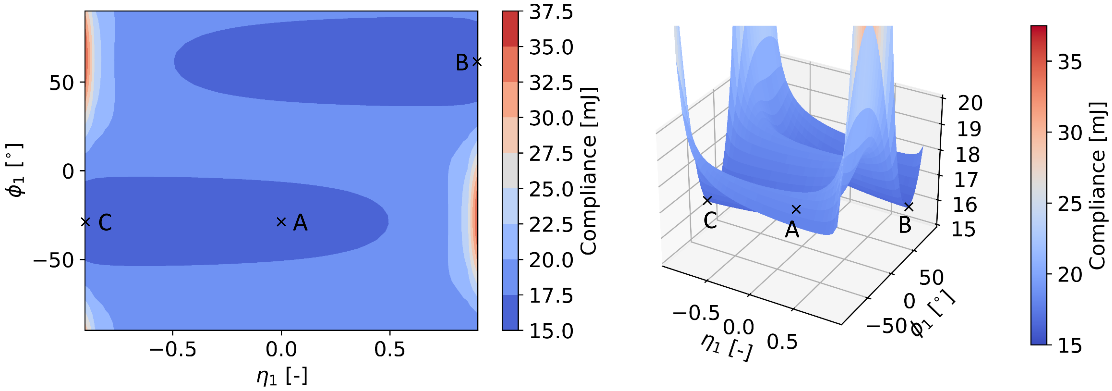

Figure 3.9: Design space of the compliance function with respect to η_1 and ϕ_1 in $]-1, 1[\times[-90°, 90°]$ when varied in the red-outlined area of Figure 3.7.

This section showed that local minima are present with respect to anisotropy variables, in which gradient optimizers can be trapped. These local minima are counter-intuitive and sub-optimal. They represent a totally different type of orthotropic behavior, be it with a compliance value close to the optimal one. Extending the design space to negative η_1 values enables to evade the spurious local optima created by the boundary $\eta_1 = 0$ through a different optimization trajectory. In subsequent results, for the sake of clarity, the absolute values of the parameter η_1 are shown, since a change of sign of η_1 corresponds to a 90° rotation of the material orthotropy axes. The orientations ϕ_1 are corrected accordingly, for easier visualization of the stiffest direction.

3.5.2 Optimization with Thermodynamic Bounds

Sequential Optimization

The sequential approach is first presented to investigate the influence of the topology and anisotropy separately. It is applied to both test case (#1) and (#2). The first step consists in obtaining a topology with an isotropic material. This step, done with only the density variables in the SplitMMA strategy and AD algorithm (η_0 and η_1 are set to 0), results in the topology solutions of the sequential optimizations in Figure 3.10 and Figure 3.11. The anisotropic components, optimized in a separate stage, of both these sequential optimizations are equally shown in Figure 3.10 and Figure 3.11. Lastly, the convergence graph for all the iterations together is also shown. In case of test case (#1), the topology and compliance are similar between both AD and SplitMMA, be it with a higher M_{nd} % for the AD algorithm. For test case (#2), the topology remains similar, be it with a higher compliance for SplitMMA. Furthermore, the local topology at the junction is different between SplitMMA and AD, with small holes emerging. Nonetheless, the disposition of the bars and junctions are coherent between both strategies.

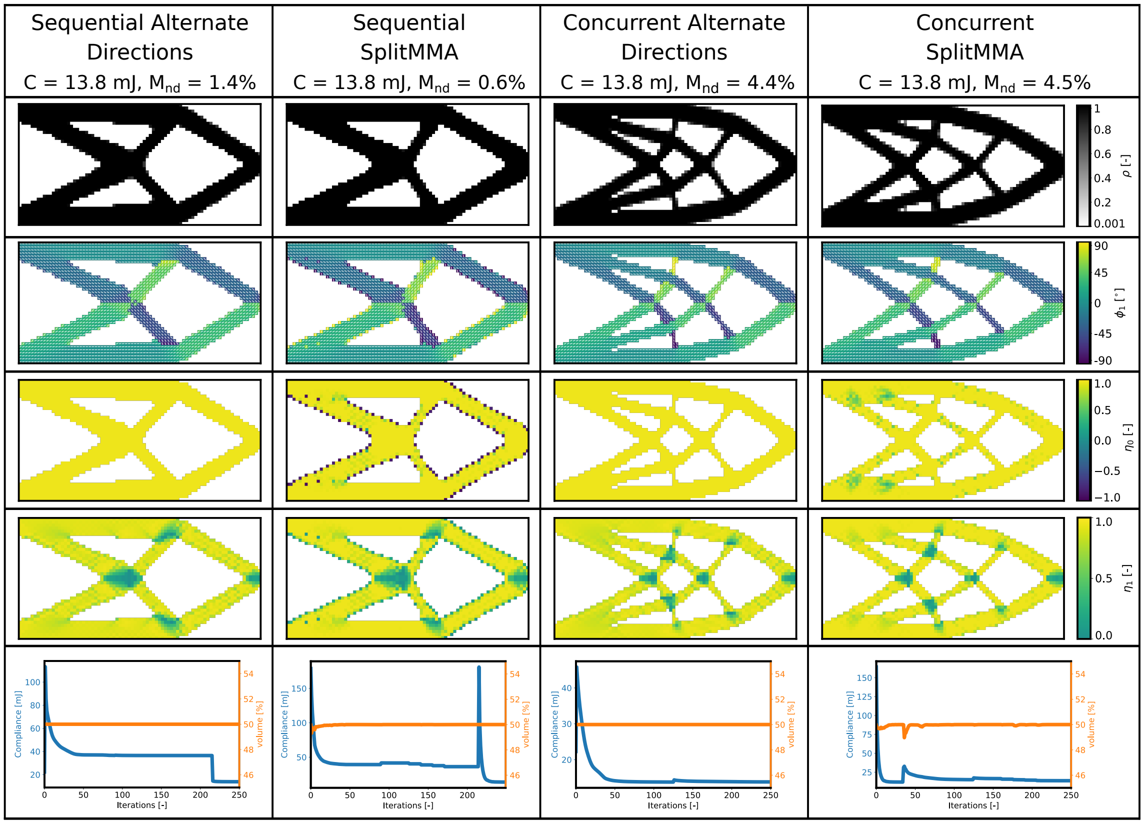

Figure 3.10: Results of the cantilever beam test case (#1) with thermodynamic bounds, for the sequential and simultaneous optimizations of the topology and anisotropy with the AD algorithm and SplitMMA strategy. Anisotropy variables are shown where $\rho \geq 0.9$.

Simultaneous Optimization

This part presents the simultaneous optimization with respect to the topology and anisotropy for compliance minimization. The results of these concurrent optimizations with the AD and SplitMMA strategy for both test cases are given in Figure 3.10 and Figure 3.12 respectively. In case of the second SplitMMA optimization (initial anisotropy only optimization) of test case (#2), the 35 initial iterations are performed only with respect to ϕ_1, η_0 and η_1, with all element densities kept at $\rho = v_f$ and SIMP p = 1. However, the total volume is greater than v_f in this step, due to the presence of the imposed full elements. When the SIMP exponent p is increased after iteration 35, the compliance is minimized with respect to all variables as in the other concurrent optimizations. The volume constraint is then satisfied.

The results for test case (#1) have similar density and anisotropy distributions, for the same compliance yet small differences in M_{nd} value. On the other hand, the SplitMMA solutions are more compliant than the AD solution for test case (#2). Nonetheless, the stiffest of the SplitMMA solutions, the one with an initial anisotropy only optimization step, resembles closely the AD solution. Furthermore, it is stiffer than any of the sequential optimization, with either the AD algorithm or SplitMMA strategy. Finally, Figure 3.15 shows the output and distribution of the anisotropic properties for the SplitMMA optimization within the thermodynamic domain for test case (#1). These distributions highlight the need of the anisotropy representation by means of a negative η_1 to be used to escape a local minima.

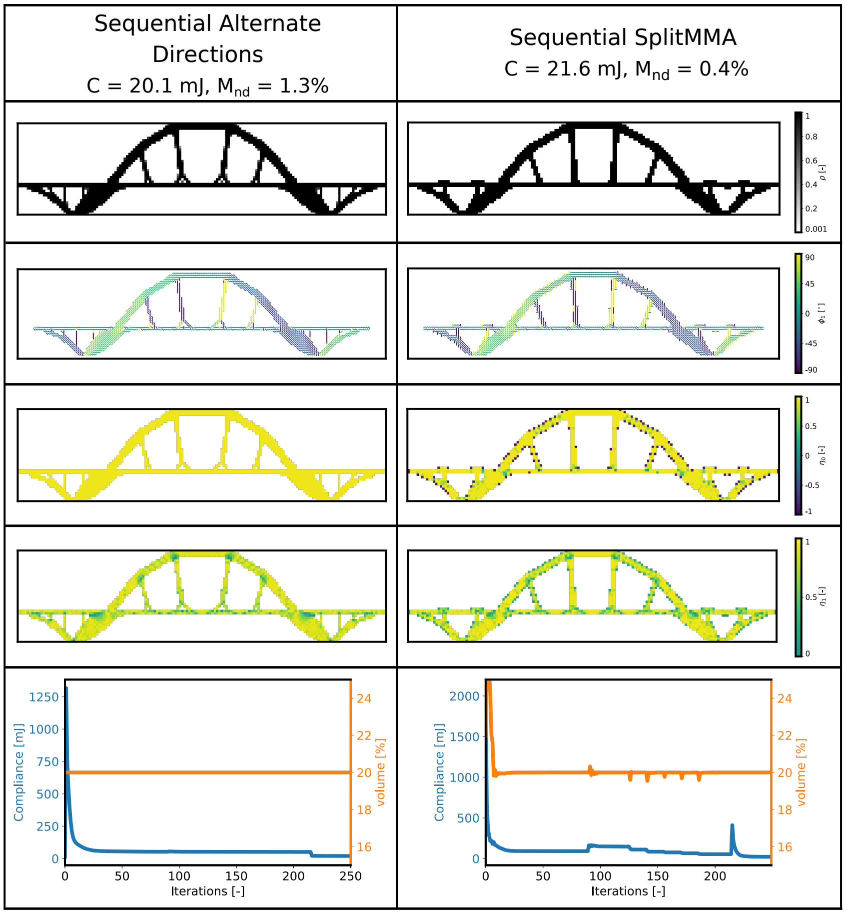

Figure 3.11: Results of the bridge test case (#2) with thermodynamic bounds, for the sequential optimizations of the topology and anisotropy with the AD algorithm and SplitMMA strategy. Anisotropy variables are shown where $\rho \geq 0.9$.

Discussion

The non-discreteness measure is important in the comparison of the solutions with AD and SplitMMA. Indeed, despite the same filter radius being used in both the SplitMMA and AD optimizations, they are not the same filter. The AD algorithm in [1] is programmed with an energy filter [187], which filters the deformation energy instead of only the densities. The most notable difference from this comes as the energy filter with a given filter radius will result in a topology with little intermediate densities. On the contrary, the density filter as used with the SplitMMA strategy with the same active filter radius will have intermediate densities due to the averaging and blurring effect on the boundary of the topology. Therefore the filter removal in SplitMMA lessens the blurring, and allows the topology to converge to more distinct density values, with lower M_{nd} %.

This has a twofold advantage. First, the distinct topology makes it easier to define the boundary of the structure for later post-processing steps in a design loop. Secondly, the intermediate densities are penalized the most by the SIMP approach. This therefore deteriorates the compliance for a similar topology with blurred boundaries. Having the intermediate densities removed and similar levels of M_{nd} facilitates the comparison of the compliance value between solutions.

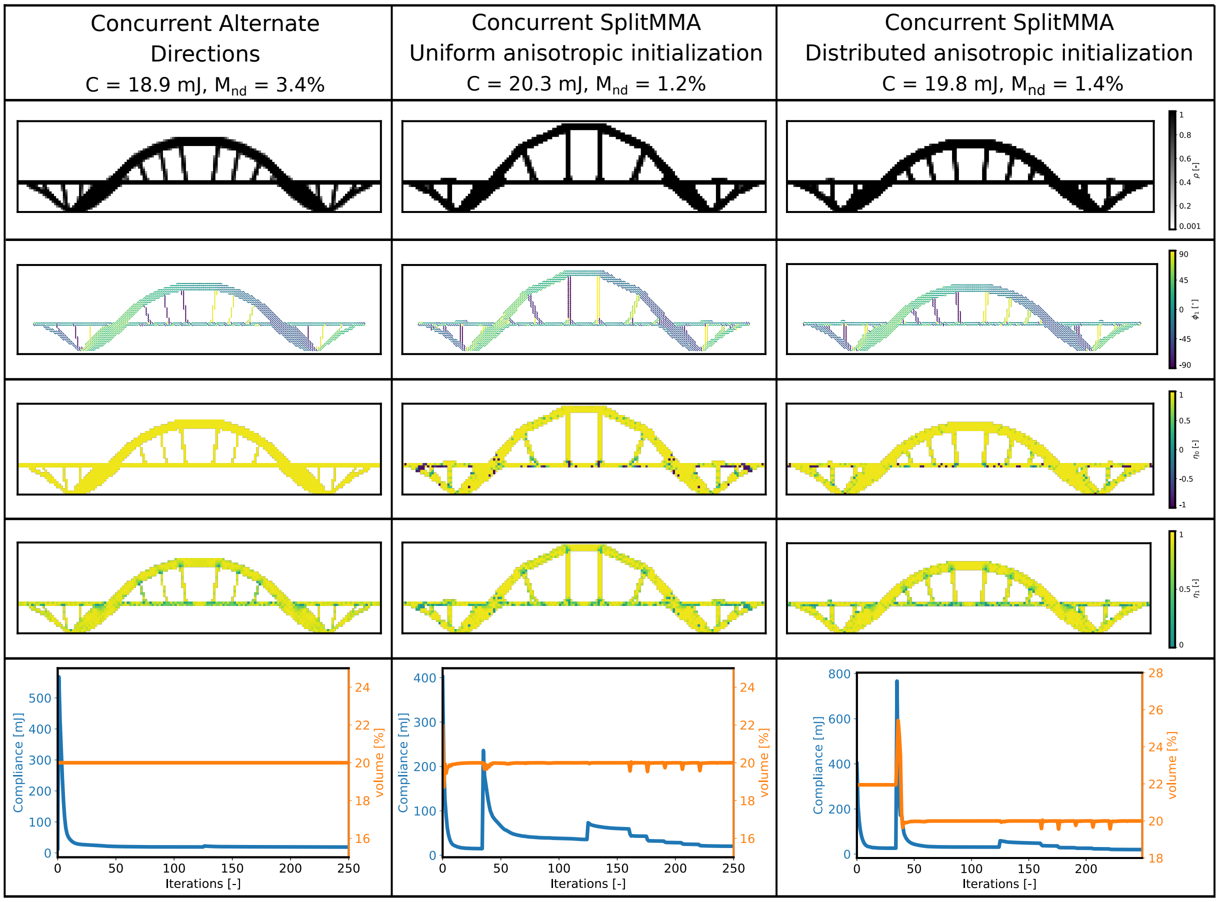

Figure 3.12: Results of the bridge test case (#2) with thermodynamic bounds, for the simultaneous optimizations of the topology and anisotropy with the AD algorithm and SplitMMA strategy. Anisotropy variables are shown where $\rho \geq 0.9$.

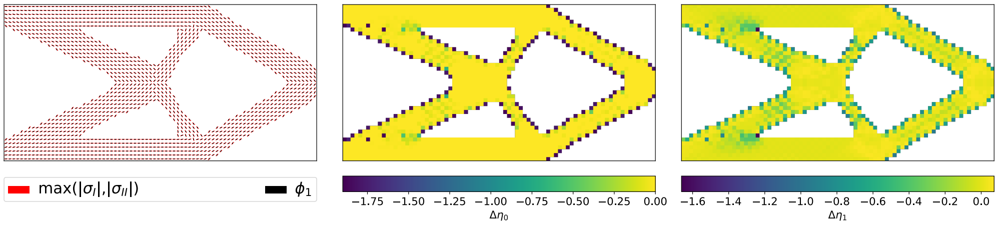

Figure 3.13: Difference between the anisotropic values obtained with SplitMMA and the optimized values obtained by applying the optimality criteria to SplitMMA solution for the sequential approach of test case (#1).

Thereafter, there is an equivalence between the isotropic topology with the AD and MMA algorithm for both test cases (the first step of the sequential optimizations). This was also reported by Fanni *et al.* [190] for optimization with isotropic material with optimality criteria, the basis of the AD algorithm, and MMA. On the other hand, both test case (#1) and (#2) show that the anisotropy changes the topology.

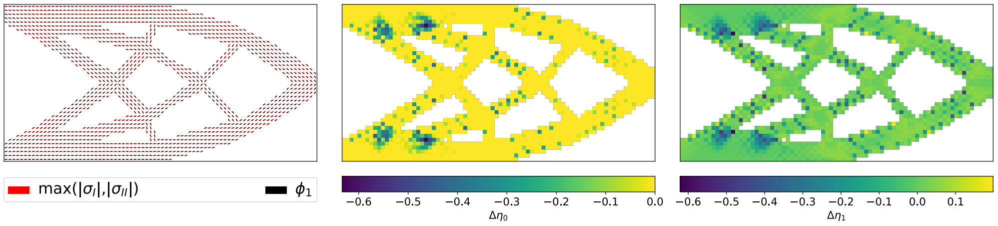

Figure 3.14: Difference between the anisotropic values obtained with SplitMMA and the optimized values obtained by applying the optimality criteria to SplitMMA solution for the concurrent approach of test case (#1).

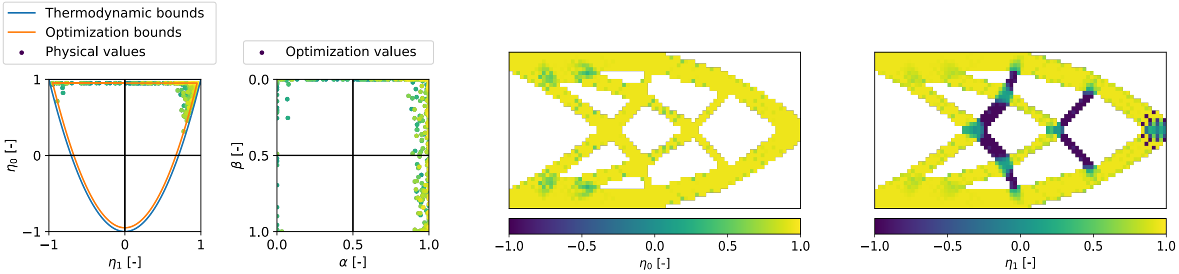

Figure 3.15: Results of the concurrent topology and anisotropy optimization with SplitMMA for test case (#1), with η_1 in $[-\eta_1^L, \eta_1^L]$: the anisotropic modules distribution within the thermodynamic bounds, the associated optimization variables α and β and the anisotropic modules on the topology. Values shown for elements with $\rho \geq 0.9$.

The comparison of the overall anisotropic distribution is in good agreement between AD and SplitMMA for all cases. Looking more in detail at η_0 of the SplitMMA solutions, its distribution is locally different along the jagged edge of the oblique bars between algorithms for the sequential approach of test case (#1) in Figure 3.10. Figure 3.13 shows the difference in optimized values of the polar parameters after having applied the optimality criteria on the final SplitMMA solution. η_0 values on the jagged edge differ significantly from the optimized values, also having a different sign. This different sign means the shape of orthotropy is different, and the overall elastic behavior changes. This leads to equally sub-optimal values for ϕ_1 and η_1. Local negative η_0 values are also present in test case (#2), but in neither test case (#1) or (#2) does it have a major impact on the global distribution and compliance value.

The AD solutions furthermore show that η_0 is constant at its upper bound. This is true regardless of the stress state [1], and the reason for the initialization choice of η_0 as the upper limit. On the other hand, the η_1 distribution is in good agreement, also when the optimality criteria are applied to the SplitMMA solution as given in Figure 3.13 and Figure 3.14. This clearly highlights that η_1 is well optimized with respect to the local stress state, with some noise present on the distributions. As a possible solution to the noise present on the η_0 and η_1 distribution, and alleviate the negative η_0 locations, further improvements could look at including a filter on these anisotropic modules to smooth the variation.

Afterwards, the ϕ_1 distribution also corresponds well between algorithms. The final orientations in SplitMMA greatly coincide with the theoretical optimality conditions used in the AD algorithm, being aligned with the maximum of the absolute value of the principal stresses. This is visible in Figure 3.13 and 3.14. A note should be made about the periodicity of the orientations: despite neighboring elements having 90° and

−90° orientations, the corresponding mechanical properties are identical. The discontinuity in the orientation field is not a source of error, but merely a periodicity effect. Therefore, to avoid 180° orientation differences being averaged out, a prospective filter should address this issue, such as the strategy proposed by Schmidt *et al.* [106]. All these elements of analysis show that the anisotropy is well optimized and conforming to the topology, and hence well taken into account in the optimization.

Both test cases also highlight the importance of the anisotropy distribution for the concurrent optimization with SplitMMA compared to the AD algorithm. This is because the optimality criteria in the AD can change the orientations and modules abruptly, as it only depends on the stress state of the current iteration. On the other hand, the variable values in the gradient approach can only evolve from the variable value of the previous iteration by the maximum stepsize allowed in MMA. The gradient-based approach seeks the best stepsize of the variables to improve the objective. However, the variable update is dictated by the validity of the gradient and its approximation, hence the variable change between iterations is usually less than optimality criteria changes. For the uniform initialization, the SIMP $\mathrm{p} = 1$ optimization step with respect to all variables is required. It allows for the interaction of the anisotropy and topology to converge to an intermediate configuration, even with these smaller steps. The intermediate convergence is due to the lack of penalization hindering any excess favoritism of any variable on the compliance. If the SIMP exponent p were to be raised too early, or the optimization started with SIMP $\mathrm{p} > 1$, the synergy between anisotropy and topology would not have time to take place, as the higher density penalization would lead the optimization. In the case of SIMP $\mathrm{p} > 1$, the smaller anisotropy variables steps and slower changes would be conforming to the already defined and predominant topology variables.

On the other hand, for the first 35 iterations in test case (#2), the optimization is carried out only with respect to the anisotropy with a uniform density. This allows to have an anisotropy distribution already conforming to the load path over the design domain at the start of the topology optimization. Then the optimization with respect to all variables is begun with SIMP $\mathrm{p} = 3$, meaning the influence of the anisotropy is directly taken into account by the topology variables. This is actually equivalent to the AD algorithm workings. Although the AD algorithm starts directly with SIMP $\mathrm{p} = 3$, its first step is to minimized the compliance with respect to the anisotropy. Thereafter, the densities are updated with the optimal anisotropy but the stress distribution of the current iteration, as one iteration is seen as a FEM analysis carried out. But the anisotropy update is a discrete change in the AD algorithm, based only on the stress field. The same effect occurs in the first 35 iterations in SplitMMA, where only the anisotropy is optimized. Only, as stated earlier, the changes can not be abrupt with a gradient-based method, but rather continuous with small steps to obtain the anisotropic field best aligned with the stress field.

Adding to the small possible variable variation between iterations with SplitMMA, allowing both positive and negative η_1 in the optimization permits to quickly switch the direction of highest stiffness between two iterations, even though the orientation ϕ_1 can only vary by a few degrees. This property is useful when the direction of principal stress flips due to bar-like feature being created during the optimization. In case of test case (#1), the initial anisotropy only optimization step is not required, and the SIMP $\mathrm{p} = 1$ optimization with respect to all variables yields a similar solution to the AD algorithm. Not requiring this initial step is attributed to the nature of this specific test case problem, where many similar local minima are present, and is therefore less sensitive to the initialization. The presence of many similar local minima is highlighted by the AD optimizations showing both the sequential and concurrent compliance are equivalent.

This approach of first optimizing the anisotropy alone leads thus to a different topology, which for the bridge test case is less bulky, but foremost also a stiffer solution. From a physical perspective, the arch is extremely stiff in bending in case of the right solution in Figure 3.12 compared to middle solution in Figure 3.12 Furthermore, with a lower height, more material can be used to obtain an additional stiffening effect by increasing the inertia of the arch and having an added support. The difference between the best AD and SplitMMA solution is because the gradient optimization is prone to getting stuck in local minima. Nonetheless, the difference is admissible, as the AD is specific to compliance minimization, but a wider range of optimization problems can be considered with the SplitMMA framework. Furthermore, SplitMMA upholds the concurrent approach yielding significant compliance gains over the sequential approach, by about 8% for the bridge case with the distributed anisotropy at the start of the topology optimization. This corresponds to the conclusion of Ranaivomiarana *et al.* [1].

All these observations allow to validate the suggested SplitMMA strategy, which is therefore well suited to incorporating anisotropy in topology optimization with thermodynamic materials. The solutions with SplitMMA converge to a similar solution to that of the benchmark AD algorithm, which is a powerful means of validation.

3.5.3 Optimization with Laminates within the Geometric Domain

Validation of Optimizations with the Geometric Bounds Optimization against the Lamination Parameters

The topology optimization with geometric bounds on the polar parameters is validated by comparing the results obtained to similar optimization results with lamination parameters on test case (#3). In the case of an orthotropic stiffness tensor, the relation between the lamination parameters and the polar parameters given by Panettieri *et al.* [191] can be expressed with normalized modules as follows:

$$\begin{aligned} V_1 &= \frac{\eta_1}{\eta_1^L}\cos 2\phi_1 \ , \\ V_2 &= \frac{\eta_1}{\eta_1^L}\sin 2\phi_1 \ , \\ V_3 &= \frac{\eta_0}{\eta_0^L}\cos 4\phi_1 \ , \\ V_4 &= \frac{\eta_0}{\eta_0^L}\sin 4\phi_1 \ . \end{aligned} \tag{3.22}$$

To reproduce the same orthotropy conditions of a balanced laminate as Peeters *et al.* [139], ϕ_1 is fixed to 0° and not optimized. Only η_0 and η_1 anisotropy variables are optimized simultaneous to the density variables. A uniform initialization is used. The optimization is performed in two steps with p = 1 and p = 3. The original results of Peeters *et al.* [139] with lamination parameters are shown in Figure 3.16. The results of with the geometric bounds on the polar parameters and the current SplitMMA strategy are shown in Figure 3.17, where the polar parameters have been converted to lamination parameters through Equation 3.22.

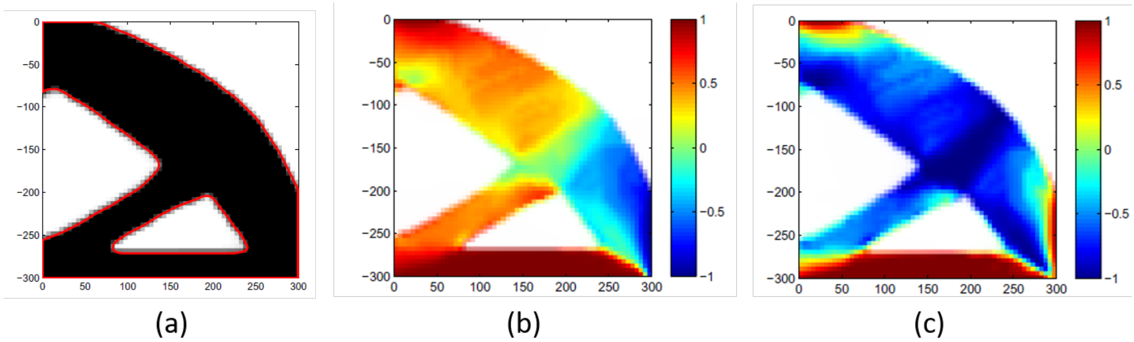

Figure 3.16: Results of Peeters *et al.* [139] for test case (#3) with lamination parameters: (a) the topology, (b) V_1 and (c) V_3.

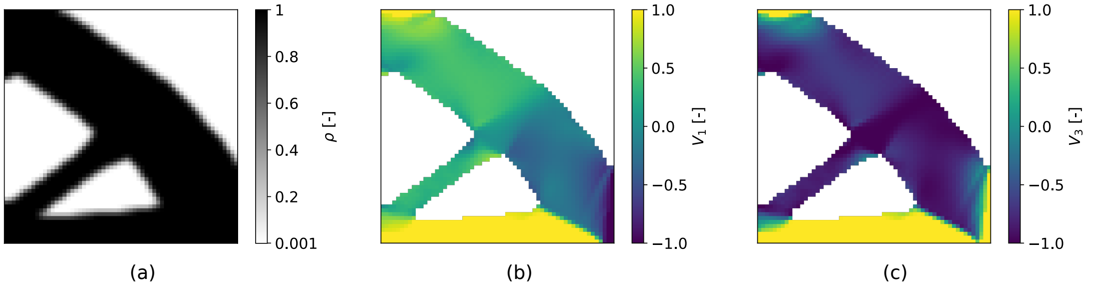

(a) (b) (c)

Figure 3.17: Optimization results of test case (#3) with geometric bounds: (a) the topology, (b) V_1 and (c) V_3.

The results of the optimization with geometric bounds in Figure 3.17, where the polar parameters have been converted to lamination parameters, are in good agreement for both topology and anisotropy distribution as compared to Peeters *et al.* [139]. This shows that the SplitMMA strategy can well incorporate simultaneous topology and anisotropy optimizations with geometric bounds.

Comparison between the Sequential and Concurrent Topology Approach for Laminates

With the incorporation of the geometric bounds in topology optimization validated, an equal comparison between the sequential and simultaneous approach can be conducted for the geometric bounds. Figure 3.18 shows the different results obtained applied to test case (#2). The sequential topology remains the same, as it is purely dictated by an isotropic topology optimization. On the other hand, the concurrent optimization with geometric bounds results in a different topology than with thermodynamic material. However, as with thermodynamic bounds, the geometric bounds solution remains less bulky, and provides a compliance improvement over the sequential approach.

Topology Optimization with Different Degree of Anisotropy

Lastly, SplitMMA can be used to simulate different degrees of freedom of the anisotropy, as defined by the constraints placed on the anisotropy design variables, and therefore the type of anisotropy that is obtained. Figure 3.19 compares solutions obtained for different materials for the same volume and mass with test case (#1). The isotropic case is optimized only with respect to the density, where $T_0 = T_0^L$, $T_1 = T_1^L$, $\eta_0 = 0$ and $\eta_1 = 0$. This corresponds to the first step of the sequential approach. The steered fiber case is optimized with respect to the density and orientation ϕ_1 only, with $T_0 = T_0^L$, $T_1 = T_1^L$, $\eta_0 = \eta_0^L$ and $\eta_1 = \eta_1^L$. The geometric case optimizes with respect to all variables, limited to the geometric bounds based on η_0^L and η_1^L. The optimization solution with thermodynamic bounds is the one from Section 3.5.2. The visual representation of the geometric feasible domain within the thermodynamic domain is shown in Figure 3.20, for the properties as listed in Table 3.2. The optimizations with steered fiber and geometric bounds use the initial anisotropy only optimization step.

Analyzing the solutions shows two important facts. First of all, all the topologies are different, demonstrating once again the importance of considering the anisotropy concurrently to the topology. Secondly, the more anisotropic freedom is given, the less compliant the solution becomes. The laminate anisotropy by means of the geometric bounds is stiffer than just steered fibers on a structure, although less than the thermodynamic bounds. Figure 3.20 shows the distribution of the anisotropic modules within the geometric domain. The reduced domain for the anisotropic modules with geometric bounds compared to the thermodynamic ones is the reason for the more compliant result: the restriction means less than ideal anisotropy can be used from a theoretical point of view. Even so, the optimized orthotropy direction ϕ_1 with geometric

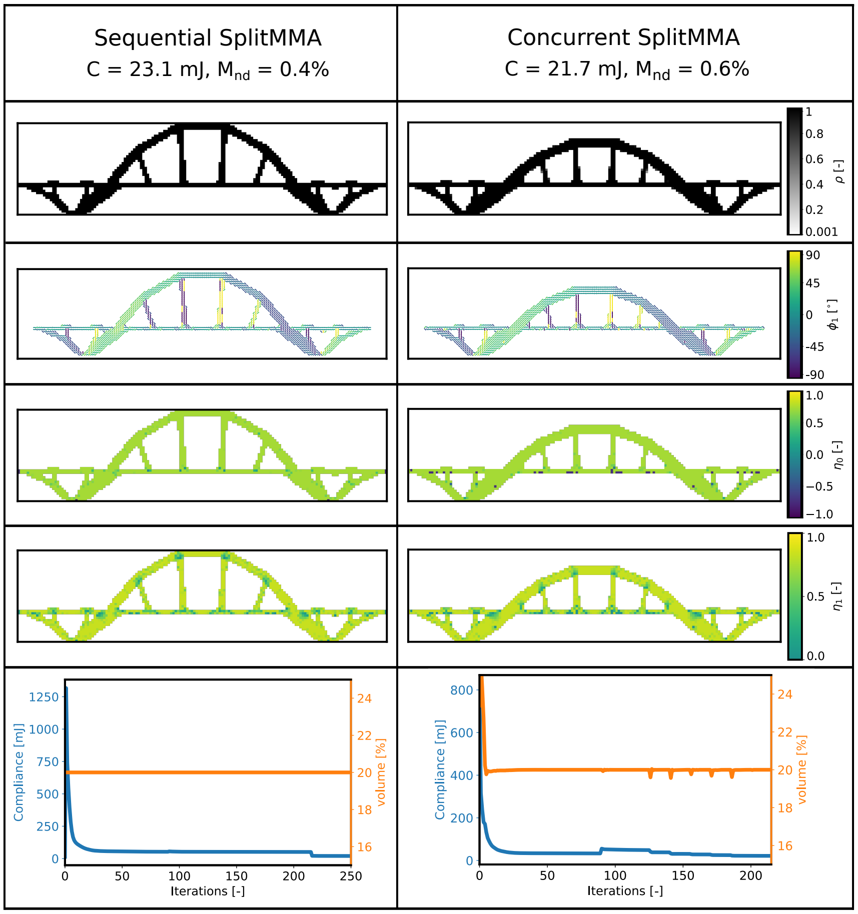

Figure 3.18: Comparison between a sequential and concurrent topology and laminate optimization.

bounds still coincides with the direction of the maximum of the absolute value of the principal stresses, as shown in Figure 3.21.

The solution with the geometric bounds holds nonetheless an advantage over its counterpart with thermodynamic bounds. Anisotropy defined by the thermodynamic bounds is valid mathematically, but part of the domain has no known corresponding material. This is for example visible where η_0 tends to 1, meaning no shear stiffness. This is where the geometric bounds are superior, as they represent a feasible stacking sequence and therefore a material which can be manufactured. However, this stacking sequence retrieval, performed in subsequent steps after the optimization, is not part of the current topic. The geometric bounds have already been used for laminates with thickness optimization before [144, 9], see Section 2.4.2, but not yet incorporated in a topology optimization routine. The current framework offers the prospect of topology and anisotropy optimization with additional optimization constraints such as strength or buckling, for future research.

3.6 Conclusion

This chapter presented and validated an optimization strategy for the simultaneous optimization of topology and material anisotropy combining the MMA algorithms and the polar method, an invariant-based repre-

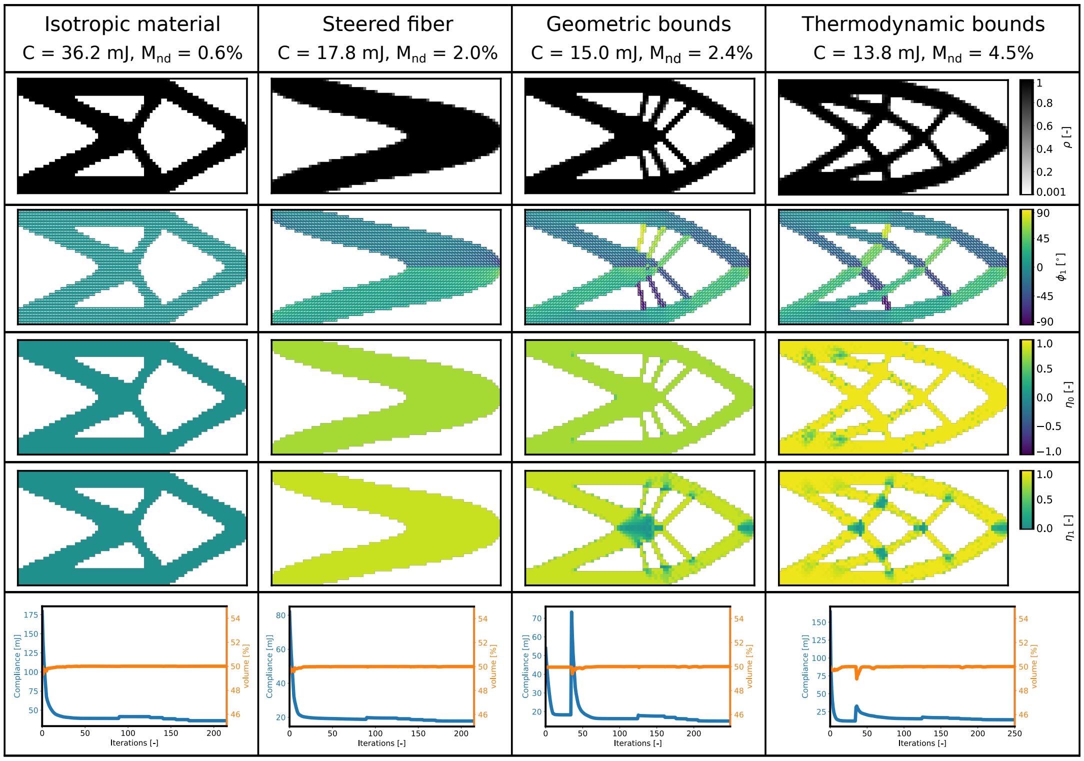

Figure 3.19: Topology and anisotropy distributions for simultaneous optimizations with different degrees of anisotropy: isotropic material design, steered-fiber design, laminated solution (geometric bounds) and general orthotropic materials (thermodynamic bounds).

sentation of the elasticity tensors. The anisotropic components are normalized to obtain a set of continuous design variables. The considered materials are either general orthotropic materials or composite laminates. A change of variables is used to implicitly satisfy either of the corresponding existence constraints during the optimization. A strategy called SplitMMA is suggested to solve the compliance minimization problem, based on the Method of Moving Asymptotes (MMA) algorithm class. The density, orientation and anisotropic modules are updated separately at each iteration, in parallel sub-problems. Each sub-problem is constructed with a different type of approximation and settings, selected to tailor best the regularity of the problem with respect to the different types of variables.

The proposed SplitMMA method is first compared with respect to the Alternate Direction (AD) algorithm in the case of general orthotropy in 2D. For both sequential and simultaneous topology and anisotropy optimizations, the SplitMMA solutions are a close match to their AD counterparts, both in objective value and variable distributions. In particular, the SplitMMA strategy preserves the improvement in compliance due the simultaneous consideration of topology and anisotropy. The importance of the anisotropy initialization in SplitMMA is highlighted to achieve the improvements, along adapting the design space to flip the principal stiffness direction transversely in a continuous manner.

The method is further validated in the case of composite laminates by comparing the results obtained with published results using density and lamination parameters as design variables. Finally, the influence of different types of material anisotropy in topology optimization are presented with novel results in the case of composite laminates. With the same prescribed mass and the same isotropic part of the material,

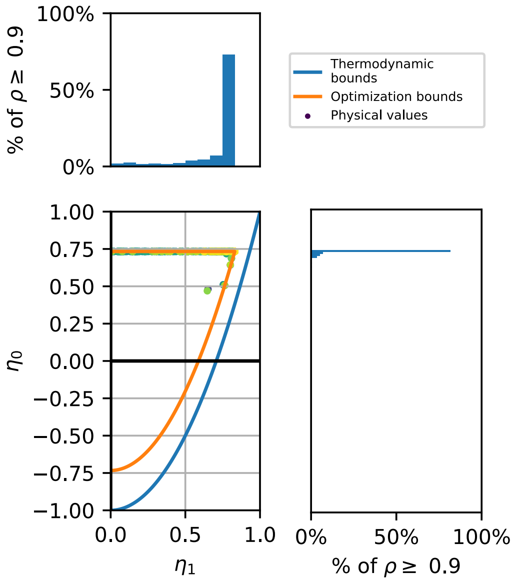

Figure 3.20: Anisotropic modules distribution within the geometric bounds for the concurrent topology and anisotropy optimization with SplitMMA for test case (#1). Modules included where $\rho \geq 0.9$.

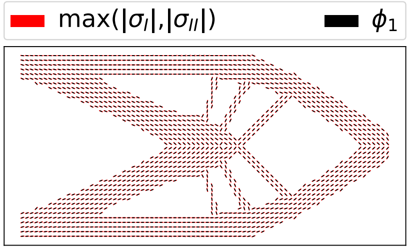

Figure 3.21: Optimized anisotropy orientation and ϕ_1 for the geometric bounds optimization of Figure 3.19. Modules shown for elements with $\rho \geq 0.9$.

the compliance of the solutions decreases with increasing anisotropy design domains, while the topologies vary. Finally, it is shown that the concurrent approach also yields stiffer results at iso-mass with geometric compared to the sequential approach.

Chapter 4

Optimization Constraint and Gradient Derivation Based on an Elliptic Stress Criterion for the Simultaneous Density and Orthotropic Material Orientation Optimization

4.1 Introduction

This chapter details the theoretical derivation and numerical implementation of the optimization constraint when strength is considered for a Uni-Directional (UD) material in topology optimization. An anisotropic material with fixed elastic modules is considered, such as a single composite UD ply, but whose orientation is allowed to vary. Three elliptic stress-based first ply failure criteria (Tsai-Wu, Tsai-Hill and Hoffman) are implemented in the derivation to represent anisotropic material failure. Chapter 6 deals with strength constraints in topology optimization with a layup of several UD plies representing a laminate.

Including failure in topology optimization is not straightforward, due to several difficulties, as identified in the state of the art in Section 2.3, and shortly summarized next. First of all, the maximum of a stress criterion can not directly be used as constraint or minimized if used as the objective. Indeed, this would lead to a non-differentiable problem, as the location of the maximum stresses would change every iteration, which in turns leads to numerical issues when gradient-based solvers are used. Secondly, stress singularities arise when the optimizer tries to remove low density elements (meaning ρ tends to ρ_{min}). The solution which removes completely low density elements lays in a lower dimension design space, which gradient-based solvers have difficulty reaching. Regulation techniques have been developed to handle these issues and are used for isotropic failure criteria. The last problem with failure consideration is linked to the computational cost of the optimization loop and obtaining the required gradient information. As failure is a local measure, if the stress criterion of each individual element is considered as optimization constraint, the amount of constraints slows down tremendously the optimization. Moreover, the gradient computation of each separate constraint requires one additional FEM analysis, further increasing the computational cost. Therefore, aggregation techniques are used to regroup the local strength constraints into few global ones, and decrease the amount of required additional FEM analysis and subsequent computational cost.

The following sections describes the selected strategy to address these numerical issues with stress concentrations. The strategy is first reviewed for an isotropic material with an isotropic failure criterion, based on the lower KS strategy of Verbart *et al.* [5]. This strategy relaxes the stress singularities and aggregates the local constraints by the same function. Afterwards, the strategy is extended to account for anisotropic stiffness and strength criteria in case of UD material. Results with this strategy are given and discussed in Chapter 5.

4.2 Isotropic Stress Criterion

4.2.1 Optimization Constraint Definition

Stress Measure

The stress vector $\boldsymbol{\sigma}_{(i)}$ of element (i), defined as $\{\sigma_x, \sigma_y, \tau_{xy}\}^T$, can be obtained from the standard stress strain relationship as given in Equation 4.1. $\boldsymbol{\varepsilon}_{(i)}$ is the strain vector of element (i), defined as $\{\varepsilon_x, \varepsilon_y, \gamma_{xy}\}^T$, and $[Q]$ the stiffness tensor. In case of a FEM analysis, the strain components are obtained from the nodal displacements $\boldsymbol{U}_{(i)}$ and the strain-displacement matrix $[B]$. This matrix is unique if all elements are the same (which is often the case in topology optimization), otherwise it must be computed for every different one. The Python FEM implementation is detailed more in Appendix B.

$$\boldsymbol{\sigma}_{(i)} = [Q_{(i)}]\boldsymbol{\varepsilon}_{(i)} \tag{4.1}$$

In a SIMP topology optimization framework, an element stress is therefore obtained by means of Equation 4.2, called the macro-stress of an homogenized element. $[Q_{0_{(i)}}]$ is the stiffness tensor of the pristine material (that can be defined by the polar formalism as given by Equation 3.7). The macro-stress naming is in relation to the macroscopic stiffness assigned to an element by means of the SIMP interpolation with an exponent p. However, if the macro-stress is used straightforwardly to perform a volume minimization with a stress constraint in topology optimization, a trivial all-void design is obtained [4].

$$\boldsymbol{\sigma}_{(i)} = [Q_{(i)}][B]\boldsymbol{U}_{(i)} = \rho_{(i)}^{p}[Q_{0_{(i)}}][B]\boldsymbol{U}_{(i)} \tag{4.2}$$

To counter this, it is better to use the micro-stress measure [68]. This represents the actual stress in the underlying microstructure. Indeed, for intermediate densities, the SIMP stiffness tensors represent the homogenized properties of a combination of void and pristine material. This results in the micro-stress being different than the macro-stress applied to the element. If the underlying microstructure is known, a true relationship can be setup between the macro and micro-stress. However, as the current aim of the optimizations is to obtain distinct density solutions (either $\rho_{\min}$ or 1), no relation is known between intermediate densities and microstructures. Therefore, an equivalent micro-stress measure is defined and used to avoid the trivial all void solution. This so-called equivalent micro-stress $\boldsymbol{\sigma}_{(i)}^{micro}$ for topology optimization problems is defined by Equation 4.3 [67]. This approximation is based on a different penalization of the elasticity matrix $[Q_{(i)}]$ by using a different exponent value r for the density, given as $r = p - q$.

$$\boldsymbol{\sigma}_{(i)}^{micro} = \frac{\boldsymbol{\sigma}_{(i)}}{\rho_{(i)}^{q}} = \frac{\rho_{(i)}^{p}}{\rho_{(i)}^{q}}[Q_{0_{(i)}}][B]\boldsymbol{U}_{(i)} = \rho_{(i)}^{r}[Q_{0_{(i)}}][B]\boldsymbol{U}_{(i)} \tag{4.3}$$

The case $q = p$ leads to the so-called stress singularity problem, where the optimal solution lays in a degenerate space difficult to reach for gradient optimizers. All elements retain a finite strain and therefore finite stress, as explained in more detail in Section 2.3. Therefore, stress relaxation techniques are used, which approximate the micro stress, yet avoid the degenerate design space. Bruggi [67] introduced a simple strategy to relax the stress singularities, the so-called *qp-approach*. This *qp-approach* is in itself a modified ϵ-approach as was suggested by Cheng and Guo [63], with the special case of ϵ being adapted as a function of the density. The value of the q exponent must satisfy $0 < q < p$, as to not use the macro-stress ($q = 0$) or be in a degenerate design space ($q = p$). This is a mathematical manipulation with no physical basis in order to solve a stress-based topology optimization and obtain distinct results. It is introduced to circumvent the problems of having all void designs or stress singularities and not being able to remove elements.

In the following, it is nonetheless chosen to implement an alternative solution proposed by Verbart *et al.* [5], where the relaxation is combined with the aggregation thanks to the use of a lower approximation of the maximum value of the strength criterion. Therefore, a micro-stress value can be used, with q equals to p. Hence the exponent r equals 0 when considering stress in a optimization constraint. This is expressed by Equation 4.4, where the dependency on $\rho^r_{(i)}$ is kept for ease of derivation of the gradient in subsequent steps.

$$\boldsymbol{\sigma}^{micro}_{(i)} = \rho^r_{(i)}[Q_{0_{(i)}}][B]\boldsymbol{U}_{(i)} \tag{4.4}$$

With a correct stress measure for a topology optimization, the remainder of the section will first discuss the case of an isotropic material, whose failure is modeled according to the Von Mises criterion. Section 4.3.1 deals with the integration of an anisotropic strength criterion. The equivalent failure measure for each element $fail_{m_{(i)}}$ is defined in Equation 4.6. For an isotropic material, it is equivalent to the Von Mises stress measure $\sigma^{VM}_{(i)}$ of an element i, where its stress components at each centroid $\boldsymbol{\sigma}_{(i)}$ is obtained according to Equation 4.5. The transformation matrix [V] is defined as in Equation 4.6 [3].

$$fail_{m_{(i)}} := \sigma^{VM}_{(i)} = \sqrt{(\boldsymbol{\sigma}^{micro}_{(i)})^T[V]\boldsymbol{\sigma}^{micro}_{(i)}} \tag{4.5}$$

$$[V] = \begin{bmatrix} 1 & -1/2 & 0 \\ -1/2 & 1 & 0 \\ 0 & 0 & 3 \end{bmatrix} \tag{4.6}$$

Thereafter, failure is reached when the Von Mises stress σ^{VM} is lower than the yield stress σ^{Y} over the isotropic material (*i.e.*, $\sigma^{VM}_{(i)} \leq \sigma^{Y}$). This condition is equivalent to Equation 4.7, where g is normalized and defined in such a way to be incorporated as an optimization constraint ($g_{(i)} \leq 0$).

$$g_{(i)} := \frac{\sigma^{VM}_{(i)}}{\sigma^{Y}} - 1 \leq 0 \tag{4.7}$$

Following the strategy proposed by Verbart *et al.* [5] and discussed in Section 2.3.2, a Mathematical Programming with Vanishing Constraints (MPVC) strategy is used, where the equivalent local constraint $\bar{g}_i$ is defined for element i as given in Equation 4.8.

$$\bar{g}_{(i)} := \rho_{(i)} g_{(i)} \leq 0 \tag{4.8}$$

Aggregation Method

Stress measure and failure is a local phenomenon, and structural optimization seeks a safe optimized design where the constraint of Equation 4.8 is satisfied for every element. However, this would increase the amount of optimization constraints and add a huge numerical cost to the analysis. On the other hand, only using the maximum value of Equation 4.8 as constraint would lead to numerical instability as the maximum function is non-differentiable. Moreover, the location of the maximum would possibly change at every iteration, which does not allow to have a control over it. Therefore, in order to reduce the amount of optimization constraints, an aggregation technique is used. The aggregation allows to regroup and approximate the maximum of all the values of interest of the elements included in the set Ω_k. Equation 4.9 shows the aggregation by means of an lower-bound Kreisselmeier-Steinhauser (KS) function [192]. This KS function can aggregate both positive and negative terms, opposite to the P-norm aggregation which can only include positive terms. Furthermore, this aggregation step also has the benefit to speed up the sensitivity calculations as discussed in Section 4.2.2.

The cluster Ω_k contains all elements whose quantity of interest are considered. This can be used to divide the structure in different zones (either geometrically or by value) to have a more precise control of the failure constraint over the design domain, as discussed in Section 2.3, but also to assign different failure properties to different regions. The influence of elements not considered in the cluster will still be taken into account by the gradient and their effect on the change in load path, as discussed in Section 4.2.2.

$$g_k^{LKS} = \frac{1}{\mu} \ln \frac{1}{N} \left(\sum_{j \in \Omega_k} \exp(\mu \bar{g}_{(j)}) \right) \tag{4.9}$$

The principle of the lower KS aggregation function is shown in Figure 4.1. The parameter μ dictates the accuracy of the approximation of the maximum. For an increase in this parameter μ, the aggregated maximum will tend to the true maximum, at the cost of numerical issues. On one hand, the function becomes much more non-linear. This can then possibly lead to bad convergence of the optimization. On the other hand, numerical overflow can occur. This happens when the $\bar{g}_i$ quantities are of larger magnitude, which combined to the exponential operation results in values too large to be handled by a computer's memory. In order to overcome these difficulties, several possibilities are available. First, $\bar{g}_i$ can be scaled down. This already happens by considering the constraint of Equation 4.7, and not aggregate the Von Mises stress directly before using that aggregated stress with the yield stress. Secondly, a continuation of the μ parameter can be considered, with a smaller value when the value of $\bar{g}_i$ is still large, and increasing μ when the value of $\bar{g}_i$ is lower. However, the aggregated value then tends to be far off the actual maximum initially, and afterwards, as the value of μ increases, so does the non-linearity of the problem. Instead, it is chosen to bound the maximum value used in the aggregation of Equation 4.9 by changing the formulation as given in Equation 4.10 [76, 193]. This ensures that no matter the magnitude of $\bar{g}$, the exponential operation always considers small magnitudes, and a constant value of μ is used. The $\bar{g}_{\max}$ is a fixed value chosen as the maximum of the $\bar{g}_i$ values to avoid numerical overflows.

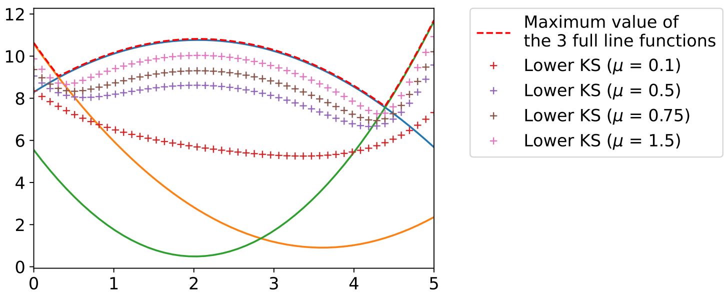

Figure 4.1: Effect of different μ values on the lower KS aggregation of the maximum of the three functions.

$$g_k^{LKS} = \bar{g}_{\max} + \frac{1}{\mu} \ln \frac{1}{N} \left(\sum_{j \in \Omega_k} \exp(\mu(\bar{g}_{(j)} - \bar{g}_{\max})) \right) \tag{4.10}$$

The lower KS function approximates the maximum value of the cluster from below. Hence, in the optimizations later on, although the constraint $g_k^{LKS} \leq 0$ will be satisfied, the actual maximum value of the system will be higher than 0 due to this approximation from beneath. The final form of the optimization constraint g_k^{LKS} is then given by Equation 4.11 for a Von Mises failure criterion, with the graphical representation of the numerical steps to obtain it shown in Figure 4.2.

$$g_k^{LKS} = \bar{g}_{\max} + \frac{1}{\mu} \ln \left[\frac{1}{N} \sum_{j \in \Omega_k} \exp \left(\mu \left[\rho_{(j)} \left(\frac{\sqrt{([Q_{0_{(j)}}][B]\boldsymbol{U}_{(j)})^T [V] [Q_{0_{(j)}}][B]\boldsymbol{U}_{(j)}}}{\sigma^Y} - 1 \right) - \bar{g}_{\max} \right] \right) \right] \tag{4.11}$$

4.2.2 Optimization Constraint Gradient

In order to obtain the gradient of the global aggregated constraint of Equation 4.11, the chain rule of the operations required to compute the g_k^{LKS} function must be applied. First, the derivative of the KS function

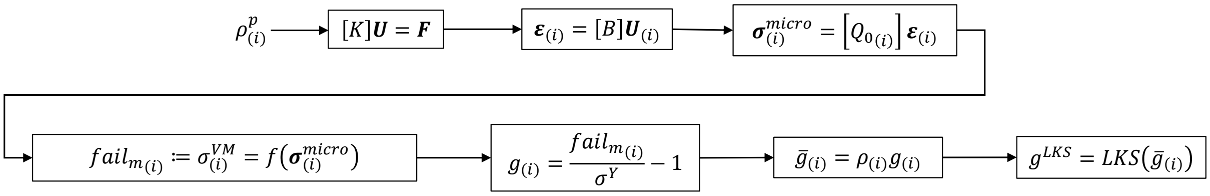

Figure 4.2: Numerical steps used to compute the value of the global failure optimization constraint for a Von Mises criterion with an isotropic material.

is given by Equation 4.12, with the last partial derivative being obtained by applying the chain rule again as to obtain the expression given in Equation 4.13.

$$\frac{\partial g_k^{LKS}}{\partial \rho_{(i)}} = \frac{\sum_{j\in\Omega_k} \exp\left(\mu(\bar{g}_{(j)} - \bar{g}_{\max})\right) \frac{\partial \bar{g}_{(j)}}{\partial \rho_{(i)}}}{\sum_{j\in\Omega_k} \exp\left(\mu(\bar{g}_{(j)} - \bar{g}_{\max})\right)} \tag{4.12}$$

$$\frac{\partial \bar{g}_{(j)}}{\partial \rho_{(i)}} = \frac{\partial \rho_{(j)}}{\partial \rho_{(i)}} g_{(j)} + \rho_{(j)} \frac{\partial g_{(j)}}{\partial fail_{m_{(j)}}} \frac{\partial fail_{m_{(j)}}}{\partial \boldsymbol{\sigma}^{micro}_{(j)}} \frac{\partial \boldsymbol{\sigma}^{micro}_{(j)}}{\partial \rho_{(i)}} \tag{4.13}$$

Each part of Equation 4.13 can be computed separately. The first term stems from the MPVC definition in Equation 4.8, and equates to δ_{ij}. Looking at the first factor of the second term, from its definition in Equation 4.7, the gradient is expressed in Equation 4.14.

$$\frac{\partial g_{(j)}}{\partial fail_{m_{(j)}}} = \frac{\partial}{\partial \sigma^{VM}_{(j)}} \left(\frac{\sigma^{VM}_{(j)}}{\sigma^{Y}} - 1 \right) = \frac{1}{\sigma^{Y}} \tag{4.14}$$

The second factor of the second term of Equation 4.13 relates the change of the Von Mises failure criterion with respect to the stress components at the centroid of the element, obtained from Equation 4.5 as Equation 4.15.

$$\frac{\partial fail_{m_{(j)}}}{\partial \boldsymbol{\sigma}^{micro}_{(j)}} = \frac{1}{\sigma^{VM}_{(j)}} [V] \boldsymbol{\sigma}^{micro}_{(j)} \tag{4.15}$$

Finally, the last factor of the second term of Equation 4.13 involves the change of the different stress components of a given element, as defined by the micro-stress of Equation 4.4. This is constituted of two parts: one is the influence on the elasticity properties of the element itself, and the other is the change in element displacement due to the influence of a different load path. It can be computed as given in Equation 4.16.

$$\frac{\partial \boldsymbol{\sigma}^{micro}_{(j)}}{\partial \rho_{(i)}} = \frac{\partial}{\partial \rho_{(i)}} \left(\rho^{r}_{(j)} [Q_{0_{(j)}}][B] \boldsymbol{U}_{(j)} \right) = \frac{\partial (\rho^{r}_{(j)} [Q_{0_{(j)}}])}{\partial \rho_{(i)}} [B] \boldsymbol{U}_{(j)} + \rho^{r}_{(j)} [Q_{0_{(j)}}][B] \frac{\partial \boldsymbol{U}_{(j)}}{\partial \rho_{(i)}} \tag{4.16}$$

The sensitivity $\frac{\partial \mathbf{U}_{(j)}}{\partial \rho_{(i)}}$ in the second term can be calculated from the equilibrium state equation as given in Equation 4.17. This assumes design independent loading, meaning $\mathbf{F}$ is not dependent on the displacement. Hence the presented gradient will only be valid for force based topology optimization, and not for displacement based. Resolving Equation 4.17 directly is known as the direct method, which has to be solved each time for every variable. This is a large system, as the size of $[K]$ depends on the degree of freedom of the system, which is proportional to the amount of elements. Therefore solving Equation 4.17 every time over again involves a high computational cost. The cost could already be lowered by reusing a LU factorization of $[K]$, saved from the earlier FEM analysis. $[K]$ is indeed constant for each iteration. Nonetheless, this method is effective with few variables, but many constraints.

$$\frac{\partial}{\partial \rho_{(i)}}\left([K]\boldsymbol{U} = \boldsymbol{F}\right) \Rightarrow \frac{\partial [K]}{\partial \rho_{(i)}}\boldsymbol{U} + [K]\frac{\partial \boldsymbol{U}}{\partial \rho_{(i)}} = \mathbf{0} \Rightarrow \frac{\partial \boldsymbol{U}}{\partial \rho_{(i)}} = -[K]^{-1}\left(\frac{\partial [K]}{\partial \rho_{(i)}}\boldsymbol{U}\right) \tag{4.17}$$

However, instead of computing Equation 4.17 directly, it can be substituted in Equation 4.16, which on its turn can be substituted together with Equation 4.14 and Equation 4.15 in Equation 4.12 to obtain Equation 4.18.

$$\begin{aligned}\frac{\partial g_k^{LKS}}{\partial \rho_{(i)}} = \frac{1}{\sum_{j\in\Omega_k}\exp\left(\mu(\bar{g}_{(j)} - \bar{g}_{\max})\right)} \sum_{j\in\Omega_k}\Bigg[\exp\left(\mu(\bar{g}_{(j)} - \bar{g}_{\max})\right)\Bigg(\delta_{ij}g_{(j)} + \rho_{(j)}\frac{1}{\sigma^Y}\left[\frac{1}{\sigma^{VM}_{(j)}}[V]\boldsymbol{\sigma}^{micro}_{(j)}\right]^T \\ \left[\frac{\partial(\rho^r_{(j)}[Q_{0_{(j)}}])}{\partial \rho_{(i)}}[B]\mathbf{U}_{(j)} - \rho^r_{(j)}[Q_{0_{(j)}}][B][K]^{-1}\left(\frac{\partial [K]}{\partial \rho_{(i)}}\mathbf{U}\right)\right]\Bigg)\Bigg]\end{aligned} \tag{4.18}$$

Expanding Equation 4.18 leads to Equation 4.19.

$$\begin{aligned}\frac{\partial g_k^{LKS}}{\partial \rho_{(i)}} = \frac{1}{\sum_{j\in\Omega_k}\exp\left(\mu(\bar{g}_{(j)} - \bar{g}_{\max})\right)} \Bigg(\sum_{j\in\Omega_k}\exp\left(\mu(\bar{g}_{(j)} - \bar{g}_{\max})\right)\Bigg[\delta_{ij}g_{(j)} \\ + \rho_{(j)}\frac{1}{\sigma^Y}\left(\frac{1}{\sigma^{VM}_{(j)}}[V]\boldsymbol{\sigma}^{micro}_{(j)}\right)^T \frac{\partial(\rho^r_{(j)}[Q_{0_{(j)}}])}{\partial \rho_{(i)}}[B]\mathbf{U}_{(j)}\Bigg] \\ - \sum_{j\in\Omega_k}\exp\left(\mu(\bar{g}_{(j)} - \bar{g}_{\max})\right)\rho_{(j)}\frac{1}{\sigma^Y}\left(\frac{1}{\sigma^{VM}_{(j)}}[V]\boldsymbol{\sigma}^{micro}_{(j)}\right)^T \rho^r_{(j)}[Q_{0_{(j)}}][B][K]^{-1}\left(\frac{\partial [K]}{\partial \rho_{(i)}}\mathbf{U}\right)\Bigg)\end{aligned} \tag{4.19}$$

Defining $\boldsymbol{\lambda}_k^T$ as the adjoint vector and corresponding to the expression in Equation 4.20, $\boldsymbol{\lambda}_k$ can be easier computed as given in Equation 4.21, as the global stiffness matrix [K] is symmetric. Equation 4.21 is known as the adjoint system, and decreases the computational cost of the gradient analysis, as it does only need to be calculated once for each constraint, regardless of the amount of variables.

$$\boldsymbol{\lambda}_k^T = \sum_{j\in\Omega_k}\left[\exp\left(\mu(\bar{g}_{(j)} - \bar{g}_{\max})\right)\rho_{(j)}\frac{1}{\sigma^Y}\left(\frac{1}{\sigma^{VM}_{(j)}}[V]\boldsymbol{\sigma}^{micro}_{(j)}\right)^T \rho^r_{(j)}[Q_{0_{(j)}}][B][K]^{-1}\right] \tag{4.20}$$

$$[K]\boldsymbol{\lambda}_k = \sum_{j\in\Omega_k}\left[\exp\left(\mu(\bar{g}_{(j)} - \bar{g}_{\max})\right)\rho_{(j)}\frac{1}{\sigma^Y}[B]^T\rho^r_{(j)}[Q_{0_{(j)}}]\left(\frac{1}{\sigma^{VM}_{(j)}}[V]\boldsymbol{\sigma}^{micro}_{(j)}\right)\right] \tag{4.21}$$

Further analyzing Equation 4.19, recalling that the exponent r equals 0 from Equation 4.4, the contribution of $\frac{\partial(\rho^r_{(j)}[Q_{0_{(j)}}])}{\partial \rho_{(i)}}$ is also 0. Moreover, δ_{ij} can be taken out of the sum. Therefore, combining these two attributes and the adjoint formulation, the stress constraint and its sensibility can be summarized as shown next. This is the gradient with respect to the filtered FEM densities. To obtain the correct gradient with respect to the real optimization densities, the chain rule of Equation 3.19 must still be applied.

All gradient computations have been implemented in Python, in combination with the self-written FEM analysis as explained in Appendix B. The values of the gradient have been verified against finite difference by means of a central scheme.

Von Mises Stress Constraint Summary with Isotropic Material

Optimization constraint

$$g_k^{LKS} = \bar{g}_{\max} + \frac{1}{\mu} \ln \left[\frac{1}{N} \sum_{j \in \Omega_k} \exp \left(\mu \left[\rho_{(j)} \left(\frac{\sqrt{([Q_{0_{(j)}}][B]\boldsymbol{U}_{(j)})^T [V][Q_{0_{(j)}}][B]\boldsymbol{U}_{(j)}}}{\sigma^Y} - 1 \right) - \bar{g}_{\max} \right] \right) \right]$$

Optimization constraint gradient

$$\frac{\partial g_k^{LKS}}{\partial \rho_{(i)}} = \frac{1}{\sum_{j \in \Omega_k} \exp\left(\mu(\bar{g}_{(j)} - \bar{g}_{\max})\right)} \left[\exp\left(\mu(\bar{g}_{(i)} - \bar{g}_{\max}) g_{(i)}\right) - \boldsymbol{\lambda}_k^T \frac{\partial [K]}{\partial \rho_{(i)}} \mathbf{U} \right]$$

Adjoint vector

$$[K]\boldsymbol{\lambda}_k = \sum_{j \in \Omega_k} \left[\exp\left(\mu(\bar{g}_{(j)} - \bar{g}_{\max})\right) \rho_{(j)} \frac{1}{\sigma^Y} [B]^T [Q_{0_{(j)}}] \left(\frac{1}{\sigma_{(j)}^{VM}} [V] \boldsymbol{\sigma}_{(j)}^{micro} \right) \right]$$

4.3 Elliptic Failure Criterion for a Combined Density and Orthotropic Material Orientation Optimization

This section presents the method to consider failure for an orthotropic material, where the anisotropic stiffness variation is only considered by means of the material orientation. This corresponds to having fixed η_0 and η_1 values, and only ϕ_1 is optimized along the density ρ for each element. For such an orthotropic material, the strength integration must be characterized differently for topology optimization than in case of an isotropic material of Section 4.2. This involves two major differences. First, failure must be defined by the correct measure for an elliptic envelope. This failure measure can then be used to incorporate strength constrain in the optimization. Secondly, the correct gradient must be obtained with respect to both the density and the additional orientation variable. The next sections shows how including an additional variable does not change the overall derivation as given in the previous section.

4.3.1 Elliptic Failure Criteria

Whereas a Von Mises criterion is well suited to consider failure for an isotropic material, it can not represent the behavior of an anisotropic one. When focusing on a UD composite material more specifically, failure is well characterized by an anisotropic elliptic failure envelope [129]. The Tsai-Wu failure criterion given in Equation 4.22 is the most widely used of such elliptic envelopes. X_t and X_c are respectively the magnitude of the tensile and compressive strength allowables along the fiber direction, whereas Y_t and Y_c are the ones in the transverse direction. S is the shear allowable. σ_1, σ_2 and τ_{12} are the stresses expressed in the ply's reference frame.

$$\frac{\sigma_1^2}{X_t X_c} + \frac{\sigma_2^2}{Y_t Y_c} - \sqrt{\frac{1}{X_t X_c} \frac{1}{Y_t Y_c}} \sigma_1 \sigma_2 + \left(\frac{1}{X_t} - \frac{1}{X_c} \right) \sigma_1 + \left(\frac{1}{Y_t} - \frac{1}{Y_c} \right) \sigma_2 + \frac{\tau_{12}}{S^2} \leq 1 \tag{4.22}$$

The failure envelope of Equation 4.22 can be written in a compact form as given in Equation 4.23, which is easier to use in the subsequent derivation. The general definition of the quadratic failure matrix F and linear failure matrix G components are given in Equation 4.24. The specific definition of these matrices for the Tsai-Wu failure criterion are listed in Equation 4.25. F^*_{12} is a stress state dependent factor, which is taken as -0.5 in case of Tsai-Wu.

$$\sigma^T[F]\sigma + \sigma^T \boldsymbol{G} \leq 1 \tag{4.23}$$

$$[F] = \begin{bmatrix} F_{11} & F_{12} & F_{13} \\ F_{12} & F_{22} & F_{23} \\ F_{13} & F_{23} & F_{33} \end{bmatrix} ; \boldsymbol{G} = \begin{Bmatrix} G_1 \\ G_2 \\ G_3 \end{Bmatrix} \tag{4.24}$$

$$[F] = \begin{bmatrix} \frac{1}{X_t X_c} & \frac{F^*_{12}}{\sqrt{X_t X_c Y_t Y_c}} & 0 \\ \frac{F^*_{12}}{\sqrt{X_t X_c Y_t Y_c}} & \frac{1}{Y_t Y_c} & 0 \\ 0 & 0 & \frac{1}{S^2} \end{bmatrix} ; \boldsymbol{G} = \begin{Bmatrix} \frac{X_c - X_t}{X_c X_t} \\ \frac{Y_c - Y_t}{Y_c Y_t} \\ 0 \end{Bmatrix} \tag{4.25}$$

The matrix system can equally be set up for other types of elliptic failure criteria. The Tsai-Hill failure criterion matrix components are given in Equation 4.26, whereas the components for the Hoffman failure criterion are given in Equation 4.27 [158]. The Tsai-Hill criterion does not differentiate between tensile and compressive allowables.

$$[F] = \begin{bmatrix} \frac{1}{X^2} & -\frac{1}{2X^2} & 0 \\ -\frac{1}{2X^2} & \frac{1}{Y^2} & 0 \\ 0 & 0 & \frac{1}{S^2} \end{bmatrix} ; \boldsymbol{G} = \{0\} \tag{4.26}$$

$$[F] = \begin{bmatrix} \frac{1}{X_t X_c} & -\frac{1}{2X_t X_c} & 0 \\ -\frac{1}{2X_t X_c} & \frac{1}{Y_t Y_c} & 0 \\ 0 & 0 & \frac{1}{S^2} \end{bmatrix} ; \boldsymbol{G} = \begin{Bmatrix} \frac{X_c - X_t}{X_c X_t} \\ \frac{Y_c - Y_t}{Y_c Y_t} \\ 0 \end{Bmatrix} \tag{4.27}$$

A representation in the σ_1-σ_2 and $\sigma_2 - \tau_{12}$ material reference plane of the different failure envelope for the allowables listed in Table 4.1 is shown in Figure 4.3. The Tsai-Hill X and Y allowables are taken as X_t and Y_t respectively.

Table 4.1: Material strength properties for different failure criteria ($E_{11} = 39$ GPa, $E_{22} = 8.4$ GPa, $G_{12} = 4.2$ GPa, $\nu_{12} = 0.26$) [8].

	X [MPa]	Y [MPa]	S [MPa]	X_t [MPa]	X_c [MPa]	Y_t [MPa]	Y_c [MPa]	F^*_{12} [-]
Tsai-Hill	1062.0	31.0	72.0	-	-	-	-	-
Hoffman	-	-	72.0	1062.0	610.0	31.0	118.0	-
Tsai-Wu	-	-	72.0	1062.0	610.0	31.0	118.0	-0.5

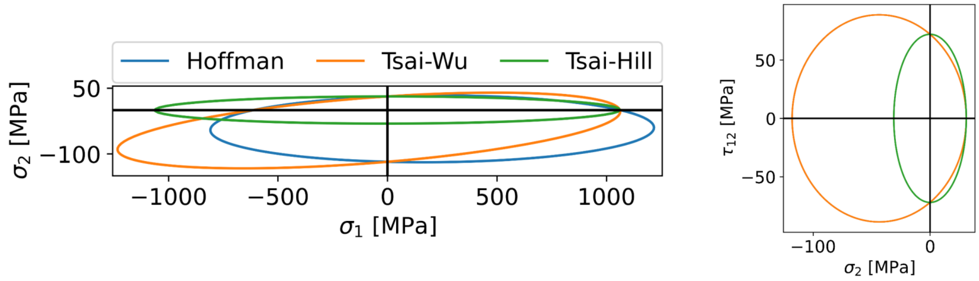

Figure 4.3: Tsai-Wu, Tsai-Hill and Hoffman elliptic failure criteria envelope in the $\sigma_1 - \sigma_2$ and $\sigma_2 - \tau_{12}$ material reference plane for the properties of Table 4.1.

The components of the matrices of Equation 4.25 can also be expressed by means of the polar formalism [158]. As the matrix representation of Equation 4.25 is expressed in the Voigt basis, the relation to the tensor components are expressed by Equation 4.28 and 4.29 respectively [158, 194].

$$F_{11} = F_{xxxx}; F_{13} = 2F_{xxxy}; F_{12} = F_{xxyy}; F_{33} = 4F_{xyxy}; F_{23} = 2F_{xyyy}; F_{22} = F_{yyyy} \tag{4.28}$$

$$G_1 = G_{xx}; G_2 = G_{yy}; G_3 = 2G_{xy} \tag{4.29}$$

The polar invariants γ_0, γ_1, λ_0, λ_1, l and the orientation ω_1 are then obtained according to Equation 4.30. These are the counterparts and have the same significance as T_0, T_1, R_0, R_1, K and ϕ_1 for the stiffness properties, as discussed in Section 2.5.

$$\begin{array}{rcllllll}
8\gamma_0 & = & F_{1111} & & - \ 2F_{1122} & + \ 4F_{1212} & & + \ F_{2222} \\
8\gamma_1 & = & F_{1111} & & + \ 2F_{1122} & & & + \ F_{2222} \\
8\lambda_0 e^{4i\omega_0} & = & F_{1111} & + \ 4iF_{1112} & - \ 2F_{1122} & - \ 4F_{1212} & - \ 4iF_{1222} & + \ F_{2222} \\
8\lambda_1 e^{2i\omega_1} & = & F_{1111} & + \ 2iF_{1112} & & & + \ 2iF_{1222} & + \ F_{2222}
\end{array} \tag{4.30}$$

In case of the linear matrix G, the invariants γ and λ, and the orientation ω are obtained as detailed in Equation 4.31.

$$\begin{aligned}
\gamma &= \frac{G_1 + G_2}{2} \\
\lambda e^{2i\omega} &= \frac{G_1 - G_2}{2} + iG_3
\end{aligned} \tag{4.31}$$

As the name indicates, all the invariants (γ, γ_0, γ_1, λ, λ_0, λ_1, l) are fixed for a given failure criteria, regardless of the reference frame. This property of the polar parametrization allows for an easy rotation of the allowables. Indeed, the failure criterion in Equation 4.25- 4.26 are computed in the local material/ply reference frame, where the stresses have been rotated in the same coordinate system. In the topology optimization routine, the stress of Equation 4.2 is calculated at each centroid in the global coordinate system. Therefore, either the stress or the allowables must be rotated to be expressed in the same reference frame. It is chosen to rotate the allowables, as the polar formalism allows to do this easily with a rotation angle equal to the material stiffness orientation ϕ_1, according to Equation 4.32 and Equation 4.33.

$$\begin{array}{rcllll}
F_{xxxx} & = & \gamma_0 & + \ 2\gamma_1 & + \ (-1)^l\lambda_0 \cos 4(\omega_1 + \phi_1) & + \ 4\lambda_1 \cos 2(\omega_1 + \phi_1) \\
F_{xxyy} & = & -\gamma_0 & + \ 2\gamma_1 & - \ (-1)^l\lambda_0 \cos 4(\omega_1 + \phi_1) & \\
F_{xxxy} & = & & & (-1)^l\lambda_0 \sin 4(\omega_1 + \phi_1) & + \ 2\lambda_1 \sin 2(\omega_1 + \phi_1) \\
F_{yyyy} & = & \gamma_0 & + \ 2\gamma_1 & + \ (-1)^l\lambda_0 \cos 4(\omega_1 + \phi_1) & - \ 4\lambda_1 \cos 2(\omega_1 + \phi_1) \\
F_{yyxy} & = & & & - \ (-1)^l\lambda_0 \cos 4(\omega_1 + \phi_1) & + \ 4\lambda_1 \sin 2(\omega_1 + \phi_1) \\
F_{xyxy} & = & \gamma_0 & & - \ (-1)^l\lambda_0 \cos 4(\omega_1 + \phi_1) &
\end{array} \tag{4.32}$$

$$\begin{array}{rcl}
G_{xx} & = & \gamma + \lambda \cos 2(\omega + \phi_1) \\
G_{yy} & = & \gamma - \lambda \cos 2(\omega + \phi_1) \\
G_{xy} & = & \lambda \sin 2(\omega + \phi_1)
\end{array} \tag{4.33}$$

4.3.2 Optimization Constraint Definition

Now that the elliptic failure criteria can be computed with quantities expressed in the same coordinate system, the failure measure can be computed. The overall procedure and reasoning of Section 4.2.1 are kept, especially considering the micro-stress definition. Only the specific parts concerning orthotropic failure are discussed in this section. The failure measure for an elliptic failure envelope is obtained by considering the safety factor s_1 of Equation 4.23, as expressed in Equation 4.34. The stresses used are still the ones obtained from Equation 4.4.

$$s_{1_{(i)}}^2 (\boldsymbol{\sigma}_{(i)}^{micro})^T [F(\phi_{1_{(i)}})] \boldsymbol{\sigma}_{(i)}^{micro} + s_{1_{(i)}} (\boldsymbol{\sigma}_{(i)}^{micro})^T \boldsymbol{G}(\phi_{1_{(i)}}) - 1 = 0 \tag{4.34}$$

The value of the safety factor $s_{1_{(i)}}$ is the positive root of Equation 4.34, as given by Equation 4.35. It is the multiplier by which the stress state must be multiplied to attain failure. A value of $s_{1_{(i)}} \geq 1$ means the current stress state remains within the feasible envelope and satisfies Equation 4.23. On the other hand, a value of $s_{1_{(i)}} < 1$ indicates failure (the stress state should be lowered). Equation 4.35 is what is called $fail_m$ in Equation 4.13.

$$fail_{m_{(i)}} := s_{1_{(i)}} = \frac{-B_{(i)} + \sqrt{B_{(i)}^2 + 4A_{(i)}}}{2A_{(i)}} \tag{4.35}$$
$$\text{with} \quad A_{(i)} = (\boldsymbol{\sigma}_{(i)}^{micro})^T [F(\phi_{1_{(i)}})] \boldsymbol{\sigma}_{(i)}^{micro} \quad \text{and} \quad B_{(i)} = (\boldsymbol{\sigma}_{(i)}^{micro})^T \boldsymbol{G}(\phi_{1_{(i)}})$$

As noted [157] and then also implemented [6, 12, 159, 168, 170] in literature, performing optimizations directly with $s_{1_{(i)}}$ would lead to load-dependent solutions. Instead, to circumvent this characteristic, it is better to use the inverse of the safety factor $s_{1_{(i)}}$ to define the failure constraint. Therefore, the local constraint $g_{(i)}$ can be expressed as given in Equation 4.36.

Moreover, using the inverse of the safety factor, the failure index, has an advantage for topology optimization. If an element has a low stress state, its safety factor would be high, meaning the aggregation would run into numerical overflow and be impossible to compute. If, on the other hand, the failure index is used in the aggregation, not only is this problem reversed, with values remaining acceptable, but furthermore, the correct elements are directly being tracked in the aggregation. Indeed, the lower KS function approximates the maximum of the provided values, meaning the aggregated value is then linked to the critical element whose stress state satisfies least the failure criteria.

$$g_{(i)} := \frac{1}{s_{1_{(i)}}} - 1 \leq 0 \tag{4.36}$$

Furthermore, the MPVC strategy is still used. Therefore, the local constraint $g_{(i)}$ of Equation 4.36 is further used to defined $\bar{g}_i$, accordingly to Equation 4.8. Lastly, the aggregated global failure constraint g_k^{LKS} is obtained by using the lower KS function of Equation 4.9 with the MPVC constraint $\bar{g}_i$. The constraint is given in Equation 4.37 and an overview of the procedure to obtain it in shown in Figure 4.4.

$$g_k^{LKS} = \bar{g}_{\max} + \frac{1}{\mu} \ln \left[\frac{1}{N} \sum_{j \in \Omega_k} \exp \left(\mu \right.\right.$$
$$\left.\left. \left[\rho_{(j)} \left(\frac{2(\boldsymbol{\sigma}_{(j)}^{micro})^T [F(\phi_1)] \boldsymbol{\sigma}_{(j)}^{micro}}{-(\boldsymbol{\sigma}_{(j)}^{micro})^T \boldsymbol{G}(\phi_1) + \sqrt{((\boldsymbol{\sigma}_{(j)}^{micro})^T \boldsymbol{G}(\phi_1))^2 + 4(\boldsymbol{\sigma}_{(j)}^{micro})^T [F(\phi_1)] \boldsymbol{\sigma}_{(j)}^{micro}}} - 1 \right) - \bar{g}_{\max} \right] \right) \right] \tag{4.37}$$

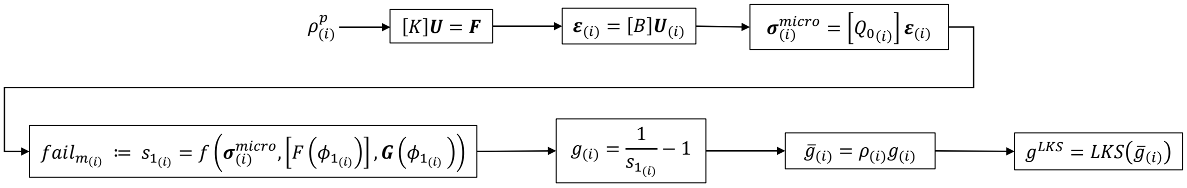

Figure 4.4: Numerical steps used to obtain the global failure optimization constraint for an elliptic failure criterion with an anisotropic material.

4.3.3 Optimization Constraint Gradient

Gradient With Respect to Density

The starting point for the derivation of an elliptic failure criteria with respect to the density variable are Equation 4.38 and Equation 4.39, repeated from Section 4.2.2.

$$\begin{aligned}\frac{\partial g_k^{LKS}}{\partial \rho_{(i)}} = {} & \frac{1}{\sum_{j\in\Omega_k} \exp\left(\mu(\bar{g}_{(j)} - \bar{g}_{\max})\right)} \left(\sum_{j\in\Omega_k} \exp\left(\mu(\bar{g}_{(j)} - \bar{g}_{\max})\right) \left[\frac{\partial \rho_{(j)}}{\partial \rho_{(i)}} g_{(j)} \right.\right. \\ & \left.\left. + \, \rho_{(j)} \frac{\partial g_{(j)}}{\partial fail_{m_{(j)}}} \left(\frac{\partial fail_{m_{(j)}}}{\partial \boldsymbol{\sigma}^{micro}_{(j)}} \right)^T \frac{\partial(\rho^r_{(j)}[Q_{0_{(j)}}])}{\partial \rho_{(i)}} [B]\mathbf{U}_{(j)} \right] - \boldsymbol{\lambda}_k^T \left(\frac{\partial [K]}{\partial \rho_{(i)}} \mathbf{U} \right) \right)\end{aligned} \tag{4.38}$$

$$[K]\boldsymbol{\lambda}_k = \sum_{j\in\Omega_k} \left[\exp\left(\mu(\bar{g}_{(j)} - \bar{g}_{\max})\right) \rho_{(j)} \frac{\partial g_{(j)}}{\partial fail_{m_{(j)}}} [B]^T \rho^r_{(j)} [Q_{0_{(j)}}] \left(\frac{\partial fail_{m_{(j)}}}{\partial \boldsymbol{\sigma}^{micro}_{(j)}} \right) \right] \tag{4.39}$$

The partial derivative $\frac{\partial g_{(j)}}{\partial fail_{m_{(j)}}}$ in case of an elliptic failure criteria is replaced with its adequate expression, obtained in Equation 4.40 from Equation 4.36.

$$\frac{\partial g_{(j)}}{\partial fail_{m_{(j)}}} := \frac{\partial}{\partial s_{1_{(j)}}} \left(\frac{1}{s_{1_{(j)}}} - 1 \right) = \frac{-1}{s^2_{1_{(j)}}} \tag{4.40}$$

To take into account the correct definition of $fail_{m_{(j)}}$, and its partial derivative $\frac{\partial fail_{m_{(j)}}}{\partial \boldsymbol{\sigma}^{micro}_{(j)}}$, in case of an elliptic failure criteria, first the chain rule of $\frac{\partial fail_{m_{(j)}}}{\partial \rho_{(i)}}$ is computed to shown, and being equivalent to the isotropic case of Equation 4.13. From the definition in Equation 4.35, Equation 4.41 is obtained.

$$\frac{\partial fail_{m_{(j)}}}{\partial \rho_{(i)}} := \frac{\partial s_{1_{(j)}}}{\partial \rho_{(i)}} = \frac{\partial s_{1_{(j)}}}{\partial \boldsymbol{\sigma}^{micro}_{(j)}} \frac{\partial \boldsymbol{\sigma}^{micro}_{(j)}}{\partial \rho_{(i)}} \tag{4.41}$$

Therefore $\frac{\partial fail_{m_{(i)}}}{\partial \boldsymbol{\sigma}^{micro}_{(j)}}$ equals to $\frac{\partial s_{1_{(i)}}}{\partial \boldsymbol{\sigma}^{micro}_{(j)}}$. This expression is a vector, as it provides the derivatives with respect to the 3 stress components. It is obtained by means of the following steps. Using the chain rule on Equation 4.35 results in Equation 4.42.

$$\begin{aligned} \frac{\partial s_1}{\partial \sigma_x^{micro}} &= \frac{\partial s_1}{\partial A} \frac{\partial A}{\partial \sigma_x^{micro}} + \frac{\partial s_1}{\partial B} \frac{\partial B}{\partial \sigma_x} \\ \frac{\partial s_1}{\partial \sigma_y^{micro}} &= \frac{\partial s_1}{\partial A} \frac{\partial A}{\partial \sigma_y^{micro}} + \frac{\partial s_1}{\partial B} \frac{\partial B}{\partial \sigma_y^{micro}} \\ \frac{\partial s_1}{\partial \sigma_{xy}^{micro}} &= \frac{\partial s_1}{\partial A} \frac{\partial A}{\partial \tau_{xy}^{micro}} + \frac{\partial s_1}{\partial B} \frac{\partial B}{\partial \tau_{xy}^{micro}} \end{aligned} \tag{4.42}$$

The partials derivatives with respect to the quadratic components A and B are obtained as shown in Equation 4.43.

$$\begin{aligned} \frac{\partial s_1}{\partial A} &= \frac{\frac{4A}{\sqrt{B^2+4A}} - 2\left(-B + \sqrt{B^2+4A}\right)}{4A^2} \\ \frac{\partial s_1}{\partial B} &= \frac{1}{2A} \left(-1 + \frac{B}{\sqrt{B^2+4A}} \right) \end{aligned} \tag{4.43}$$

The partial derivatives of the quadratic components with respect to the micro-stress are then obtained as given in Equation 4.44.

$$\begin{aligned} \frac{\partial A}{\partial \sigma_x^{micro}} = 2\sigma_x^{micro}F_{11} + 2F_{12}\sigma_y^{micro};\ \frac{\partial A}{\partial \sigma_y^{micro}} = 2\sigma_y^{micro}F_{22} + 2F_{12}\sigma_x^{micro};\ \frac{\partial A}{\partial \tau_{xy}^{micro}} = 2\tau_{xy}^{micro}F_{66} \\ \frac{\partial B}{\partial \sigma_x^{micro}} = F_1;\ \frac{\partial B}{\partial \sigma_y^{micro}} = F_2;\ \frac{\partial B}{\partial \tau_{xy}^{micro}} = 0 \end{aligned} \tag{4.44}$$

Once the values of Equation 4.43 and Equation 4.44 are obtained, they are assembled in a vector according to Equation 4.42 to obtain $\frac{\partial fail_{m_{(j)}}}{\partial \boldsymbol{\sigma}_{(j)}}$. Then combining it with Equations 4.38, 4.39 and 4.40, and furthermore considering that r is still taken as 0, the gradient of an elliptic failure criteria with respect to the density is given by Equation 4.45 and the adjoint vector of Equation 4.46. Again, this is the gradient with respect to the filtered FEM densities. To obtain the correct gradient with respect to the real optimization densities, the chain rule of Equation 3.19 must still be applied.

$$\frac{\partial g_k^{LKS}}{\partial \rho_i} = \frac{1}{\sum_{j\in\Omega_k} \exp\left(\mu(\bar{g}_{(j)} - \bar{g}_{\max})\right)}\left[\exp\left(\mu(\bar{g}_{(i)} - \bar{g}_{\max})\right) - \boldsymbol{\lambda}_k^T \frac{\partial [K]}{\partial \rho_{(i)}}\mathbf{U}\right] \tag{4.45}$$

$$[K]\boldsymbol{\lambda}_k = \sum_{j\in\Omega_k}\left[\exp\left(\mu(\bar{g}_{(j)} - \bar{g}_{\max})\right)\rho_{(j)}\left(\frac{-1}{s_{1_{(j)}}^2}\right)[B]^T\rho_{(j)}^r[Q_{0_{(j)}}]\left(\frac{\partial s_{1_{(j)}}}{\partial \boldsymbol{\sigma}_{(j)}^{micro}}\right)\right] \tag{4.46}$$

Gradient With Respect to the Material Orientation

To obtain the orientation gradient, the partial derivative of $\bar{g}$ in Equation 4.12 must first be adjusted. This is expressed in Equation 4.47.

$$\frac{\partial \bar{g}_{(j)}}{\partial \phi_{1_{(i)}}} = \rho_{(j)}\frac{\partial g_{(j)}}{\partial fail_{m_{(j)}}}\frac{\partial fail_{m_{(j)}}}{\partial \phi_{1_{(i)}}} \tag{4.47}$$

where the last part is given by Equation 4.48.

$$\frac{\partial fail_{m_{(j)}}}{\partial \phi_{1_{(i)}}} := \frac{\partial s_{1_{(j)}}}{\partial \phi_{1_{(i)}}} = \frac{\partial s_{1_{(j)}}}{\partial \boldsymbol{\sigma}_{(j)}^{micro}}\frac{\partial \boldsymbol{\sigma}_{(j)}^{micro}}{\partial \phi_{1_{(i)}}} + \frac{\partial s_{1_{(j)}}}{\partial [F_{(j)}]}\frac{\partial [F_{(j)}]}{\partial \phi_{1_{(i)}}} + \frac{\partial s_{1_{(j)}}}{\partial \boldsymbol{G}_{(j)}}\frac{\partial \boldsymbol{G}_{(j)}}{\partial \phi_{1_{(i)}}} \tag{4.48}$$

This entails two facts. The first one comes from Equation 4.47, where the first term of Equation 4.13 is not present anymore, meaning there is also no more δ_{ij} dependency in the subsequent gradient (such as in Equation 4.18). Secondly, $[F]$ and $\boldsymbol{G}$ contain the failure allowables expressed in the global reference frame. These are rotated with respect to the local material frame, by means of ϕ_1, as explained in Section 4.3.1. Therefore, this rotation effect on $[F]$ and $\boldsymbol{G}$ must also be accounted for in the gradient. This is the influence of the last 2 terms in Equation 4.48. In the first term, the first factor $\frac{\partial s_{1_{(j)}}}{\partial \boldsymbol{\sigma}_{(j)}^{micro}}$ does remain the same as Equation 4.42. The second factor, $\frac{\partial \boldsymbol{\sigma}_{(j)}^{micro}}{\partial \phi_{1_{(i)}}}$, given in Equation 4.49, is obtained similarly to Equation 4.16, with the substitution of Equation 4.17.

$$\frac{\partial \boldsymbol{\sigma}_{(j)}^{micro}}{\partial \phi_{1_{(i)}}} = \frac{\partial}{\partial \phi_{1_{(i)}}}\left(\rho_{(j)}^r[Q_{0_{(j)}}][B]\boldsymbol{U}\right) = \frac{\partial(\rho_{(j)}^r[Q_{0_{(j)}}])}{\partial \phi_{1_{(i)}}}[B]\boldsymbol{U} - \rho_{(j)}^r[Q_{0_{(j)}}][B][K]^{-1}\left(\frac{\partial [K]}{\partial \phi_{1_{(i)}}}\boldsymbol{U}\right) \tag{4.49}$$

The terms of Equation 4.50 have been obtained by means of a central difference scheme.

$$
\begin{aligned}
\frac{\partial s_{1_{(j)}}}{\partial [F_{(j)}]}\frac{\partial [F_{(j)}]}{\partial \phi_{1_{(i)}}} &\approx \frac{s_{1_{(j)}}([F_{(j)}(\phi_{1_{(i)}}+\Delta\phi_1)])-s_{1_{(j)}}([F_{(j)}(\phi_{1_{(i)}}-\Delta\phi_1)])}{2\Delta\phi_1}\\
\frac{\partial s_{1_{(j)}}}{\partial \boldsymbol{G}_{(j)}}\frac{\partial \boldsymbol{G}_{(j)}}{\partial \phi_{1_{(i)}}} &\approx \frac{s_{1_{(j)}}(\boldsymbol{G}_{(j)}(\phi_{1_{(i)}}+\Delta\phi_1))-s_{1_{(j)}}(\boldsymbol{G}_{(j)}(\phi_{1_{(i)}}-\Delta\phi_1))}{2\Delta\phi_1}
\end{aligned}
\tag{4.50}
$$

Combining Equation 4.47-4.50 in Equation 4.12, Equation 4.51 is obtained.

$$
\begin{aligned}
\frac{\partial g_k^{LKS}}{\partial \phi_{1_{(i)}}} = \frac{1}{\sum_{j\in\Omega_k}\exp\left(\mu(\bar{g}_{(j)}-\bar{g}_{\max})\right)} \Bigg(\sum_{j\in\Omega_k}\exp\left(\mu(\bar{g}_{(j)}-\bar{g}_{\max})\right)\Bigg[\rho_{(j)}\frac{\partial g_{(j)}}{\partial fail_{m_{(j)}}}\Bigg(\Bigg(\frac{\partial fail_{m_{(j)}}}{\partial \boldsymbol{\sigma}_{(j)}^{micro}}\Bigg)^T \\
\frac{\partial(\rho_{(j)}^r[Q_{0_{(j)}}])}{\partial \phi_{1_{(i)}}}[B]\mathbf{U} + \frac{\partial s_{1_{(j)}}}{\partial F_{(j)}}\frac{\partial F_{(j)}}{\partial \phi_{1_{(i)}}} + \frac{\partial s_{1_{(j)}}}{\partial \boldsymbol{G}_{(j)}}\frac{\partial \boldsymbol{G}_{(j)}}{\partial \phi_{1_{(i)}}}\Bigg)\Bigg] - \boldsymbol{\lambda}_k^T\Bigg(\frac{\partial [K]}{\partial \phi_{1_{(i)}}}\mathbf{U}\Bigg)\Bigg)
\end{aligned}
\tag{4.51}
$$

Again, an adjoint vector can be defined as given in Equation 4.53, resulting in Equation 4.52.

$$
\begin{aligned}
\frac{\partial g_k^{LKS}}{\partial \phi_{1_{(i)}}} = \frac{1}{\sum_{j\in\Omega_k}\exp\left(\mu(\bar{g}_{(j)}-\bar{g}_{\max})\right)} \Bigg(\sum_{j\in\Omega_k}\exp\left(\mu(\bar{g}_{(j)}-\bar{g}_{\max})\right)\Bigg[\rho_{(j)}\left(\frac{-1}{s_{1_{(j)}}^2}\right)\Bigg(\Bigg(\frac{\partial fail_{m_{(j)}}}{\partial \boldsymbol{\sigma}_{(j)}^{micro}}\Bigg)^T \\
\frac{\partial([Q_{0_{(j)}}])}{\partial \phi_{1_{(i)}}}B\mathbf{U} + \frac{\partial s_{1_{(j)}}}{\partial [F_{(j)}]}\frac{\partial [F_{(j)}]}{\partial \phi_{1_{(i)}}} + \frac{\partial s_{1_{(j)}}}{\partial \boldsymbol{G}_{(j)}}\frac{\partial \boldsymbol{G}_{(j)}}{\partial \phi_{1_{(i)}}}\Bigg)\Bigg] - \boldsymbol{\lambda}_k^T\Bigg(\frac{\partial [K]}{\partial \phi_{1_{(i)}}}\mathbf{U}\Bigg)\Bigg)
\end{aligned}
\tag{4.52}
$$

$$
[K]\boldsymbol{\lambda}_k = \sum_{j\in\Omega_k}\left[\exp\left(\mu(\bar{g}_{(j)}-\bar{g}_{\max})\right)\rho_{(j)}\left(\frac{-1}{s_{1_{(j)}}^2}\right)[B]^T\rho_{(j)}^r[Q_{0_{(j)}}]\left(\frac{\partial s_{1_{(j)}}}{\partial \boldsymbol{\sigma}_{(j)}^{micro}}\right)\right]
\tag{4.53}
$$

It can be seen that the adjoint vector in Equation 4.53 is the same as the one in Equation 4.46 for the gradient with respect to the density, meaning that just one linear problem must be solved per constraint with the adjoint term, regardless of the number (and type) of variables.

Finally, the optimization constrain and its gradients with respect to the density ρ and material orientation ϕ_1 can be summarized as given next, knowing that r equals 0 from the previous equations.

Elliptic Failure Criterion Constraint Summary with Anisotropic Material

Optimization constraint

$$
\begin{aligned}
g_k^{LKS} = \bar{g}_{\max} + \frac{1}{\mu}\ln\Bigg[\frac{1}{N}\sum_{j\in\Omega_k}\exp\Bigg(\mu \\
\Bigg[\rho_{(j)}\Bigg(\frac{2(\boldsymbol{\sigma}_{(j)}^{micro})^T[F(\phi_1)]\boldsymbol{\sigma}_{(j)}^{micro}}{-(\boldsymbol{\sigma}_{(j)}^{micro})^T\boldsymbol{G}(\phi_1)+\sqrt{((\boldsymbol{\sigma}_{(j)}^{micro})^T\boldsymbol{G}(\phi_1))^2+4(\boldsymbol{\sigma}_{(j)}^{micro})^T[F(\phi_1)]\boldsymbol{\sigma}_{(j)}^{micro}}}-1\Bigg)-\bar{g}_{\max}\Bigg]\Bigg)\Bigg]
\end{aligned}
$$

Optimization constraint gradient

$$
\frac{\partial g_k^{LKS}}{\partial \rho_{(i)}} = \frac{1}{\sum_{j\in\Omega_k}\exp\left(\mu(\bar{g}_{(j)}-\bar{g}_{\max})\right)}\left[\exp\left(\mu(\bar{g}_{(i)}-\bar{g}_{\max})g_{(i)}\right)-\boldsymbol{\lambda}_k^T\frac{\partial [K]}{\partial \rho_{(i)}}\mathbf{U}\right]
$$

$$
\begin{aligned}
\frac{\partial g_k^{LKS}}{\partial \phi_{1_{(i)}}} = {} & \frac{1}{\sum_{j\in\Omega_k} \exp\left(\mu(\bar{g}_{(j)} - \bar{g}_{\max})\right)} \Bigg(\sum_{j\in\Omega_k} \exp\left(\mu(\bar{g}_{(j)} - \bar{g}_{\max})\right) \Bigg[\rho_{(j)} \left(\frac{-1}{s^2_{1_{(j)}}}\right) \Bigg(\left(\frac{\partial fail_{m_{(j)}}}{\partial \boldsymbol{\sigma}^{micro}_{(j)}}\right)^T \\
& \frac{\partial([Q_{0_{(j)}}])}{\partial \phi_{1_{(i)}}} B\mathbf{U} + \frac{\partial s_{1_{(j)}}}{\partial [F_{(j)}]} \frac{\partial [F_{(j)}]}{\partial \phi_{1_{(i)}}} + \frac{\partial s_{1_{(j)}}}{\partial \boldsymbol{G}_{(j)}} \frac{\partial \boldsymbol{G}_{(j)}}{\partial \phi_{1_{(i)}}} \Bigg)\Bigg)\Bigg] - \boldsymbol{\lambda}_k^T \left(\frac{\partial [K]}{\partial \phi_{1_{(i)}}} \mathbf{U} \right)\Bigg)
\end{aligned}
$$

Adjoint vector

$$
[K]\boldsymbol{\lambda}_k = \sum_{j\in\Omega_k} \left[\exp\left(\mu(\bar{g}_{(j)} - \bar{g}_{\max})\right) \rho_{(j)} \left(\frac{-1}{s^2_{1_{(j)}}}\right) [B]^T \rho^r_{(j)} [Q_{0_{(j)}}] \left(\frac{\partial s_{1_{(j)}}}{\partial \boldsymbol{\sigma}^{micro}_{(j)}} \right) \right]
$$

4.4 Towards Complex Application Cases

This small sections details the considerations that should be incorporated to the methods outlined previously to consider more complex optimization cases, not implemented here as it was not the main scope of the research. The required changes to the numerical implementation are discussed, and necessitates very few conceptual changes. The more complex application cases involve multi-loading, considering other failure criteria and switching to 3D optimizations.

4.4.1 Advanced Failure Criterion

Three different elliptic failure criteria were presented (Tsai-Wu, Tsai-Hill and Hoffman). Nonetheless, the current procedure allows to incorporate more complex failure criteria in 2D , such as presented by Li *et al.* [195], or even higher order criteria. In case of strength criteria taking into account different failure mechanisms, such as Hashin or Puck, the local constraint definition and aggregation could be done separately for each condition in the criteria. Indeed, as all the optimization constraints are satisfied at the end of the optimization, it means that each individual local constraint and condition will be satisfied, despite not having been checked in the same optimization constraint, and no failure is predicted by the strength criterion.

4.4.2 Adapting to 3D Optimization

The whole procedure outlined previously does not change if 3D elements are considered in the FEM analysis; only the shape of the matrices is altered in order to match the number of degrees of freedom and stress components for each element. For example, the [B] matrix becomes a (6,24) matrix instead of (3,8), and the failure criterion uses the full stress field (it depends on all 6 components). Also the stiffness tensor $[Q_0]$ becomes a (6,6) matrix instead of (3,3). In case of 3D anisotropy, the stiffness tensor can not be represented by the polar formalism, and requires another adequate parametrization to be efficiently used in the optimization, such as the one proposed by Ranaivomiarana for transversely isotropic material [2]. However, a 3D strength criteria can also not be defined anymore by the polar formalism, and should follow the orientation definition of the 3D anisotropy.

4.4.3 Commercial FEM Integration

If a commercial FEM software is to be used (such as MSC NASTRAN or ALTAIR OptiStruct), there are several possibilities to interface with it. The mechanical response can be obtained in each element, and post-processed according to Equation 4.54 to obtain the correct constraint based on the micros stress.

$$
\boldsymbol{\sigma}^{micro}_{(i)} = \frac{\boldsymbol{\sigma}^{FEM}_{(i)}}{\rho^p_{(i)}} \tag{4.54}
$$

However, obtaining the gradient is not as straightforward. Two options are available: use the internal scripting of a FEM software, or calculate the gradient oneself. The former option involves using the internal relation of a FEM software to compute the aggregation in the input file, which then allows the FEM software to compute the gradient afterwards. This however has the disadvantage of not knowing which method the FEM software will use to calculate the gradient, *i.e.* whether the aggregation is recognized and the adjoint formulation will be used or instead the more computational costly direct method. The latter direct approach will always be implemented in the software and obtain the gradients, as it is the most basic one, but the computation time can become prohibitive for large system (both the required amount of gradients scales with increasing the number of elements, so does the computation of one FEM analysis for a larger and more costly FEM to be solved). The other option consists in calculating the adjoint vector oneself by means of Equation 4.55. To do this, the fictive force vector on the right hand side of Equation 4.55 should be computed, and be applied to the nodes of the FEM model. The FEM analysis is then solved with the same displacement boundary conditions, and the resulting displacement vector corresponds to the adjoint vector λ_k. Nonetheless, to set up this fictive force vector, the knowledge of $[B]$, the strain-displacement matrix, is required for each type of element in the FEM implementation.

$$[K]\boldsymbol{\lambda}_k = \sum_{j \in \Omega_k} \left[\exp\left(\mu(\bar{g}_{(j)} - \bar{g}_{\max})\right) \rho_{(j)} \frac{\partial g_{(j)}}{\partial fail_{m_{(j)}}} [B]^T [Q_{0_{(j)}}] \left(\frac{\partial fail_{m_{(j)}}}{\partial \boldsymbol{\sigma}^{micro}_{(j)}} \right)^T \right] \tag{4.55}$$

Finally, once the adjoint vector is obtained, the integration rule of Equation 3.16 to obtain the elementary stiffness matrix must also be known to obtain the partial derivatives, especially with respect to the anisotropy, as this is included in the integration (see Equation 3.16).

4.4.4 Multi-Loading Optimizations

Multi loading of a structure is an inherent feature of practical engineering applications. Two major types of optimization problems can be characterized: with a load independent objective function or a load dependent one. An example of the former consists in volume minimization, whereas the latter includes compliance or a stress criterion optimization.

When the objective does not depend on the loading, multiple load cases can be used straightforwardly with this example. Indeed, each mechanical response (such as compliance, stress criterion,...) can be easily incorporated as constraint for all the individual load cases.

When the objective is load dependent, such as the compliance, all measures for the different load cases can not be minimized directly. Instead, a weighted sum approach of the different values can be used as objective. This however requires to attribute weight to each load case separately, and its importance to the final design. Alternatively, the optimization problem could be altered by using a bound formulation strategy [125, 196]. A bound formulation strategy consists in minimizing the maximum of separate values. Finally, as an example for compliance, the problem could also just be formulated as the compliance minimization for a single load case, whereas the compliance of other load cases is incorporated as constraints. All previous comments are also valid for other load dependent constraints, be it a stress criterion or other such as buckling, vibrations, etc...

4.5 Conclusion

This chapter provides the methodology to obtain the optimization constraint in case of anisotropic failure with a UD material. It considers the case where only the density and material orientation changes during the optimization (the peculiarities of an homogenized stiffness but unknown laminate layup by means of the polar parameters is discussed in Chapter 6). An anisotropic stress-based strength criterion is used to define the local element-wise strength constraint, by using the polar formalism to express the strength properties in the global reference frame depending on the local orientation of the ply. Furthermore, the relaxation and regulation techniques used with isotropic material are integrated in case of anisotropic stress-based strength. It is also shown how to obtain the gradient of the optimization constraint with respect to the density and orientation variable by using the adjoint vector. Finally, a small discussion is provided on extending the method for more practical and complex cases, such as considering multiple load cases or requiring the use of commercial FEM solver among others.

Chapter 5

Stress-Based Density and Material Orientation Topology Optimization: Applications

5.1 Introduction

This chapter is dedicated to the results of stress-based topology optimizations. First, a benchmark case with an isotropic material and strength criterion is used as verification and reference. Afterwards, anisotropic features are gradually introduced in the optimizations. The case of additive manufacturing is considered, with isotropic stiffness but anisotropic strength depending on the printing direction. Thereafter, anisotropic stiffness is used with an anisotropic strength criterion, but for fixed orientations. For all these cases, the optimization is only carried out with respect to the density variables, as the anisotropy remains constant. Lastly, topology and fiber orientations, representing a UD composite ply, are optimized with strength constraint. This is equivalent of fiber steering.

5.2 Different Problem Formulations

With the use of a gradient-based strategy and the inclusion of stress constraints in the framework of topology optimization, several problems can now be defined. The considered problems in this chapter are a volume minimization with a stress-based strength constraint (Problem 2), a volume minimization with a compliance and a stress-based strength constraint (Problem 3) and a volume minimization problem with a compliance constraint (Problem 4). Finally, the case of compliance minimization with volume and stress-based strength constraint (Problem 5) is also considered. These different formulations will be used to evaluate the effect on the optimized solution.

Following the optimizations presented in Section 3.5, C is the compliance, calculated as $\mathbf{U}^T[K]\mathbf{U}$. v_f the volume ratio of the structure, obtained as $V(\rho)/V_0$, with $V(\rho)$ the sum of all filtered densities and V_0 the volume of the design space. Finally, g_k^{LKS} is the stress constraint as defined by Equation 4.11 or Equation 4.37 depending on the material anisotropy in the optimization, for cluster k. The optimization bounds on the orientations ϕ_1 have been extended compared to the compliance minimization problem, to leave more design freedom to the optimization for these more complex problems. A normalization parameter N_0 is also used for the objective, and adapted for each problem to control the convergence of the optimization. Indeed, the optimization process may becomes divergent for certain settings. Svanberg [188] explains that the objective value should ideally be in the range $[1, 100]$. N_0 is therefore used to scale the objective value to follow this guideline. Furthermore, using this N_0 factor changes the relative magnitude of the constraint and objective values. In general, the larger the objective value is, the more the optimization will focus on improving the objective. On the other hand, a lower objective value will lead the optimization to emphasis more on satisfying the optimization constraint. This parameter will further be discussed in Section 5.5.3.

$$\begin{aligned} \min_{\boldsymbol{\rho},\boldsymbol{\phi}_1} \quad & v_f(\boldsymbol{\rho})/N_0 \\ \text{s.t.} \quad & g_k^{LKS}(\boldsymbol{\rho},\boldsymbol{\phi}_1) \leq 0 \\ & \boldsymbol{\rho} \in [\rho_{\min}, 1] \\ & \boldsymbol{\phi_1} \in [-3\pi/2, 3\pi/2] \end{aligned} \qquad \text{(Problem 2)}$$

$$\begin{aligned} \min_{\boldsymbol{\rho},\boldsymbol{\phi}_1} \quad & v_f(\boldsymbol{\rho})/N_0 \\ \text{s.t.} \quad & C(\boldsymbol{\rho},\boldsymbol{\phi}_1) \leq C_0 \\ & g_k^{LKS}(\boldsymbol{\rho},\boldsymbol{\phi}_1) \leq 0 \\ & \boldsymbol{\rho} \in [\rho_{\min}, 1] \\ & \boldsymbol{\phi_1} \in [-3\pi/2, 3\pi/2] \end{aligned} \qquad \text{(Problem 3)}$$

$$\begin{aligned} \min_{\boldsymbol{\rho},\boldsymbol{\phi}_1} \quad & v_f(\boldsymbol{\rho})/N_0 \\ \text{s.t.} \quad & C(\boldsymbol{\rho},\boldsymbol{\phi}_1) \leq C_0 \\ & \boldsymbol{\rho} \in [\rho_{\min}, 1] \\ & \boldsymbol{\phi_1} \in [-3\pi/2, 3\pi/2] \end{aligned} \qquad \text{(Problem 4)}$$

$$\begin{aligned} \min_{\boldsymbol{\rho},\boldsymbol{\phi}_1} \quad & C(\boldsymbol{\rho},\boldsymbol{\phi}_1)/N_0 \\ \text{s.t.} \quad & V(\boldsymbol{\rho})/V_0 \leq v_f \\ & g_k^{LKS}(\boldsymbol{\rho},\boldsymbol{\phi}_1) \leq 0 \\ & \boldsymbol{\rho} \in [\rho_{\min}, 1] \\ & \boldsymbol{\phi_1} \in [-3\pi/2, 3\pi/2] \end{aligned} \qquad \text{(Problem 5)}$$

All optimizations going forward will be applied on the L-bracket test case, represented in Figure 5.1. It has a mesh size of 1 × 1 mm^2, with the top face clamped. A downwards load F is distributed over the top 5 right most nodes at the force introduction location. The total load magnitude is adapted for each case, depending on the material properties. The black zone consists in 5 × 5 elements whose properties are not optimized. These 25 elements are given isotropic elastic properties, represented by T_0 and T_1, when the anisotropy is optimized in the following results. These elements are kept constant as to avoid having numerical stress concentration due to the load introduction. Furthermore, only one stress cluster k is considered in the optimization, and it consists of all elements which are optimized. The k index is therefore drop in subsequent notations for g_k^{LKS}. Depending on the optimization, a prescribed volume fraction v_f or prescribed compliance value C_0 is also used and indicated.

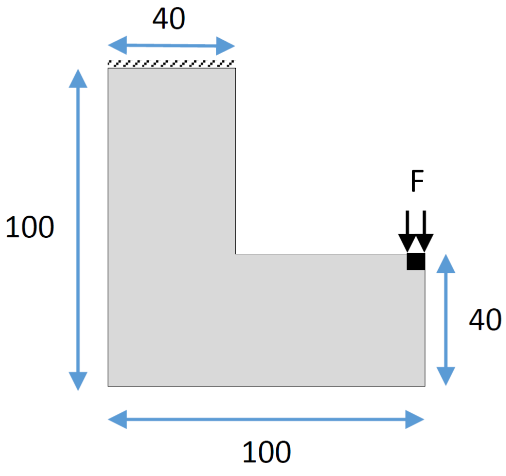

Figure 5.1: L-bracket test case representation.

MMA Parametrization for Stress Inclusion

The optimizations of Section 3.5.2 consisted in compliance minimization with a volume constraint. Both these functions behave with regularity with respect to density and anisotropic modules, and the monotonous MMA approximation turned out to be well suited in both cases. This allowed to use exploratory algorithm settings for the MMA approximation, and perform larger variable changes per iterations as the gradient retained a greater validity around the current iteration point. However, when considering stress in topology optimization, the design space is much more non-linear and therefore requires a tighter control on the approximations and variable changes as to not have a divergent optimization. This is done by using a tighter approximation validity region, and is controlled with two settings. The first option involves a direct control through the *move* setting, dictating the maximum variable change between two successive iterations. The second option has a more indirect control, and restricts the asymptotes distance. By having tighter asymptotes, a more conservative approximation is used and limits the changes. This latter option was implemented by means of external move limits, as suggested by Verbart *et al.* [5] and employed by Coniglio [197]. Concerning the orientations and its GCMMA approximation, it is not altered as by itself it is already more conservative to take into account the non-monotonous influence of the material orientation on the design criterion.

The initialization for all these optimizations starts with $\rho = 1$. All the optimization are done for a fixed 1000 iterations each, with a fixed SIMP $p = 3$ exponent. All relevant SplitMMA strategy properties are given in Table 5.1.

Table 5.1: MMA and GCMMA algorithm settings for the SplitMMA strategy with strength constraints.

	MMA ρ	GCMMA ϕ_1	MMA α & β
epsimin	10^{-10}	10^{-10}	10^{-10}
raa0	10^{-4}	0.01	10^{-4}
raa0eps	-	10^{-6}	-
move	0.5	-	0.5
external move limit	0.1	-	0.1
albefa	0.1	0.98	0.1
asyinit	0.1	0.7	0.1
asyincr	1.1	1.2	1.1
asydecr	0.8	0.6	0.8

5.3 Stress-Based Topology Optimization with Isotropic Stiffness and Strength

This first section is dedicated to the verification of the method presented in Chapter 4 and its implementation with isotropic stiffness and a Von Mises criterion. More specifically, the influence of the aggregation parameter μ on the optimized topology and maximum local strength constraint is first investigated and decided upon for the rest of the research. This is followed by a comparison of different optimization problems and the influence on the optimized solution. The settings and properties used in the following optimizations are given in Table 5.2. The mechanical properties being isotropic, the optimizations are carried out only with respect to the density variables.

5.3.1 Influence of the Aggregation Parameter μ

The influence of the aggregation parameter μ in Equation 4.11 is investigated, by performing the volume minimization of Problem 2 with values of μ equal to $10, 20, 30$ and 40. The results of these four optimizations are given in Figure 5.2. The normalization parameter N_0 is set to 25.

Table 5.2: Isotropic material properties and optimization parameters for a strength-based topology optimization.

Modules	Values	Polar parameters	Values
E [GPa]	69.7	T_0^L [GPa]	26.9
G_{12} [GPa]	26.9	T_1^L [GPa]	24.7
ν_{12} [-]	0.29	η_1^L [-] $=\eta_0^L$ [-]	0

F [N]	C_0 [mJ]	σ^Y [MPa]	R_ρ [mm]	μ [-]
200.0	25.0	45.0	2.0	30.0

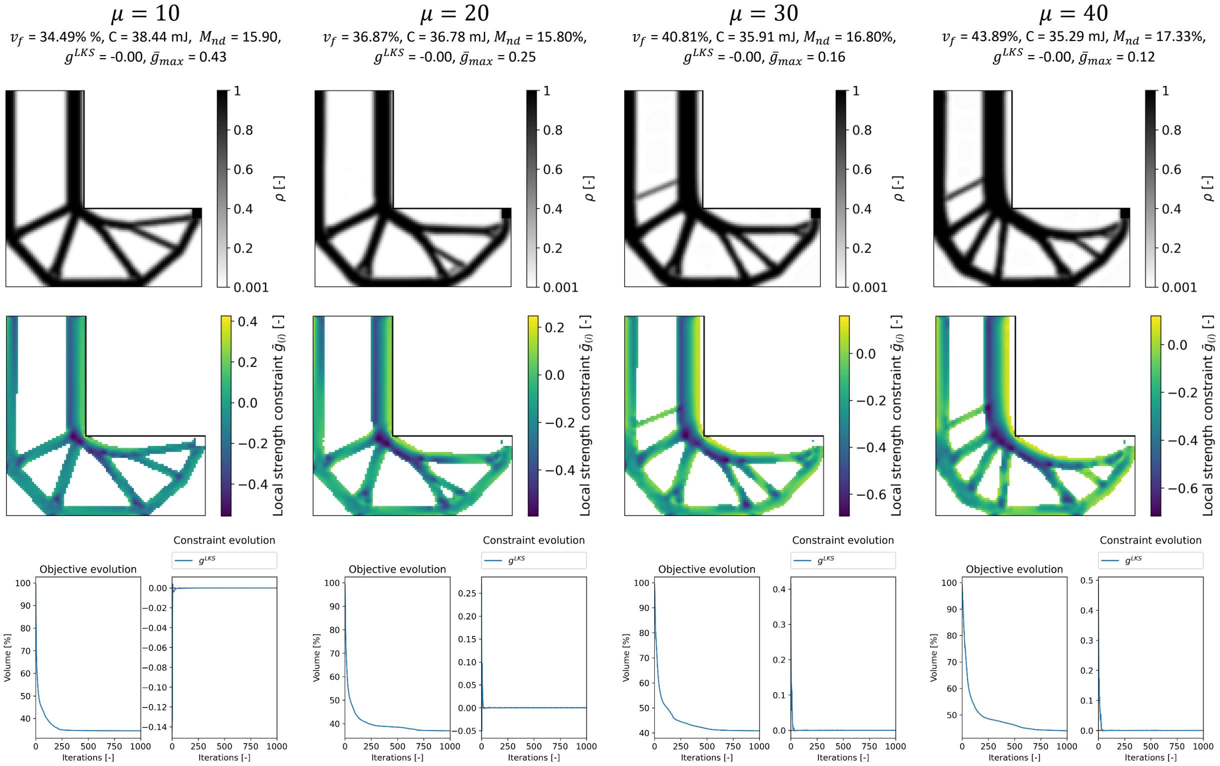

Figure 5.2: Influence of the aggregation parameter μ on stress-based topology optimization with an isotropic material and a Von Mises criterion. Information shown for optimized elements with a final density ≥ 0.3.

First looking at the convergence properties of these four optimizations, it is visible that the strength optimization constraint g^{LKS} in all four cases is satisfied. Furthermore, once the constraint is satisfied, the objective (volume) reduction happens sharply at the beginning before leveling out. The local aggregation constraint $\bar{g}_{(j)}$ is violated on the structure, as the lower KS aggregation underestimates the maximum. Nonetheless, the optimization is successful in creating a rounding at the re-entrant corner to alleviate the stress concentration, such as the results in literature as presented in Section 2.3.2.

Looking at the final properties of the four optimizations, several effects are visible due to changing the value of μ. Going from the smallest to the highest μ value optimization results, the maximum $\bar{g}_{(j)}$ decreases, dropping from 0.43 to 0.12. On the contrary, the volume increases. This can be explained by the fact that a lower μ allows for a higher stress limit, which for a given load means less material. This in turns translates to a lower total volume. Finally, all four optimizations yield solutions with features which are well solicited.

An aggregation value $\mu = 30$ is chosen to perform all subsequent optimizations which uses the lower KS. For this value, the underestimation is only about 15%, but increasing the value further does not yield substantial gains in the underestimation. Moreover, if μ is chosen too high, the approximation of the maximum becomes increasingly non-linear. Its smooth approximation tends to become non-differentiable again. This has not been experienced as an issue with the selected μ value. This μ value influences the global behavior of the topology, by creating a rounder feature at the re-entrant corner but also shifting the right vertical bar away from the domain boundary. Finally, the chosen μ value lays within the range of values recommended by Verbart *et al.* [5]. If needed, the fact that the lower KS underestimates the maximum could be addressed by using a rectifier approach, as the ones discussed in Section 2.3. Alternatively, the maximum error of an aggregation function can be related to the number of elements and aggregation parameter [6].

5.3.2 Influence of the Optimization Problem Formulation

The effect of including different optimization constraints for the minimization of the volume is investigated with isotropic stiffness. Problem 2, Problem 3 and Problem 4 are carried out only with respect to the density variable, with their results shown in Figure 5.3. The properties in Table 5.2 are still used, with an aggregation parameter $\mu = 30$, and $N_0 = 25$. For Problem 4, the algorithm settings of Table 3.4 are used. For this case, there is no need for more conservative settings as both the compliance and volume functions are regular and monotonous.

The results for these different optimization problems highlight several points. First, when volume minimization is carried out only considering compliance and not strength (Problem 4), a stress concentration at the re-entrant corner is formed. In this example, the Von Mises stress has a maximal magnitude of 109.5 MPa in an element of density 0.79, which is equivalent to $\bar{g}_{\max} = 1.13$ when evaluated with the limit of $\sigma^Y = 45$ MPa for this problem. Alternatively, only considering elements with $\rho \geq 0.95$, the highest Von Mises stress is 64.3 MPa, with an equivalent $\bar{g}_{\max} = 0.41$. As stated early, having such overshoot compared to a target stress is not wishful for practical engineering applications. It is a traditional result found in literature.

When the volume minimization is constrained with both compliance and strength (Problem 3), the overall distribution does not change. Mostly, a local radius appears at the re-entrant corner to alleviate the stress constraint. It is interesting to note that this would also be the procedure to remove stress concentration in a design office, by adding a small radius at sharp corners. Moreover, it can be noted that the structure is far from uniformly solicited. The final volume value ($v_f = 31.2\%$) is higher than the previous case, which is to account for the material redistribution at the re-entrant corner and changes to alleviate the stress constraint. The constraints are well respected and taken into account in the optimization, as displayed in the convergence graph.

Lastly, when only strength is taken account for in the volume minimization (Problem 2), a much more pronounced rounding and change in the material distribution is obtained. Furthermore, a lighter structure than in the previous two cases is obtained, be it with compliance only as outcome. It is more compliant, which is logical as the topology is not designed for stiffness, but also the lower volume which by itself already makes it less stiff. The M_{nd} is similar between the first two problems in this discussion, meaning the compliance values can be compared. On the other hand, the M_{nd} of the third problem is higher, which also worsen the comparison of compliance. This behavior of higher M_{nd} and more intermediate density elements in the optimized solution is explained partly due to the optimization problem formulation, but also to the lack of compliance consideration in the optimization: the SIMP interpolation with $p > 1$ indeed penalizes interme-

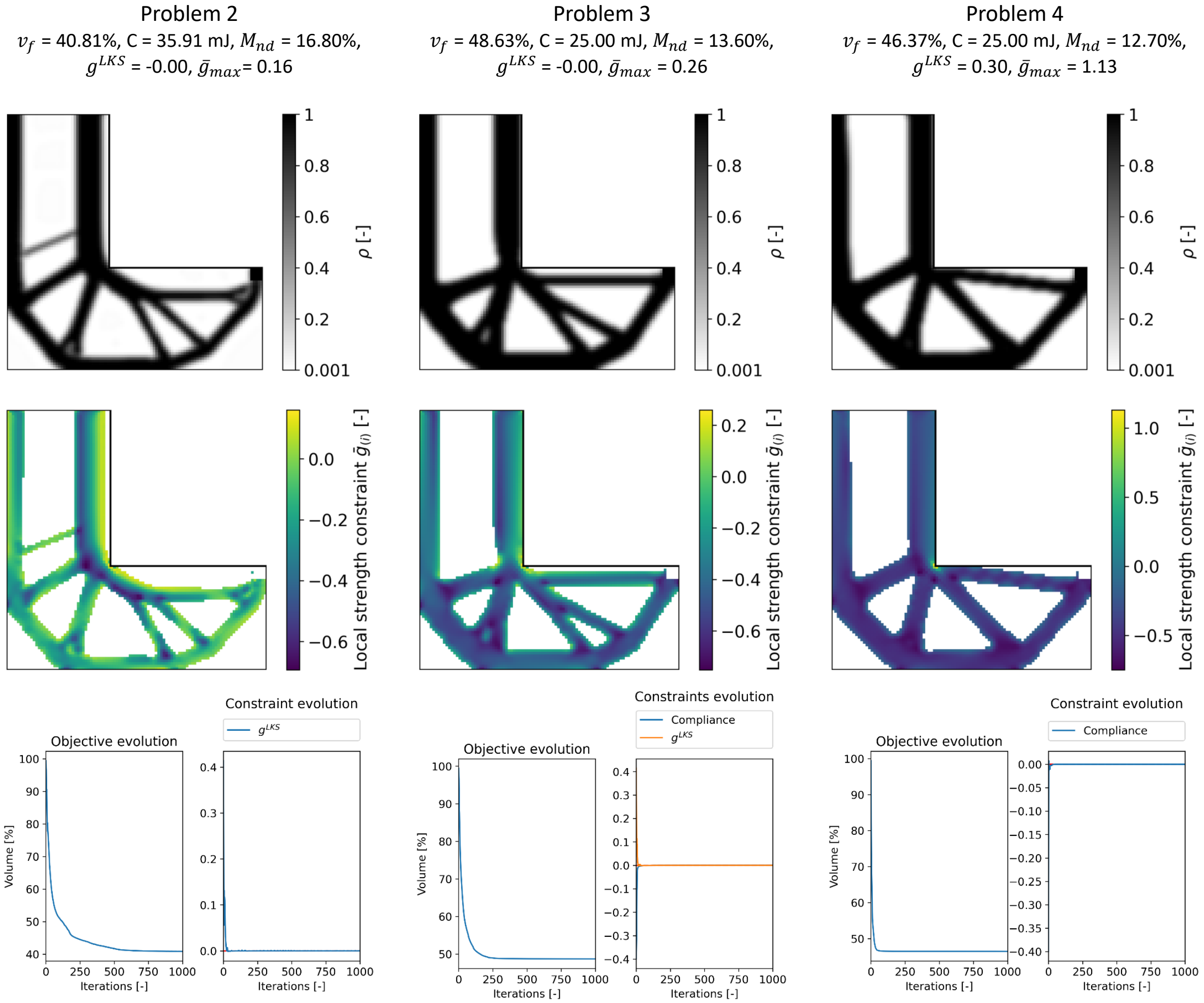

Figure 5.3: Influence of the optimization problem (Problem 2, Problem 3 and Problem 4) with an isotropic material and a Von Mises criterion. Information shown for optimized elements with a final density ≥ 0.3.

diate densities for compliance. Therefore, there is an incentive to remove intermediate densities as much as possible, and to reduce the volume. By not considering the compliance, this incentive is lost, and only an indirect mechanism penalizes intermediate densities through the micro-stress. These three basic examples show the difference in results depending on the problem formulation. With the use of the gradient-based optimization strategy, designers have much more freedom to adapt the problem to their needs, by giving the possibility to adapt or consider the pertinent formulation depending on the requirements, such as being the lightest or having more engineering constraints.

Another important discussion for these simple isotropic problems concerns the convergence rate, and associated computational cost, for the different formulations. The convergence graphs are already shown in Figure 5.3, with a more detailed view of the topologies throughout the iterations displayed in Figure 5.4. For Problem 4, the formulation only taking compliance into consideration, convergence and a discrete solution are obtained quickly, after 75 iterations. This has two reason. The first one is dependent on the algorithm settings, where for this case, the settings of Table 3.4 have been used. As both the volume and compliance design space are regular and monotonous, the approximated MMA sub-problem still represents the design

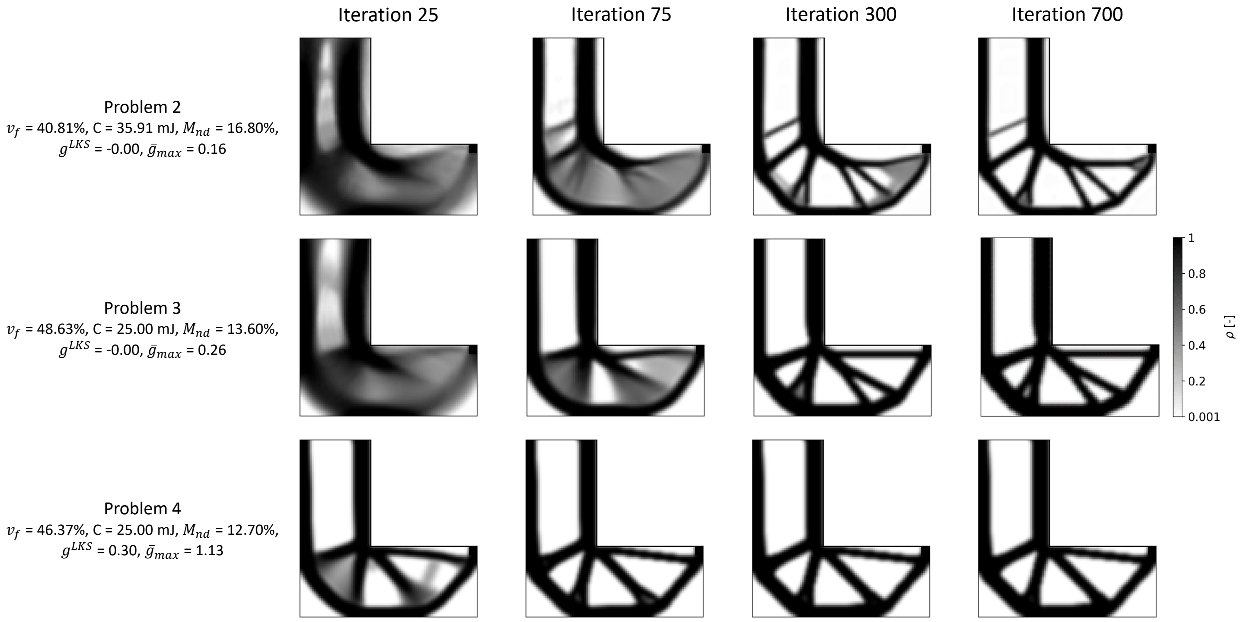

Figure 5.4: Topology convergence rate of the solutions of Figure 5.3 with isotropic material, for a volume minimization with a strength constraint (Problem 2), a volume minimization with a strength and compliance constraint (Problem 3) and a volume minimization with a compliance constraint (Problem 4).

space well away from the current iteration point. This allows for variable changes per iteration, and therefore less iterations are required to remove intermediate densities. The second reason for faster convergence furthermore specifically targets those intermediate densities. As already addressed, the SIMP interpolation penalizes those intermediate densities in case of compliance, which drives them towards distinct results.

On the other hand, when only strength is included, the MMA settings are more restrictive (Section 5.2 and Table 5.1) as the problem involves a more non-linear response and therefore the validity of the gradient information has to be bounded further. This already entails that a larger number of iterations will be required, as the variable change per iteration is less. Furthermore, only an indirect penalization of the intermediate densities is involved through the micro-stress. The optimized solution is only obtained after around 700 iterations. Moreover, some light gray zones ($\rho \in [\rho_{\min}, 0.1]$) remain at the end of the optimization. This was also reported by Verbart *et al.* [5]. This effect is much less when compliance is considered alongside failure in the problem, due to the already discussed SIMP penalization and tendency to converge to real distinct solutions. Moreover, still with the same algorithm settings, the final topology is obtained faster in the volume minimization considering both compliance and strength, after only around 300 iterations. This shows the effect of a direct penalization, but also the more conservative settings to handle stress-based topology optimization problems. Therefore, an idea to further accelerate convergence, is to penalize the intermediate densities in the objective, by introducing a similar penalizing interpolation for the volume calculation, left as a future possibility.

As a conclusion, several optimization problems with isotropic stiffness and strength have been discussed. The importance of strength consideration have been discussed to reduce stress concentration. Without compliance constraint, lighter structures are obtained with only strength consideration. Furthermore, the influence of more conservative algorithm settings to obtain convergence are discussed. It lengthens the optimization process, be it that with a direct penalization, such as is the case of compliance, the convergence can be improved. Nonetheless, the gradient-based framework allows for a versatile use and permutation of different constraints or objective. This part also served as a demonstration and verification of the correct integration of stress constraints in topology optimization for isotropic material before moving on to include anisotropy.

5.4 Stress-Based Topology Optimization with Isotropic Stiffness and Strength Anisotropy Induced by 3D Printing

The first consideration of anisotropy in a stress-based topology optimization represents the one assumed in additive manufacturing under particular printing conditions. As in the work of Mirzendehdel *et al.* [12], an isotropic material is used, assumed to be printed in alternative ±45 raster layers in the XY plane parallel to the machine flatbed. Furthermore, the printing direction Z is defined as the direction perpendicular to the flatbed of the machine, along which the part is extruded. The local strength of such part can then be characterized with a transverse anisotropic strength behavior by means of a Tsai-Wu failure envelope, with the direction of orthotropy aligned with the printing direction. The weaker direction is aligned with the printing direction, while the stiffness tensor of the material remains isotropic.

In the following, 2D topology optimization are performed in the YZ plane. The structure is supposed to be extruded in the X direction. In the YZ plane, the strength is supposed orthotropic. Optimization and material properties used herein are given in Table 5.3. Solutions to a volume minimization with a Tsai-Wu strength constraint (Problem 2) are shown in Figure 5.5 for different printing directions. The printing direction and therefore weakest axis is represented by the yellow arrow (Z axis) in the results. Furthermore, the anisotropic strength criterion in the $\sigma_1 - \sigma_2$ material reference plane is indicated for the different orientations. It is rotated with respect to the global reference plane by the rotation indicating the printing direction.

Table 5.3: 3D Printing induced material properties and optimization parameters for a strength-based topology optimization [12].

Modules	Values	Polar parameters	Values
E [GPa]	69.7	T_0^L [GPa]	26.9
G [GPa]	26.9	T_1^L [GPa]	24.7
ν [-]	0.29	η_1^L [-] $= \eta_0^L$ [-]	0

F [N]	R_ρ [mm]	μ [-]	Z_t [MPa]	Z_c [MPa]	Y_t [MPa]	Y_c [MPa]	S [MPa]
200.0	2.5	30.0	19.8	35.0	29.6	38.0	10.0

The direction of weakest strength influences the final result. In all cases, a rounding is introduced at the re-entrant corner, be it with a different shape for each case. Moreover, all solutions present designs with well solicited features. In case of the printing direction Z at 0°, the topology resembles the one with an isotropic strength criterion. This can be explained by the fact that as there is no stiffness anisotropy, hence the load path is not influenced. Furthermore, the structure is mostly solicited transverse to the printing direction, in the direction of equivalent tensile and compressive allowables. For the case of printing at 45°, the tensile allowable in the $\sigma_1 - \sigma_2$ plane for right vertical bar is higher than in case of 0° orientation. This means a smaller cross-section is possible, and explains the reduced volume. This is in turn associated with the highest compliance, which is expected, as only the presence of material influences the compliance.

The solution with the printing direction at 90° ends up with the highest volume of all solutions. This is a consequence of the weakest axis being aligned with the load. Furthermore, the lower tensile allowable is the most solicited one in the right vertical bar. As a quick estimation, the tensile load seen by this bar is about

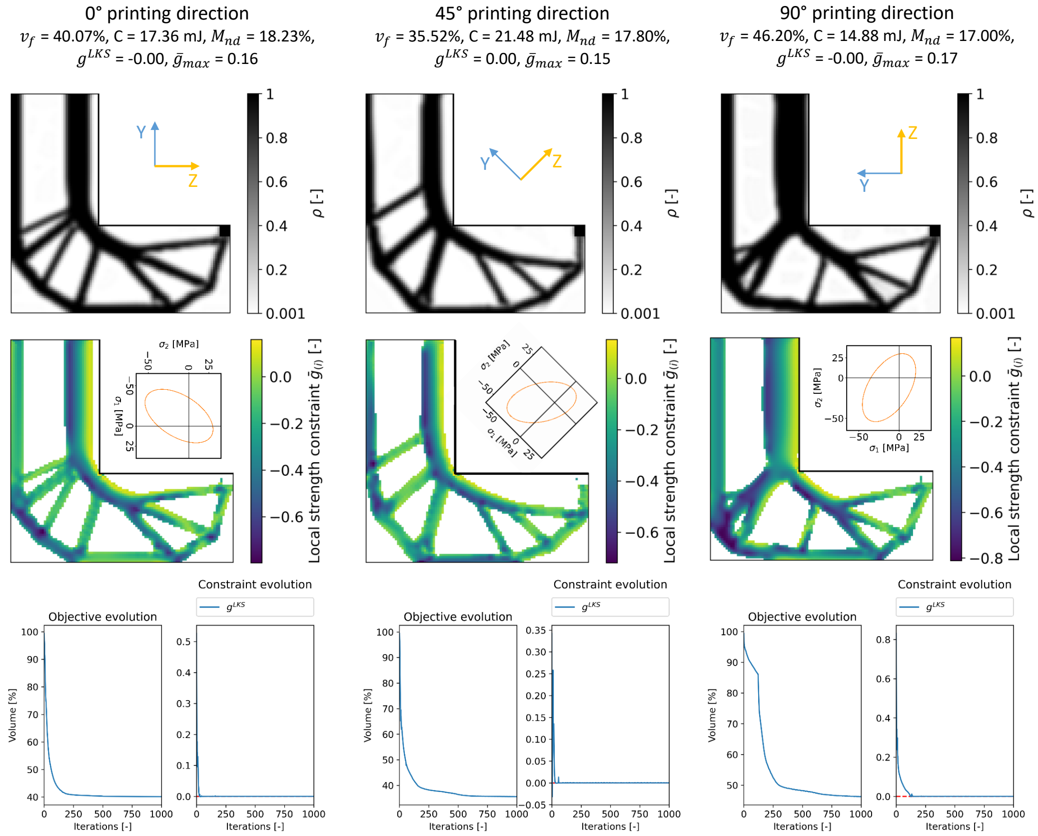

Figure 5.5: Solutions for volume minimization with a Tsai-Wu strength constraint representing additive manufacturing for different printing (extrusion) directions corresponding to the Z axis. Information shown for optimized elements with a final density ≥ 0.3.

twice the applied load. In combination with the lowest tensile allowable, it explains the need for the largest cross-section. It is the opposite for the left vertical bar: the compressive allowable is much higher, and it sees a compressive load with magnitude roughly the same as the applied load. This only requires a smaller cross-section. Nonetheless, with anisotropic strength and this difference in compressive and tensile allowables, a solution designed for one applied load direction is not the optimized one for the reverse loading. Indeed, Figure 5.6 shows the local constraint distribution on the optimized 90° solution with an opposite applied load.

With this reverse loading, the solution yields several bars with an excessive local strength constraint $\bar{g}$, even taking the underestimation of the lower KS approach into account. This means the structure would fail under the reverse loading. Instead, Figure 5.7 shows the optimized solution for the reverse loading. The major material build-up for the right vertical bar has disappeared, not because of the magnitude of the stress it experiences, which is similar, but because it is in compression now. Combined with the higher compressive allowable, this results in a sleeker bar. A similar phenomena is less visible for the left bar, as the load magnitude is lower, and results in a much lighter structure.

This first consideration of anisotropic strength, yet isotropic stiffness, showed that for the same optimization problem, different optimized topologies are obtained depending on the orientation of anisotropy. Naturally, when the local stresses are aligned with the weakest anisotropy direction, wider features are created. This influence is clearly identifiable on the final design, and therefore should carefully be taken care of,

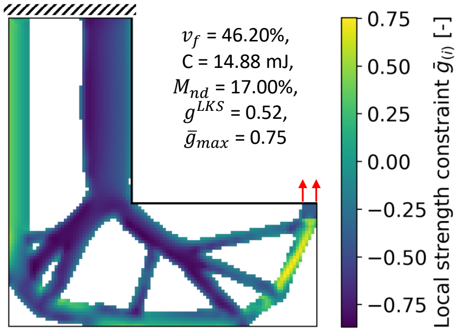

Figure 5.6: Local strength constraint for the 90° printing direction solution with a reverse loading condition. Information shown for optimized elements with a final density ≥ 0.3.

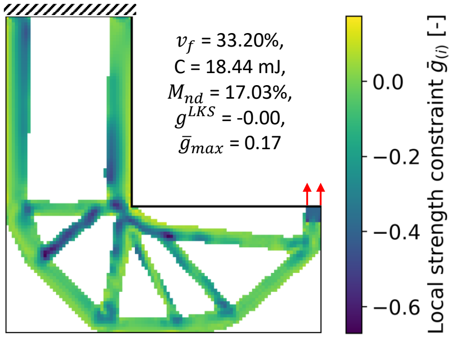

Figure 5.7: Local strength constraint of the optimized solution for additive manufacturing at 90° with a reverse applied load. Information shown for optimized elements with a final density ≥ 0.3.

with a good load case identification. Design engineers should carefully consider the printing direction for optimal additive manufacturing pieces when it comes to their strength consideration. Finally, the convergence graphs show the correct consideration of the strength constraint in the optimization.

5.5 Stress-Based Topology Optimization with Fixed Anisotropic Stiffness and Strength

The use of anisotropy is further extended to the stiffness tensor, be it with a fixed orientation for this section. Both strength and stiffness are orthotropic, with the same principal direction X aligned with the fibers and Y transverse to the fiber. The used properties are listed in Table 5.4. The strength and stiffness material properties corresponds to the one used by Ma *et al.* [8], with the exception of the transverse tensile allowable Y_t. The Y_t allowable has been multiplied by 3 for this part. This is because the initial allowable is about an order of magnitude smaller than the other ones, and introduces difficulties to find an optimized topology for a fixed UD orientation transverse to the applied load. In the optimization of Ma *et al.* [8], the fiber orientation is also varied to align the strongest direction with the loading.

Table 5.4: Fixed orthotropic UD material properties and optimization parameters for a strength-based topology optimization [8].

Modules	Values	Polar parameters	Values
E_{11} [GPa]	39.0	T_0^L [GPa]	7.6
E_{22} [GPa]	8.4	T_1^L [GPa]	6.6
G_{12} [GPa]	4.2	η_0^L [-]	0.44
ν_{12} [-]	0.26	η_1^L [-]	0.55

X_t [MPa]	X_c [MPa]	Y_t [MPa]	Y_c [MPa]	S [MPa]
1062.0	610.0	93.0	118.0	72.0

F [N]	R_ρ [mm]	μ [-]
200.0	2.0	30.0

5.5.1 Tsai-Wu Failure Criterion

Volume minimization with a strength constraint (Problem 2) is treated herein, still only with respect to the density variables as the UD material orientation is kept constant. A Tsai-Wu criterion is employed to characterize failure. The failure envelope in the $\sigma_1 - \sigma_2$ material reference plane is represented in Figure 5.8. Figure 5.9 shows the local strength constraint $\bar{g}_{(i)}$ on the topology consisting of element with $\rho \geq 0.3$ for optimizations carried out for the following UD orientations: 0° (= 180°), 30°, 45°, 60°, 90°, 120°, 135° and 150°. The normalization factor has been adapted for each case, as follows: N_0 is set to 50 for the optimization with orientations in $]0°, 90°]$, whereas N_0 is taken as 25 for the cases with orientations in $]90°, 180°]$. The solution for 0° and 180° are from the same optimization.

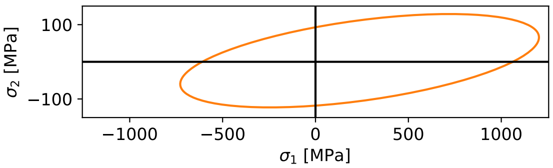

Figure 5.8: Tsai-Wu failure criterion envelope for the properties of Table 5.4 in the $\sigma_1 - \sigma_2$ material reference plane.

Compared to the additive manufacturing case with an isotropic stiffness, these solutions are more sensitive to the material orientation. This is because the load path is more influenced, as the anisotropic stiffness is also involved in directing the loads, preferably along the direction of the fibers. For instances, for orientations in $]0°, 90°[$, the lower right oblique bar follows the UD orientation, whereas this is the case for the lower left oblique bar for the UD orientations $]90°, 180°[$.

The local strength constraints $\bar{g}_{(i)}$ are mostly uniformly distributed over the whole structure, showing similar failure level. As mentioned before, although the aggregated optimization constraint is satisfied, some of these local constraints are above 0, meaning the failure criterion is not satisfied. This is a consequence of the underestimation of the lower KS. Nonetheless, similar failure levels does not mean similar failure mechanisms. The different strength allowables result in different failure mechanism being active, as the local loading path is not always in line with the fiber direction. For example, for the 0° case, the transverse allowable is critical in the vertical bars. On the contrary, shearing failure can be seen in the 90° case in the near horizontal top right bar. Furthermore, depending on the orientations, a rounding is obtained to the re-entrant corner. Other solutions present a sharper corner, where stress concentration are avoided due to the fiber direction and anisotropy directing load away, such as with the 45° case.

Finally, different final volumes are obtained, with the lowest one for the 90° solution. This is logical, as the point of highest loading and stress is located in the vertical bars. Furthermore, with 90° UD orientation, the fiber and strongest allowables are aligned with this loading. The topology for the 90° orientation is given in Figure 5.10. It shows that the vertical bar are not distinct, with a density of about 0.7. This is due to those large longitudinal allowables of the UD material. Compared to failure at other locations which happens for a more complex stress condition. Even with lower densities, and indirect inherent penalization, intermediate densities still means that a high strength capability is retained for the material. The filter radius dictates the minimal bar width and therefore the only way to increase the local strength constraint to be more solicited, is for the optimization to decrease the density, not to have element densities of 1 at that location.

Checking this is done by considering a compliance minimization with volume and strength constraints (Problem 5) for fixed orientations at 90°, a Tsai-Wu failure criterion and a volume v_f of 25.92%. This volume constraint corresponds to a 25% increase over the solution of the 90° UD optimization in Figure 5.9. This increase is provided to this new optimization to reach full density in the vertical bars. Indeed, as the structure

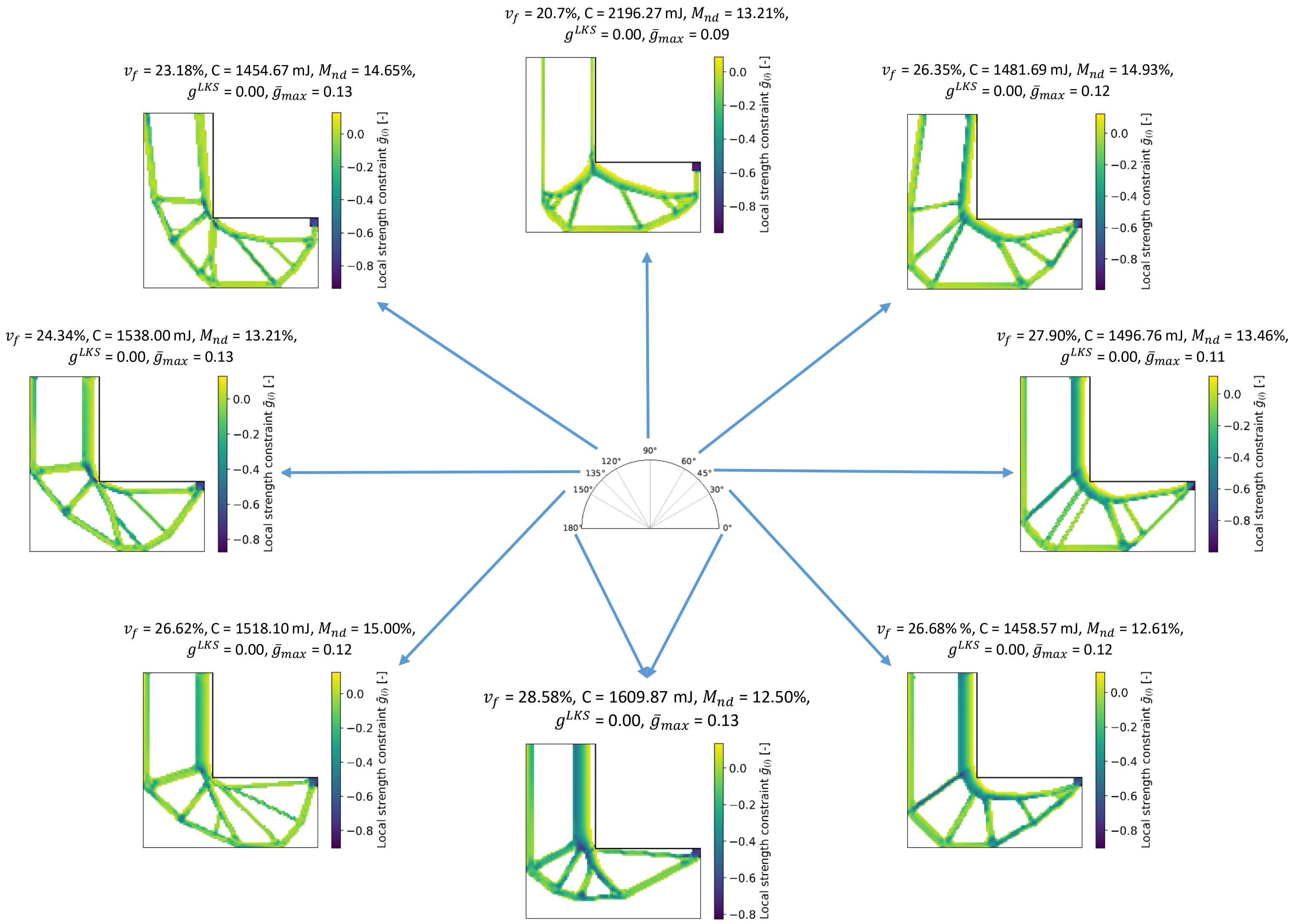

Figure 5.9: Local strength constraint of the results for volume minimization with a Tsai-Wu criterion for a range of fixed UD orientations. Information shown for optimized elements with a final density ≥ 0.3.

is well solicited, material can not be taken elsewhere to obtain fully distinct vertical bars. The solution of this optimization is shown in Figure 5.11.

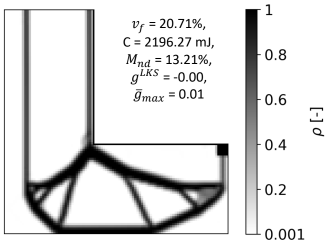

Figure 5.10: Topology for a volume minimization with a Tsai-Wu failure criterion and fibers at 90° (Problem 2), as shown in Figure 5.9.

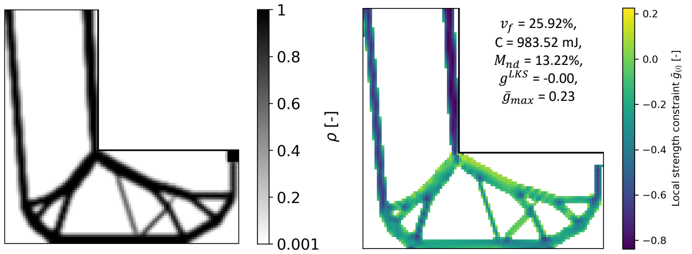

Figure 5.11: Results of a compliance minimization with fixed UD fibers at 90°, a Tsai-Wu criterion and a 25% increase of volume compared to the topology of Figure 5.10 (Problem 5). Information shown for optimized elements with a final density ≥ 0.3.

The solution to Problem 5 shows that indeed the vertical bar now becomes distinct, as the intermediate densities are outed to reduce the compliance. Hence, due to this effect but also additional volume, the compliance value is also much lower (from 2196.27 mJ in Figure 5.10 to 983.52 mJ in Figure 5.11). Furthermore, the topology itself does not change much, except for some additional bars. These are mainly due to the increase in volume being used, as any volume increase reduce the compliance objective of the optimization. Looking at the local constraint $\bar{g}_{(i)}$ for the final result, it shows that the vertical bars are now far from being critical with full densities. Nonetheless, the lower part remains well solicited, as it was already distinct and critical in the initial optimization.

5.5.2 Influence of the Choice of the Failure Criterion

The influence of different elliptic failure criteria on the final result is also investigated, for a Tsai-Wu, Tsai-Hill and Hoffman criteria as described in Section 4.3.1. The results are shown in Figure 5.13. The X and Y allowable for the Tsai-Hill criterion are taken as X_t and Y_t respectively. A representation of all three criteria is given in Figure 5.12 in the $\sigma_1 - \sigma_2$ and $\sigma_2 - \tau_{12}$ material reference plane. The Tsai-Hill criterion has the most conservative transverse envelope, but least longitudinally. This is because Y_t and X_t are the smallest and largest allowable in the transverse and longitudinal direction respectively. Nonetheless, all three envelope have similar shapes. This is also recognized in the optimization results, where the overall distribution of material remains similar for the optimizations with different failure criteria. There are local differences, depending on the predominant stress component (shear, longitudinal or transverse), which influences the local failure mode, and further, final volume. Lastly, for a given fixed orientation, the solution with the highest volume has the lowest compliance.

The aim of these simulations is not to indicate which failure criteria is best suited for topology optimization, merely to show the feasible incorporation of different failure criteria. The specific choice of a criterion is left to the user, depending on the material and strength characterization.

5.5.3 Influence of the Optimization Objective Normalization

The effect of the normalization factor N_0 on the objective, as used in Problem 2- Problem 5, is shown next. It changes the optimization by granting more or less importance to satisfying the constraints, depending on the relative magnitude of the constraints and objective. All constraints are already normalized by their bounding value, so acting on the relative magnitude happens through normalizing the objective value. Figure 5.14

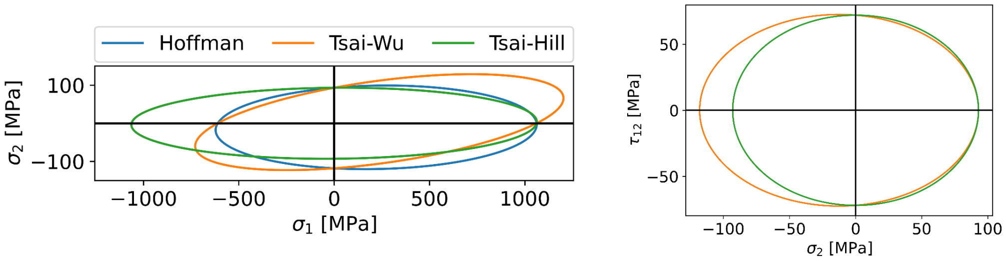

Figure 5.12: Tsai-Wu, Tsai-Hill and Hoffman elliptic failure criteria envelope in the $\sigma_1 - \sigma_2$ and $\sigma_2 - \tau_{12}$ material reference plane for the properties of Table 5.4.

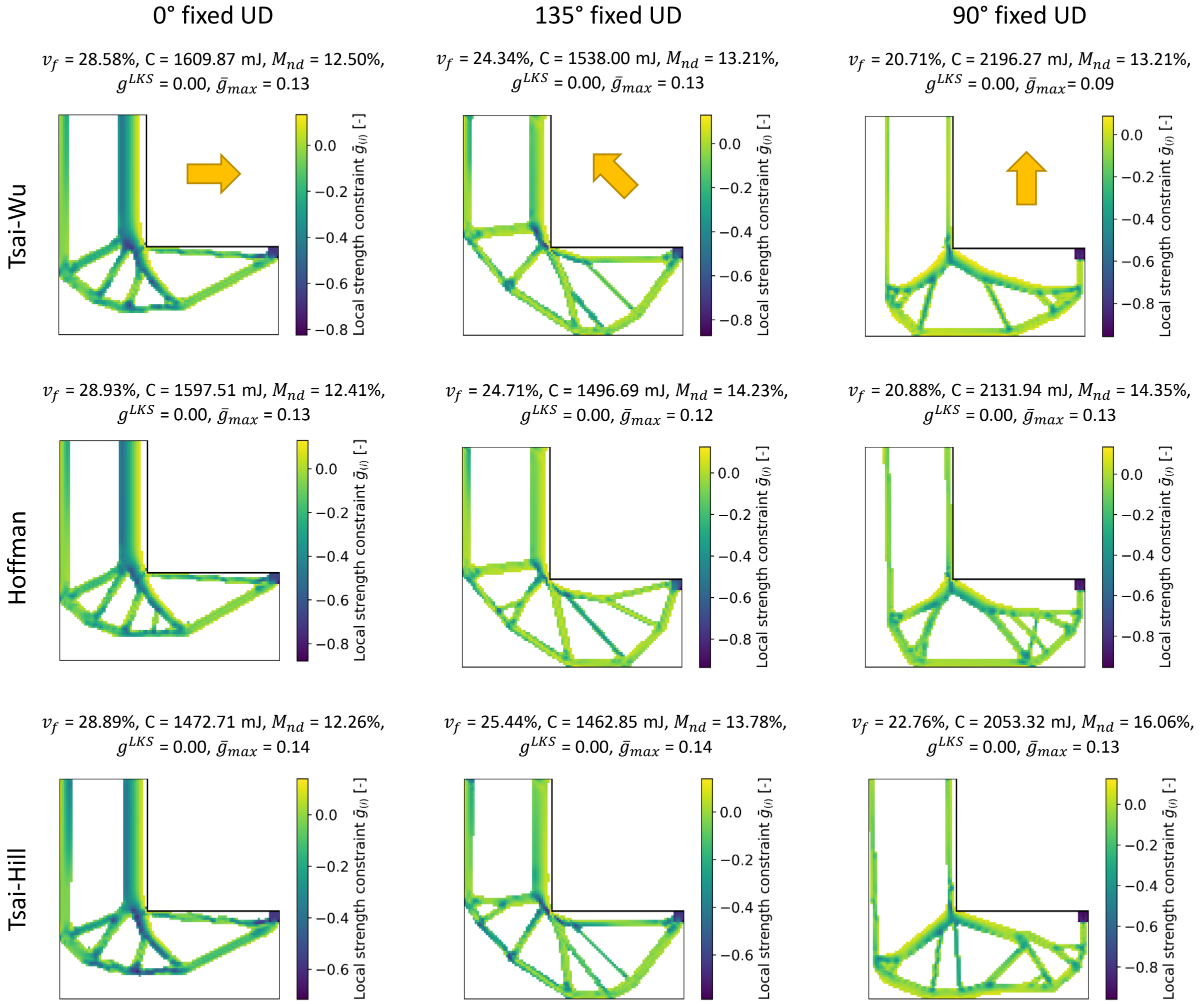

Figure 5.13: Local strength constraint of the results for volume minimization with different elliptic failure criteria for 0°, 45° and 90° UD orientations. Information shown for optimized elements with a final density ≥ 0.3.

shows the results of the optimization of Problem 2 with a 90° UD fiber and Tsai-Hill failure criteria. It corresponds to the same case as the top right result in Figure 5.13, be it that the normalization factor N_0 now equals 25 instead of 50. Despite using the same conservative MMA settings, the optimization has now gone to an unfeasible point by removing all the material first, resulting in a maximum local constraint exploding to large values. The focus was too much on minimizing the objective. Instead, by using a higher normalization factor for the solution in Figure 5.13, the objective value is lower, and the focus is emphasized on satisfying the constraint, before starting to reduce the objective.

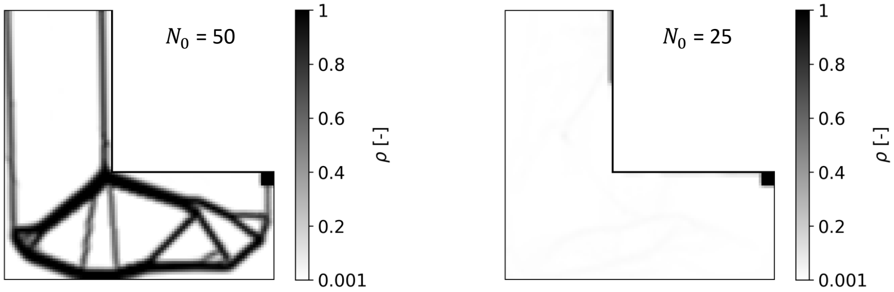

Figure 5.14: Comparison of the final topology for volume minimization with a Tsai-Hill criterion and UD fibers at 90°: on the left, the solution of Figure 5.13 with $N_0 = 50$, and on the right unsuccessful $N_0 = 25$.

Figure 5.15 shows the optimization result, still for Problem 2 and a UD orientation of 90°, but with a Tsai-Wu failure criteria. It corresponds to right middle in Figure 5.13, with N_0 again equal to 25 instead of 50. The optimization converges well, with a final volume of 14.1%. A different topology is obtained, with the upper bars slightly inclined. This is assigned to the Tsai-Wu envelope allowing for σ_1 stresses larger than X_t or X_c when some transverse stress σ_2 is also present, introduced by the inclination. This however, means a longer bar is obtained, which in turn increases the total volume. It shows that this normalization setting influence the optimization process.

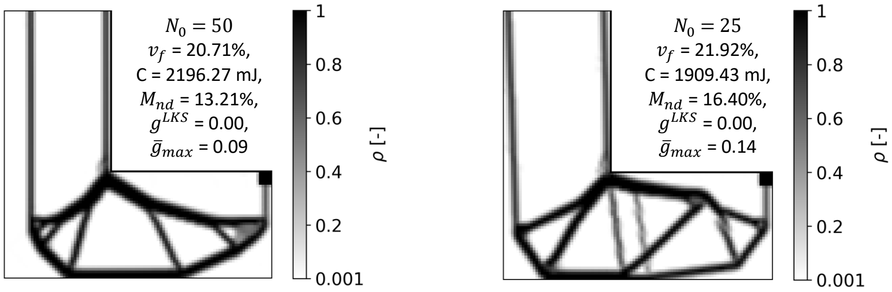

Figure 5.15: Comparison of the final topology for volume minimization with a Tsai-Wu criterion and UD fibers at 90°: on the left, the solution of Figure 5.13 with $N_0 = 50$, and on the right with $N_0 = 25$.

As with the selection of the settings for the MMA algorithm, the normalization factor modifies the optimization problem and the path taken to solve it. All these parameters have several influences. First, there is no unique setting to obtain the best solution for a range of problems. This means a certain experience is required in tuning those parameters first to converge to a feasible solution. Thereafter, they can be tuned in order to find a better optimum. It should also be noted, as already addressed earlier in Section 3.5.2, and touched upon again in subsequent sections, the starting anisotropy distribution for the topology optimization is more important for which local minima is obtained. All these become additional considerations to take into account when using a gradient-based topology optimization tool with anisotropy.

5.6 Concurrent Density and Material Orientation Optimization for Steered UD Composite Fibers

This sections is dedicated to the optimization with respect to both density and orientation of a Uni-Directional (UD) material with strength considerations. The optimizations are solved with the SplitMMA strategy of Section 3.3. The stiffness properties of Table 5.4 are still used together with the properties listed in Table 5.5. In this case, the initial tensile transverse allowable Y_t has been used, as the UD fiber is allowed to rotated and align with the direction of largest stress.

Table 5.5: Optimization and UD fiber [8] properties for simultaneous topology and orientation optimization with strength constraint.

R_ρ [mm]	R_{ϕ_1} [mm]	μ [-]	X_t [MPa]	X_c [MPa]	Y_t [MPa]	Y_c [MPa]	S [MPa]
2.0	2.0	30.0	1062.0	610.0	31.0	118.0	72.0

5.6.1 Filter on Material Orientations

R_{ϕ_1} represents the filter radius used for the material orientations. It is based on the same approach as the density filter (Equation 3.3) as explained in Section 3.2.1 and Section 3.4, but applied to the orientation variables. This filter serves to obtain a smoother anisotropy distribution during the optimization. Without this, checkerboard like phenomena appears on the orientations, which can adversely affect the filtered density variable. Indeed, with discontinuities on the orientations and therefore the anisotropy, the spatial variations of the density gradient are less regular, which propagates to the variables during the optimization. Applying a filter on both orientation and density, leads to a more homogenized and continuous stiffness distribution over the optimized part. This is a beneficial effect for the load path and subsequent stress distribution. It ensures that no local stress concentration due to stiffness mismatch is optimized instead of actual stress concentration due to the geometry and load cases. Nonetheless, this simple linear filter could average out some orientations which are π apart, *e.g.*, 90° and $-90°$ which represent the same stiffness tensor would lead to an orientation of 0°. This effect will be discussed in the results. A different filter taking near opposite orientations into account is left as possibility for future work, the focus herein lays in incorporating the strength constraints.

5.6.2 Initial Material Orientation Influence

As was discussed in Section 3.5.2, the initial anisotropy distribution for topology optimization is important and further corroborated here. The volume minimization with strength constraint optimization of Problem 2 is considered, with an applied load of 400 N, a Tsai-Wu criterion and a normalization factor of 50. All elements start off with a density of 1, and the effect of the initial orientations is investigated. Three cases are considered: the orientations are uniformly initialized with either 0° and 90° or the initial orientation distribution comes from a compliance minimization problem first, where the density are fixed. The latter is similar to the initialization phase used in Section 3.5.2 in the case of simultaneous material anisotropy and density optimization, where a compliance minimization is performed first with respect to the anisotropy design variables only for the given load case. This allows the anisotropy to align with the load path, providing the initialization of anisotropy for a subsequent optimization. In the present case, the optimization constraints and objective are different between the two optimization step, but this is not a problem as long as the design variables remain the same. The results of optimizations with these three initialization strategies are shown in Figure 5.16.

The results show three different topologies, with the one starting from 90° and the one from the compliance minimization having similar main features. These two also have a similar volume, with the latter one being the lightest, whereas the 0° is by far the heaviest. Analyzing the results further, it shows that the

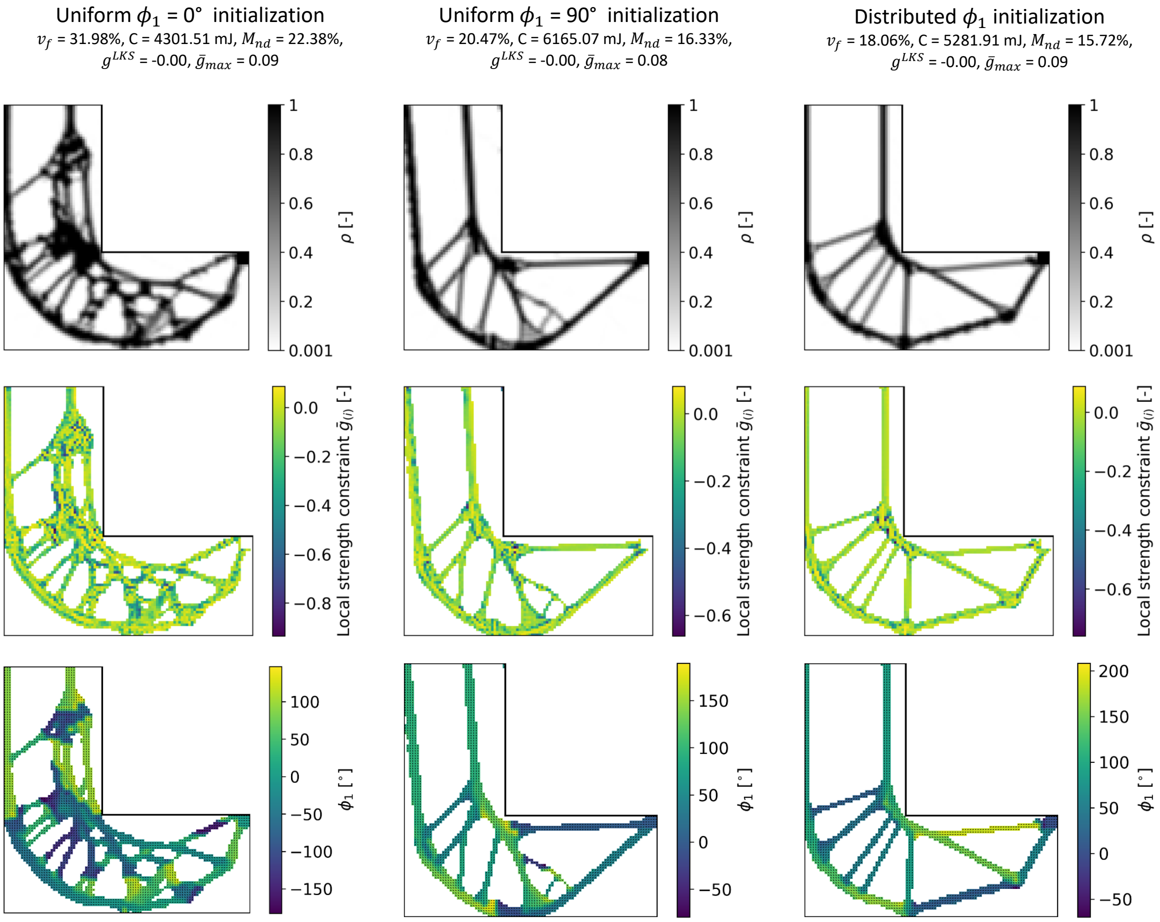

Figure 5.16: Local strength constraint of the results for volume minimization with a Tsai-Wu criterion for both topology and orientation optimization of a UD ply with different initialization of the orientations: uniform $\phi_1 = 0°$ on the left, uniform $\phi_1 = 90°$ in the middle and distributed ϕ_1 on the right. Information shown for optimized elements with a final density ≥ 0.3.

local strength constraint $\bar{g}_{(i)}$ is consistently distributed and a design with well solicited features is obtained for all three initializations. Nonetheless, the issue of well solicited intermediate density bars, as discussed in Section 5.5.1, is still present as a result of the optimization problem formulation.

The result from the 0° initialization suffers from many small bars created within the structure and material build-up locations with local strength constraint discontinuities. The optimized orientation in the vertical bars is a full 90° rotation from the initialization, which was obtained for the left bar. For the right one, transverse failure is already present at the start of the optimization, as shown in Figure 5.17. This is due to both the stress magnitude being higher for the right hand side, and the different nature of the load, either compressive in the left bar and tensile in the right one, which involves different failure allowables (Yc and Yt respectively). The algorithm tries to satisfy the strength constraints by rotating some orientations counter-clockwise and other clockwise. This then involves a detrimental averaging effect of the linear filter on the material orientations. Spurious 0° orientations are generated by averaging $\pm\phi_1$ orientation in adjacent elements. This generates local stress concentrations that lead to the material density build-up that can be seen in the middle of the bar. The optimizer is trapped in a sub-optimal solution, due to the linear orientation filter.

The material build-up is a result of poor transverse strength properties of the UD material. This happens when the material cannot be properly aligned with the main load path, as discussed previously, or in locations of complex multi-direction loading, such as at junctions, as seen with the $\phi_1 = 90°$ and the distributed ϕ_1 initialization. Furthermore, opposite to the $\phi_1 = 0°$ initialization, these $\phi_1 = 90°$ and the distributed ϕ_1 initializations do not have initial violated local strength constraint in the left upper area of the L-bracket, as they have the higher longitudinal allowables aligned with the load path. Moreover, the distributed ϕ_1 initialization has orientations following the load path, which also decreases the value of the local strength constraints in the right horizontal part, as visible in Figure 5.17. The $\phi_1 = 90°$ initialization shows higher local strength constraint, where it is solicited in shear. Nonetheless, the final topology for the $\phi_1 = 90°$ and the distributed ϕ_1 initializations seem more efficient than the one obtained with the $\phi_1 = 0°$ initialization. In both case the material orientation is well aligned with the bar orientations. Nonetheless the distributed ϕ_1 initialization gives the best result, with both the lowest volume and compliance.

Lastly, where guessing which uniform anisotropy initialization (*i.e.*, 0° or 90°) would be the best starting value in the case of a uniform ϕ_1 initialization is problem specific and not trivial. Using a first optimization step by minimizing the compliance with respect to the anisotropy with fixed uniform densities will align the anisotropy with the load path, and can be applied to any case. Aligning the strongest material orientation with the load path seems a sound engineering basis, and already yields the lowest local strength constraint distribution of all initialization as seen in Figure 5.17. Therefore, a two step initialization strategy is used for the remaining optimizations. This strategy yields the solution with the lowest volume, a lower initial stress concentration and applicable to any load case. The first step consists in aligning the anisotropy with the load path by performing a compliance minimization with respect to the anisotropy only and SIMP $p = 1$ for a uniform and fixed density distribution. This solution is then the start point for the second step, consisting in a strength-based topology optimization with respect to both density and anisotropy simultaneously with SplitMMA.

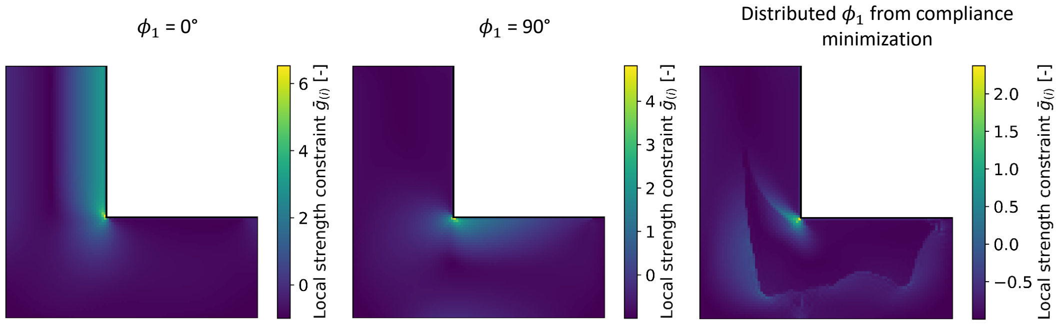

Figure 5.17: Initial local strength constraint distribution for the optimization of Figure 5.16.

5.6.3 Influence of the Choice of the Anisotropic Failure Criterion

A comparison of optimizations with different elliptic failure criteria is performed with Tsai-Wu, Tsai-Hill and Hoffman envelopes (described in Section 4.3.1). The optimization problem consists in volume minimization with strength constraint (Problem 2). An applied load of 400 N and a normalization factor $N_0 = 50$ are still used. The initial densities are 1, with the distributed orientations ϕ_1 obtained from a first compliance minimization step as explained in Section 5.6.2. The local constraints $\bar{g}_{(i)}$ for densities greater than 0.3 are shown for the three cases in Figure 5.19. The X and Y allowables for the Tsai-Hill criterion are taken as X_t and Y_t respectively. A representation of all three envelopes is given in Figure 5.18 in the $\sigma_1 - \sigma_2$ material reference plane.

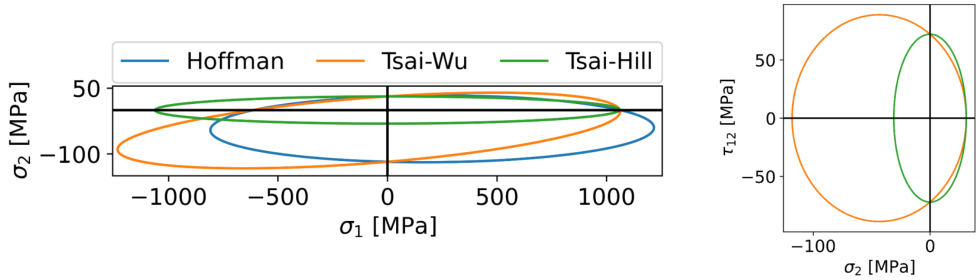

Figure 5.18: Tsai-Wu, Tsai-Hill and Hoffman elliptic failure criteria envelopes in the $\sigma_1 - \sigma_2$ material reference plane for the properties of Table 5.5.

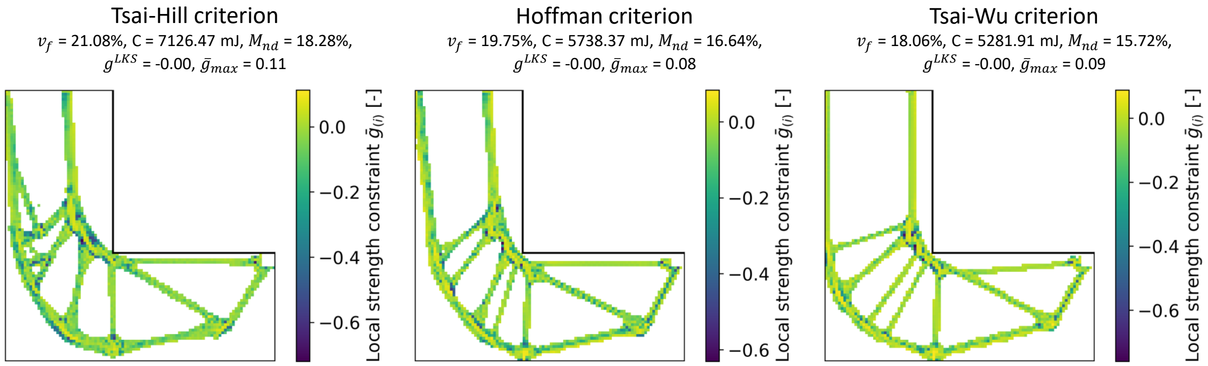
Tsai-Hill criterion

v_f = 21.08%, C = 7126.47 mJ, M_{nd} = 18.28%, g^{LKS} = -0.00, $\bar{g}_{max}$ = 0.11

Hoffman criterion

v_f = 19.75%, C = 5738.37 mJ, M_{nd} = 16.64%, g^{LKS} = -0.00, $\bar{g}_{max}$ = 0.08

Tsai-Wu criterion

v_f = 18.06%, C = 5281.91 mJ, M_{nd} = 15.72%, g^{LKS} = -0.00, $\bar{g}_{max}$ = 0.09

Figure 5.19: Local strength constraint of the results for volume minimization with Tsai-Wu, Tsai-Hill and Hoffman failure criteria for both density and material orientation optimization of a UD ply. Information shown for optimized elements with a final density ≥ 0.3.

As with the earlier comparison of different failure criteria with fixed orientation in Section 5.5.2, the heaviest solution is the one with the more conservative failure criterion, being the Tsai-Hill here. This solution presents the lowest transverse allowables, meaning it has the most material build-up at junctions to satisfy the optimization constraint. On the contrary, the lightest structure is the one with the largest failure envelope, represented by the Tsai-Wu criterion. Nonetheless, all solutions are uniformly stressed. The final topologies are similar, although the Tsai-Wu solution retains vertical bars. For the other two optimizations, these bars have a small inclination with respect to the vertical. This is associated to being in a particular local minima, and corresponds to the behavior of other solutions shown previously.

Comparing the final compliance yields remarkable values: the heaviest solution has the highest compliance. This is because compliance is only considered as an output, and no explicitly during the optimization. Furthermore, the compliance is not only dependent on the volume, but also on the distributed anisotropy. The presented solution is a minimum which fulfills the strength constraint, but is not particularly stiff. Other equivalent minima could be present which stratify the strength constraint and are stiffer.

5.6.4 Influence of an Increased Loading

This part investigates the effect of a higher applied load on the optimized solution. A volume minimization problem with strength constraint (Problem 2) is treated, with a total applied load F = 800 N, a normalization factor $N_0 = 1$. The densities start with a uniform density of 1, while a distributed orientation field comes from a compliance minimization step with respect to the material orientations for fixed densities. In this case 1500 iterations have been used, as the convergence takes longer to occur than in Section 5.6.2, beyond the 1000 iterations. The solution is shown in Figure 5.20.

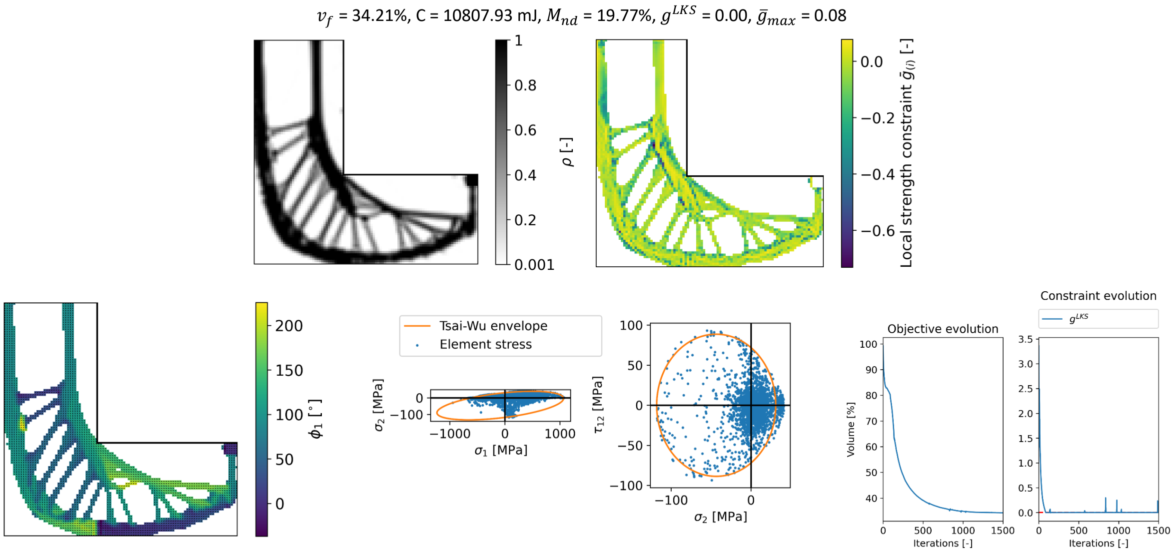

Figure 5.20: Solution for a volume minimization with a Tsai-Wu failure criterion for both topology and orientation optimization of a UD ply with an increased load F = 800 N. Information shown for optimized elements with a final density ≥ 0.3.

For this case, looking at the optimization evolution graph, the objective only arrives at a plateau after around 1250 iterations. Detailing the constraint evolution, it is visible that for early iterations, the strength constraint is not fulfilled. The optimization therefore first tries to reduce and satisfy the strength constraint whilst barely improving the objective. Once the constraint is satisfied, the focus of the optimization is back on the objective minimization. Nonetheless, there are some violations of the strength constraint during the optimization process. This corresponds to subsequent oscillations in the objective. This is however no issue for the gradient-based strategy, which can recover from these infeasible points to return to the feasible domain and thereafter continue the optimization. These local infeasible points are a consequence of allowing a step-size too large for any variable with respect to the trust region of the gradient representing the local behavior of the constraint.

Inspecting the optimized solution, the topology exhibits two loaded sections, forming a sort of arch at the inner and outer part, with smaller bars between them. The orientations are well aligned with the bars, except for junction locations or filter transitions between opposite orientations. The stress distribution are mostly contained within the Tsai-Wu envelope in the $\sigma_1 - \sigma_2$ and $\sigma_2 - \tau_{12}$ material reference plane. Some stress state are beyond the envelope, which corresponds to elements with a local constraint greater than 0. Finally, there are some intermediate densities floating around the boundary, which are not connected to the rest of the structure. These are numerical artifacts appearing in the solution, as these regions' strength constraint is well satisfied and could be removed altogether. The small bars within the topology suffer from being partially loaded, with resulting intermediate densities. They are difficult to remove for the algorithm with this problem formulation.

Therefore, the same test case is treated with a different problem formulation. A volume minimization with a strength constraint is still carried out, but also with an added compliance constraint (Problem 3). The compliance constraint C_0 is set at 5500 mJ, which is just over half the one of the solution in Figure 5.20. The normalization factor N_0 is to set to 25. The results of this optimization are shown in Figure 5.21. Despite the new problem formulation, the overall topology remains similar to the solution in Figure 5.20. It can be stated that the problem is therefore driven by the strength constraint, as most of the bars in the new solution are still highly solicited. Nonetheless, the right vertical bar has become thicker to be stiffer, as have the inner bars by being more distinct. Furthermore, the floating intermediate densities at the boundary have been removed.

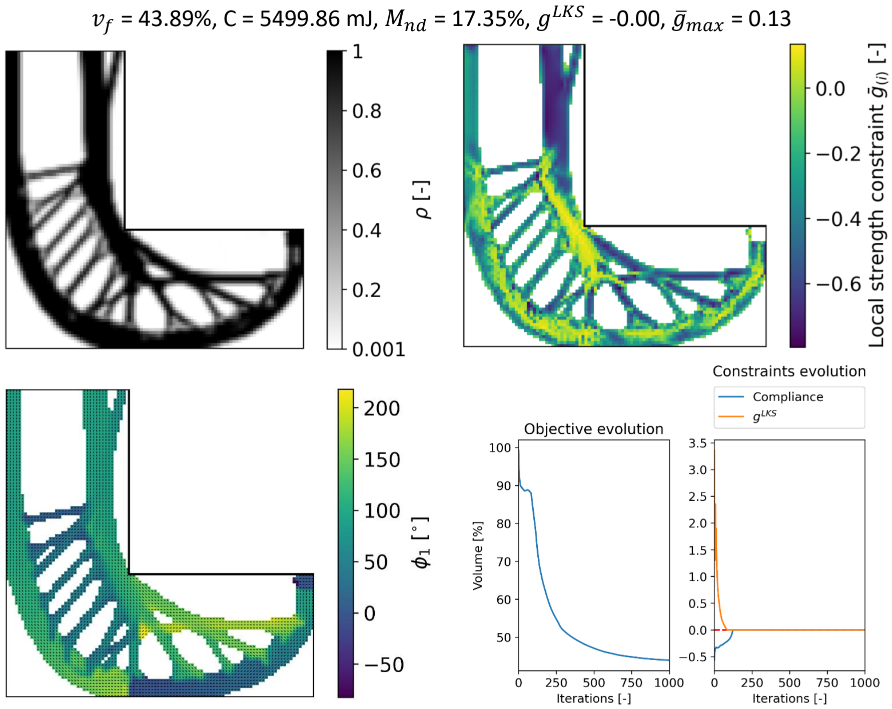

Figure 5.21: Solution for a volume minimization with compliance and a Tsai-Wu failure criterion for both topology and orientation optimization of a UD ply with an increased load. Information shown for optimized elements with a final density ≥ 0.3.

Concerning the anisotropy, the final orientations follow well the features, even at junctions, as the outcome of the optimization has not placed major material build-up at the junctions. This is because the smaller inner bars do not carry large loads compared to the massive outer bars forming arch-like shape. Therefore, less multi-directional strength is required at the junctions, represented by the build-ups. Finally, looking at the outcomes, a higher volume than in Figure 5.20 is obtained. This is due to the intermediate density bars becoming distinct, but also the thicker vertical bars to account for the compliance constraint. Concerning the convergence of the optimization, the compliance with the initial full volume is of course largely satisfied, but not the strength constraint. With the decrease in volume, the compliance constraint becomes active. At the same time, the emerging topology in combination with the anisotropy alignment reduces the strength constraint. Once both constraints are satisfied and active, the volume is gradually and regularly minimized. This example showed that increasing the load of the problem influences the optimized solution, both topology and conforming anisotropy-wise. However, the optimization will not find a solution for all values of the applied load. There is a relation between the material properties, considered load cases and design domain (represented by the underlying mesh), for which there exists feasible solutions. This should be evaluated beforehand by users of such topology optimization tools, as it is problem specific.

5.6.5 Comparison with Literature

The method is also compared with literature for Problem 5, with the results of Ma *et al.* [8]. It consists in a compliance minimization with strength and volume constraint. The original results are given in Figure 5.22, where the solution obtained with the current method is shown in Figure 5.23. The optimization is performed with an applied load F = 200 N, a normalization factor $N_0 = 1$, a volume fraction v_f constrained at 40% and started with $\mu = 30$. The densities are initialized as $\rho = 1$ and, whereas distributed material orientations are initialized from a preliminary compliance minimization step. Furthermore, to reduce the overshoot of the local strength constraints, the aggregation parameter μ is increased after 500 iterations by 75 every 25 iterations.

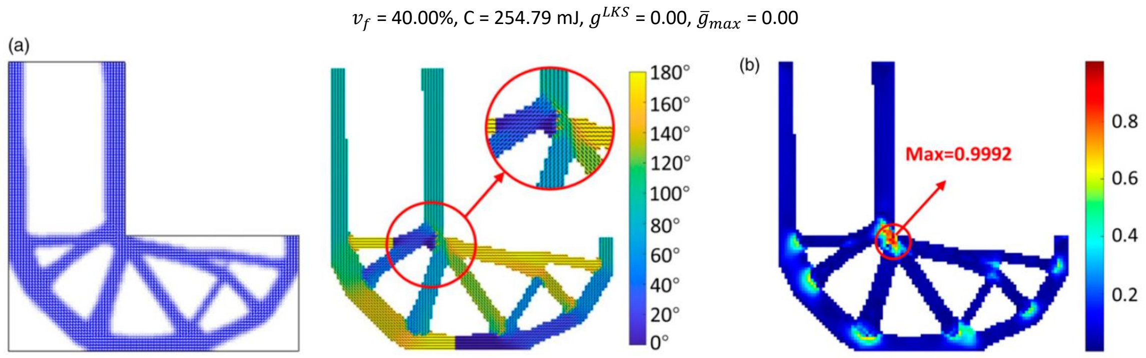

Figure 5.22: Results obtained by Ma *et al.* [8] for topology and orientation optimization for compliance minimization with volume and a Tsai-Wu failure criterion with a UD fiber: (a) density and fiber distribution, (b) Tsai–Wu value distribution.

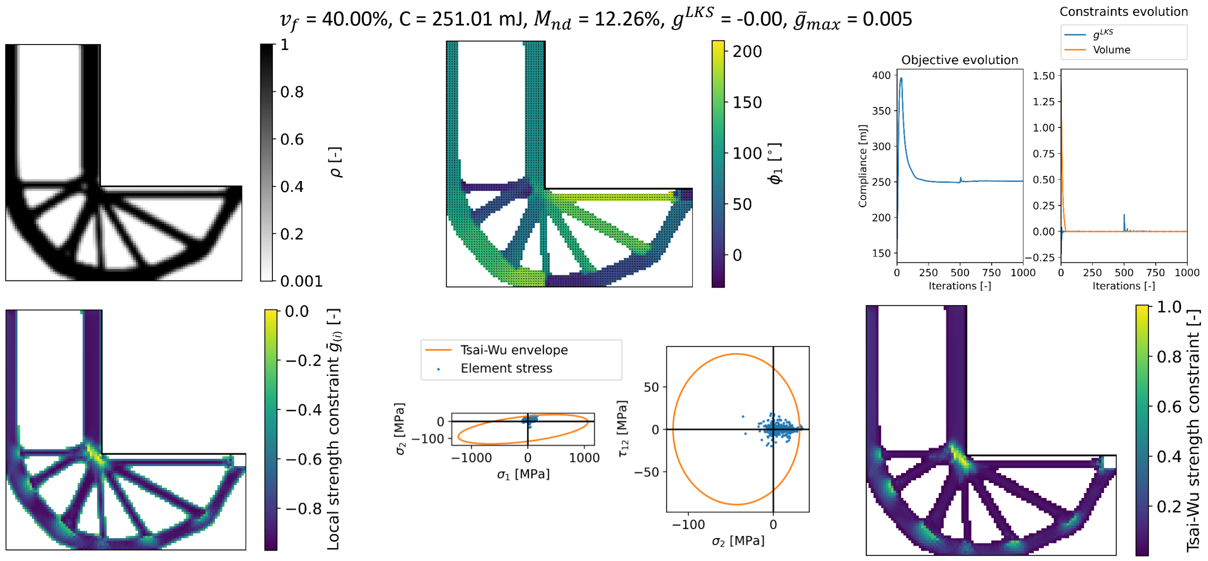

Figure 5.23: Solution for a compliance minimization with volume and a Tsai-Wu failure criterion for both density and material orientation optimization of a UD ply (Problem 5). Information shown for optimized elements with a final density ≥ 0.3.

The amount of bars and their location differs between both cases. Nonetheless, the general trend of the optimized piece is retained. The stress concentrations and high local strength constraints are in similar places, at the re-entrant corner and junctions. Moreover, with the gradual increase of the aggregation parameter μ, it is possible to achieve a solution whose local strength constraint are well enough satisfied in combination with a lower KS approach. Indeed, the maximum local strength value has about a 0.5% overshoot, which is well within acceptable limits. The increase in μ does introduce some constraint violation during the iterations, as seen in the convergence graph, but is well recovered by the SliptMMA strategy. Finally, local stress concentrations are still obtained at orientation transitions. This is noticeable for the ones within bar, such as the bottom bar in Figure 5.23.

5.7 Conclusion

This chapter showed the implementation and results of the SplitMMA gradient-based optimization strategy for stress-based problems with anisotropic material properties. It is first verified for a simple isotropic case with a Von Mises criterion. The effect of different optimization problems are discussed. As the lower KS aggregation function underestimates the maximum, the optimization constraint is satisfied, while the local constraints have a value higher than 0. Afterwards, anisotropic stress criteria have successfully been integrated for different problem types. It has first been considered along isotropic stiffness, representing the behavior along the printing direction in additive manufacturing. This showed that results obtained with an anisotropic failure criterion, differentiating between tensile and compressive allowables, are not necessarily satisfied for a reverse loading. Design offices should therefore carefully define the load cases for the use of topology optimization. Moreover, the difference in tensile and compressive allowable leads to more massive features for parts subjected to the lower of the two.

UD material was thereafter considered, combining anisotropic stiffness and strength behavior. Volume minimization optimizations were first carried out only with respect to the density for a range of fixed UD orientations. This showed that due to the large difference in longitudinal and transverse allowables, the final densities in only longitudinal loaded features become intermediate values. This is explained by the fact that the associated allowables are an order of magnitude larger compared to the other ones, and that even penalized intermediate densities are still strong enough to carry the load and fulfill the strength criterion. If compliance consideration is integrated in the optimization, the penalization of these intermediate density is stronger and the solution converges to distinct results. This is followed by a comparison of different failure criteria (Tsai-Hill, Hoffman and Tsai-Wu) in the optimization. It revealed that the final results are similar, be it heavier with the more conservative failure criteria. Lastly, the effect of numerical settings is discussed in achieving convergence to local minima. A range of settings is possible to intervene in the behavior of the optimization, but are problem specific and require some experience from the user. Optimal numerical settings are not given.

The last optimization problems treated in this chapter focus on the optimization with respect to both the topology and orientation of a UD material. The effect of different orientation initializations is investigated, leading to different local minima. Due to the high strength anisotropy, uni-directional loaded features are slender, but junction locations with complex loading condition get a material build-up as transverse allowables lead to earlier failure. Furthermore, a simple linear orientation filter is included to help obtain a more continuous stiffness and subsequent stress distribution. It nonetheless introduces numerical transitions between opposite orientations, leading to another material build-up and failure locations. Using the initialization of a compliance minimization with respect to only the orientation yielded a lighter solution, while being logical by having the orientations aligned with the features. Moreover, this initialization also provides a logical starting point by having the orientations align with the local load path, and can be applied to any load case. Afterwards, the effect of considering different failure criteria is again investigated, resulting in similar topologies between the criteria, be it still obtaining the heaviest solution with the more conservative envelope. The influence of a higher applied load is then checked, with resulting thicker bar sections, and for different optimization problem formulation. Including compliance consideration helps to remove a large amount of intermediate densities. Finally, the strategy compares well with recent literature for compliance minimization with a volume and Tsai-Wu constraint. The current method is successfully extended to reduce the overshoot of the local constraint by less than 1%, by increasing the aggregation parameter towards the end of the optimization. These results conclude strength-based optimization with UD material. In the next chapter, the case of laminates consisting of a stacking of UD plies is considered in strength-based topology optimization.

Chapter 6

Topology Optimization of Laminates taking a Conservative Strain Envelope into account

6.1 Introduction

This chapter is dedicated to the inclusion of a strength criterion in topology optimization, in the specific case when composite laminates are considered. A strain-based criterion is formulated, as the polar parameters are used to represent the macroscopic homogenized membrane stiffness tensor of the laminate. Thus, the stacking sequence is unknown. Such strain criterion could entail for example a first ply failure in the laminate layup, but also represent a damage criterion value for aircraft applications.

The anisotropy variables considered in the subsequent topology optimizations are that of an orthotropic laminate. The feasibility domain for laminates is represented by the geometric bounds on the polar parameters η_0 and η_1, as described in Section 3.2.3. The remapping of Section 3.2.4 is still used to enforce these geometric bounds. The optimization variables per element therefore become ρ, ϕ_1, α and β. Similarly to the different optimization problems of Chapter 5, different formulation are used in this chapter to evaluate the effect on the optimized solutions. The considered problems are a volume minimization with a strain-based strength constraint (Problem 6), a volume minimization with a compliance and a strain-based strength constraint (Problem 7), and finally a volume minimization with a compliance constraint (Problem 8). The initialization for all these optimizations starts with $\rho = 1$. All the optimizations are performed for 1000 iterations each, with a fixed SIMP $p = 3$ exponent. The SplitMMA properties of Table 5.1 are still used. Finally, only one cluster for the optimization constraint consisting of the optimized elements is considered.

$$
\begin{aligned}
\min_{\boldsymbol{\rho},\boldsymbol{\phi}_1,\boldsymbol{\alpha},\boldsymbol{\beta}} \quad & v_f(\boldsymbol{\rho})/N_0 \\
\text{s.t.} \quad & C(\boldsymbol{\rho},\boldsymbol{\phi}_1,\boldsymbol{\alpha},\boldsymbol{\beta}) \leq C_0 \\
& g_k^{LKS}(\boldsymbol{\rho},\boldsymbol{\phi}_1,\boldsymbol{\alpha},\boldsymbol{\beta}) \leq 0 \\
& \boldsymbol{\rho} \in [\rho_{\min}, 1] \\
& \boldsymbol{\phi_1} \in [-3\pi/2, 3\pi/2] \\
& \boldsymbol{\alpha},\boldsymbol{\beta} \in [0,1] \times [0,1]
\end{aligned}
\tag{Problem 6}
$$

$$
\begin{aligned}
\min_{\boldsymbol{\rho},\boldsymbol{\phi}_1} \quad & v_f(\boldsymbol{\rho})/N_0 \\
\text{s.t.} \quad & V(\boldsymbol{\rho})/V_0 \leq v_f \\
& g_k^{LKS}(\boldsymbol{\rho},\boldsymbol{\phi}_1,\boldsymbol{\alpha},\boldsymbol{\beta}) \leq 0 \\
& \boldsymbol{\rho} \in [\rho_{\min}, 1] \\
& \boldsymbol{\phi_1} \in [-3\pi/2, 3\pi/2]
\end{aligned}
\tag{Problem 7}
$$

$$\begin{aligned} \min_{\boldsymbol{\rho},\boldsymbol{\phi}_1,\boldsymbol{\alpha},\boldsymbol{\beta}} \quad & C(\boldsymbol{\rho},\boldsymbol{\phi}_1,\boldsymbol{\alpha},\boldsymbol{\beta})/N_0 \\ \text{s.t.} \quad & g_k^{LKS}(\boldsymbol{\rho},\boldsymbol{\phi}_1,\boldsymbol{\alpha},\boldsymbol{\beta}) \leq 0 \\ & \boldsymbol{\rho} \in [\rho_{\min}, 1] \\ & \boldsymbol{\phi_1} \in [-3\pi/2, 3\pi/2] \\ & \boldsymbol{\alpha},\boldsymbol{\beta} \in [0,1]\times[0,1] \end{aligned} \qquad \text{(Problem 8)}$$

6.2 Conservative Strain Envelope Definition

When including a strength constraint in topology optimization for the optimization with respect to the anisotropic modules η_0 and η_1 in the geometric domain, an elliptic stress criterion as discussed in Section 4.3.1 can not be used straightforwardly. Indeed, when first ply failure for a composite is evaluated, a classical stress-based criterion is use to check each individual ply, with all quantities of interest expressed in a common reference frame, often that of the ply. That means that the applied laminate stresses are transformed to the ply reference frame through the local ply orientation. However, when considering the case of laminate optimization by means of the geometric bounds, the elastic properties are represented by an homogenized stiffness tensor. Thus, the corresponding physical stacking sequence is unknown, hence the orientations of the separate plies making up the laminate are also unknown. This means an elliptic failure criterion can not be applied to each ply separately. To counter this limitation, it is chosen to express a strain-based criterion as optimization constraint.

In the 2D framework of the present work, only in-plane loading and displacements are considered. Hence, the strains are constant over the thickness of an element, and all plies making up the laminate will therefore experience the same strains in the global reference frame, regardless of their orientations. It is the stiffness difference related to the orientation and change of reference frame that alters the stress in each ply, and leads to some plies failing before others. Nonetheless, as the strains are equal for all plies, it is a useful measure to define a strength criterion. Such criterion can be applied by a conservative strain envelope, as developed by IJsselmuiden *et al.* [167]. This envelope is constructed in such a way that no failure occurs according to a Tsai-Wu failure criterion expressed with strains in a global reference frame, regardless of the ply's orientation. It is a conservative approximation, as it uses the common admissible domain in the $\varepsilon_x, \varepsilon_y$ and $\gamma_x y$ space for any orientation, as represented in Figure 6.1. Depending on the base ply's stiffness and strength properties, two different cases are possible. The envelop of the admissible domain is defined by the intersection of a second-order equation and a fourth-order equation, as given by Equation 6.1. The critical envelope corresponds to the smallest positive real root s_1 of either condition. A more detailed explanation of the conservative envelope is given in Appendix A.

$$\begin{aligned} f_1(s_1) &:= a_{12}s_1^2 + a_{11}s_1 + a_{10} = 0 \\ f_2(s_1) &:= a_{24}s_1^4 + a_{23}s_1^3 + a_{22}s_1^2 + a_{21}s_1 + a_{20} = 0 \end{aligned} \tag{6.1}$$

The different a_{12} - a_{20} coefficients are given by Equation 6.2, based on the material properties $u_1 - u_6$ (given in Appendix A) and the strain invariants I_1 and I_2, defined in Equation 6.3. The material properties are constant in the optimization, as they only depend on the base ply used (*i.e.*, R_0^L, R_1^L, K^L and X_t, X_c, Y_t, Y_c, S). On the other hand, the strain invariants vary for each element at each iteration.

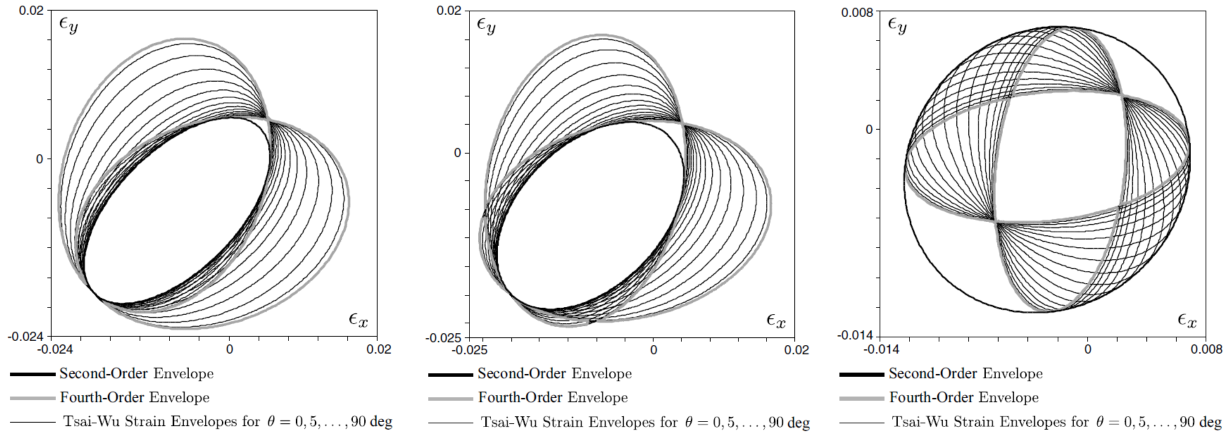

Figure 6.1: Second-order and fourth-order strain envelopes for any ply orientation for a Tsai-Wu failure criterion [167].

$$\begin{aligned} a_{10} &= u_4^2 + 4u_1 - 4u_6 \\ a_{11} &= -4u_2 I_1 (u_1 - u_6) + 2u_4 u_5 I_1 \\ a_{12} &= 4u_6^2 I_2^2 - 4u_3 I_1^2 (u_1 - u_6) \\ a_{20} &= 1 \\ a_{21} = -2u_2 I_1; a_{22} &= -2u_3 I_1^2 + u_2^2 I_1^2 - I_2^2 \left(u_4^2 + 2u_1\right) \\ a_{23} &= 2u_2 I_1^3 u_3 - I_2^2 (2u_4 u_5 I_1 - 2u_1 u_2 I_1) \\ a_{24} &= u_1^2 I_2^4 - I_2^2 \left(u_5^2 I_1^2 - 2u_1 u_3 I_1^2\right) + u_3^2 I_1^4 \end{aligned} \tag{6.2}$$

$$\begin{aligned} I_1 &= \varepsilon_x + \varepsilon_y \\ I_2 &= \sqrt{\left(\frac{\varepsilon_x - \varepsilon_y}{2}\right)^2 + \left(\frac{\gamma_{xy}}{2}\right)^2} \end{aligned} \tag{6.3}$$

Alternatively, a user-defined envelope expressed in global strains as shown in Equation 6.4 is also integrated, analogous to the elliptical Tsai-Wu criterion of Equation 4.23. $\boldsymbol{\varepsilon}^T$ contains the strain components $\{\varepsilon_x, \varepsilon_y, \gamma_{xy}\}$. The coefficients of $[M]$ and $\boldsymbol{N}$ in Equation 6.5 are the strains equivalent of the maximal allowable stresses (X_t, X_c, Y_t, Y_c, S) in Equation 4.23. These coefficients can be chosen as to represent a different envelope than Equation 6.1. It could be based on damage tolerance or limits for fatigue. The formulation of such user-defined envelope is not limited to the condition of Equation 6.4, and can be extended to higher degree relationships, as long as it is differentiable with respect to the strains to be incorporated in the current framework.

$$s_1^2 \boldsymbol{\varepsilon}^T [M] \boldsymbol{\varepsilon} + s_1 \boldsymbol{\varepsilon}^T \boldsymbol{N} - 1 = 0 \tag{6.4}$$

$$[M] = \begin{bmatrix} \frac{1}{\varepsilon_{x_t} \varepsilon_{x_c}} & \frac{M_{12}^*}{\sqrt{\varepsilon_{x_t} \varepsilon_{x_c} \varepsilon_{y_t} \varepsilon_{y_c}}} & 0 \\ \frac{M_{12}^*}{\sqrt{\varepsilon_{x_t} \varepsilon_{x_c} \varepsilon_{y_t} \varepsilon_{y_c}}} & \frac{1}{\varepsilon_{y_t} \varepsilon_{y_c}} & 0 \\ 0 & 0 & \frac{1}{\gamma_{xy_{\max}}^2} \end{bmatrix}; \boldsymbol{N} = \begin{Bmatrix} \frac{\varepsilon_{x_c} - \varepsilon_{x_t}}{\varepsilon_{x_t} \varepsilon_{x_c}} \\ \frac{\varepsilon_{y_c} - \varepsilon_{y_t}}{\varepsilon_{y_t} \varepsilon_{y_c}} \\ 0 \end{Bmatrix} \tag{6.5}$$

6.3 Equivalent Strain Value for the Optimization Constraint

This sections deals with the integration of a strain-based criterion in the topology optimization framework. First of all, an approach which uses an equivalent strain measure is tested, given by Equation 6.6. The equivalent strain, $\boldsymbol{\varepsilon}_{eq}$, is a function of the element's density depending on the power t. This is a similar idea as not using the macro stress directly in the computation of a strength criterion, but instead the micro stress. The equivalent strain will be the one used in either criterion of Equation 6.1 or Equation 6.5. The element's strains $\boldsymbol{\varepsilon}$ are obtained by means of Equation 6.7, where [B] is the strain displacement matrix obtained from the FEM formulation, and $\boldsymbol{U}_{(i)}$ the node displacements. The influence and selection of the t exponent value is discussed in Section 6.5.

$$\boldsymbol{\varepsilon}_{eq} = \rho^t \boldsymbol{\varepsilon} \tag{6.6}$$

$$\boldsymbol{\varepsilon}_{(i)} = [B]\boldsymbol{U}_{(i)} \tag{6.7}$$

As the criterion used herein is still an elliptic type with a load multiplier, the procedure to obtain the optimization constraint follows the one of Section 4.3.2, without the rotation effect. $fail_m$ is defined as the load multiplier s_1 satisfying Equation 6.1 or Equation 6.4, obtained by means Equation 6.8 or Equation 6.9 respectively. Thereafter, the local failure constraint g_i is obtained by means of Equation 6.10.

$$fail_m := s_1 = \min([\text{real}(\text{root}^+(f_1)), \text{real}(\text{root}^+(f_2))]) \tag{6.8}$$

$$fail_m := s_1 = \frac{-B + \sqrt{B^2 + 4A}}{2A} \quad \text{with} \quad A = \boldsymbol{\varepsilon}_{eq}^T [M] \boldsymbol{\varepsilon}_{eq} \quad \text{and} \quad B = \boldsymbol{\varepsilon}_{eq}^T \boldsymbol{N} \tag{6.9}$$

$$g_{(i)} := \frac{1}{fail_{m_{(i)}}} - 1 \leq 0 \tag{6.10}$$

Furthermore, the MPVC approach is also still used, therefore the total local constraint $\bar{g}_{(i)}$ is given by Equation 6.11.

$$\bar{g}_{(i)} := \rho_{(i)} g_{(i)} \leq 0 \tag{6.11}$$

Finally, the computational cost linked to the number of optimization constraints and their gradient still prevails. The lower KS aggregation function is used to reduce the amount of optimization constraints. Furthermore, the relaxation properties will be used in junction with the suggested equivalent strain measure to overcome possible strain singularities. These strain singularities are expected difficulties to remove low density elements and attain solutions laying in a degenerate space, equivalent to the stress singularities in stress-based optimizations. Therefore, the aggregated optimization constraint of the local constraints $\bar{g}_{(i)}$ is given by Equation 6.12. The strategy of using $\bar{g}_{\max}$, the maximum of the local constraint, to avoid numerical instabilities with the exponential function is still used, as explained in Section 4.2.1. An overview of the approach to obtain the optimization constraint is given in Figure 6.2.

$$g_k^{LKS} = \bar{g}_{\max} + \frac{1}{\mu} \ln \left[\frac{1}{N} \sum_{j \in \Omega_k} \exp \left(\mu \left[\rho_{(j)} \left(\frac{1}{s_{1_{(j)}}} - 1 \right) - \bar{g}_{\max} \right] \right) \right] \tag{6.12}$$

6.4 Conservative Strain Envelope Gradient Definition

This section details the gradient computations with a strain-based criterion with respect to any of the topology and anisotropy variables, represented by ψ_i in the subsequent steps. The gradient definition is similar to the one for stress-based constraints, except no rotation is involved, and the strain does not depend on the

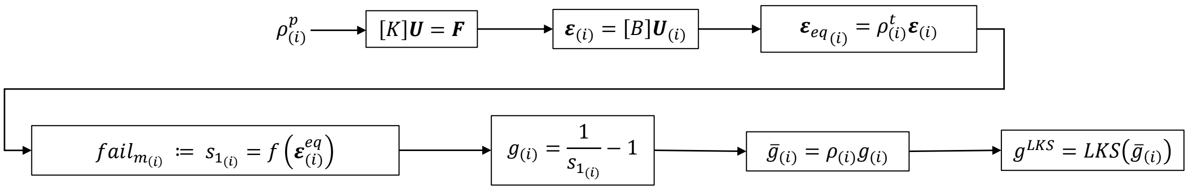

Figure 6.2: Steps used to obtain the global failure optimization constraint for a strain-based criterion.

stiffness tensor. Starting from the aggregation derivative of Equation 4.12, the chain rule of the local strain constraint $\bar{g}_{(j)}$ is given by Equation 6.13.

$$\frac{\partial \bar{g}_{(j)}}{\partial \psi_{(i)}} = \frac{\partial(\rho_{(j)})}{\partial \psi_{(i)}} g_{(j)} + \rho_{(j)} \frac{\partial g_{(j)}}{\partial fail_{m_{(j)}}} \left(\frac{\partial fail_{m_{(j)}}}{\partial \boldsymbol{\varepsilon}_{eq_{(j)}}} \right)^T \frac{\partial \boldsymbol{\varepsilon}_{eq_{(j)}}}{\partial \psi_{(i)}} \tag{6.13}$$

The first part of Equation 6.13 is straightforward, and only computed for the density variables. For the second part, the first term $\frac{\partial g_{(j)}}{\partial fail_{m_{(i)}}}$ is given by Equation 4.40. The second term, the vector $\frac{\partial fail_{m_{(i)}}}{\partial \boldsymbol{\varepsilon}_{eq_{(j)}}}$, is obtained by means of a central finite difference scheme, regardless of the conservative envelope of Equation 6.8 or the user defined envelope of Equation 6.9. It has a negligible computational cost.

$$\frac{\partial fail_{m_{(j)}}}{\partial \boldsymbol{\varepsilon}_{eq_{(j)}}} \approx \frac{fail_{m_{(j)}}(\boldsymbol{\varepsilon}_{eq_{(j)}} + \Delta\boldsymbol{\varepsilon}_{eq}) - fail_{m_{(j)}}(\boldsymbol{\varepsilon}_{eq_{(j)}} - \Delta\boldsymbol{\varepsilon}_{eq})}{2\Delta\boldsymbol{\varepsilon}_{eq}} \tag{6.14}$$

Thereafter, from the equivalent strain definition of Equation 6.6, the last part of the derivative can be obtained. As for a stress constraint gradient, this part involves the change of the load path due to the change in stiffness of an element. Using the same approach in Section 4.2.2, with the substitution of Equation 4.17, Equation 6.15 is obtained.

$$\frac{\partial \boldsymbol{\varepsilon}_{eq_{(j)}}}{\partial \psi_{(i)}} = \frac{\partial \rho^t_{(j)}}{\partial \psi_{(i)}} [B]\boldsymbol{U}_{(j)} - \rho^t_{(j)}[B][K]^{-1} \left(\frac{\partial [K]}{\partial \psi_{(i)}} \boldsymbol{U} \right) \tag{6.15}$$

Finally, combining Equation 4.12 and Equation 4.40 with the derived expressions, Equation 6.16 with the adjoint vector $\boldsymbol{\lambda}_k$ of Equation 6.17 are obtained for the gradient with respect to any topology or anisotropic variable $\psi_{(i)}$. As the failure criterion is already expressed in the global coordinate system, no part of the gradient depends on the rotation and change of reference frame. The adjoint vector still is the same regardless of the variable gradient. Hence, the total cost to compute the gradient with respect to all variables is still equivalent to solving one additional FEM analysis. Furthermore, the gradient with respect to the remapping variables α and β to enforce the geometric bounds on the anisotropy, are still obtained from the chain rule of Equation 3.18. In a similar way, the filter operations are taken care of by means of Equation 3.19.

$$\begin{aligned} \frac{\partial g^{LKS}_k}{\partial \psi_{(i)}} = {} & \frac{1}{\sum_{j\in\Omega_k} \exp\left(\mu(\bar{g}_{(j)} - \bar{g}_{\max})\right)} \left(\sum_{j\in\Omega_k} \left[\exp\left(\mu(\bar{g}_{(j)} - \bar{g}_{\max})\right) \right.\right. \\ & \left.\left. \left(\frac{\partial \rho_{(j)}}{\partial \psi_{(i)}} g_{(j)} + \frac{\partial g_{(j)}}{\partial fail_{m_{(j)}}} \left(\frac{\partial fail_{m_{(j)}}}{\partial \boldsymbol{\varepsilon}_{eq_{(j)}}} \right)^T \frac{\partial \rho^t_{(j)}}{\partial \psi_{(i)}} [B]\boldsymbol{U}_{(j)} \right) \right] - \boldsymbol{\lambda}^T_k \left(\frac{\partial [K]}{\partial \psi_{(i)}} \boldsymbol{U} \right) \right) \end{aligned} \tag{6.16}$$

$$[K]\boldsymbol{\lambda}_k = \sum_{j\in\Omega_k} \exp\left(\mu(\bar{g}_{(j)} - \bar{g}_{\max})\right) \frac{\partial g_{(j)}}{\partial fail_{m_{(j)}}} \rho^t_{(j)} [B]^T \left(\frac{\partial fail_{m_{(j)}}}{\partial \boldsymbol{\varepsilon}_{eq_{(j)}}} \right)^T \tag{6.17}$$

Elliptic Strain Constraint Summary with Anisotropic Material

Optimization constraint

$$g_k^{LKS} = \bar{g}_{\max} + \frac{1}{\mu}\ln\left[\frac{1}{N}\sum_{j\in\Omega_k}\exp\left(\mu\left[\rho_{(j)}\left(\frac{1}{s_{1_{(j)}}}-1\right)-\bar{g}_{\max}\right]\right)\right]$$

Optimization constraint gradient

$$\frac{\partial g_k^{LKS}}{\partial\psi_{(i)}} = \frac{1}{\sum_{j\in\Omega_k}\exp\left(\mu(\bar{g}_{(j)}-\bar{g}_{\max})\right)}\left(\sum_{j\in\Omega_k}\left[\exp\left(\mu(\bar{g}_{(j)}-\bar{g}_{\max})\right)\right.\right.$$
$$\left.\left.\left(\frac{\partial\rho_{(j)}}{\partial\psi_{(i)}}g_{(j)} + \frac{\partial g_{(j)}}{\partial fail_{m_{(j)}}}\left(\frac{\partial fail_{m_{(j)}}}{\partial\boldsymbol{\varepsilon}_{eq_{(j)}}}\right)^T\frac{\partial\rho^t_{(j)}}{\partial\psi_{(i)}}[B]\boldsymbol{U}_{(j)}\right)\right] - \boldsymbol{\lambda}_k^T\left(\frac{\partial[K]}{\partial\psi_{(i)}}\boldsymbol{U}\right)\right)$$

Adjoint vector

$$[K]\boldsymbol{\lambda}_k = \sum_{j\in\Omega_k}\exp\left(\mu(\bar{g}_{(j)}-\bar{g}_{\max})\right)\frac{\partial g_{(j)}}{\partial fail_{m_{(j)}}}\rho^t_{(j)}[B]^T\left(\frac{\partial fail_{m_{(j)}}}{\partial\boldsymbol{\varepsilon}_{eq_{(j)}}}\right)^T$$

6.5 Validation of the Strain-Based Topology Optimization

This sections deals with the influence of the t exponent value in the equivalent strain definition of Equation 6.6 for a strain-based topology optimization. As a validation step for strain-based topology optimization, a comparison with a stress-based optimization is conducted. A volume minimization with a Von Mises stress constraint for an isotropic material is considered, as defined in Problem 9. The stress constraint is translated to an equivalent strain constraint. The optimization uses the properties listed in Table 6.1, and is performed for 1000 iterations. One cluster is still being used, consisting of all the elements which are being optimized.

$$\begin{aligned} \min_{\boldsymbol{\rho}} \quad & v_f(\boldsymbol{\rho}) \\ \text{s.t.} \quad & g^{LKS}(\varepsilon\boldsymbol{\rho}) \leq 0 \\ & \boldsymbol{\rho} \in [\rho_{\min}, 1] \end{aligned} \tag{Problem 9}$$

Table 6.1: Stress and strain-based topology optimization properties with an isotropic material and Von Mises criterion.

F [N]	R_ρ [mm]	N	μ [-]	T_0 [GPa]	T_1 [GPa]	σ^Y [MPa]
200.0	2.5	50.0	30.0	26.9	24.7	50.0

The stress-based optimization constraint g_k^{LKS} is defined by means of Equation 4.11, whereas the strain-based optimization is defined by the user-defined envelope of Equation 6.4. To obtain the equivalent strain coefficient for Equation 6.5, the following procedure has been used. For a range of test strain combinations, the load multiplier s_1 of the Von Mises stress can be obtained from Equation 6.18. [V] is the transformation matrix of Equation 4.6 and the stress-strain relationship of Equation 4.1 has been used. Therefore the load multiplier to reach the yield stress σ^Y is given by Equation 6.19.

$$\sigma^{VM}(s_1) = \sqrt{s_1\sigma^T[V]s_1\sigma} = \sqrt{(s_1[Q]\varepsilon)^T[V](s_1[Q]\varepsilon)} \tag{6.18}$$

$$\sigma^{VM}(s_1) = \sigma^Y \rightarrow s_1 = \frac{\sigma^Y}{\sqrt{([Q]\varepsilon)^T[V][Q]\varepsilon}} \tag{6.19}$$

Thereafter, the coefficients of the user-defined strain envelope can be found by matching the Von Mises criterion expressed in strains, as shown in Figure 6.3. The corresponding coefficient values are given in Table 6.2. All ε_{x_t}, ε_{x_c}, ε_{y_t} and ε_{y_c} are given the same value, which equals s_1 for any test strain vector with 0 shear strain in Equation 6.19. M^*_{12} is set to 0, as for the given stiffness properties, there is no apparent interaction between ε_x and ε_y. Lastly, $\gamma_{xy_{\max}}$ equals s_1 as obtained for the test strain vector $\boldsymbol{\varepsilon}^T$ $\{0, 0, 1\}$ in Equation 6.19.

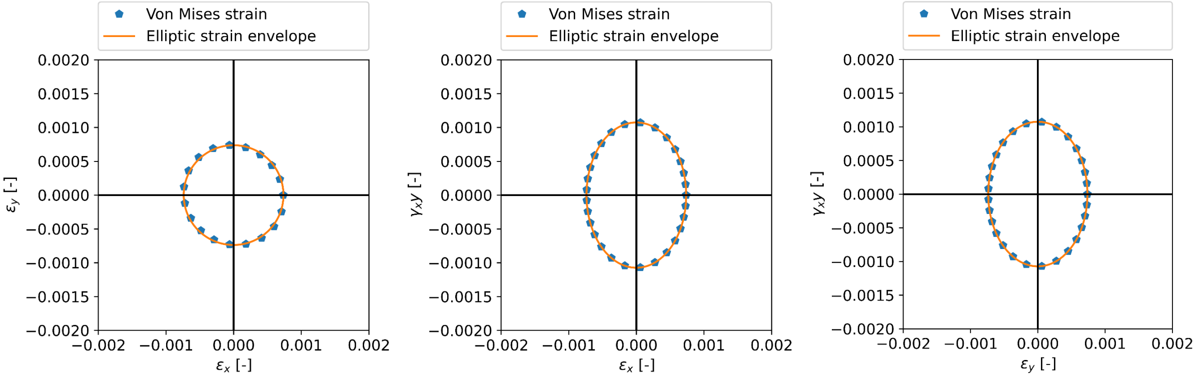

Figure 6.3: Von Mises stress criterion expressed in terms of global strains and its approximated strain envelope.

Table 6.2: Strain coefficient for the user-defined envelope to express a Von Mises stress criterion in terms of global strains.

ε_{x_t} [-]	ε_{x_c} [-]	ε_{y_t} [-]	ε_{y_c} [-]	M^*_{12} [-]	$\gamma_{xy_{\max}}$ [-]
7.37e-4	7.37e-4	7.37e-4	7.373e-4	0	1.07e-3

The results of the stress-based and strain-based optimization with $t = 0$ and $t = 1$ are shown in Figure 6.4. Figure 6.5 shows the final topologies for an additional range of t exponents for non-conclusive optimizations. Both strain-based optimizations give reasonable results. Looking at the convergence plot, especially of the constraint evolution, of all three successful optimizations, both stress-based and strain-based with $t = 0$ start with a high violated constraint which is satisfied in a similar fashion throughout the iterations. On the other hand, the strain-based $t = 1$ optimization starts with a satisfied constraint. This is due to the implementation and density filter, which assigns an intermediate density for the border elements where the stress concentration is located. Having this intermediate density in combination with the $t = 1$ exponent in Equation 6.6 under-predicts the local constraint by exaggerating the reduction of the strain value. It does however not hinder the optimization to correctly satisfy the constraint during the iterations for full density elements. Once the optimization constraint is satisfied, all three objective minimization behave similarly, with the $t = 1$ optimization converging faster initially. Comparing solutions, the strain-based $t = 0$ topology and local constraint distribution resembles closely the stress-based solution. This is corroborated by the similar mechanical properties, such as the final volume and compliance. On the contrary, despite the $t = 1$ strain-based solution having similar bar distributions, its final volume is far lower than the stress-based case.

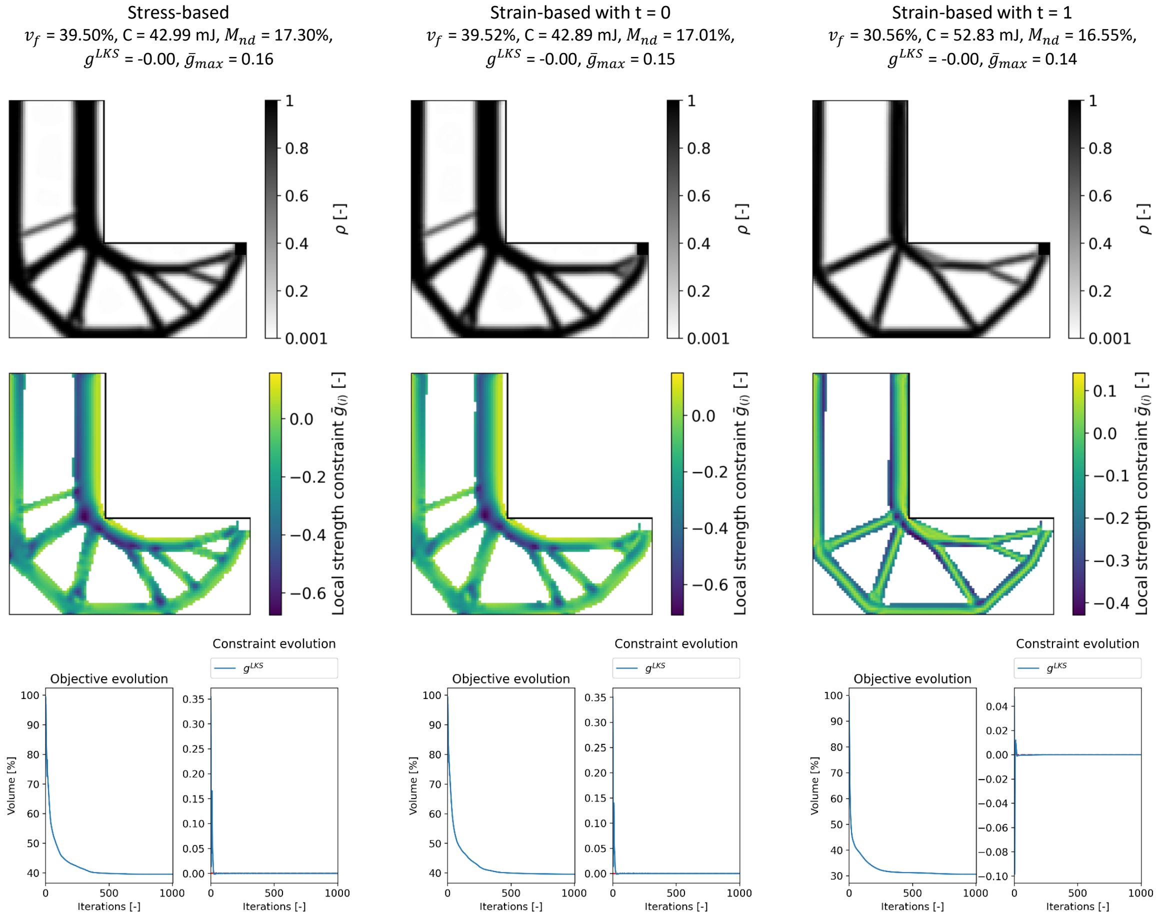

Figure 6.4: Comparison of a volume minimization strength-based topology optimization with a stress-based and strain-based formulation of the Von Mises criterion, and for different t values for ε_{eq} of Equation 6.6.

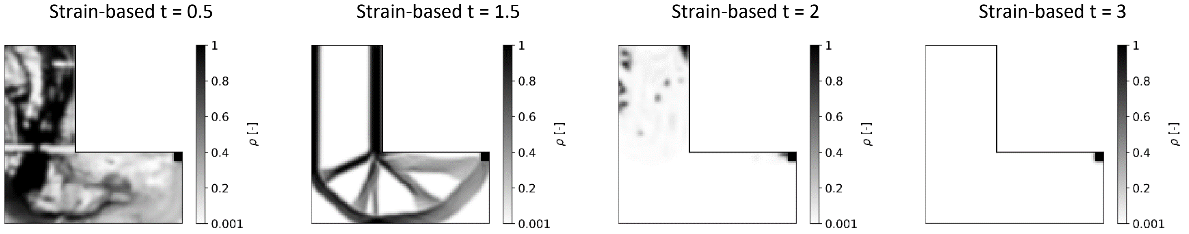

Figure 6.5: Unsuccessful strain-based topology optimization with different t values for ε_{eq} of Equation 6.6.

It shows again that it under-predicts the strength constraint. This is because there is too much incentive for the solution to have intermediate densities, by reducing their strain values. This allows to easier satisfy the constraint. This effect is visible at all bar edges where there are intermediate densities due to the filter, and the constraint is very low compared to the inside of the bars. This is the opposite of the stress-based and $t = 0$ case, where these outer densities have at least an equally local constraint $\bar{g}_{(i)}$ value than the inner ones of the bars. Finally, the $t = 1$ optimization was not able to remove all the intermediate material just right of the re-entrant corner, not providing a fully converged structure.

Hence, the best way to perform a strain-based optimization is with an exponent $t = 0$ in Equation 6.6, meaning $\boldsymbol{\varepsilon}_{eq}$ is just defined by Equation 6.7. There is no influence or need of altering the strain values for low density, and possible singularity problems are resolved by the relaxation property of the lower KS function. This provides results similar to a stress-based topology optimization. The $t = 0$ value also makes sense, as with the stress-based approach, the aggregation happens with the pristine stiffness tensor $[Q_0]$ to relate micro-stress to the strain in Equation 4.4. When only the strains are considered, there is no more dependency on the stiffness $[Q_0]$, yet the strain measure is not altered. This section shows that strain based topology optimization is feasible, using an exponent $t = 0$.

6.6 Topology and Anisotropy Optimization with a Conservative Tsai-Wu Strain Envelope

This section considers the volume minimization problem with a strain-based constraint (Problem 6). It compares the case of a single UD ply, which is rotated, to the case of a laminate restricted by the geometric bounds. The strength constraint is in both cases enforced by the conservative Tsai-Wu envelope formulation of Equation 6.1, as both optimizations are based on the same material. The material properties are the ones already used in Section 5.6, repeated in Table 6.3. The specific conservative strain envelope for this material is dictated by the fourth-order envelopes, as shown in Figure 6.6. Each optimization is initialized with densities = 1, and an anisotropy distribution stemming from a preliminary compliance minimization step (35 iterations). The total applied load is 200 N, and a normalization factor $N_0 = 50$. This is a lower load magnitude compared to the case where the actual UD allowables are considered in Section 5.6, as a conservative envelope is used. This feature is well illustrated in Figure 6.6, where the horizontal blue envelope are the allowable strain for a 0° ply, and the vertical one for a 90° ply. The conservative envelope is the orange part, which only uses part of the full allowable strain for a given orientation. The green line represents the strain envelope for a 45° ply. A filter on the orientations is still used, but not extended to the modules.

Table 6.3: Optimization parameters and UD ply [8] properties for optimizations with a conservative Tsai-Wu strain-based constraint.

Modules	Values	Polar parameters	Values
E_{11} [GPa]	39.0	T_0^L [GPa]	7.6
E_{22} [GPa]	8.4	T_1^L [GPa]	6.6
G_{12} [GPa]	4.2	η_0^L [-]	0.44
ν_{12} [-]	0.26	η_1^L [-]	0.55

R_ρ [mm]	R_{ϕ_1} [mm]	μ [-]	X_t [MPa]	X_c [MPa]	Y_t [MPa]	Y_c [MPa]	S [MPa]
2.0	2.0	30.0	1062.0	610.0	31.0	118.0	72.0

6.6.1 Considering Material Orientations for a Uni-Directional Ply

The solution considering fiber steering is shown in Figure 6.7. The solution is has similar characteristics to that in Section 5.6, with the fiber orientations aligned with the bars. Looking at the local strength constraint, the solution is however not fully solicited, especially in the left and lower bars. These are compressive members, with higher strains allowables as is visible in Figure 6.6. It means their cross-sections could be reduced to be more solicited, however the density filter does not allow for smaller bar sizes. Instead, the densities could

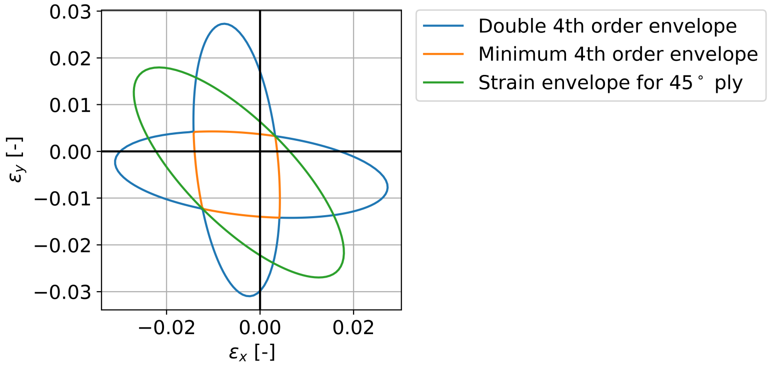

Figure 6.6: Conservative Tsai-Wu strain envelope for the material properties in Table 6.3.

become intermediate for those bars, as in Section 5.5. This is not achieved for the current solution. This is attributed to the discontinuity in the fourth-order envelope, where the gradient does not characterize the design space well. Therefore the optimization remains trapped in a local minimum for those compressive bars. Nonetheless, the convergence graph shows that the strain constraint is well satisfied and well taken into account by the SplitMMA strategy when it comes to topology and UD orientation optimization. Furthermore, ensuing results with a smooth definition of the strain envelope can obtain much more solicited bars for strain-based topology optimization.

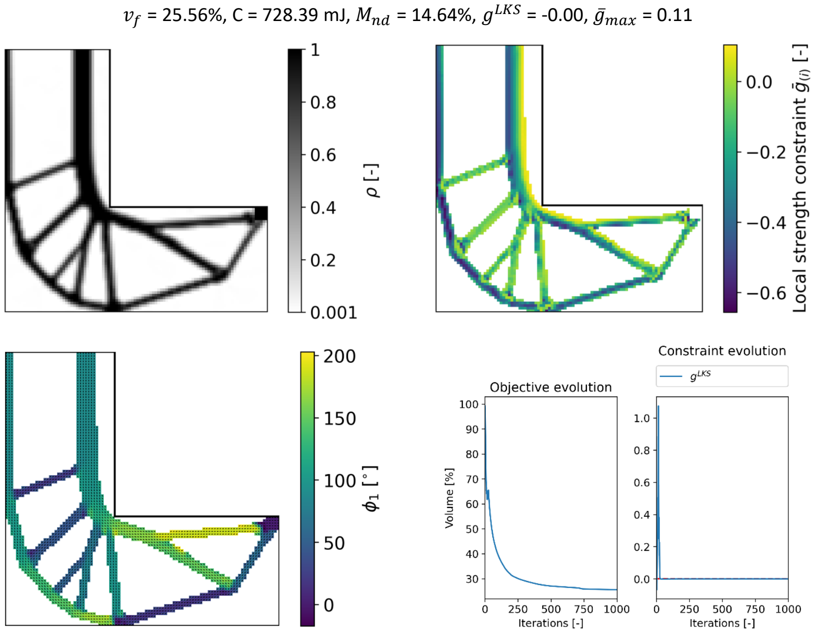

Figure 6.7: Solution for a volume minimization with respect to both material density and orientation, with a conservative Tsai-Wu strain criterion for both topology and orientation optimization of a UD ply. Information shown for optimized elements with a final density ≥ 0.3.

The same optimization, a volume minimization with strength constraint with respect to density and material orientation, can be performed, but taking the actual stress-based Tsai-Wu criterion into account (Problem 2). These results are displayed in Figure 6.8. It shows that a much lighter solution is obtained (a volume of 12.76% versus 25.56%), where the bars with the stress-based criterion are much thinner. The bars are restricted from becoming even more thinner by the density filter. So most densities have an intermediate value. In case of the strain-based conservative envelope, only part of the high material strength is retained, as shown in Figure 6.6. When the stress-based criterion is used instead, the complete strength performance of the UD fiber can be used, requiring less volume.

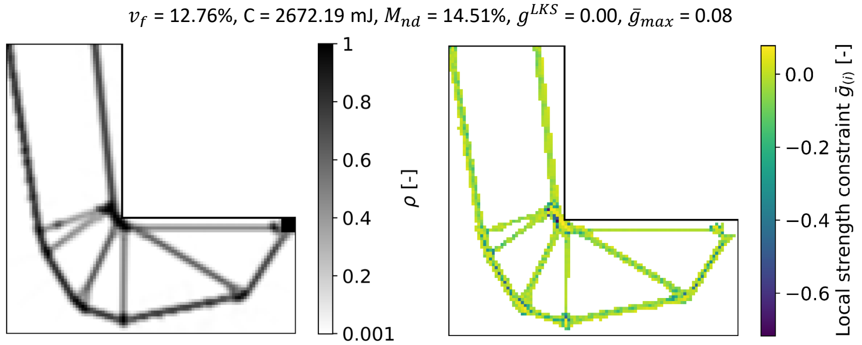

v_f = 12.76%, C = 2672.19 mJ, M_{nd} = 14.51%, g^{LKS} = 0.00, $\bar{g}_{max}$ = 0.08

Figure 6.8: Solution for a volume minimization with respect to both material density and orientation, with a Tsai-Wu stress criterion for both topology and orientation optimization of a UD ply. Information shown for optimized elements with a final density ≥ 0.3.

6.6.2 Considering Laminates

The solution of the optimization with a conservative strain envelope considering a laminate is shown in Figure 6.9. The anisotropy, both material orientation and modules, is initialized from the preliminary compliance minimization. The optimized laminate solution is less stiff and heavier than the fiber steering solution of Figure 6.7, with a different topology. This has several reasons, starting with the initialization of both problems, displayed in Figure 6.10.

It can be seen that not all the initial anisotropy conditions are equivalent to that of a UD ply (represented by $\eta_0/\eta_0^L = \eta_1/\eta_1^L = 1$). Furthermore, the $\eta_0/\eta_0^L = -1$ lines are induced by the orientation filter and transition zone of opposite orientation. This effect remains visible in the optimized solution. As already discussed in Section 5.6, a better filter taking into account opposite orientation could be integrated in the future. Moreover, a filter has not been used with the modules, but could also reduce the noise and variation as suggested in Section 3.5.2. It would be best to consider a filter which considers the physical tensor quantities, as they provide the actual stiffness distribution. Nonetheless, both solutions start from different points, where the laminate one already contains some inconsistencies, and obviously end in a different local minima. This local minima is just a less good one than the UD case, where the compressive bars are still not fully solicited.

The optimization with a laminate is therefore also attempted starting from the distributed UD initialization, with results shown in Figure 6.11. A similar topology is obtained as in Figure 6.10, but smoother anisotropy fields are obtained, as the optimization is not influenced by the initialization defects on the anisotropic modules due to the orientation filter. The solution of Figure 6.11 also has a lower volume (27.57% vs 28.57%) than the solution in Figure 6.9 (28.57%). Nonetheless, despite the laminate case encompassing the UD condition and starting from the same design point, neither laminate optimization does tend to the UD solution, both topology and volume-wise.

This is because the laminate optimization problem has more variables by means of the anisotropic modules and therefore a more complex design space. The gradient with respect to those additional variables will

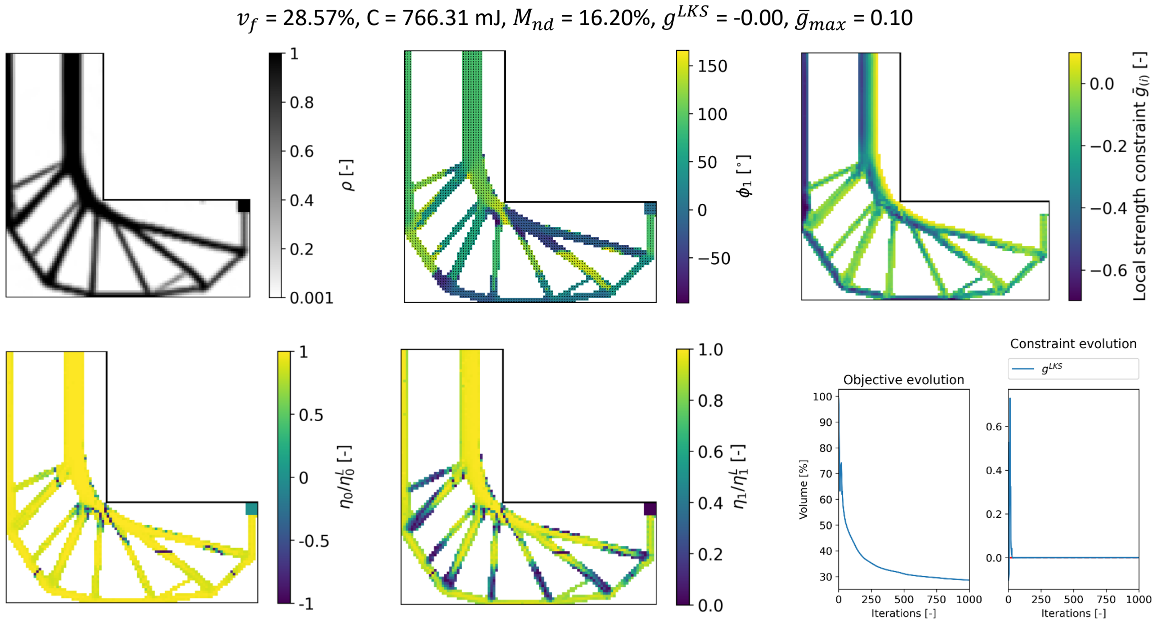

Figure 6.9: Solution for a volume minimization with a conservative Tsai-Wu strain criterion considering the topology and a laminate. Information shown for optimized elements with a final density ≥ 0.3.

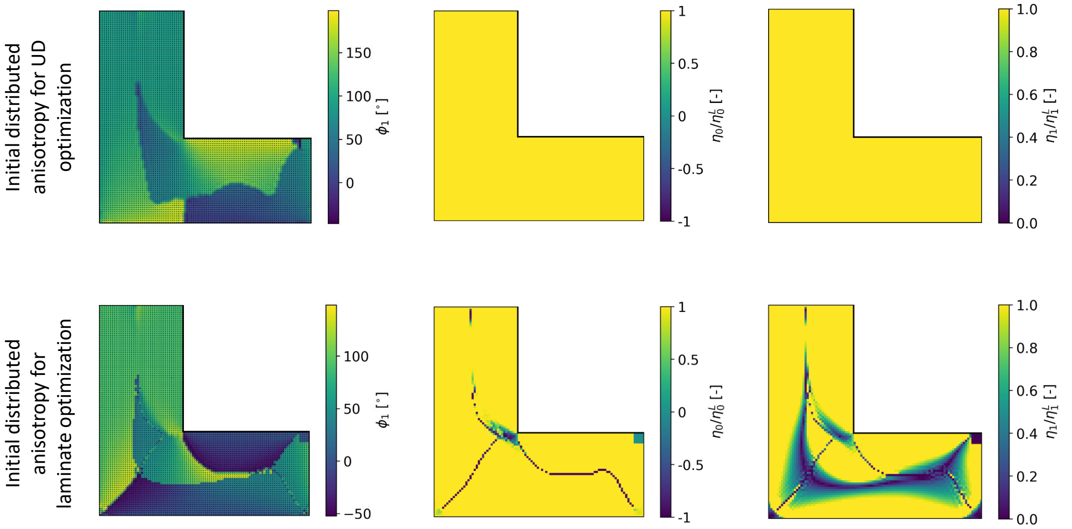

Figure 6.10: Anisotropy initialization for a UD orientation or laminate topology optimization.

numerically never be 0, and therefore influences the solution to using different stiffness properties which still fulfill the constraint requirement. Looking at the anisotropy distribution of the optimized solution, there are locations in the smaller bars where the orientations are not aligned with the bars. This correspond to $\eta_1/\eta_1^L = 0$ values, meaning square anisotropy. This entails that the stiffness properties along ϕ_1 and orthogonal to it are the same. The reason for this material stiffness distribution is that the only incentive is to satisfy the strain constraint, which the obtained distribution fulfills. There is no compliance consideration,

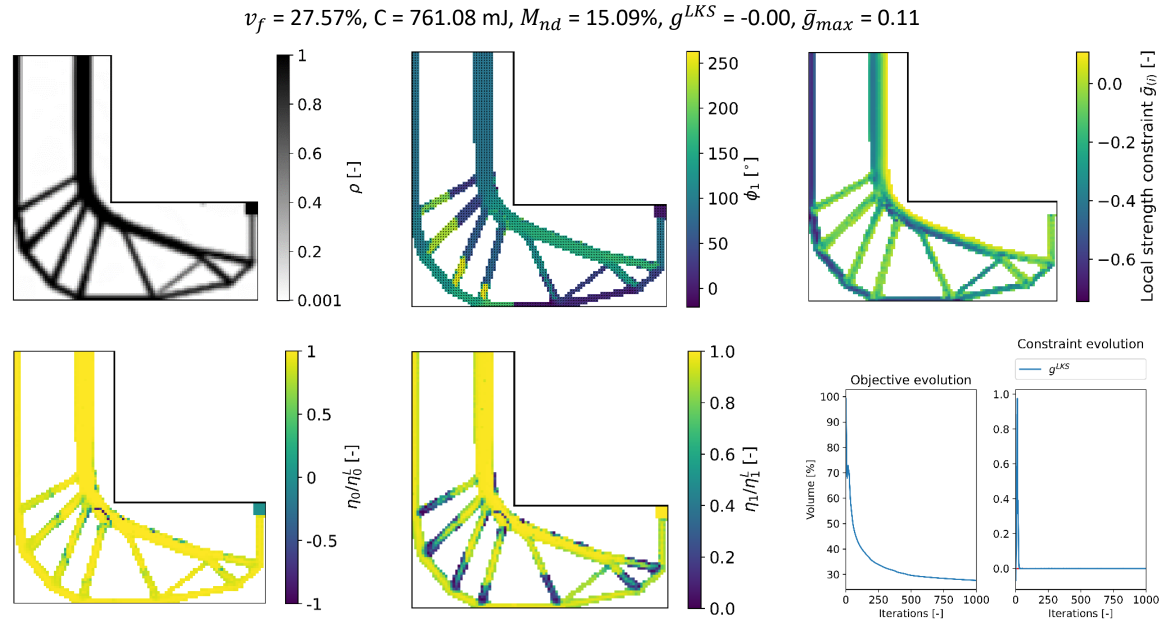

Figure 6.11: Solution for a volume minimization with a conservative Tsai-Wu strain criterion considering the topology and a laminate. Information shown for optimized elements with a final density ≥ 0.3.

the latter favoring $\eta_1/\eta_1^L = 1$ conditions. These initialization issues are problem specific for a volume minimization where no stiffness is considered. As was shown in Section 3.5.2, the distributed anisotropy initialization is important for compliance minimization. Therefore, the anisotropy for a laminate is still used in subsequent optimizations. Finally, observing the convergence graphs shows that SplitMMA can well satisfy the optimization constraint without considering cross-influence of variables with strain-based constraints, and also decrease the objective as asked. It also shows the compatible of the strain-based optimization with the remapping of the geometric bounds for the anisotropic modules and their domain of existence.

6.7 Influence of Different Optimization Problem Formulations with a User-Defined Envelope

This section considers different problem formulations for topology optimization with laminates and a user defined strain envelope. The aim is to evaluate the effect of changing the optimization problem formulation (changing the objective, but also considering different constraints) on the optimized solutions. The material stiffness properties of Table 6.3 are still being used. The strain-envelope properties are given in Table 6.4, and is represented in Figure 6.12 along the previously used conservative Tsai-Wu strain envelope. The current user-defined envelope allows for higher tensile strain allowables compared to the Tsai-Wu strain envelope. This is chosen as to not favor compressive regions in the final topology, which in a real structure would lead to buckling. The initial anisotropy distribution for the topology optimization is obtained from a compliance minimization problem with respect to the anisotropy variables only at fixed densities of 1 for all cases. Each optimization is performed for 1000 fixed iterations, and a total applied load of 400 N.

Table 6.4: Optimization parameters and user-defined strain envelope properties for optimizations with a strain-based constraint.

R_ρ [mm]	R_{ϕ_1} [mm]	μ [-]	ε_{x_t} [-]	ε_{x_c} [-]	ε_{y_t} [-]	ε_{y_c} [-]	M_{12}^* [-]	$\gamma_{xy_{\max}}$ [-]
2.0	2.0	30.0	0.012	0.012	0.01	0.011	-0.5	0.005

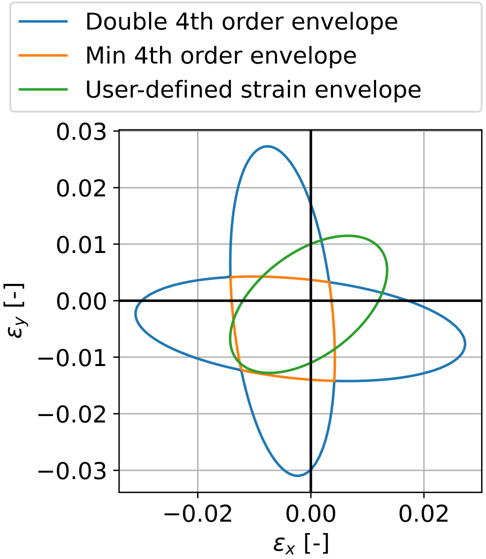

Figure 6.12: User-defined and conservative Tsai-Wu strain envelope.

6.7.1 Volume Minimization with a Strain-Based Strength Constraint

The initial optimization problem consists in a volume minimization with a strain-based constraint (Problem 6), with a normalization factor $N_0 = 50$. It serves as a benchmark for a comparison with subsequent different problem formulations, both in variable distributions and optimized mechanical properties. The results of this optimization are displayed in Figure 6.13.

Similarly to Figure 6.9, the optimized design exhibit well solicited features. The re-entrant corner has moved to the left, creating a small local radius. That radius is not as large as in case of isotropic material. In the current case, the anisotropic stiffness distribution can also be used to relieve the stress concentration, by adapting the load path. The anisotropy variables behave similarly as in case of Figure 6.9, showing the same distribution properties (transition in ϕ_1 with resulting $\eta_0/\eta_0^L = 0$, $\eta_1/\eta_1^L = 0$ in the smaller bars) for the same reasons explained beforehand. Nonetheless, is can be noted that the right vertical bar has a smaller width difference to the left bar than in Figure 6.9. This is because the tensile and compressive allowables are much closer in magnitude. The right bar width is still larger than the left bar, as the right bar has a higher internal loading, as can be estimated from static equilibrium.

6.7.2 Compliance Minimization with a Volume Constraint

This part deals with compliance minimization with a volume constraint representing 3.12. The volume constraint is based on the final volume v_f of the solution in Figure 6.13, namely 31.5%. A normalization factor N_0 of 25 is used. The results of the optimization can be seen in Figure 6.14.

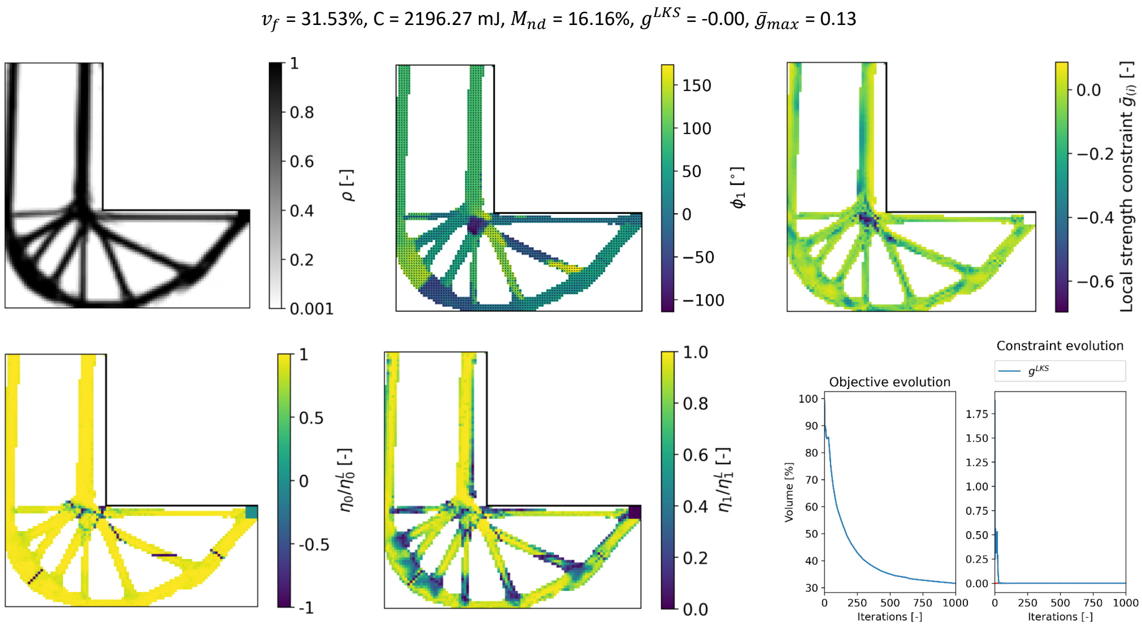
v_f = 31.53%, C = 2196.27 mJ, M_{nd} = 16.16%, g^{LKS} = -0.00, $\bar{g}_{max}$ = 0.13

Figure 6.13: Results of a volume minimization considering laminates with a user-defined strain-envelope constraint. Information shown for optimized elements with a final density ≥ 0.3.

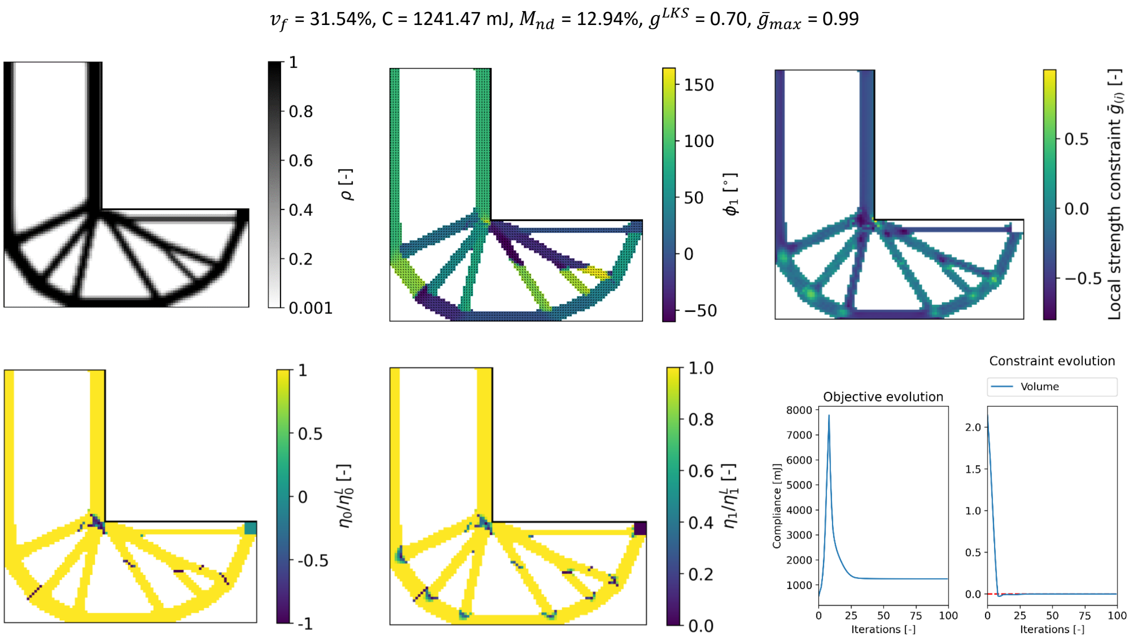
v_f = 31.54%, C = 1241.47 mJ, M_{nd} = 12.94%, g^{LKS} = 0.70, $\bar{g}_{max}$ = 0.99

Figure 6.14: Results of a topology optimization considering laminates for a compliance minimization with volume constraint. Information shown for optimized elements with a final density ≥ 0.3.

The figure shows the local strength constraint $\bar{g}_{(i)}$ evaluated with the same user-defined envelope than previously. It clearly highlights the local stress concentration. On the other hand, the compliance value has decreased a lot, with a decrease of 43.5% from 2196.23 mJ to 1241.47 mJ. This is to be expected, as the compliance is the objective to minimize. But it should also be noted that in case of Figure 6.13, stiffness is not a design criterion. The better compliance value is also obtained thanks to the anisotropic modules' distribution as given in Figure 6.15. Figure 6.15a shows the anisotropic modules for compliance minimization. Most of the modules have a value of $\eta_0/\eta_0^L = 1$ and tend to be pure UD ($\eta_1/\eta_1^L = 1$) or have a square symmetry of a balanced number of 0° and 90° layers cross-ply ($\eta_1 = 0$). Instead, Figure 6.15b shows the anisotropic modules' distribution corresponding to Figure 6.13. The modules are more dispersed over the domain, as the optimization for Figure 6.13 does not consider any stiffness, either as objective or constraint.

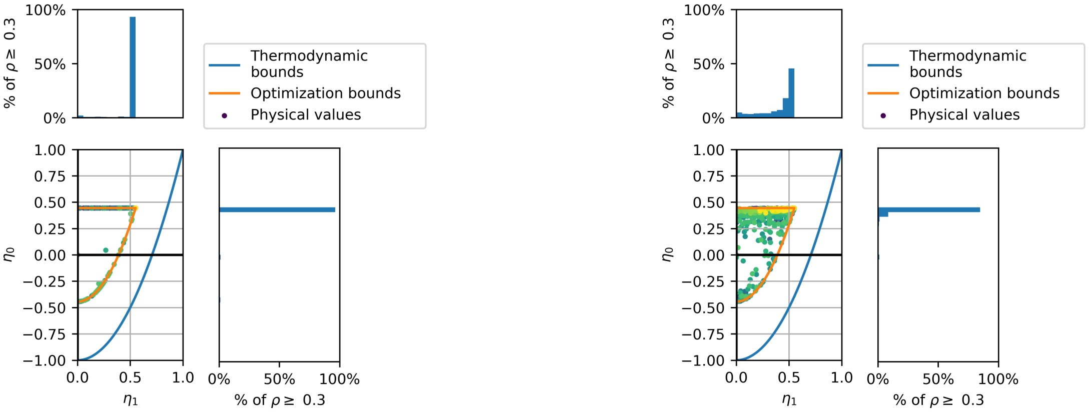

(a) Results of a compliance minimization with volume constraint of Figure 6.14.

(b) Results of a volume minimization with strain constraint of Figure 6.13.

Figure 6.15: Anisotropic modules' distribution within the geometric and thermodynamic domain.

6.7.3 Volume Minimization with Strain-Based Strength and Compliance Constraints

Both previous optimizations were based on only two design criteria, with either a strength constrained volume minimization or a volume constrained compliance minimization, for a 400 N load case. The current optimization problem will investigate the effect of considering all three criteria (volume, stiffness and strength) into a single topology optimization. In this case, it will more precisely be a volume minimization, according to Problem 6, with a compliance constraint of 1241.52 mJ as obtained in Figure 6.14 and the user-defined strain envelope. A normalization factor $N_0 = 25$ is used. The results are shown in Figure 6.16.

The optimized volume is 33.3%, about a 5% increase over the solution in Figure 6.14. As the applied load magnitude is still low, the right angle topology has reappeared at the re-entrant corner but the stress concentration has been alleviated by adapting the anisotropy during the optimization. The vertical bars have a low local strength constraint, as their primordial aim is for stiffness maximization and therefore have an associated larger width. This is opposite to the smaller bars at the bottom. These have for the majority a large local strength constraint, hinting at them being more constrained by the strength requirement. As these locations also show η_1/η_1^L variables which are not close to the stiffness condition, this could suggest being stuck in a local minima. When performing an optimization, the constraints are there to be satisfied, whereas the objective to be minimized. Therefore, the constraints do not drive the optimization once satisfied, showing the variable distribution in the lower bars not being exactly in accordance with the case of stiffness minimization. Furthermore, the volume objective in this case does not depend on the anisotropy. The anisotropy therefore only acts on the constraints, and through them indirectly on the volume. The dual optimization problem will be considered next, explicitly minimizing the compliance.

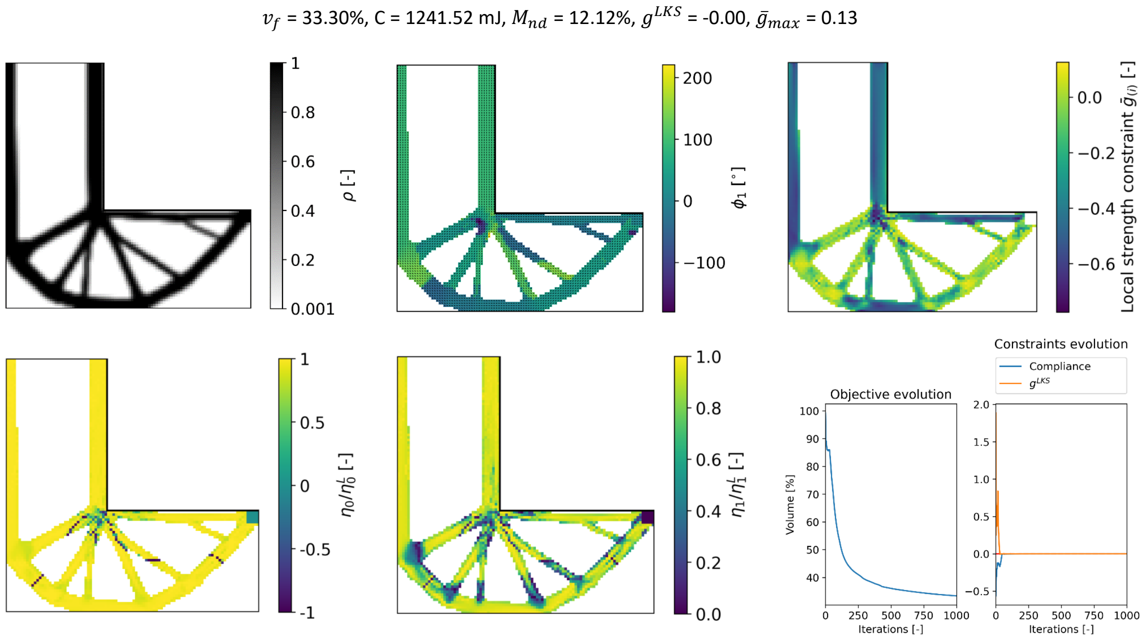

Figure 6.16: Results of a volume minimization considering laminates with user-defined strain-envelope and compliance constraints. Information shown for optimized elements with a final density ≥ 0.3.

6.7.4 Compliance Minimization with Strain-Based Strength and Volume Constraints

Lastly, a compliance minimization with volume and strength constraints (Problem 8) is carried out. The v_f volume constraint is kept at 31.51%, and a normalization factor $N_0 = 25$. The results are shown in Figure 6.17.

It could first be thought that as the solution in Figure 6.13 is well solicited, using that volume constraint would lead to an infeasible point. This would have likely been the case with an isotropic material. Nonetheless, a stiffer solution is found which is less strength constrained. This can be explained by the fact that beside the topology, the material anisotropy is also used in first satisfying the strength constraint and thereafter the compliance minimization. The constraints' evolution shows that the optimization initially tries to satisfy the volume constraint, reducing the volume from all full elements towards the target volume density. However in doing so, the strength constraint rises as it is more important in intermediate density elements. But once close to the target volume, the optimization starts creating a more distinct solution, and converging to full density elements at high local constraint zones, bringing the strength constraint under control and towards 0. The volume is even increased momentarily by the optimization algorithm to ensure the strength constraint is satisfied, before the volume constraint becoming itself satisfied. Due to this behavior of fixed maximal volume raising the strength constraint, compliance minimization with strength constraint and maximal volume are more difficult to satisfy than volume minimization with strength and maximum compliance constraints. This latter minimization type has the advantage of having a low compliance and lower strength constrained at full density, and can start removing material once the mechanical constraints are satisfied.

Despite being a compliance minimization, there remains some intermediate densities at the junctions in Figure 6.17. These intermediate density zones are dictated by the strain constraint. Nonetheless, the major characteristics of the topology are identifiable in the final result, and it can serve as an initial point to be used in post-processing and a later design phase. Finally, looking at the modules' distribution in the geometric domain shown in Figure 6.18, they are much more in line with the results of the optimization in

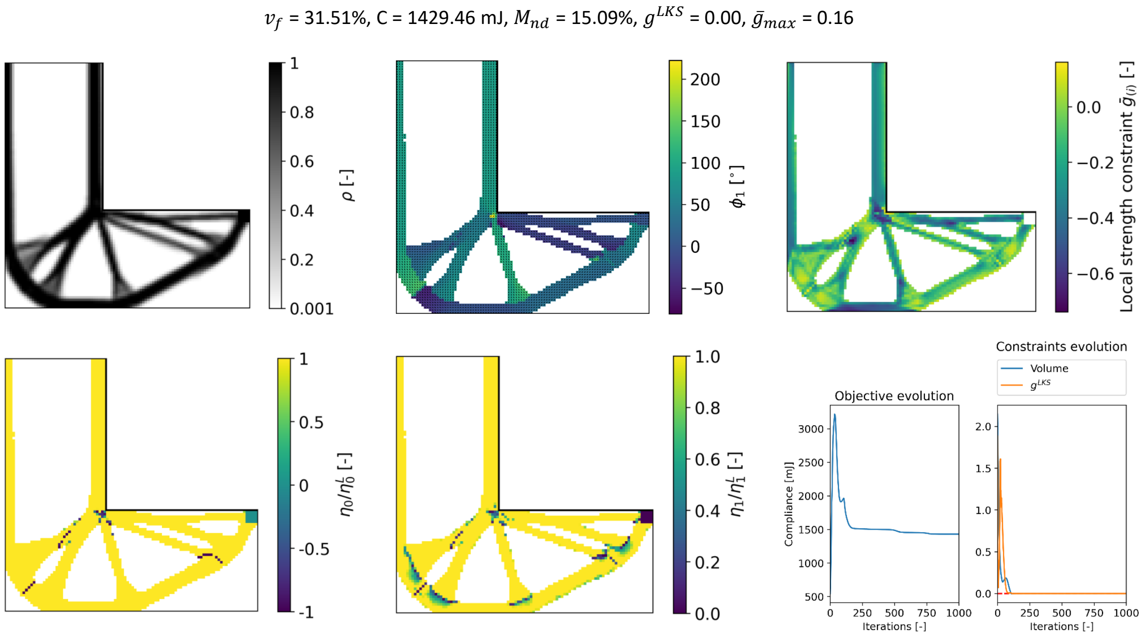

Figure 6.17: Results of a compliance minimization considering laminates with user-defined strain-envelope and volume constraints. Information shown for optimized elements with a final density ≥ 0.3.

Figure 6.14, representing either cross-plies or UD material. This is because the anisotropy is now directly used for improving the objective.

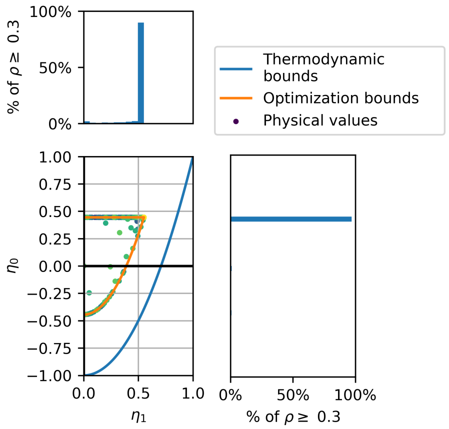

Figure 6.18: Anisotropic module distribution within the geometric and thermodynamic domain for the compliance minimization with a user-defined strain-envelope and volume constraints of Figure 6.17.

These different optimization problem formulations and results showed that taking volume, compliance and strength consideration into topology optimization with anisotropy is successful with the SplitMMA strategy. In Section 5.6, it was discussed how a correct initialization of the anisotropy already provides better solutions. This section shows that including strength considerations in the optimization allows to obtain practical designs. Furthermore, only considering volume and strength in the optimization results in feasible designs, but not the most coherent ones from a mechanical point of view. Indeed, the anisotropy distribution is quite dispersed. Adding compliance, either as objective or constraint, helps to stabilize the optimization by considering a mechanical responds for which there is a clear favored anisotropy condition.

Whether the best optimization problem then becomes a volume minimization with compliance and strength constraints, or a compliance minimization with volume and strength constraints depends on the designer's needs. Compliance minimization with a volume constraint has the advantage of not requiring an *a priori* knowledge of a compliance target value. Such compliance target can be difficult to estimate, as it is a structural characteristic not often used as a design requirement. Nonetheless, evaluating which volume constraint results in a feasible point for a given load case is also difficult on the other hand, and requires several optimizations with different volume constraint. Volume minimization would be the more logical optimization problem, as lighter designs are often pursued. Additionally, the initial iterations with 100% volume have a higher chance of being a feasible point, and afterwards, the optimization only starts removing elements once the strength constraint is satisfied. But as stated earlier, evaluating the compliance constraint target becomes more difficult. This could perhaps be replaced by an alternative stiffness measure, such as the maximum displacement at certain locations. Integrating such constraint is now feasible with a gradient-based strategy, and is left as a possibility for future research. Ultimately, the selection of the adequate problem formulation remains based on the engineer's knowledge of their design, and the need for the largest structural improvement, either stiffness or volume-wise.

6.8 Indirect Buckling Delay Control

The anisotropic strength criteria used as optimization constraint allow to distinguish between tensile and compressive allowables. This section is dedicated to the influence of changing the compressive allowables, and more particularly on the possibility to use it to indirectly promote a tensile stress state in the structure and increase the buckling critical load. Both a stress-based optimization with UD ply (as in Section 5.6) and a laminate with a strain-based constraint are investigated.

6.8.1 Influence of the Compressive Allowable Value X_c with a Uni-Directional Ply

This section investigates the effect of reducing the compressive stress allowable value X_c on the optimized solution. A volume minimization with a Tsai-Wu stress criterion constraint is treated (Problem 2). A total applied load of 400 N is used, with a normalization factor $N_0 = 1$, and a uniform initialization of the densities ρ as 1. The orientations are initialized from a preliminary compliance minimization step. The material stiffness properties of Table 5.4, whereas the strength properties and optimization parameters of Table 5.5 are used. Solutions of the optimization for a range of X_c allowable is shown in Figure 6.19. The solution with the initial $X_c = 610$ MPa is the right result in Figure 5.16.

The load path and main features do not differ much between the solutions with decreasing values of X_c, but the smaller inner bars tend to disappear. On the other hand, the bars' width changes a lot. For all cases, with the decrease in compressive allowable, the outer bars increase in width to experience a lower stress state. This goes with an increase in total volume. For the case $X_c = 400$ MPa and the case $X_c = 200$ MPa, the material orientations remain mostly aligned with the bars. On the contrary, the orientations are oblique to the compressive bars in case of $X_c = 100$ MPa. For this condition, the transverse compressive allowable Y_c is higher than the longitudinal one, which results in the logical alignment of the UD material with the direction of highest local strength for the least area and mass. Furthermore, with the lower compressive longitudinal allowable, all allowables except the tensile longitudinal one, X_t, Y_t, Y_c, S, tend to become closer in magnitude. This creates less material build-up at junctions, as the material can be more uniformly loaded. Furthermore, changing the magnitude of the compressive allowable X_c influence the shape of the Tsai-Wu envelope. For a lower magnitude of the compressive allowable, the Tsai-Wu envelope in the positive $\sigma_1 - \sigma_2$ (upper right) quadrant increases in size. This is illustrated with the different envelopes for each X_c value in Figure 6.20. This leads to the right vertical bar in tension to become a little thinner when a lower X_c value.

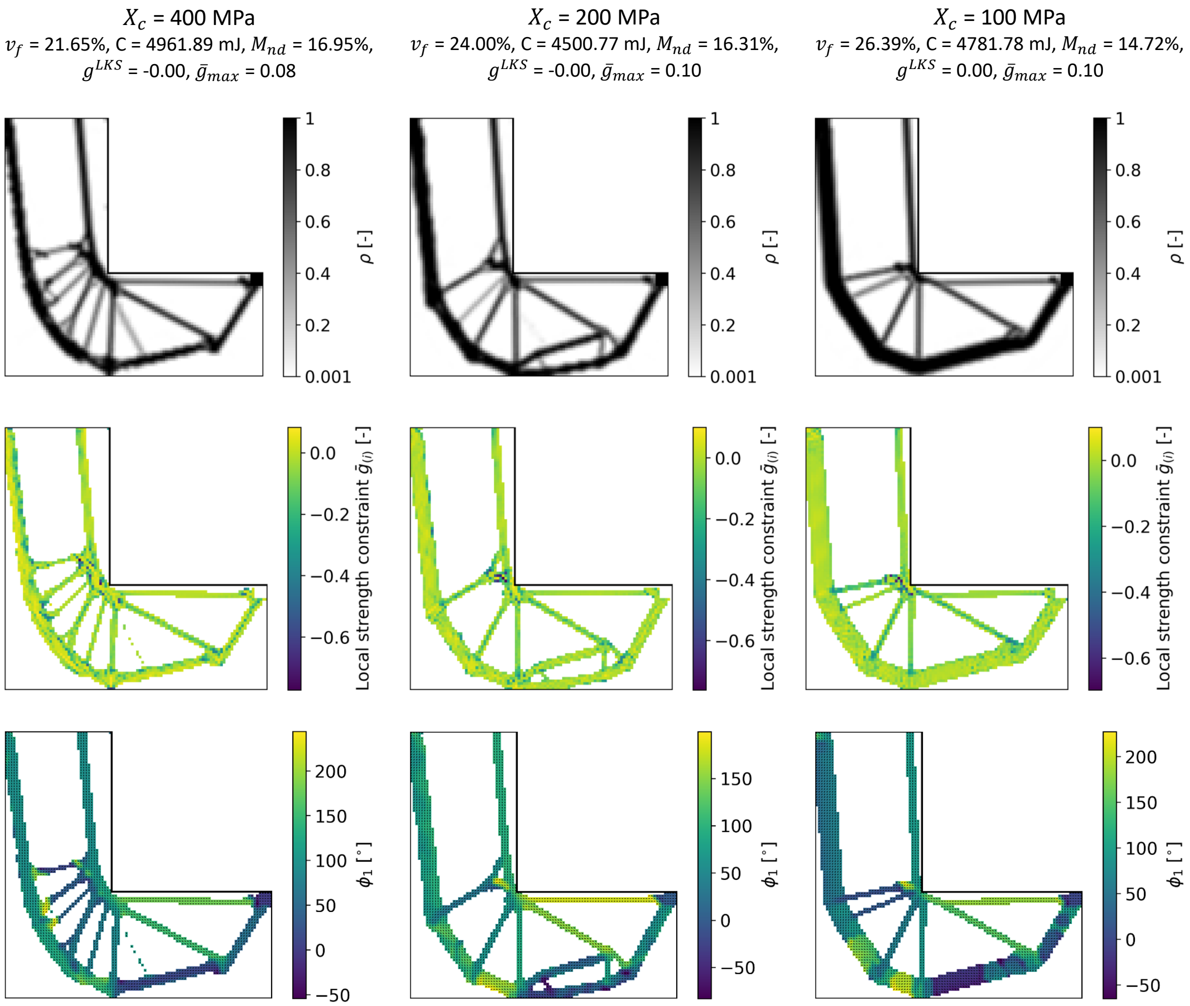

X_c = 400 MPa
v_f = 21.65%, C = 4961.89 mJ, M_{nd} = 16.95%, g^{LKS} = -0.00, $\bar{g}_{max}$ = 0.08

X_c = 200 MPa
v_f = 24.00%, C = 4500.77 mJ, M_{nd} = 16.31%, g^{LKS} = -0.00, $\bar{g}_{max}$ = 0.10

X_c = 100 MPa
v_f = 26.39%, C = 4781.78 mJ, M_{nd} = 14.72%, g^{LKS} = 0.00, $\bar{g}_{max}$ = 0.10

Figure 6.19: Results of a volume minimization with respect to material orientation and density with a Tsai-Wu strength constraint for a range of longitudinal compressive allowable X_c. Information shown for optimized elements with a final density ≥ 0.3.

At the end of the optimization, a linear buckling analysis input file for OptiStruct is created. This involves only using elements with $\rho \geq 0.3$, as to avoid spurious buckling mode appearing in the analysis in low density regions. The stiffness tensor components are then provided in the input file according to Equation 3.2. The buckling analysis consists in in-plane buckling with only the membrane ($[A]$) stiffness tensor of the material. The results of a linear eigenvalue buckling analysis for four X_c allowable solutions (the right solution in Figure 5.16 and the ones in Figure 6.19) are given in Figure 6.20 and Table 6.5.

The lower compressive allowables show an increase in critical buckling load factor λ_{crit}. This is because the compressive bars of the topology have become more massive, which has a twofold benefit: the experienced stress is lowered, but simultaneously a higher cross section and therefore inertia is obtained. The buckling eigenmode, and therefore the critical buckling location, is also changed. Nonetheless, the increase in buckling load also comes at the cost of a volume increase.

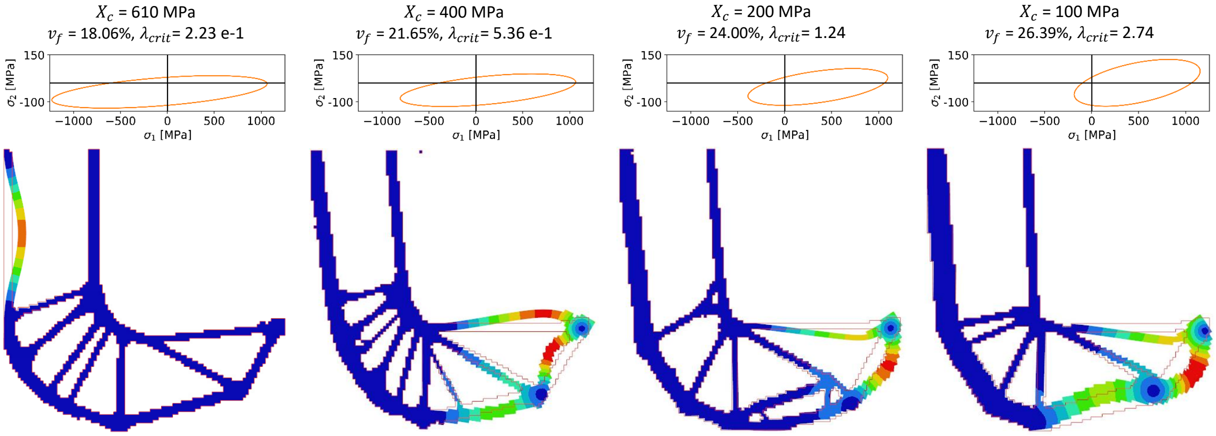

Figure 6.20: Buckling load multiplier λ_{crit} and eingenmode for the optimized designs with decreasing X_c values. Respective solutions are the right solution in Figure 5.16 and the ones in Figure 6.19. Information shown for optimized elements with a final density ≥ 0.3.

Table 6.5: Volume and buckling load multiplier differences for the results with different longitudinal compressive allowable X_c.

X_c [MPa]	v_f [%]	Difference with $X_c = 610$ MPa case [%]	λ_{crit} [-]	Difference with $X_c = 610$ MPa case [%]
610	18.06	0.00	0.223	0.00
400	21.65	19.84	0.536	140.36
200	24.00	32.79	1.24	456.05
100	26.39	45.99	2.74	1128.70

6.8.2 Influence of the Compressive Stress Allowable Values with a Laminate

A similar approach is tested on an optimization with laminates (*i.e.*, geometric bounds) and a strain envelope. The compressive strain allowable in both x and y direction are reduced. However, doing so changes the ellipse, and increased tension is allowed. Therefore, the tensile strain allowables are also adapted as to obtain a strain envelope similar to the original one in tension. The reduced compressive allowable values are given in Table 6.6, which can be compared to the original compressive allowable values given in Table 6.4 for a volume minimization with a strain-based constraint (Problem 6). The difference in strain envelope and results of the buckling analysis are shown in Figure 6.21. The reference solution corresponds to the one in Figure 6.13. The reduced compressive allowable optimization was carried out with a normalization factor $N_0 = 25$, with full density and anisotropy distribution coming from a preliminary compliance minimization step.

Table 6.6: User-defined strain envelope reduced allowable values.

ε_{x_t} [-]	ε_{x_c} [-]	ε_{y_t} [-]	ε_{y_c} [-]	M_{12}^* [-]	$\gamma_{xy_{\max}}$ [-]
0.012	0.0065	0.01	0.0065	0	0.004

Similar conclusions can be drawn as with the stress-based comparison in the previous section. In this case, an 80% increase in buckling load is obtained, for a 6% volume increase due to both lower loading on the compressive bars and an increased area. Nonetheless, using the volume difference on the high compressive allowables solution could already improve the buckling load factor, and lessen the difference at iso-mass.

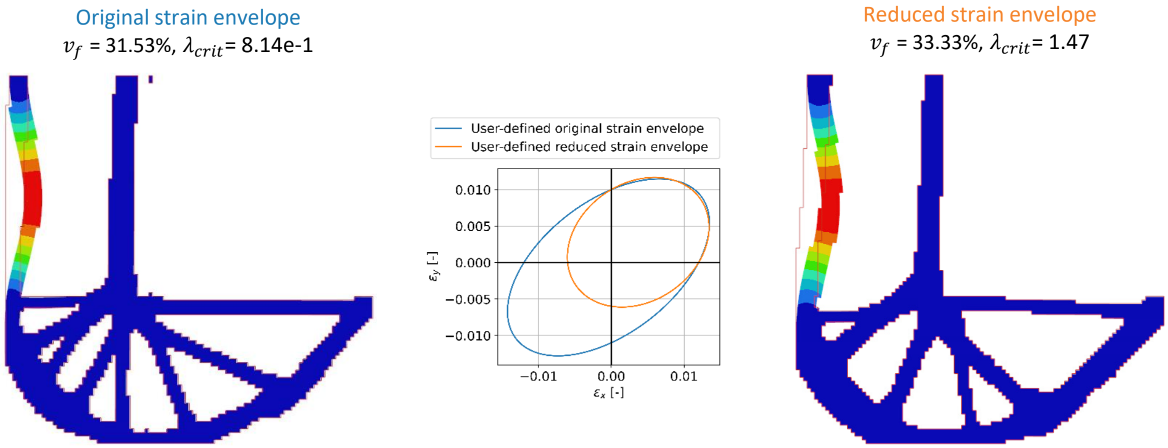

Figure 6.21: Buckling load multiplier λ_{crit} and eingenmode for the optimized designs. Information shown for optimized elements with a final density ≥ 0.3.

This approach shows that the critical buckling load can be increased, but does however not provide a direct control on the way to do, as buckling is only a post-processing result. It would be interesting to compare these solutions with equivalent results for topology optimizations which explicitly take buckling constraints into account.

6.9 Conclusion

This chapter was dedicated to incorporating strength constraints in the topology optimization of laminates. By using the homogenized stiffness of laminates, represented by means of the polar parameters, the actual stacking sequence and ply orientations are unknown. Therefore applying a stress-based elliptic criterion as presented in the previous chapter is not possible, since such a stress-based criterion can not be expressed at the ply level in which the allowables are defined. Hence, strain-based strength criteria have been introduced. Both a conservative envelope representing the common admissible strain space with a Tsai-Wu failure criterion for any ply orientation and a user-defined envelope are considered. The latter one can stem from other design requirements than ultimate strength, and represent a damage tolerance or fatigue envelope. As little research has been conducted into strain-based topology optimization, a framework to take strain criteria into account was first developed. The method is based on the lower KS function, for both its aggregation and relaxation properties, applied to a strain criterion. The method is compared and validated against a stress-based topology optimization with an isotropic material and Von Mises criterion. It showed coherent results, with similar mechanical properties and variable distributions in the optimized designs.

With the strain-based framework set-up, optimizations with anisotropy could be carried out. First, the conservative envelope for any ply orientation is used in an optimization with steered fiber, followed by one with laminates. Surprisingly, the optimized fiber steering solution turned out to be lighter than the laminate case. This is attributed to the different initialization point, and local minima in which the laminate get stuck. Thereafter, several topology optimization problems with laminates and a user-defined strain constraint are carried out. It is notable that when no stiffness constraint is added to the optimization, the anisotropic modules are more dispersed in the geometric domain and do not tend to the distribution for compliance minimization. The condition for compliance minimization consists predominantly with UD fibers in the bars, and cross-plies at junctions. This is because in simple volume minimization with strength constraint, there is no compliance consideration, and therefore the anisotropy is only optimized with respect to satisfying the given constraints. These examples show the correct consideration of strain-based constraints with topology along anisotropy optimization with the SplitMMA strategy. Some problems prevails, such as the numerical strength concentration due to a linear filter on the orientations. These could be alleviated with a more advanced filter, as discussed in Section 2.4.4.

Lastly, the influence of the compressive allowable values is investigated. It shows that with a lower value, the compressive zones become more massive. In case of a stress-based topology optimization for UD material, if the longitudinal allowable is lowered beyond the transverse one, the compressive zones remain massive, but the orientation become transverse to the bars as the compressive transverse allowable becomes the highest compressive allowable. This is well identified by the SplitMMA strategy to obtain a better solution. Reducing the compressive allowables is used in an successful attempt to increase the critical buckling load in both stress and strain-based topology optimization. This is a consequence of compressive bars having wider cross-sections and being less loaded when reducing the domain of admissible compressive strains or stresses. Nonetheless, this strategy remains an indirect control for buckling delay, as it is only checked on post-processed results. Moreover, solutions with lower compressive allowables also have a higher final volume, but far below the critical load multiplier improvement (v_f +6% and λ_{crit} +80%). Some of the improvement could be lost by using the volume difference on the high compressive allowable solution.

Chapter 7

Conclusion and Perspectives

7.1 Conclusion

With the rise of new manufacturing techniques, both the material distribution and anisotropic properties, such as stiffness and strength, can be controlled. To take advantage of these combined new possibilities, novel design methods have been developed, such as topology optimization. Published studies show that taking topology and material anisotropy simultaneously into account in the optimizations result in stiffer solutions than considering them separately. Nonetheless, stiffness is not always the major requirement for the design of structures, additional engineering requirements could be more critical, such as buckling or strength. Integrating such additional requirements as constraints in topology optimizations has been a research topic of interest for the past 15 years, and has shown to already alter the optimized topology with isotropic material. The aim of this research is to incorporate strength constraints in a simultaneous topology and distributed material anisotropy optimization, with a particular emphasis on composite laminates.

Chapter 2 consists in a literature review of topology and anisotropy optimization, whose principal conclusions can be summarized as follows. Two major problems are identified in stress-based topology optimizations with isotropic material: stress singularities and computational cost. The first one involves the optimal design point being in a degenerate design space, which gradient-based solvers have difficulties reaching. The algorithms encounter difficulties to make intermediate density elements disappear. Several relaxation techniques have been suggested and are employed successfully to remediate this problem. On the other hand, efficiently obtaining the gradient information in strength-based problems is solved by reducing the amount of optimization constraints, mostly by means of an aggregation function. This allows to use an adjoint formulation to compute the gradient. The strategy of using a lower Kreisselmeier-Steinhauser (KS) aggregation function is identified as proving at the same time both the required relaxation and reduction in number of constraints, and has been used in the subsequent modeling in this research. Concerning the anisotropy definition for optimizations, several parametrizations for composite laminates are used. Each individual ply can be represented, but to obtain a more regular variation of the design space, the preferred parametrization consist in representing the homogenized stiffness of the laminate, without explicit layup definition. This can be done using lamination parameters or by means of the geometric bounds on the polar parameters. For their invariant definition of the stiffness tensor, the polar parameters are further used in this research. The polar parameters can also represent any admissible stiffness tensor by means in thermodynamic domain, which encompasses the geometric domain. The corresponding thermodynamic bounds on the polar parameters have been used in topology optimization for compliance minimization, by means of optimality criteria in the Alternate Directions (AD) algorithm. On the other hand, the geometric bounds on the polar parameters have only been used in thickness optimizations, by means of gradient-based algorithms. Finally, only a limited number of research papers considers anisotropic strength in the optimizations. Therefore literature for just anisotropy optimizations is also reviewed, and more specifically for composite laminates. During a detailed design stage, failure in laminates is characterized by means of a first ply failure. This consists in applying an elliptic failure criterion to each separate ply, with all applied stresses and strength properties expressed in the local ply's reference frame. At a conceptual design stage, with an homogenized stiffness representation of composite laminates, where no stacking sequence is known, conservative strain-based envelopes are available. Such envelopes define in terms of global strains the boundary of the safety region for a ply-based failure criterion for any ply orientation. The first objective of this research is to incorporate strength constraints in a simultaneous topology and anisotropy optimization. This requires the development of an appropriate gradient-based framework. In the following, this optimization framework is used to consider either thermodynamic or geometric bounds to represent material anisotropic stiffness, and stress-based or strain-based failure criterion. This will also allow to consider the geometric bounds on the polar parameters.

Chapter 3 consisted thus in developing a gradient-based optimization strategy and framework taking both topology and distributed anisotropy into account. The polar formalism is used to represent a 2D orthotropic stiffness tensor, defined by five invariants quantities and the direction of orthotropy. Only the polar parameters dictating the anisotropic part of the stiffness tensor are used in the optimization. Both the thermodynamic and geometric bounds can be introduced implicitly in the optimization, and are satisfied by a remapping operation to new optimization variables. A gradient-based optimization strategy, called SplitMMA, is introduced to solve the optimization. This strategy is based on the Methods of Moving Asymptotes (MMA) algorithm. It uses different approximations depending on the optimization variable to solve different approximated sub-problems in parallel. The approximations are chosen based on the regularity of the design space with respect to each variable. The compliance and volume gradients can be easily obtained by the self-adjoint property of these quantities for the corresponding minimization problem. The validation of the gradient-based strategy is performed with the thermodynamic bounds by comparing SplitMMA results against results obtained with the AD algorithm. The importance of being able to switch the orientation transversely by a continuous change of the anisotropic modules when distinct bars appear in the topology optimization is first highlighted. Thereafter, the importance of the anisotropy distribution at the beginning of the topology optimization is also shown. Different and better solutions are obtained with the initial anisotropy distribution coming from a distinct first step compliance minimization. This first compliance minimization problem is solved with respect to the anisotropic variables for a fixed uniform density field. This enables the anisotropy to conform to the load path. Afterwards, as no optimality criteria exist for the geometric domain, nor have they been used in topology optimization, optimizations with the geometric bounds on the polar parameters have successfully been compared to results obtained with lamination parameters. Finally, novel results consisting in a comparison of the optimized design with increasing anisotropy freedom (isotropic, steered fiber, laminates and thermodynamic bounds) is performed, where the more design freedom yields stiffer designs. With the successful definition of a gradient-based optimization strategy that considers anisotropy in a topology optimization, the fundamental framework for strength consideration is available. The incorporation of strength requirements is then addressed.

In Chapter 4, a stress-based anisotropic strength constraint and its gradient are then derived for elliptic criteria, in case the orientation of an anisotropic material is allowed to change. Anisotropic strength criteria are used to define the failure index, representing the load multiplier to achieve failure. The inverse of the failure index is used to setup a local strength constraint. Moreover, as anisotropic strength properties are expressed in the material reference frame aligned with the material orientation, they have to be expressed in common frame with the applied stresses. To this end, the strength allowables are expressed with the polar formalism, and rotated from the material reference frame to the global one, where the mechanical analysis stresses are computed. Both the reduction of the number of constraints and the relaxation of the stress singularity problem are performed with a lower KS aggregation function. This allows to define the gradient by means of the adjoint formulation to decrease the computational cost. The adjoint formulation has been implemented in an in-house FEM routine, used for all the presented results.

Chapter 5 compares stress-based optimizations for different anisotropic properties, both stiffness and strength wise. Results are first obtained for optimizations with respect to material density for fixed anisotropic properties, followed by optimizations with respect to both material orientation and density. Anisotropic strength is first considered in additive manufacturing for a fixed layer stacking direction, yet the stiffness remains isotropic. For volume minimization, wider bars appear when those are solicited in the direction with lower allowables to reduced the stress magnitude. Moreover, a design obtained for one load direction will not sustain the reverse loading because of the dysymmetric allowables. Thereafter, both strength and stiffness anisotropy are considered, with a UD ply for a range of fixed orientations. The final topologies exhibit bars aligned with the fixed orientations. Volume minimizations with only strength constraints yield intermediate density values for elements loaded along the fiber with higher longitudinal strength than transversely. Including an additional stiffness consideration, as either objective or constraint, in the optimization results in distinct final topologies, as the SIMP model penalizes intermediate density elements. For optimizations with respect to both density and material orientation, a linear filter is applied to smooth the orientation distribution. This creates some local abrupt transitions for neighboring opposite orientations, which are different value wise but not mechanically, and introduce artificial stress concentration due to the stiffness mismatch. For volume minimization considering strength, the optimized result obtained with initial orientations stemming from a compliance minimization step yields the lowest volume and most coherent orientation distribution compared to uniform orientation initializations. UD fibers are well aligned within bars, using the higher strength allowables along the fibers. However, material build-up is present at junctions where multi-axial stress states are experienced. Furthermore, more conservative anisotropic strength criteria result logically in heavier solutions. The lower KS strategy underestimates the maximum of the aggregated constraint, so despite a satisfied optimization constraint, the local strength constraints yield a value exceeding the failure criteria. Finally, a gradual increase in the aggregation parameter towards the end of the optimization is able to reduce the overshoot of the local strength constraint to less than 1%. This is an acceptable level of accuracy for design phases.

Finally, the case of laminate optimization with a strength constraint is considered in Chapter 6, where both the orientation and modules of the homogenized material are optimized along the topology. However, as the polar parameters with geometric bounds represent a homogenized stiffness behavior, the actual stacking sequence of the laminate is unknown. A stress-based criterion can therefore not be applied to individual plies. A strain-based condition as suggested in literature is used to express a minimal admissible strain envelope as not to have failure with a Tsai-Wu criterion for any ply orientation. An alternatively user-defined envelope is also proposed, which can represent a different failure envelope, such as damage tolerance or fatigue limits. Nonetheless, as no extensive research is available on strain-based topology optimization, such framework is first investigated. The approach based on the lower KS function is chosen for both relaxation and reduction of the amount of optimization constraints. As the strain conditions are expressed in the global coordinate system, the constraint and its gradient do not require a rotation operation. The strain-based framework is first verified with a stress-based Von Mises criterion for isotropic material. Thereafter, the conservative Tsai-Wu strain envelope is successfully used in a volume minimization problem for either a UD ply or laminate. But although the latter case considers additional design variables, these drive the solution to a local minimum, and a lighter solution than the UD case could not be obtained. A user-defined envelope is then used to compare several optimization problem formulations, where the influence of the choice of the objective and constraints is investigated. Different solutions with the same volume can be achieved, but with different stiffness values as the anisotropy can be used to tailor a solution to a particular need with respect to the problem formulation. The application of the problem formulation is dependent on the need of a user. Lastly, as the strength criteria allow to differentiate between tensile and compressive allowables, an investigation on the influence of the compressive allowable is performed. First the stress-based case with UD plies is considered, where decreasing the longitudinal compressive allowable results in thicker compressive bars. Additionally, decreasing the longitudinal compressive compressive allowable below the transverse one results in the optimized orientations being oblique to the bars. The lower compressive allowable is also used in a strategy to indirectly increase the critical buckling load factor. Substantial improvements (+80%) are obtained for a reduced volume increase (+6%) in volume minimization problems. Similar results are obtained when considering lower compressive strain allowables in an optimization with laminates. These examples show the successful development of a framework for topology and anisotropy optimization with strength constraints, which opens the possibility for implementation in design offices and for further research.

7.2 Perspectives

The possibilities offered by this research are manifold. Some part concerns the methodology directly, with research directions which were not explored, and other are about the future possibilities. First of all, the current framework allows to incorporate strength constraints and anisotropy in topology optimization with an in-house FEM implementation. Nonetheless, for larger optimization problems with more elements and therefore optimization variables, the optimization should be coupled with a more-advanced FEM solver. That FEM solver should preferably allow to control the efficient computation of the gradients by means of the adjoint formulation. Thereafter, with the gradient-based topology and anisotropy optimization framework, additional constraints can be incorporated such as buckling or vibrations. The direct consideration of a buckling requirement will also yield a far better control over the increase in critical load, compared to the indirect compressive allowable decrease strategy. Adding to the versatility offered by the framework, the considered overall structural stiffness of the structure could also be replaced by a maximum deflection constraint. This has a direct physical meaning, and furthermore is more relevant and applicable for practical designs than compliance.

On the other hand, an idea to further accelerate convergence and improve upon the current framework, is to penalize the intermediate densities in the objective, by introducing a similar penalizing interpolation for the volume calculation, left as a future possibility. Moreover, a more advance filtering techniques on the anisotropy should be incorporated, as to avoid numerical concentrations and propagate sub-optimal anisotropy variable values. An orientation filter such as suggested by Schmidt *et al.* [106] would be a first improvement, but a filter directly applied on the stiffness tensor would be ideal, as this would directly take the physical properties into account, and regroup all variables. Moreover, a strategy was presented herein to decrease the aggregation error of the local constraints due to the lower KS to less than 1%. Further work could focus to make the stress and strain-based topology work with a rectifier approach to obtain a final optimized result which satisfies the local constraint over the complete domain, with possible inspiration from recent research [81].

Thereafter, both the thermodynamic and geometric domain of the polar parameters represent a material stiffness homogenization. This is appreciated as a first optimization step for a better behaved and more continuous design domain, but a second step is still required to obtain an actual physical representation. In case of the geometric domain, a matching stacking sequence should still be found for each element. This can be achieved by restricting the domain of existence to known stacking sequences in the optimizations as done by Savine [145]. Alternatively, for the more general case where no restriction is imposed, the stacking sequence can be retrieved by a second optimization step. On the other hand, although not used extensively in this research, the thermodynamic domain can also be seen as representing any microstructure. This could be used for research aimed with reverse identification, for instance deshomogenization methods.

Lastly, this research only considered in-plane loading in 2D. The polar parameters, and specifically the geometric bounds, can also be used in shell theory to represent bending, coupling and transverse shear stiffness anisotropy. This would allow to consider 3D load cases and physical response of laminates. In particular, it would allow to consider out-of-plane buckling for the optimized structures. A possible approach would be by considering anisotropy coupled with feature mapping techniques such as Smith and Norato [27]. By the projection method, a plate is represented which can move in a 3D space by means of control points, where the plate representation allows to define laminate properties on it. This can be coupled with the current strength or strain-based approach. Another possibility is to consider volumetric 3D topology optimization problems, with a 3D anisotropic stiffness representation, such as for transversely isotropic material as proposed by Ranaivomiarana [2]. To obtain coherent results, the parametrization should be identified in providing a means to change the orientation of the material transversely by a continuous change of the modules. The subsequent anisotropy initialization importance and strength constraint optimization are expected to be as effective as in 2D, and offer no increased difficulties.

Communications

Journal Article

L. Vertonghen, F.-X. Irisarri, D. Bettebghor, B. Desmorat. Gradient-based concurrent topology and anisotropy optimization for mechanical structures. In Computer Methods in Applied Mechanics and Engineering, vol. 412, p. 116069, July 2023.

Conference Proceedings

L. Vertonghen, F.-X. Irisarri, D. Bettebghor, B. Desmorat. Optimisation simultanée de la topologie et de l'anisotropie. In 2022 15ème colloque national en calcul des structures, Hyères-les-Palmiers, France. CSMA 2022.

L. Vertonghen, F.-X. Irisarri, D. Bettebghor, B. Desmorat. Simultaneous topology and anisotropy optimization by means of a gradient-based algorithm. In 20th European Conference on Composite Materials, Lausanne, Suisse. ECCM20.

Presentations

L. Vertonghen, F.-X. Irisarri, D. Bettebghor, B. Desmorat. Optimisation simultanée de la topologie et de l'anisotropie. In 2022 15ème colloque national en calcul des structures, Hyères-les-Palmiers, France. CSMA 2022.

L. Vertonghen, F.-X. Irisarri, D. Bettebghor, B. Desmorat. Simultaneous topology and anisotropy optimization by means of a gradient-based algorithm. In 20th European Conference on Composite Materials, Lausanne, Switzerland. ECCM20.

L. Vertonghen, F.-X. Irisarri, D. Bettebghor, B. Desmorat. Considering Failure in a Concurrent Topology and Composite Laminate Optimization. In 15th World Congress on Computational Mechanics, Yokohama, Japan. WCCM2022.

L. Vertonghen, F.-X. Irisarri, D. Bettebghor, B. Desmorat. Otpimisation Topologique de Structures Composites. Journée thématique F2M "Méthodes Avancées Numérique", April 2022.

Bibliography

[1] N. Ranaivomiarana, F.-X. Irisarri, D. Bettebghor, and B. Desmorat, “Concurrent optimization of material spatial distribution and material anisotropy repartition for two-dimensional structures,” *Continuum Mechanics and Thermodynamics*, vol. 31, pp. 133–146, Jan. 2019.

[2] N. Ranaivomiarana, *Simultaneous optimization of topology and material anisotropy for aeronautic structures.* Thesis, Sorbonne Université - ONERA, Mar. 2019.

[3] X. Gao, Y. Li, H. Ma, and G. Chen, “Improving the overall performance of continuum structures: A topology optimization model considering stiffness, strength and stability,” *Computer Methods in Applied Mechanics and Engineering*, vol. 359, p. 112660, Feb. 2020.

[4] C. Le, J. Norato, T. Bruns, C. Ha, and D. Tortorelli, “Stress-based topology optimization for continua,” *Structural and Multidisciplinary Optimization*, vol. 41, pp. 605–620, Apr. 2010.

[5] A. Verbart, M. Langelaar, and F. v. Keulen, “A unified aggregation and relaxation approach for stress-constrained topology optimization,” *Structural and Multidisciplinary Optimization*, vol. 55, pp. 663–679, Feb. 2017.

[6] T. Roiné, *Intégration des critères de tenue mécanique et de dimensionnement de structures lattices multi-matériau dans la méthode d’optimisation topologique basée sur les entités NURBS.* PhD thesis, 2022.

[7] E. Lund, “Discrete Material and Thickness Optimization of laminated composite structures including failure criteria,” *Structural and Multidisciplinary Optimization*, vol. 57, pp. 2357–2375, June 2018.

[8] G. Ma, W. Yang, and L. Wang, “Strength-constrained simultaneous optimization of topology and fiber orientation of fiber-reinforced composite structures for additive manufacturing,” *Advances in Structural Engineering*, vol. 25, pp. 1636–1651, May 2022.

[9] M. I. Izzi, A. Catapano, and M. Montemurro, “Strength and mass optimisation of variable-stiffness composites in the polar parameters space,” *Structural and Multidisciplinary Optimization*, vol. 64, pp. 2045–2073, Oct. 2021.

[10] K. Svanberg, “The method of moving asymptotes—a new method for structural optimization,” *International Journal for Numerical Methods in Engineering*, vol. 24, pp. 359–373, Feb. 1987.

[11] P. Vannucci, “A Note on the Elastic and Geometric Bounds for Composite Laminates,” *Journal of Elasticity*, vol. 112, pp. 199–215, July 2013.

[12] A. M. Mirzendehdel, B. Rankouhi, and K. Suresh, “Strength-based topology optimization for anisotropic parts,” *Additive Manufacturing*, vol. 19, pp. 104–113, Jan. 2018.

[13] S. C. Subedi, C. S. Verma, and K. Suresh, “A Review of Methods for the Geometric Post-Processing of Topology Optimized Models,” *Journal of Computing and Information Science in Engineering*, vol. 20, Dec. 2020.

[14] A. Mitchell, “The Limits of Economy of Material in Frame Structures,” *Philosophical Magazine*, vol. 8, no. 6, pp. 589–597, 1904.

[15] H. A. Eschenauer and N. Olhoff, “Topology optimization of continuum structures: A review*,” *Applied Mechanics Reviews*, vol. 54, pp. 331–390, July 2001.

[16] G. I. N. Rozvany, “A critical review of established methods of structural topology optimization,” *Structural and Multidisciplinary Optimization*, vol. 37, pp. 217–237, Jan. 2009.

[17] M. P. Bendsøe, “Optimal shape design as a material distribution problem,” *Structural optimization*, vol. 1, pp. 193–202, Dec. 1989.

[18] M. P. Bendsøe and O. Sigmund, *Topology Optimization.* Berlin, Heidelberg: Springer Berlin Heidelberg, 2004.

[19] O. Sigmund, “A 99 line topology optimization code written in Matlab,” *Structural and Multidisciplinary Optimization*, vol. 21, pp. 120–127, Apr. 2001.

[20] O. Sigmund, “On the Design of Compliant Mechanisms Using Topology Optimization,” *Mechanics of Structures and Machines*, vol. 25, pp. 493–524, Jan. 1997.

[21] P. D. Dunning, E. Ovtchinnikov, J. Scott, and H. A. Kim, “Level-set topology optimization with many linear buckling constraints using an efficient and robust eigensolver: buckling constrained topology optimization,” *International Journal for Numerical Methods in Engineering*, vol. 107, pp. 1029–1053, Sept. 2016.

[22] M. P. Bendsøe and O. Sigmund, “Material interpolation schemes in topology optimization,” *Archive of Applied Mechanics*, vol. 69, pp. 635–654, Nov. 1999.

[23] M. Bruyneel, “Optimization of laminated composite structures: problems, solution procedures and applications,” *Composite Materials Research Progress*, pp. 51–107, 2008.

[24] O. Sigmund, “Morphology-based black and white filters for topology optimization,” *Structural and Multidisciplinary Optimization*, vol. 33, pp. 401–424, Apr. 2007.

[25] T. Nomura, A. Kawamoto, T. Kondoh, E. M. Dede, J. Lee, Y. Song, and N. Kikuchi, “Inverse design of structure and fiber orientation by means of topology optimization with tensor field variables,” *Composites Part B: Engineering*, vol. 176, p. 107187, Nov. 2019.

[26] Y. Zhou, T. Nomura, E. Zhao, and K. Saitou, “Large-Scale Three-Dimensional Anisotropic Topology Optimization of Variable-Axial Lightweight Composite Structures,” *Journal of Mechanical Design*, vol. 144, July 2021.

[27] H. Smith and J. Norato, “Topology optimization of structures made of fiber-reinforced plates,” *Structural and Multidisciplinary Optimization*, vol. 65, p. 58, Jan. 2022.

[28] N. Boddeti, Y. Tang, K. Maute, D. W. Rosen, and M. L. Dunn, “Optimal design and manufacture of variable stiffness laminated continuous fiber reinforced composites,” *Scientific Reports*, vol. 10, p. 16507, Oct. 2020.

[29] M. Stolpe and K. Svanberg, “An alternative interpolation scheme for minimum compliance topology optimization,” *Structural and Multidisciplinary Optimization*, vol. 22, pp. 116–124, Sept. 2001.

[30] A. Díaz and O. Sigmund, “Checkerboard patterns in layout optimization,” *Structural optimization*, vol. 10, pp. 40–45, Aug. 1995.

[31] O. Sigmund and J. Petersson, “Numerical instabilities in topology optimization: A survey on procedures dealing with checkerboards, mesh-dependencies and local minima,” *Structural optimization*, vol. 16, pp. 68–75, Aug. 1998.

[32] R. B. Haber, C. S. Jog, and M. P. Bendsøe, “A new approach to variable-topology shape design using a constraint on perimeter,” *Structural optimization*, vol. 11, pp. 1–12, Feb. 1996.

[33] F. Wang, B. S. Lazarov, and O. Sigmund, “On projection methods, convergence and robust formulations in topology optimization,” *Structural and Multidisciplinary Optimization*, vol. 43, pp. 767–784, June 2011.

[34] B. S. Lazarov and O. Sigmund, “Filters in topology optimization based on Helmholtz-type differential equations,” *International Journal for Numerical Methods in Engineering*, vol. 86, no. 6, pp. 765–781, 2011.

[35] K. Svanberg, “On the convexity and concavity of compliances,” *Structural optimization*, vol. 7, pp. 42–46, Feb. 1994.

[36] S. Rojas-Labanda and M. Stolpe, “Automatic penalty continuation in structural topology optimization,” *Structural and Multidisciplinary Optimization*, vol. 52, pp. 1205–1221, Dec. 2015.

[37] X. Guo, W. Zhang, and W. Zhong, “Doing Topology Optimization Explicitly and Geometrically—A New Moving Morphable Components Based Framework,” *Journal of Applied Mechanics*, vol. 81, May 2014.

[38] H. A. Smith, J. A. Norato, J. D. Deaton, and R. M. Kolonay, “Topology Optimization for Buckling via Geometry Projection,” *AIAA SCITECH 2022 Forum*, 2022.

[39] F. Savine, F.-X. Irisarri, C. Julien, A. Vincenti, and Y. Guerin, “A component-based method for the optimization of stiffener layout on large cylindrical rib-stiffened shell structures,” *Structural and Multidisciplinary Optimization*, vol. 64, pp. 1843–1861, Oct. 2021.

[40] F. Wein, P. D. Dunning, and J. A. Norato, “A review on feature-mapping methods for structural optimization,” *Structural and Multidisciplinary Optimization*, vol. 62, pp. 1597–1638, Oct. 2020.

[41] G. Allaire, F. Jouve, and A.-M. Toader, “Structural optimization using sensitivity analysis and a level-set method,” *Journal of Computational Physics*, vol. 194, pp. 363–393, Feb. 2004.

[42] G. Allaire and F. Jouve, “Minimum stress optimal design with the level set method,” *Engineering Analysis with Boundary Elements*, vol. 32, pp. 909–918, Nov. 2008.

[43] N. P. van Dijk, K. Maute, M. Langelaar, and F. van Keulen, “Level-set methods for structural topology optimization: a review,” *Structural and Multidisciplinary Optimization*, vol. 48, pp. 437–472, Sept. 2013.

[44] S. Rojas-Labanda and M. Stolpe, “Benchmarking optimization solvers for structural topology optimization,” *Structural and Multidisciplinary Optimization*, vol. 52, pp. 527–547, Sept. 2015.

[45] G. Allaire, Z. Belhachmi, and F. Jouve, “The homogenization method for topology and shape optimization. Single and multiple loads case,” *Revue Européenne des Éléments Finis*, vol. 5, pp. 649–672, Jan. 1996.

[46] R. Balamurugan, C. V. Ramakrishnan, and N. Swaminathan, “A two phase approach based on skeleton convergence and geometric variables for topology optimization using genetic algorithm,” *Structural and Multidisciplinary Optimization*, vol. 43, pp. 381–404, Mar. 2011.

[47] G.-C. Luh and C.-Y. Lin, “Structural topology optimization using ant colony optimization algorithm,” *Applied Soft Computing*, vol. 9, pp. 1343–1353, Sept. 2009.

[48] G.-C. Luh, C.-Y. Lin, and Y.-S. Lin, “A binary particle swarm optimization for continuum structural topology optimization,” *Applied Soft Computing*, vol. 11, pp. 2833–2844, Mar. 2011.

[49] O. Sigmund, “On the usefulness of non-gradient approaches in topology optimization,” *Structural and Multidisciplinary Optimization*, vol. 43, pp. 589–596, May 2011.

[50] Y. M. Xie and G. P. Steven, “A simple evolutionary procedure for structural optimization,” *Computers & Structures*, vol. 49, pp. 885–896, Dec. 1993.

[51] D. Manickarajah, Y. M. Xie, and G. P. Steven, “An evolutionary method for optimization of plate buckling resistance,” *Finite Elements in Analysis and Design*, vol. 29, pp. 205–230, June 1998.

[52] X. Y. Yang, Y. M. Xie, G. P. Steven, and O. M. Querin, “Bidirectional Evolutionary Method for Stiffness Optimization,” *AIAA Journal*, vol. 37, pp. 1483–1488, Nov. 1999.

[53] S. Mukherjee, D. Lu, B. Raghavan, P. Breitkopf, S. Dutta, M. Xiao, and W. Zhang, “Accelerating Large-scale Topology Optimization: State-of-the-Art and Challenges,” *Archives of Computational Methods in Engineering*, vol. 28, pp. 4549–4571, Dec. 2021.

[54] C. Fleury and V. Braibant, “Structural optimization: A new dual method using mixed variables,” *International Journal for Numerical Methods in Engineering*, vol. 23, no. 3, pp. 409–428, 1986.

[55] K. Svanberg, “A Class of Globally Convergent Optimization Methods Based on Conservative Convex Separable Approximations,” *SIAM Journal on Optimization*, vol. 12, pp. 555–573, Jan. 2002.

[56] K.-T. Zuo, L.-P. Chen, Y.-Q. Zhang, and J. Yang, “A hybrid topology optimization algorithm for structural design,” *Engineering Optimization*, vol. 37, pp. 849–866, Dec. 2005.

[57] E. Holmberg, B. Torstenfelt, and A. Klarbring, “Stress constrained topology optimization,” *Structural and Multidisciplinary Optimization*, vol. 48, pp. 33–47, July 2013.

[58] F. V. Senhora, O. Giraldo-Londoño, I. F. M. Menezes, and G. H. Paulino, “Topology optimization with local stress constraints: a stress aggregation-free approach,” *Structural and Multidisciplinary Optimization*, vol. 62, pp. 1639–1668, Oct. 2020.

[59] T. Roiné, M. Montemurro, and J. Pailhès, “Stress-based topology optimization through non-uniform rational basis spline hyper-surfaces,” *Mechanics of Advanced Materials and Structures*, vol. 29, pp. 3387–3407, Sept. 2022.

[60] K. Suresh and M. Takalloozadeh, “Stress-constrained topology optimization: a topological level-set approach,” *Structural and Multidisciplinary Optimization*, vol. 48, pp. 295–309, Aug. 2013.

[61] L. Xia, L. Zhang, Q. Xia, and T. Shi, “Stress-based topology optimization using bi-directional evolutionary structural optimization method,” *Computer Methods in Applied Mechanics and Engineering*, vol. 333, pp. 356–370, May 2018.

[62] G. Sved and Z. Ginos, “Structural optimization under multiple loading,” *International Journal of Mechanical Sciences*, vol. 10, pp. 803–805, Oct. 1968.

[63] G. D. Cheng and X. Guo, “Epsilon-relaxed approach in structural topology optimization,” *Structural optimization*, vol. 13, pp. 258–266, June 1997.

[64] G. A. da Silva, N. Aage, A. T. Beck, and O. Sigmund, “Local versus global stress constraint strategies in topology optimization: A comparative study,” *International Journal for Numerical Methods in Engineering*, vol. 122, no. 21, pp. 6003–6036, 2021.

[65] P. Duysinx and O. Sigmund, “New developments in handling stress constraints in optimal material distribution,” in *7th AIAA/USAF/NASA/ISSMO Symposium on Multidisciplinary Analysis and Optimization*, (St. Louis,MO,U.S.A.), American Institute of Aeronautics and Astronautics, Sept. 1998.

[66] J. Pereira, E. Fancello, and C. Barcellos, "Topology optimization of continuum structures with material failure constraints," *Structural and Multidisciplinary Optimization*, vol. 26, pp. 50–66, Jan. 2004.

[67] M. Bruggi, "On an alternative approach to stress constraints relaxation in topology optimization," *Structural and Multidisciplinary Optimization*, vol. 36, pp. 125–141, Aug. 2008.

[68] P. Duysinx and M. P. Bendsøe, "Topology optimization of continuum structures with local stress constraints," *International Journal for Numerical Methods in Engineering*, vol. 43, pp. 1453–1478, Dec. 1998.

[69] G. A. da Silva, A. T. Beck, and O. Sigmund, "Stress-constrained topology optimization considering uniform manufacturing uncertainties," *Computer Methods in Applied Mechanics and Engineering*, vol. 344, pp. 512–537, 2019.

[70] H. Svärd, "Interior value extrapolation: a new method for stress evaluation during topology optimization," *Structural and Multidisciplinary Optimization*, vol. 51, pp. 613–629, Mar. 2015.

[71] M. Kočvara and M. Stingl, "Free material optimization for stress constraints," *Structural and Multidisciplinary Optimization*, vol. 33, pp. 323–335, Apr. 2007.

[72] M. Shimoda, H. Azegami, and T. Sakurai, "Numerical Solution for Min-Max Problems in Shape Optimization. Minimum Design of Max. Stress and Max. Displacement.," *JSME International Journal Series A*, vol. 41, Jan. 1998.

[73] G. J. Kennedy and J. E. Hicken, "Improved constraint-aggregation methods," *Computer Methods in Applied Mechanics and Engineering*, vol. 289, pp. 332–354, June 2015.

[74] C. Y. Kiyono, S. L. Vatanabe, E. C. N. Silva, and J. N. Reddy, "A new multi-p-norm formulation approach for stress-based topology optimization design," *Composite Structures*, vol. 156, pp. 10–19, Nov. 2016.

[75] W. Achtziger and C. Kanzow, "Mathematical programs with vanishing constraints: optimality conditions and constraint qualifications," *Mathematical Programming*, vol. 114, pp. 69–99, July 2008.

[76] S. Coniglio, C. Gogu, R. Amargier, and J. Morlier, "Engine Pylon Topology Optimization Framework Based on Performance and Stress Criteria," *AIAA Journal*, vol. 57, pp. 5514–5526, Dec. 2019.

[77] G. Capasso, J. Morlier, M. Charlotte, and S. Coniglio, "Stress-based topology optimization of compliant mechanisms using nonlinear mechanics," *Mechanics & Industry*, vol. 21, no. 3, p. 304, 2020.

[78] M. Bruggi and P. Duysinx, "Topology optimization for minimum weight with compliance and stress constraints," *Structural and Multidisciplinary Optimization*, vol. 46, pp. 369–384, Sept. 2012.

[79] J. París, F. Navarrina, I. Colominas, and M. Casteleiro, "Global versus local statement of stress constraints in topology optimization of continuum structures," in *Computer Aided Optimum Design in Engineering X*, vol. I, (Myrtle Beach, USA), pp. 13–23, WIT Press, Apr. 2007.

[80] J. París, F. Navarrina, I. Colominas, and M. Casteleiro, "Block aggregation of stress constraints in topology optimization of structures," *Advances in Engineering Software*, vol. 41, pp. 433–441, Mar. 2010.

[81] J. A. Norato, H. A. Smith, J. D. Deaton, and R. M. Kolonay, "A maximum-rectifier-function approach to stress-constrained topology optimization," *Structural and Multidisciplinary Optimization*, vol. 65, p. 286, Sept. 2022.

[82] D. Yang, H. Liu, W. Zhang, and S. Li, "Stress-constrained topology optimization based on maximum stress measures," *Computers & Structures*, vol. 198, pp. 23–39, Mar. 2018.

[83] E. Lee, K. A. James, and J. R. R. A. Martins, “Stress-constrained topology optimization with design-dependent loading,” *Structural and Multidisciplinary Optimization*, vol. 46, pp. 647–661, Nov. 2012.

[84] Y. Luo and Z. Kang, “Topology optimization of continuum structures with Drucker–Prager yield stress constraints,” *Computers & Structures*, vol. 90-91, pp. 65–75, Jan. 2012.

[85] F. Ferrari and O. Sigmund, “Revisiting topology optimization with buckling constraints,” *Structural and Multidisciplinary Optimization*, vol. 59, pp. 1401–1415, May 2019.

[86] S. Zargham, T. A. Ward, R. Ramli, and I. A. Badruddin, “Topology optimization: a review for structural designs under vibration problems,” *Structural and Multidisciplinary Optimization*, vol. 53, pp. 1157–1177, June 2016.

[87] Y. Zhou and K. Saitou, “Gradient-based multi-component topology optimization for stamped sheet metal assemblies (MTO-S),” *Structural and Multidisciplinary Optimization*, vol. 58, pp. 83–94, July 2018.

[88] K.-T. Zuo, L.-P. Chen, Y.-Q. Zhang, and J. Yang, “Manufacturing- and machining-based topology optimization,” *The International Journal of Advanced Manufacturing Technology*, vol. 27, pp. 531–536, Jan. 2006.

[89] Y. Xu, J. Zhu, Z. Wu, Y. Cao, Y. Zhao, and W. Zhang, “A review on the design of laminated composite structures: constant and variable stiffness design and topology optimization,” *Advanced Composites and Hybrid Materials*, vol. 1, pp. 460–477, Sept. 2018.

[90] G. Bertolino and M. Montemurro, “Two-scale topology optimisation of cellular materials under mixed boundary conditions,” *International Journal of Mechanical Sciences*, vol. 216, p. 106961, Feb. 2022.

[91] D. Li, W. Liao, N. Dai, and Y. M. Xie, “Anisotropic design and optimization of conformal gradient lattice structures,” *Computer-Aided Design*, vol. 119, p. 102787, Feb. 2020.

[92] T. Kumar and K. Suresh, “A density-and-strain-based K-clustering approach to microstructural topology optimization,” *Structural and Multidisciplinary Optimization*, vol. 61, pp. 1399–1415, Apr. 2020.

[93] E. Duriez, J. Morlier, M. Charlotte, and C. Azzaro-Pantel, “A well connected, locally-oriented and efficient multi-scale topology optimization (EMTO) strategy,” *Structural and Multidisciplinary Optimization*, vol. 64, pp. 3705–3728, Dec. 2021.

[94] J. Wu, O. Sigmund, and J. P. Groen, “Topology optimization of multi-scale structures: a review,” *Structural and Multidisciplinary Optimization*, vol. 63, pp. 1455–1480, Mar. 2021.

[95] N. Boddeti, D. W. Rosen, K. Maute, and M. L. Dunn, “Multiscale optimal design and fabrication of laminated composites,” *Composite Structures*, vol. 228, p. 111366, Nov. 2019.

[96] Y. Zhou, T. Nomura, and K. Saitou, “Anisotropic Multicomponent Topology Optimization for Additive Manufacturing With Build Orientation Design and Stress-Constrained Interfaces,” *Journal of Computing and Information Science in Engineering*, vol. 21, July 2020.

[97] C. J. Brampton, K. C. Wu, and H. A. Kim, “New optimization method for steered fiber composites using the level set method,” *Structural and Multidisciplinary Optimization*, vol. 52, pp. 493–505, Sept. 2015.

[98] V. S. Papapetrou, C. Patel, and A. Y. Tamijani, “Stiffness-based optimization framework for the topology and fiber paths of continuous fiber composites,” *Composites Part B: Engineering*, vol. 183, p. 107681, Feb. 2020.

[99] D. Jiang, R. Hoglund, and D. E. Smith, “Continuous Fiber Angle Topology Optimization for Polymer Composite Deposition Additive Manufacturing Applications,” *Fibers*, vol. 7, p. 14, Feb. 2019.

[100] X. Yan, Q. Xu, H. Hua, D. Huang, and X. Huang, “Concurrent topology optimization of structures and orientation of anisotropic materials,” *Engineering Optimization*, vol. 52, pp. 1598–1611, Sept. 2020.

[101] P. Zhang, J. Liu, and A. C. To, “Role of anisotropic properties on topology optimization of additive manufactured load bearing structures,” *Scripta Materialia*, vol. 135, pp. 148–152, July 2017.

[102] C. Dapogny, R. Estevez, A. Faure, and G. Michailidis, “Shape and topology optimization considering anisotropic features induced by additive manufacturing processes,” *Computer Methods in Applied Mechanics and Engineering*, vol. 344, pp. 626–665, Feb. 2019.

[103] J. Liu and H. Yu, “Concurrent deposition path planning and structural topology optimization for additive manufacturing,” *Rapid Prototyping Journal*, vol. 23, pp. 930–942, Jan. 2017.

[104] T. Nomura, E. M. Dede, J. Lee, S. Yamasaki, T. Matsumori, A. Kawamoto, and N. Kikuchi, “General topology optimization method with continuous and discrete orientation design using isoparametric projection,” *International Journal for Numerical Methods in Engineering*, vol. 101, no. 8, pp. 571–605, 2015.

[105] Y. Zhou, T. Nomura, and K. Saitou, “Multi-component topology and material orientation design of composite structures (MTO-C),” *Computer Methods in Applied Mechanics and Engineering*, vol. 342, pp. 438–457, Dec. 2018.

[106] M.-P. Schmidt, L. Couret, C. Gout, and C. B. W. Pedersen, “Structural topology optimization with smoothly varying fiber orientations,” *Structural and Multidisciplinary Optimization*, vol. 62, pp. 3105–3126, Dec. 2020.

[107] H. Smith and J. Norato, “Simultaneous material and topology optimization of composite laminates,” *Computer Methods in Applied Mechanics and Engineering*, vol. 404, p. 115781, Feb. 2023.

[108] J. Lee, D. Kim, T. Nomura, E. M. Dede, and J. Yoo, “Topology optimization for continuous and discrete orientation design of functionally graded fiber-reinforced composite structures,” *Composite Structures*, vol. 201, pp. 217–233, Oct. 2018.

[109] M. Bruyneel, “A general and effective approach for the optimal design of fiber reinforced composite structures,” *Composites Science and Technology*, vol. 66, pp. 1303–1314, Aug. 2006.

[110] S. Setoodeh, M. Abdalla, and Z. Gürdal, “Combined topology and fiber path design of composite layers using cellular automata,” *Structural and Multidisciplinary Optimization*, vol. 30, pp. 413–421, Dec. 2005.

[111] D. R. Jantos, K. Hackl, and P. Junker, “Topology optimization with anisotropic materials, including a filter to smooth fiber pathways,” *Structural and Multidisciplinary Optimization*, vol. 61, pp. 2135–2154, May 2020.

[112] J. Zowe, M. Kočvara, and M. P. Bendsøe, “Free material optimization via mathematical programming,” *Mathematical Programming*, vol. 79, pp. 445–466, Oct. 1997.

[113] A. Ben-Tal, M. Kovara, A. Nemirovski, and J. Zowe, “Free Material Design via Semidefinite Programming: The Multiload Case with Contact Conditions,” *SIAM Review*, vol. 42, pp. 695–715, Jan. 2000.

[114] F. Schury, M. Stingl, and F. Wein, “Efficient Two-Scale Optimization of Manufacturable Graded Structures,” *SIAM Journal on Scientific Computing*, vol. 34, pp. B711–B733, Jan. 2012.

[115] J. Hu, M. Li, X. Yang, and S. Gao, “Cellular structure design based on free material optimization under connectivity control,” *Computer-Aided Design*, vol. 127, p. 102854, Oct. 2020.

[116] M. Tyburec, M. Doškář, J. Zeman, and M. Kružík, “Modular-topology optimization of structures and mechanisms with free material design and clustering,” *Computer Methods in Applied Mechanics and Engineering*, vol. 395, p. 114977, May 2022.

[117] A. G. Weldeyesus and M. Stolpe, “Free material optimization for laminated plates and shells,” *Structural and Multidisciplinary Optimization*, vol. 53, pp. 1335–1347, June 2016.

[118] P. Vannucci, “Plane Anisotropy by the Polar Method,” *Meccanica*, vol. 40, pp. 437–454, Dec. 2005.

[119] O. Sigmund and S. Torquato, “Design of materials with extreme thermal expansion using a three-phase topology optimization method,” *Journal of the Mechanics and Physics of Solids*, vol. 45, pp. 1037–1067, June 1997.

[120] L. V. Gibiansky and O. Sigmund, “Multiphase composites with extremal bulk modulus,” *Journal of the Mechanics and Physics of Solids*, vol. 48, pp. 461–498, Mar. 2000.

[121] C. Y. Kiyono, E. C. N. Silva, and J. N. Reddy, “A novel fiber optimization method based on normal distribution function with continuously varying fiber path,” *Composite Structures*, vol. 160, pp. 503–515, Jan. 2017.

[122] X. Guo, W. S. Zhang, M. Y. Wang, and P. Wei, “Stress-related topology optimization via level set approach,” *Computer Methods in Applied Mechanics and Engineering*, vol. 200, pp. 3439–3452, Nov. 2011.

[123] Q. H. Doan, D. Lee, J. Lee, and J. Kang, “Design of buckling constrained multiphase material structures using continuum topology optimization,” *Meccanica*, vol. 54, pp. 1179–1201, June 2019.

[124] J. Stegmann and E. Lund, “Discrete material optimization of general composite shell structures,” *International Journal for Numerical Methods in Engineering*, vol. 62, no. 14, pp. 2009–2027, 2005.

[125] E. Lund, “Buckling topology optimization of laminated multi-material composite shell structures,” *Composite Structures*, vol. 91, pp. 158–167, Nov. 2009.

[126] C. Luo and J. K. Guest, “Optimizing Topology and Fiber Orientations With Minimum Length Scale Control in Laminated Composites,” *Journal of Mechanical Design*, vol. 143, Sept. 2020.

[127] S. N. Sørensen, R. Sørensen, and E. Lund, “DMTO – a method for Discrete Material and Thickness Optimization of laminated composite structures,” *Structural and Multidisciplinary Optimization*, vol. 50, pp. 25–47, July 2014.

[128] D. Peeters and M. Abdalla, “Optimization of Ply Drop Locations in Variable-Stiffness Composites,” *AIAA Journal*, vol. 54, no. 5, pp. 1760–1768, 2016.

[129] C. Kassapoglou, *Design and Analysis of Composite Structures: With Applications to Aerospace Structures.* Wiley, 2nd ed., 2013.

[130] M. Nicol, *Compréhension et modélisation de l’influence de la séquence d’empilement sur les scénarios d’endommagement dans des composites stratifiés de plis unidirectionnels.* PhD thesis, Université Paris-Saclay, 2023.

[131] V. B. Hammer, M. P. Bendsøe, R. Lipton, and P. Pedersen, “Parametrization in laminate design for optimal compliance,” *International Journal of Solids and Structures*, vol. 34, pp. 415–434, Feb. 1997.

[132] D. M. J. Peeters, *Design Optimisation of Practical Variable Stiffness and Thickness Laminates.* Thesis, Delft University of Technology, 2017.

[133] S. W. Tsai and T. H. Hahn, *Introduction to Composite Materials.* Lancaster: Technomic Publishing Company, 1980.

[134] S. W. Tsai and N. H. Pagano, “Invariant properties of composite materials,” tech. rep., 1968.

[135] S. T. IJsselmuiden, *Optimal Design of Variable Stiffness Composite Structures Using Lamination Parameters.* PhD thesis, Delft University of Technology, 2011.

[136] Z. Wu, G. Raju, and P. M. Weaver, “Framework for the Buckling Optimization of Variable-Angle Tow Composite Plates,” *AIAA Journal*, vol. 53, pp. 3788–3804, July 2015.

[137] S. Setoodeh, M. M. Abdalla, and Z. Gürdal, “Design of variable–stiffness laminates using lamination parameters,” *Composites Part B: Engineering*, vol. 37, pp. 301–309, June 2006.

[138] M. A. Albazzan, R. Harik, B. F. Tatting, and Z. Gürdal, “Efficient design optimization of nonconventional laminated composites using lamination parameters: A state of the art,” *Composite Structures*, vol. 209, pp. 362–374, Feb. 2019.

[139] D. Peeters, D. van Baalen, and M. Abdallah, “Combining topology and lamination parameter optimisation,” *Structural and Multidisciplinary Optimization*, vol. 52, pp. 105–120, July 2015.

[140] X. Tong, W. Ge, X. Gao, and Y. Li, “Optimization of Combining Fiber Orientation and Topology for Constant-Stiffness Composite Laminated Plates,” *Journal of Optimization Theory and Applications*, vol. 181, pp. 653–670, May 2019.

[141] X. Tong, W. Ge, X. Gao, and Y. Li, “Simultaneous optimization of fiber orientations and topology shape for composites compliant leading edge,” *Journal of Reinforced Plastics and Composites*, vol. 38, pp. 706–716, Aug. 2019.

[142] R. Z. G. Bohrer and I. Y. Kim, “Concurrent topology and stacking sequence optimization of composite laminate plates using lamination parameters,” *Composite Structures*, vol. 276, p. 114556, Nov. 2021.

[143] Z. Hu, O. Vambol, and S. Sun, “A hybrid multilevel method for simultaneous optimization design of topology and discrete fiber orientation,” *Composite Structures*, vol. 266, p. 113791, June 2021.

[144] M. Montemurro, A. Pagani, G. A. Fiordilino, J. Pailhès, and E. Carrera, “A general multi-scale two-level optimisation strategy for designing composite stiffened panels,” *Composite Structures*, vol. 201, pp. 968–979, Oct. 2018.

[145] F. Savine, *Simultaneous optimization of unconventional stiffener layouts and composite layups applied to large cylindrical shell structures.* These de doctorat, Sorbonne université, June 2022.

[146] A. Jibawy, C. Julien, B. Desmorat, A. Vincenti, and F. Léné, “Hierarchical structural optimization of laminated plates using polar representation,” *International Journal of Solids and Structures*, vol. 48, pp. 2576–2584, Sept. 2011.

[147] M. Montemurro, A. Vincenti, and P. Vannucci, “Design of the elastic properties of laminates with a minimum number of plies,” *Mechanics of Composite Materials*, vol. 48, pp. 369–390, Sept. 2012.

[148] A. Vincenti, P. Vannucci, and M. R. Ahmadian, “Optimization of Laminated Composites by Using Genetic Algorithm and the Polar Description of Plane Anisotropy,” *Mechanics of Advanced Materials and Structures*, vol. 20, pp. 242–255, Mar. 2013.

[149] M. Montemurro, A. Vincenti, and P. Vannucci, “A Two-Level Procedure for the Global Optimum Design of Composite Modular Structures—Application to the Design of an Aircraft Wing,” *Journal of Optimization Theory and Applications*, vol. 155, pp. 24–53, Oct. 2012.

[150] M. Montemurro and A. Catapano, “A New Paradigm for the Optimum Design of Variable Angle Tow Laminates,” in *Variational Analysis and Aerospace Engineering: Mathematical Challenges for the Aerospace of the Future* (A. Frediani, B. Mohammadi, O. Pironneau, and V. Cipolla, eds.), Springer Optimization and Its Applications, pp. 375–400, Cham: Springer International Publishing, 2016.

[151] M. Montemurro, “An extension of the polar method to the First-order Shear Deformation Theory of laminates,” *Composite Structures*, vol. 127, pp. 328–339, Sept. 2015.

[152] M. Montemurro and A. Catapano, “On the effective integration of manufacturability constraints within the multi-scale methodology for designing variable angle-tow laminates,” *Composite Structures*, vol. 161, pp. 145–159, Feb. 2017.

[153] F.-X. Irisarri, D. H. Bassir, N. Carrere, and J.-F. Maire, “Multiobjective stacking sequence optimization for laminated composite structures,” *Composites Science and Technology*, vol. 69, pp. 983–990, June 2009.

[154] F.-X. Irisarri, M. M. Abdalla, and Z. Gürdal, “Improved Shepard’s Method for the Optimization of Composite Structures,” *AIAA Journal*, vol. 49, pp. 2726–2736, Dec. 2011.

[155] P. Vannucci and G. Verchery, “A special class of uncoupled and quasi-homogeneous laminates,” *Composites Science and Technology*, vol. 61, pp. 1465–1473, Aug. 2001.

[156] S. C. Tan, “A Progressive Failure Model for Composite Laminates Containing Openings,” *Journal of Composite Materials*, vol. 25, pp. 556–577, May 1991.

[157] A. A. Groenwold and R. T. Haftka, “Optimization with non-homogeneous failure criteria like Tsai–Wu for composite laminates,” *Structural and Multidisciplinary Optimization*, vol. 32, pp. 183–190, Sept. 2006.

[158] A. Catapano, B. Desmorat, and P. Vannucci, “Invariant formulation of phenomenological failure criteria for orthotropic sheets and optimisation of their strength,” *Mathematical Methods in the Applied Sciences*, vol. 35, no. 15, pp. 1842–1858, 2012.

[159] M. Akbulut and F. O. Sonmez, “Optimum design of composite laminates for minimum thickness,” *Computers & Structures*, vol. 86, pp. 1974–1982, Nov. 2008.

[160] G. Narayana Naik, S. Gopalakrishnan, and R. Ganguli, “Design optimization of composites using genetic algorithms and failure mechanism based failure criterion,” *Composite Structures*, vol. 83, pp. 354–367, June 2008.

[161] H. Ding, B. Xu, W. Li, and X. Huang, “Design of curvilinear variable-stiffness composites considering stiffness, strength and manufacturability,” *Structural and Multidisciplinary Optimization*, vol. 65, p. 244, Aug. 2022.

[162] J. Liu, J. Yan, and H. Yu, “Stress-constrained topology optimization for material extrusion polymer additive manufacturing,” *Journal of Computational Design and Engineering*, vol. 8, pp. 979–993, June 2021.

[163] M. Doğru, “An improved algorithm for optimization of composite plates using tsai-wu criteria,” *Journal of the Faculty of Engineering and Architecture of Gazi University*, vol. 32, pp. 821–829, Jan. 2017.

[164] H. A. Deveci, L. Aydin, and H. Seçil Artem, “Buckling optimization of composite laminates using a hybrid algorithm under Puck failure criterion constraint,” *Journal of Reinforced Plastics and Composites*, vol. 35, pp. 1233–1247, Aug. 2016.

[165] R. H. Lopez, M. A. Luersen, and E. S. Cursi, “Optimization of laminated composites considering different failure criteria,” *Composites Part B: Engineering*, vol. 40, pp. 731–740, Dec. 2009.

[166] F. X. Irisarri, F. Laurin, F. H. Leroy, and J. F. Maire, “Computational strategy for multiobjective optimization of composite stiffened panels,” *Composite Structures*, vol. 93, pp. 1158–1167, Feb. 2011.

[167] S. T. IJsselmuiden, M. M. Abdalla, and Z. Gürdal, “Implementation of Strength-Based Failure Criteria in the Lamination Parameter Design Space,” *AIAA Journal*, vol. 46, pp. 1826–1834, July 2008.

[168] A. Khani, S. T. IJsselmuiden, M. M. Abdalla, and Z. Gürdal, "Design of variable stiffness panels for maximum strength using lamination parameters," *Composites Part B: Engineering*, vol. 42, pp. 546–552, Apr. 2011.

[169] C. Fleury and L. A. Schmit, "Dual methods and approximation concepts in structural synthesis," Tech. Rep. NASA-CR-3226, Dec. 1980. NTRS Author Affiliations: California Univ. NTRS Document ID: 19810005835 NTRS Research Center: Legacy CDMS (CDMS).

[170] Z. Hong, D. Peeters, and Y. Guo, "Efficient strength optimization of variable stiffness laminates using lamination parameters with global failure index," *Computers & Structures*, vol. 271, p. 106856, Oct. 2022.

[171] A. Catapano and M. Montemurro, "On the correlation between stiffness and strength properties of anisotropic laminates," *Mechanics of Advanced Materials and Structures*, vol. 26, pp. 651–660, Apr. 2019.

[172] A. Catapano and M. Montemurro, "Strength Optimisation of Variable Angle-Tow Composites Through a Laminate-Level Failure Criterion," *Journal of Optimization Theory and Applications*, vol. 187, pp. 683–706, Dec. 2020.

[173] Y. Xu, Y. Gao, C. Wu, J. Fang, G. Sun, G. P. Steven, and Q. Li, "On design of carbon fiber reinforced plastic (CFRP) laminated structure with different failure criteria," *International Journal of Mechanical Sciences*, vol. 196, p. 106251, Apr. 2021.

[174] M. Kočvara, M. Stingl, and J. Zowe, "Free material optimization: recent progress," *Optimization*, vol. 57, pp. 79–100, Feb. 2008.

[175] J. Haslinger, M. Kočvara, G. Leugering, and M. Stingl, "Multidisciplinary Free Material Optimization," *SIAM Journal on Applied Mathematics*, vol. 70, pp. 2709–2728, Jan. 2010.

[176] A. G. Weldeyesus, "Free material optimization with local stress constraints for laminated structures," *Engineering Optimization*, vol. 52, pp. 567–582, Apr. 2020.

[177] E. Duriez, *Combining Eco-Design and Multiscale Topology Optimization for 3D printed microarchitectured structures.* PhD thesis, 2022.

[178] A. L. F. d. Silva, R. A. Salas, E. C. Nelli Silva, and J. N. Reddy, "Topology optimization of fibers orientation in hyperelastic composite material," *Composite Structures*, vol. 231, p. 111488, Jan. 2020.

[179] G. Verchery, "Les invariants des tenseurs d'ordre 4 du type de l'élasticité," *Mechanical Behavior of Anisotropic Solids/Comportment Méchanique des Solides Anisotropes*, pp. 93–104, 1982.

[180] C. Julien, *Conception Optimale de l'Anisotropie dans les Structures Stratifiées à Rigidité Variable par la Méthode Polaire-Génétique.* PhD thesis, UPMC, 2010.

[181] P. Vannucci and B. Desmorat, "Analytical bounds for damage induced planar anisotropy," *International Journal of Solids and Structures*, vol. 60-61, pp. 96–106, May 2015.

[182] G. Cheng and P. Pedersen, "On sufficiency conditions for optimal design based on extremum principles of mechanics," *Journal of the Mechanics and Physics of Solids*, vol. 45, pp. 135–150, Jan. 1997.

[183] A. Vincenti and B. Desmorat, "Optimal Orthotropy for Minimum Elastic Energy by the Polar Method," *Journal of Elasticity*, vol. 102, pp. 55–78, Jan. 2011.

[184] P. Vannucci, "A Special Planar Orthotropic Material," *Journal of elasticity and the physical science of solids*, vol. 67, pp. 81–96, May 2002.

[185] P. Vannucci, "On Special Orthotropy of Paper," *Journal of Elasticity*, vol. 99, pp. 75–83, Mar. 2010.

[186] P. Pedersen, “On optimal orientation of orthotropic materials,” *Structural optimization*, vol. 1, pp. 101–106, June 1989.

[187] B. Desmorat, “Structural rigidity optimization with frictionless unilateral contact,” *International Journal of Solids and Structures*, vol. 44, pp. 1132–1144, Feb. 2007.

[188] K. Svanberg, “MMA and GCMMA – two methods for nonlinear optimization,” tech. rep., 2007.

[189] M. Bruyneel, P. Duysinx, and C. Fleury, “A family of MMA approximations for structural optimization,” *Structural and Multidisciplinary Optimization*, vol. 24, pp. 263–276, Oct. 2002.

[190] M. Fanni, M. Shabara, and M. Alkalla, “A Comparison between Different Topology Optimization Methods.,” *MEJ. Mansoura Engineering Journal*, vol. 38, pp. 13–24, Dec. 2013.

[191] E. Panettieri, M. Montemurro, and A. Catapano, “Blending constraints for composite laminates in polar parameters space,” *Composites Part B: Engineering*, vol. 168, pp. 448–457, July 2019.

[192] G. Kreisselmeier and R. Steinhauser, “Systematic control design by optimizing a vector performance index,” in *Computer Aided Design of Control Systems* (M. A. Cuenod, ed.), pp. 113–117, Pergamon, Jan. 1980.

[193] J. R. R. A. Martins and N. M. K. Poon, “On structural optimization using constraint aggregation,” in *Proceedings of the 6th World Congress on Structural and Multidisciplinary Optimization*, (Rio de Janeiro, Brazil), May 2005.

[194] P. Vannucci, *Anisotropic Elasticity.* No. 85 in Lecture Notes in Applied and Computational Mechanics, Singapore: Springer Singapore : Imprint: Springer, 1st ed. 2018 ed., 2018.

[195] S. Li, M. Xu, and E. Sitnikova, “The Formulation of the Quadratic Failure Criterion for Transversely Isotropic Materials: Mathematical and Logical Considerations,” *Journal of Composites Science*, vol. 6, p. 82, Mar. 2022.

[196] E. Lindgaard and J. Dahl, “On compliance and buckling objective functions in topology optimization of snap-through problems,” *Structural and Multidisciplinary Optimization*, vol. 47, no. 5, pp. 409–421, 2013.

[197] Coniglio Simone, *Optimisation topologique à formalisme Eulérien et Lagrangien appliquée à la conception d’un ensemble propulsif.* PhD thesis, Institut Supérieur de l’Aéronautique et de l’Espace, 2019.

Appendix A

Tsai-Wu Criterion Strain Invariants

The conservative strain envelope dictated by a Tsai-Wu criterion for possible orientation is presented in more details here, with the relationship to the material properties. It is a summary of the work by IJsselmuiden *et al.* [167]. Figure A.1 shows the two possible cases, where the admissible space is either dictated by a second-order or fourth-order envelope depending on the base ply's mechanical properties. The different envelope are defined by the positive real roots s_1 of Equation A.1, where the envelope linked to the smallest s_1 is the most critical one. In case of the fourth-order envelope condition, two s_1 and therefore distinct envelopes are defined. The admissible space is then determined by the common space to both fourth-order envelope, still represented by the lowest s_1. As the type of envelope is a property of the base ply, once the type of envelope is *a priori* known, it is remains constant during the optimization and can be implemented as a constraint.

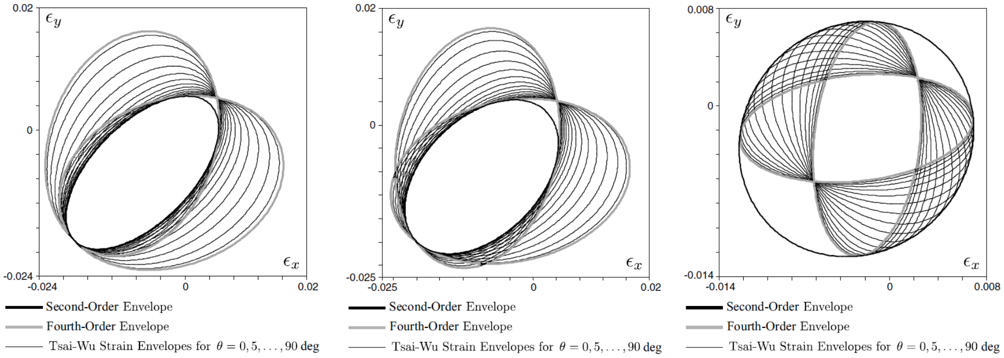

Figure A.1: Second-order and fourth-order strain envelopes for any ply orientation for a Tsai-Wu failure criterion [167].

$$\begin{aligned} f_1(s_1) &= a_{12}s_1^2 + a_{11}s_1 + a_{10} \\ f_2(s_1) &= a_{24}s_1^4 + a_{23}s_1^3 + a_{22}s_1^2 + a_{21}s_1 + a_{20} \end{aligned} \tag{A.1}$$

The different a_{10} - a_{24} coefficients are given by Equation A.2, based on the strain invariants I_1 and I_2, defined in Equation A.3, and the material properties $u_1 - u_6$ given in Equation A.4.

$$\begin{aligned} a_{10} = u_4^2 + 4u_1 - 4u_6; a_{11} &= -4u_2 I_1(u_1 - u_6) + 2u_4 u_5 I_1 \\ a_{12} &= 4u_6^2 I_2^2 - 4u_3 I_1^2(u_1 - u_6); a_{20} = 1 \\ a_{21} = -2u_2 I_1; a_{22} &= -2u_3 I_1^2 + u_2^2 I_1^2 - I_2^2\left(u_4^2 + 2u_1\right) \\ a_{23} &= 2u_2 I_1^3 u_3 - I_2^2(2u_4 u_5 I_1 - 2u_1 u_2 I_1) \\ a_{24} &= u_1^2 I_2^4 - I_2^2\left(u_5^2 I_1^2 - 2u_1 u_3 I_1^2\right) + u_3^2 I_1^4 \end{aligned} \tag{A.2}$$

$$\begin{aligned} I_1 &= \varepsilon_x + \varepsilon_y \\ I_2 &= \sqrt{\left(\frac{\varepsilon_x - \varepsilon_y}{2}\right)^2 + \left(\frac{\gamma_{xy}}{2}\right)^2} \end{aligned} \tag{A.3}$$

$$\begin{aligned} u_1 = G_{11} + G_{22} - 2G_{12}; u_2 &= \frac{G_1 + G_2}{2} \\ u_3 = \frac{G_{11} + G_{22} + 2G_{12}}{4}; u_4 &= G_1 - G_2 \\ u_5 = G_{11} - G_{22}; u_6 &= G_{66} \end{aligned} \tag{A.4}$$

The G coefficients are dependent on the stiffness and strength properties according to Equation A.5. Q_{ii} are the components of the stiffness tensor of the UD base ply, whereas F_{ii} are the strength properties of a Tsai-Wu failure criterion with F_{12}^* equal to -0.5 obtained from Equation A.6. X_t and X_c are the magnitude of the tensile and compressive allowables along the fiber direction, whereas Y_t and Y_c represent the magnitude of the traverse allowables. Lastly, S is the magnitude of the shear strength. Both Q_{ii} and F_{ii} are computed in the material reference frame, and remain constant for a given base ply.

$$\begin{aligned} G_{11} &= Q_{11}^2 F_{11} + Q_{12}^2 F_{22} + 2F_{12} Q_{11} Q_{12} \\ G_{22} &= Q_{12}^2 F_{11} + Q_{22}^2 F_{22} + 2F_{12} Q_{12} Q_{22} \\ G_{12} &= Q_{11} Q_{12} F_{11} + Q_{12} Q_{22} F_{22} + F_{12} Q_{12}^2 + F_{12} Q_{11} Q_{22} \\ G_1 &= Q_{11} F_1 + Q_{12} F_2; G_2 = Q_{12} F_1 + Q_{22} F_2 \\ G_{66} &= 4Q_{66}^2 F_{66} \end{aligned} \tag{A.5}$$

$$\begin{aligned} F_{11} = \frac{1}{X_t X_c}; F_{22} &= \frac{1}{Y_t Y_c}; F_1 = \frac{1}{X_t} - \frac{1}{X_c} \\ F_2 = \frac{1}{Y_t} - \frac{1}{Y_c}; F_{12} &= \frac{-1}{2\sqrt{X_t X_c Y_t Y_c}}; F_{66} = \frac{1}{S^2} \end{aligned} \tag{A.6}$$

The strain envelope is also applicable with out-of-plane displacement in shell kinematics. The most critical strain is then obtained as a combination of the in-plane strains ε, the local curvature κ and the through the thickness location from the mid-plane z, according to Equation A.7.

$$\varepsilon = \varepsilon + \kappa z \tag{A.7}$$

Appendix B

Finite Element Model

This appendix details the Finite Element Model implementation. It is constructed for a four node 2D linear plane element with a plain stress assumption. The elements are defined with an isoparametric representation, using a change to natural coordinates (ξ and η) to compute all required information. The natural coordinates are expressed by means of Equation B.1 from the element's node coordinate (x and y) and their respective dimensions (l and w).

$$\begin{aligned} \xi &= \frac{2x}{l} - 1 \\ \eta &= \frac{2y}{w} - 1 \end{aligned} \tag{B.1}$$

Linear shape functions are used, resulting in the strain-displacement relationship $[B]$ according to Equation B.2. $\boldsymbol{\varepsilon}_{(i)}$ are the element's strains, whereas $\boldsymbol{U}_{(i)}$ are the node's displacement, with u and v are respectively the nodal displacement in the x and y direction. The $[B]$ matrix is computed as $[B] = [A][M]$. $[A]$ is obtained from the Jacobian $[J]$ according to Equation B.4 and Equation B.5. $[M]$ is defined by means of Equation B.6.

$$\boldsymbol{\varepsilon}_{(i)} = [B]\boldsymbol{U}_{(i)} \rightarrow \begin{Bmatrix} \varepsilon_x \\ \varepsilon_y \\ \gamma_{xy} \end{Bmatrix}_{(i)} = [B] \begin{Bmatrix} u_1 \\ v_1 \\ u_2 \\ v_2 \\ u_3 \\ v_3 \\ u_4 \\ v_4 \end{Bmatrix} \tag{B.2}$$

$$[B] = [A][M] \tag{B.3}$$

$$[J] = \begin{bmatrix} \frac{\partial x}{\partial \xi} & \frac{\partial y}{\partial \xi} \\ \frac{\partial x}{\partial \eta} & \frac{\partial y}{\partial \eta} \end{bmatrix} \tag{B.4}$$

$$[A] = \frac{1}{\det[J]} \begin{bmatrix} J_{22} & -J_{12} \\ -J_{21} & J_{22} \end{bmatrix} \tag{B.5}$$

$$[M] = \frac{1}{4} \begin{bmatrix} -(1-\eta) & 0 & (1-\eta) & 0 & (1+\eta) & 0 & -(1+\eta) & 0 \\ -(1-\xi) & 0 & -(1+\xi) & 0 & (1+\xi) & 0 & (1-\xi) & 0 \\ 0 & -(1-\eta) & 0 & (1-\eta) & 0 & (1+\eta) & 0 & -(1+\eta) \\ 0 & -(1-\xi) & 0 & -(1+\xi) & 0 & (1+\xi) & 0 & (1-\xi) \end{bmatrix} \tag{B.6}$$

The elementary stiffness matrix $[k_{(i)}]$ is then given by Equation B.7. A reduced integration scheme is used to solve the integral of Equation B.7, resulting in Equation B.8. $[Q_{(i)}]$ is the matrix representation in Voigt's basis of the element's stiffness tensor. The point $(0,0)$ is the integration point in the natural coordinates of the elements. The strain vector $\boldsymbol{\varepsilon}_{(i)}$ used in the strength analysis is also computed at the $(0,0)$ integration point with the $[B]$ matrix.

$$[k_{(i)}] = \iint_{\eta\xi} [B]^T [Q_{(i)}][B] \det[J] d\eta d\xi \tag{B.7}$$

$$[k_{(i)}] \approx 2[B(0,0)]^T [Q_{(i)}][B(0,0)] \tag{B.8}$$

Incorporating strength constraints in a simultaneous material anisotropy and topology optimization of composite laminate structures

This research funded by Airbus Atlantic focuses on merging material and structural design further. A density-based framework for topology optimization is adopted, in which material anisotropic stiffness is incorporated as additional design variables. Material stiffness is characterized by means of the polar parameters, an invariant-based representation of the elasticity tensor. The considered design space of the polar parameters is described by the thermodynamic bounds for the general case of 2D orthotropic materials, or by the geometric bounds to restrict the scope to composite laminates. In the optimizations, either domain of existence is enforced through a remapping as optimization bounds. A gradient-based optimization strategy is formulated based on the Method of Moving Asymptotes, in which density and anisotropy variables are optimized in parallel. The method is validated against optimality criteria optimizations for compliance minimization. Thereafter, strength constraints are incorporated for topology and unidirectional fiber steering optimizations using a lower KS aggregation method. Elliptic stress criteria, such as the Tsai-Wu failure criterion, are considered to define material failure. As these criteria are expressed in the material reference frame, the rotation effect of the fiber is taken into account for the computation of both the optimization constraint and its gradient. Finally, to extend strength considerations to the more general case of laminates, a conservative strain envelope is employed. This envelope represents the maximal allowed deformation for any possible ply orientation. The corresponding optimization constraint is formulated based on the strains in the global frame. To this end, a strain-based topology framework is proposed and validated against stress-based optimizations with isotropic material. Finally, the method is applied to show the influence of material anisotropy, both for stiffness and strength, on the optimized solutions.

Keywords: DISTRIBUTED ANISOTROPY; SIMP; POLAR PARAMETERS; STRESS; STRAIN; ELLIPTIC FAILURE CRITERION

Incorporation de contraintes de résistance dans une optimisation simultanée de la topologie et de l'anisotropie de structures composites stratifiés

Cette recherche financée par Airbus Atlantic a pour ambition de combiner la conception du matériau et celle de la structure. Une approche d'optimisation topologique basée sur la densité est adoptée, dans laquelle la rigidité anisotrope des matériaux est incorporée comme variable de conception supplémentaire. La rigidité des matériaux est caractérisée au moyen des paramètres polaires, une représentation du tenseur d'élasticité basée sur des invariants. L'espace de conception des paramètres polaires est décrit par les bornes thermodynamiques dans le cas général des matériaux orthotropes 2D, ou par les bornes géométriques pour restreindre le champ d'application aux stratifiés composites. Dans les optimisations, l'un ou l'autre domaine d'existence est converti en bornes d'optimisation au moyen d'une opération de changement de variable. Une stratégie d'optimisation à gradient basée sur la méthode des asymptotes mobiles (*Method of Moving Asymptotes*) est proposée, dans laquelle les variables de densité et d'anisotropie sont optimisées en parallèle. La méthode est validée en comparant avec une méthode à critère d'optimalité pour la minimisation de la compliance. Par la suite, des contraintes de résistance sont incorporées dans l'optimisation topologique de pièces composites unidirectionnelles, pour lesquelles l'anisotropie du matériau est paramétrée par l'orientation de la fibre, en utilisant une méthode d'agrégation de type *lower* KS. Des critères elliptiques en contraintes, tels que le critère de rupture Tsai-Wu, sont considérés pour définir la tenue mécanique du matériau. Ces critères étant exprimés dans le repère local du matériau, l'effet de rotation de la fibre est pris en compte pour le calcul de la contrainte d'optimisation et de son gradient. Enfin, pour étendre la prise en compte de la résistance au cas plus général des stratifiés, une enveloppe de déformation maximale admissible est utilisée. Cette enveloppe représente la déformation maximale autorisée pour toutes les orientations possibles de plis. La contrainte d'optimisation correspondante est formulée à partir des déformations exprimées dans le repère global. À cette fin, une approche d'optimisation topologique basée sur les déformations a été proposée et validée par rapport à des optimisations basées sur les contraintes mécaniques dans le cas d'un matériau isotrope. Enfin, la méthode est appliquée pour montrer l'influence de l'anisotropie du matériau, tant pour la rigidité que pour la résistance, sur les solutions optimisées.

Mots clés : ANISOTROPIE DISTRIBUEE ; SIMP ; PARAMETRES POLAIRES ; CONTRAINTES MECANIQUES ; DEFORMATION ; CRITERE DE RUPTURE ELLIPTIQUE

ONERA
THE FRENCH AEROSPACE LAB

BP 80100 - Chemin de la Hunière FR-91123 PALAISEAU CEDEX - Tél. : +33 1 80 38 60 60 - Fax : +33 1 80 38 65 10

www.onera.fr